JAERI-M
88-271

BREAK LOCATION EFFECTS ON PWR SMALL BREAK LOCA PHENOMENA

— INADEQUATE CORE COOLING IN LOWER PLENUM BREAK TEST AT LSTF —

January 1989

Mitsuhiro SUZUKI

日本原子力研究所
Japan Atomic Energy Research Institute

JAERI-Mレポートは，日本原子力研究所が不定期に公刊している研究報告書です。
入手の問合わせは，日本原子力研究所技術情報部情報資料課（〒319-11茨城県那珂郡東海村）あて，お申しこしください。なお，このほかに財団法人原子力弘済会資料センター（〒319-11茨城県那珂郡東海村日本原子力研究所内）で複写による実費頒布をおこなっております。

JAERI-M reports are issued irregularly.
Inquiries about availability of the reports should be addressed to Information Division Department of Technical Information, Japan Atomic Energy Research Institute, Tokai-mura, Naka-gun, Ibaraki-ken 319-11, Japan.

©Japan Atomic Energy Research Institute, 1989

編集兼発行　日本原子力研究所
印　　刷　いばらき印刷㈱

JAERI-M 88-271

Break Location Effects on PWR Small Break LOCA Phenomena
-Inadequate Core Cooling in Lower Plenum Break Test at LSTF-

Mitsuhiro SUZUKI

Department of Reactor Safety Research
Tokai Research Establishment
Japan Atomic Energy Research Institute
Tokai-mura, Naka-gun, Ibaraki-ken

(Received December 26, 1988)

The report presents experimental results of a small lower plenum break test of SB-PV-01 conducted at the Large-Scale Test Facility (LSTF) of the Rig-of-Safety Assessment (ROSA)-IV※ program. This test simulates a loss-of-coolant accident (LOCA) caused by instrument tubes break (break area corresponds to 0.5% of the cold leg flow area) in a Westinghouse-type pressurized water reactor (PWR) assuming both manual actuation for all of the high pressure injection (HPI) systems and failure of the auxiliary feedwater systems. The report clarifies long-term system responses, especially the core cooling conditions related to the primary mass inventory. Also it clarifies break location effects on small break LOCA phenomena by comparing other five similar LOCA tests with break locations at cold leg, hot leg, upper head, pressurizer top (TMI-type) and SG U-tubes. It is concluded that the lower plenum break is the severest on core heatup due to the highest break flow rate and the least primary mass recovery after the ECCS actuation among the six tests.

Keywords : ROSA-IV, LSTF, PWR, Small Break LOCA, Core Cooling, Lower Plenum Break, Break Locations, Mass Inventory, ECCS

※ ROSA-IV Group ; Reactor Safety Laboratory 1
Kanji TASAKA, Yutaka KUKITA, Yasuo KOIZUMI, Yoshinari ANODA
Mitsuhiro SUZUKI, Hideaki ASAKA, Hiroshige KUMAMARU, Hideo
NAKAMURA, Taisuke YONOMOTO, Nobuo YAMAMOTO, Kazuo HIRATA,*1
Hiroyori MURAKAMI,*1 Hiroki GOTOH*1 and P. Clement*2

※ ROSA-IV Group ; Safety Facility Engineering Service Division
Motoji SHIMIZU, Tomosaburo OHKI, Yoshiyuki HANAWA, Hideo ITO
Hideki OHSAKI, Takao OHWADA, Tomotoshi NISHIKIZAWA and Masayuki
OGAWA

*1 On leave from Sumitomo Heavy Industry Ltd. (SHI)
*2 On leave from Commissariat at l'Energie Atomique (CEA), France

PWRの小破断冷却材喪失事故事象に及ぼす破断位置の影響
－LSTF下部プレナム破断実験における炉心冷却不全事象－

日本原子力研究所東海研究所原子炉安全工学部
鈴木　光弘

（1988年12月26日受理）

本報はROSA－Ⅳ※計画の大型非定常試験装置（LSTF）において実施された下部プレナム小破断実験，SB－PV－01の結果をまとめたものである。この実験はウエスチングハウス型加圧水型原子炉（PWR）における計装管破断冷却材喪失事故（LOCA）を想定したものであり（破断面積は低温側配管流路面積の0.5％に相当する），全高圧注入系の手動作動と補助給水系不作動とを仮定した。本報は，下部プレナム破断実験における長時間のシステム挙動，特に，1次系保有水量と関連づけた炉心冷却条件を明らかにした。また同様の条件を持つ他の五実験，（低温側配管，高温側配管，上部ヘッド，加圧器頂部（TMI模擬）及び蒸気発生器Uチューブの破断実験）と比較することにより，小破断LOCAに及ぼす破断位置の影響について明らかにした。これらの中で最も炉心冷却が悪いのは下部プレナム破断である。

東海研究所：〒319－11 茨城県那珂郡東海村白方字白根2－4

※ROSA－Ⅳグループ；安全工学第1研究室
田坂　完二，久木田　豊，小泉　安郎，安濃田良成，鈴木　光弘，浅香　英明，熊丸　博滋
中村　秀夫，与能木泰介，山本　信夫，平田　和男，[*1]村上　洋偉，[*1]後藤　博樹，[*1]P.Clement[*2]

※ROSA－Ⅳグループ；安全試験技術室
清水　元治，大木友三郎，塙　嘉幸，伊藤　秀雄，大崎　秀機，大和田孝雄
錦沢　友俊，小川　政行

＊1　住友重工業（株）より派遣
＊2　仏国原子力庁より派遣

Contents

1. Introduction 1
2. Test Facility and Instrumentation 3
2.1 Test Facility 3
2.2 Instrumentation 4
3. Test Conditions and Procedure for SB-PV-01 Test 5
4. Data Reduction and Qualification 7
4.1 Data Reduction 7
4.2 Data Qualification 7
5. Experimental Results of 0.5% Lower Plenum Break Test, SB-PV-01 . 9
5.1 Major Events Related to Primary Pressure 9
5.2 Flow Patterns and Temperature Distribution in Primary Loops.. 11
5.3 Fluid Density and Water Level in Primary System 13
5.4 Primary Mass Distribution and Core Thermal Responses 16
5.5 Break Flow Rate and Discharged Primary Mass 20
5.6 Effect of ECCS on Primary Mass Balance 22
5.7 Estimation of Primary Mass Inventory 23
5.8 Fluid Behaviors in SG Secondary System and Other Data 26
5.9 Summary of 0.5% Lower Plenum Break Test Results 28
6. Effects of Break Locations on 0.5% Small Break LOCA Phenomena .. 33
6.1 Test Conditions for Six Break Location Parameter Tests 33
6.2 Brief Explanation of Five Test Results 35
6.3 Break Location Effects on Overall System Responses 42
6.4 Break Location Effects on Break Flow and Primary Mass Inventory 49
7. Conclusions 54
Acknowledgment 57
References 58

Appendix A Instrument Location 162
Appendix B Experiment Description Summary for SB-PV-01 188
Appendix C Measurement List and All Experiment Data (Microfiches) for SB-PV-01 193
Appendix D Estimation of Remaining Primary Mass in SB-PV-01 Test before HPI Actuation (t = 1670 s) 194

目　　次

1. 緒　言 …… 1
2. 試験装置及び計測 …… 3
2.1 試験装置 …… 3
2.2 計　測 …… 4
3. 0.5％下部プレナム破断，SB－PV－01の実験条件と手順 …… 5
4. データ処理及び評価 …… 7
4.1 データ処理 …… 7
4.2 データ評価 …… 7
5. 0.5％下部プレナム破断，SB－PV－01の実験結果 …… 9
5.1 1次系圧力と主要事象 …… 9
5.2 1次系ループの流動形態と温度分布 …… 11
5.3 1次系の流体密度及び水位 …… 13
5.4 1次系冷却水分布と炉心温度変化 …… 16
5.5 破断流量及び放出1次系水量 …… 20
5.6 1次系マスバランスに及ぼすECC流量の効果 …… 22
5.7 1次系保有水量の評価 …… 23
5.8 SG 2次系の流体挙動，その他のデータ …… 26
5.9 0.5％下部プレナム破断実験結果のまとめ …… 28
6. 0.5％小破断LOCAに及ぼす破断位置の影響 …… 33
6.1 6つの破断位置効果実験の実験条件 …… 33
6.2 5つの実験結果要約 …… 35
6.3 破断位置の全体的システム挙動に及ぼす影響 …… 42
6.4 破断位置の流出流量及び1次系保有水量に及ぼす影響 …… 49
7. 結　言 …… 54
謝　辞 …… 57
参考文献 …… 58
付録A 計測位置 …… 162
付録B SB－PV－01実験条件一覧 …… 188
付録C SB－PV－01の計測リスト及び全実験データ（マイクロフィッシェ） …… 193
付録D SB－PV－01実験におけるHPI作動前（1670 s）の1次系残存水量評価 …… 194

Abbreviations

ACC-Cold	: Cold water accumulator
ACC-Hot	: Hot water accumulator
ADQ	: Automatic data qualification
CA	: Chromel-Alumel thermocouple
CB	: Core barrel
CL-A,CL-B	: Cold leg of primary loop-A, Cold leg of primary loop-B
COL-A,COL-B	: Cross-over leg of primary loop-A, Cross-over leg of primary loop-B
CP	: Conduction probe
CPT	: Conduction probe with thermocouple
DC	: Downcomer
DP	: Differential pressure measurement
DT	: Temperature difference measurement
ECC	: Emergency core cooling
ECCS	: Emergency core cooling system
FE	: Flow rate measurement
HLA,HLB	: Hot leg of primary loop-A, Hot leg of primary loop-B
HPIS	: High pressure injection system
JC	: Jet condenser
LCP	: Lower core plate
LOCA	: Loss-of-coolant accident
LPIS	: Low pressure injection system
LSA,LSB	: Loop Seal A, Loop Seal B
LSTF	: Large Scale Test Faciltiy
LE	: Liquid level measurement
MF	: Momentum flux measurement
MI	: Miscellaneous measurement
PA	: Auxiliary feedwater pump
PCA,PCB	: Reactor coolant pump in primary loop-A, Reactor coolant pump in primary loop-B
PE	: Pressure measurement
PF	: Main feedwater pump
PH	: High pressure injection pump
PJ	: Charging pump
PL	: Low pressure injection pump
PORV	: Power operated relief valve
PPR	: Pressurizer spray pump
PR	: Pressurizer
PV	: Pressure vessel
PWR	: Pressurized water reactor
RHR	: Residual heat removal system
RO	: Orifice
ROSA-IV	: Rig of Safety Assessment Number 4
RV	: Relief valve
RWST	: Simulated refueling water storage tank
SBLOCA	: Small break loss-of-coolant accident
SGA,SGB	: Steam generator A, Steam generator B
ST	: Break flow storage tank
SV	: Safety valve
TC	: Thermocouple
TE	: Fluid temperature measurement
UCP	: Upper core plate
UCSP	: Upper core support plate
UH	: Upper head
UP	: Upper plenum

List of Tables

Table 2.1 Major design characteristics of LSTF and PWR
Table 2.2 LSTF instruments list

Table 3.1 Initial conditions for RUN SB-PV-01
Table 3.2 Operational setpoints and conditions for RUN SB-PV-01
Table 3.3 ECCS conditions for RUN SB-PV-01
Table 3.4 Core power decay curve

Table 5.1 Chronology of events for RUN SB-PV-01
Table 5.2 Collapsed water levels in primary system in SB-PV-01 test
Table 5.3 A time sequential list of transient maximum heater rod surface temperature during 1400 and 1800 s
Table 5.4 Maximum heater rod surface temperature during all test period in SB-PV-01 test
Table 5.5 Average break flow rates measured by Venturi meter and calculated from catch tank level change
Table 5.6 Injected HPI water calculated from RWST level data
Table 5.7 Estimation of primary remaining mass in SB-PV-01 test (t = 1670 s)
Table 5.8 Discharged and remaining masses for primary system in SB-PV-01 test

Table 6.1 Major test conditions for six break location parameter tests
Table 6.2 Comparison of break line pipings for six tests
Table 6.3 Chrolonogy of major events for six break location parameter tests
Table 6.4 Discharged primary fluid mass for six break location parameter tests
Table 6.5 Comparison of average break flow rates derived from ST level data for six tests
Table 6.6 Estimation of two-phase break flow conditions for five tests (assuming a constant slip ratio of K=5)
Table 6.7 Remaining primary fluid mass in five break location parameter tests

Table 6.8 Primary mass inventory ratio for key events in five tests
Table 6.9 Efficiency of ECC water accumulation in primary system

List of Figures

Fig. 1.1 Outline of 4-loop PWR
Fig. 1.2 Instrument tubes at the bottom of pressure vessel

Fig. 2.1 General structure of Large Scale Test Facility (LSTF)
Fig. 2.2 Break unit
Fig. 2.3 Details of ST tank
Fig. 2.4 Break flow line for SB-PV-01 test
(a) A vertical view, (b) A plane view
Fig. 2.5 Construction and configuration of break orifice
Fig. 2.6 Core cross section and heater rod arrangement

Fig. 3.1 ECCS actuation logic

Fig. 5.1 Representative pressures in primary and secondary systems related with major events
(a) Initial blowdown phase (until 450 s)
(a) Whole test period (until 3600 s)
Fig. 5.2 Water level in pressurizer
Fig. 5.3 Total core power
Fig. 5.4 Pressurizer heater power
Fig. 5.5 PC-A,B pump speeds
Fig. 5.6 Primary loop flow rates (high range)
(a) Loop-A, (b) Loop-B
Fig. 5.7 Fluid temperatures in pressurizer and loop-A and B
(a) Hot leg temperatures for operator detection
(b) Pressurizer and Loop-A, (c) Loop-B
Fig. 5.8 Fluid temperatures in downcomer, lower plenum, upper plenum and upper head
Fig. 5.9 Temperature distributions in primary system before break and before scram trip

Fig. 5.10 Fluid densities at loop-A hot leg
Fig. 5.11 Fluid densities at loop-A cold leg
Fig. 5.12 Fluid densities at loop-B hot leg
Fig. 5.13 Fluid densities at loop-B cold leg
Fig. 5.14 Collapsed water levels in up- and down-flow sides of six instrumented U-tubes in SG-A (a through f)
Fig. 5.15 Differential pressures in loop-seal regions
(a) Loop-seal A, (b) Loop-seal B
Fig. 5.16 Responses of PV mass inventory in SB-PV-01 test
(a) Water level and differential pressures in PV with timings of transient primary mass distribution
(b) Measuring spans for PV differential pressures
Fig. 5.17 Transient primary mass distribution for SB-PV-01 test
(a) Initiation of break (t = 0 s) ;
Forced circulation in subcooled primary system except for saturated pressurizer at 15.5 MPa
(b) Two-phase natural circulation (t = 520 s) ;
Phase separation at top of hot and cold legs at 8.2 MPa
(c) Reflux cooling mode at SGs (t = 1200 s) ;
Almost emptied U-tubes and cold legs at 8.1 MPa
(d) Initiation of core dryout (t = 1500 s) ;
Core mixture level decrease and small amount of remaining water in hot and cold legs at 8.0 MPs
(e) Detection of core dryout (t = 1670 s) ;
Superheated steam at hot legs, whole core dryout and no heat exchange at SGs at 7.9 MPa
(f) Before ACC and ACH actuation (t = 2050 s) ;
Lowest primary mass and downcomer mass recovery under HPI injection into cold legs at 4.6 MPa
Fig. 5.18 Representative heater rod surface temperatures in high-power bundle (B-15)
Fig. 5.19 Representative heater rod surface temperatures in middle-power bundle (B-22)
Fig. 5.20 Representative heater rod surface temperatures in low-power bundle (B-03)
Fig. 5.21 Representative heater rod surface temperatures at outer region of B-03 bundle
Fig. 5.22 Heater rod surface temperatures at nine axial elevetions

Fig. 5.23 Dryout and quench timings of heater rods and collapsed levels in upper and lower plena
Fig. 5.24 Break flow rate at No.2 Venturi-meter
Fig. 5.25 Fluid densities at break unit
Fig. 5.26 Integrated discharged water mass at catch tank
Fig. 5.27 ECC water injection flow rates
(a)HPI and charging systems
(b)Accumulators of ACC and ACH
Fig. 5.28 Water levels for ACC, ACH and RWST tanks
Fig. 5.29 Total injection flow rate compared with break flow rate
(a) Time responses of flow rates,
(b) Flow rates related to primary pressure
Fig. 5.30 Major events related to primary mass inventory in SB-PV-01 test
Fig. 5.31 Representative pressure at steam dome in SG-A and SG-B
Fig. 5.32 Wide range water levels in SG-A and SG-B
Fig. 5.33 Water flow rates in four SG downcomer pipngs
(a) SG-A, (b) SG-B
Fig. 5.34 Steam and feedwater flow rates
(a) SG-A, (b) SG-B
Fig. 5.35 Fluid temperatures in steam dome, feedwater and boiler section of SG-A
Fig. 5.36 Fluid temperatures in steam dome, feedwater and boiler section of SG-B
Fig. 5.37 Distribution of primary fluid temperatures at lowest level of six SG-A U-tubes (Position 1)
(a) Up-flow side, (b) Down-flow side
Fig. 5.38 Distribution of primary fluid temperatures at middle level of six SG-A U-tubes (Position 6)
(a) Up-flow side, (b) Down-flow side
Fig. 5.39 Distribution of primary fluid temperatures at highest level of six SG-A U-tubes (Positions 10-11)
Fig. 5.40 Fluid temperatures of injection water for HPI, charging system, ACC, ACH and in RWST
Fig. 5.41 Differential pressures in SG-A U-tubes
(a) Up-flow side, (b) Down-flow side
Fig. 5.42 Differential pressures in SG-B U-tubes
(a) Up-flow side, (b) Down-flow side

Fig. 5.43 Differential pressure across lower core support plate
Fig. 5.44 Differential pressure across upper core plate
Fig. 5.45 Differential pressure between upper head and downcomer top
Fig. 5.46 Differential pressure across PC-A pump
Fig. 5.47 Differential pressure across PC-B pump
Fig. 5.48 Conduction probe signals in SG-A U-tube 1 (Short tube)
Fig. 5.49 Conduction probe signals in SG-A U-tube 2 (Middle)
Fig. 5.50 Conduction probe signals in SG-A U-tube 3 (Long tube)

Fig. 6.1 Six break locations in the LSTF primary system
(a) Total system flow diagram
(b) Break locations in primary system
(c) Height and elevation of the LSTF system
Fig. 6.2 Total core power in six tests
(a) Power curve in a short range (until 1350 s)
(b) Power curve in a long range (until 7200 s)
Fig. 6.3 Major results for upper head break LOCA test (SP2)
(a) Primary and secondary pressures and primary flow rate
(b) Break flow rate and break density (Beam B)
(c) Water level and differential pressures
(d) Heater rod surface temperatures (high-power bundle)
Fig. 6.4 Major results for cold leg break LOCA test (SCC)
(a) Primary and secondary pressures and primary flow rate
(b) Discharged mass and reduced break flow
(c) Water level and differential pressures
(d) Heater rod surface temperatures (high-power bundle)
Fig. 6.5 Major results for hot leg break LOCA test (SH3)
(a) Primary and secondary pressures and primary flow rate
(b) ST level and reduced break flow
(c) Water level and differential pressures
(d) Heater rod surface temperatures (high-power bundle)
Fig. 6.6 Major results for pressurizer top break LOCA test (SB3)
(a) Primary and secondary pressures and primary flow rate
(b) Discharged primary mass in ST tank
(c) Water level and differential pressures
(d) Heater rod surface temperatures (high-power bundle)

Fig. 6.7 Major results for SG U-tube break LOCA test (SS1)
(a) Primary and secondary pressures
(b) Primary and break flow rates
(c) Water level and differential pressures
(d) Heater rod surface temperatures (high-power bundle)
Fig. 6.8 Comparison of primary pressure responses for six tests
(a) Early pressure transient (until 1350 s)
(b) Long pressure transient (until 7200 s)
Fig. 6.9 Effect of break elevations on key event timings (SB3 test with 0.45% break area)
Fig. 6.10 Comparison of PCT for five tests
Fig. 6.11 Comparison of discharged primary mass for six tests
Fig. 6.12 Effect of break elevations on average break flow rates and two-phase flow conditions for equivalent 0.5% break area
(a) Average break flow rates for two-phase and steam flows in five tests
(b) Average void fraction and steam quality in two-phase flow for five tests (assuming a constant slip ratio of K=5)
Fig. 6.13 Primary remaining fluid mass and key events in five tests (SB3 test with 0.45% break area)

1. Introduction

The severe reactor accident at the power plant of Three Mile Island Unit 2 (TMI-2)[(1)-(3)] in March 1979 led to a significant review on the reactor safety management and also to a extensive reorientation of the safety research program for the commercial-type light water reactor (LWR). The severer reactor accident at the power plant of Chernobyl Unit 4 in April 1986 indicated again the significance of the reactor safety management.

In the view-point of LWR thermal-hydraulic safety, it is important to keep the primary water level above the core top level and to keep the core cooling capability in any phases of loss-of-coolant accident (LOCA) or transient. In small break LOCAs and plant operational transients with long-term system responses, it is necessary to take account of some operator actions and/or multi-failure assumptions on the safety related equipments as in the two severe accidents. Therefore it is of great interest in LWR simulation systems to investigate the gravity controlling phenomena, interactions between the primary and secondary systems, and core cooling conditions during the small break LOCAs or transients with degraded safety related equipments.

Integral experiments for small break LOCAs and transients in a PWR system have been established[(4)-(7)] and performed[(8)-(51)] at the Large-Scale Test Facility (LSTF) in the Rig-of-Safety Assessment (ROSA)-IV program. The ROSA-IV/LSTF is a 1/48 volumetrically scaled pressurized water reactor (PWR) system with an electric heating core and full height components simulating a Westinghouse-type four-loop PWR with 3423 MWt core power (see Fig.1.1).

This LSTF research covers subjects on (A) experimental parameters of break areas, break orientations or configurations, break locations, and with or without some operator actions on the safety related equipments such as the emergency core cooling systems (ECCSs) in small break LOCAs, (B) various operational transients including the plant recovery procedures and (C) other key phenomena related to the core cooling conditions such as natural circulation flow and heat transfer mode at the steam generators (SGs) and core level depression mechanisms. In addition to these, (D) computer code assessments and model improvements have been performed.

The primary objectives of this report are to experimentally clarify (1) characteristic phenomena in a small break LOCA simulating an instant-

aneous rupture of 24 instrument tubes (see Fig.1.2, their total break area corresponds to 0.5% of the cold leg flow area) at bottom of the reactor pressure vessel (RPV), and (2) effects of primary system break location on the small break LOCA phenomena by using the LSTF system.

The 0.5% lower plenum break test of SB-PV-01 (SP1) was conducted as one of the break location parameter tests with assumptions of operator action on the high pressure injection (HPI) systems and failures of the auxiliary feedwater systems as in the TMI-2 accident. The effects of different break locations are investigated by comparing the experimental results of the following break location tests, i.e., the cold leg break of SB-CL-12 (SCC), hot leg break of SB-HL-03 (SH3), upper head break of SB-PV-02 (SP2), pressurizer top break (as a result of one PORV stuck-open, TMI-type) of AT-SB-03 (SB3) and 3.2 U-tubes break of SB-SG-01 (SS1) in addition to the SB-PV-01 test. The break area for the AT-SB-03 test was 0.45% of the scaled cold leg flow area. The break elevations are the lowest for the lower plenum break, highest for the pressurizer top and between these two extreme cases for other four break location tests.

Discussed in chapter 5 are the characteristic phenomena observed in the lower plenum break test including the thermal interactions between the primary and secondary systems, primary fluid flow patterns, discharged and remaining fluid masses, and consequent core thermal responses. An initial primary fluid mass for the LSTF system was experimentally derived. The effects of break location are described in chapter 6 with respect to the overall system responses, break flow rate and two-phase flow conditions, ECC water accumulation efficiency, primary mass inventory and core cooling conditions. All of the SB-PV-01 test data are presented in Appendix C (microfiche) in addition to their data qualification list.

In the previous study,[38] the effects of the lowest break location were shortly clarified on the break flow and both timings of the steam discharge at the break and the core dryout initiation. References (39) and (46) analyzed the mechanisms that controlled the break flow quality transitions especially in the cold leg and hot leg breaks, and the break location effects on the integrated break flow rate among five 0.5% break tests. However, the effects of break elevations on core cooling phenomena and transient primary mass inventory were not discussed in detail in these studies. These are precisely investigated in this report.

2. Test Facility and Instrumentation

2.1 Test Facility

The LSTF shown in Fig.2.1 is a 1/48 volumetrically scaled model of a Westinghouse-type 3423 MWt four-loop PWR and has the same major component elevations as the reference PWR. Furthermore, the LSTF is designed to be operated at the same high pressures and temperatures and in the same way of the principal component responses in an operational transient of the reference PWR.

Shown in Table 2.1 are major dimensions of the LSTF system. The four primary loops of the reference PWR are represented by two equal-volume loops. Therefore, a steam generator (SG) has a volumetric scaling factor of 1/24 to the reference PWR SG and has 141 U-tubes with full length simulation. The steam and feedwater systems are connected to each SG to simulate the secondary system responses in the LOCA or the transients in PWR. The pressurizer (PR) is connected to one of the hot legs (loop-A). The hot and cold legs were sized to conserve the volume scaling and the ratio of the length to the square root of pipe diameter, i.e., $L/\sqrt{D}$ for the reference PWR. Thus, the flow regime transitions in the primary loops will be simulated (reference 52).

The pressure vessel consists of the upper head, upper plenum, core, lower plenum and downcomer. The core bypass volume in the reference PWR is included in the downcomer region. The fluid volume distribution in these regions is similar to that in the reference PWR. And small leak flow paths in the PWR system are also simulated in the LSTF by the spray nozzles between the downcomer top and the upper head, and the leak lines between the hot legs and the downcomer.

The break line for the lower plenum break test is connected between the break unit (see Fig.2.2) and the catch tank (ST) vapor sparger pipe (see Fig.2.3) as shown in Figs.2.4 (a) and (b). The break flow is limitted by the break orifice (see Fig.2.5) with 7.2 mm I.D. in the break unit and is condensed in the ST tank, in which a 8B vapor sparger pipe with 89 × 7 holes of 9.0 mm I.D. at the lower surface is located at 1.42 m height above the tank bottom (see Fig.2.3). The same break orifice was used for other break location tests except for the pressurizer top break test (AT-SB-03), in which 6.83 mm I.D. (0.45% break area) orifice was used. The break lines between the break unit and the ST tank for six tests

differ each other. The primary fluid mass is discharged into the SG secondary system in the U-tube break test (SB-SG-01) and therefore, the ST tank is not used. The break orientation for the cold and hot leg breaks is horizontal at the middle of the pipe height.

Shown in Fig.2.6 is a cross sectional view of the LSTF core. There are 1064 heater rods and 104 non-heating instrumented rods in addition to the tie and dummy rods. The heater rods are arranged in square array. The heater rod bundle No.1-12 are the low-power rod bundles with radial peaking factor of 0.66, No.13-20 are the high-power rod bundles with the factor of 1.51 and No.21-24 are the middle-power rod bundles with the factor of 1.00. The axial peaking factor is 1.495 for all of the heater rods.

Three types of emergency core cooling systems (ECCSs) are prepared, i.e., the high pressure injection (HPI) and high pressure charging systems, two accumulators (ACC and ACH) and low pressure injection (LPI) system. The flow capacities of these ECCSs can cover 1/48 scaled flow rate of each full mode operation in the reference PWR.

2.2 Instrumentation

Over 2000 instruments shown in Table 2.2 are available for making various types of measurements in LSTF. The data in the plots are identified by a combination of a two-letter prefix indicating the type of measurement and a number unique to each instrument location. Detailed information on the measurements and instrumentation system is available in Appendix A and in reference (7).

Most numerous (about 70%) are the thermocouples that measure the fluid (TE) and metal wall (TW) temperatures and temperature differences (DT). Other conventional instruments include pressure (PE) and differential pressure (DP) transducers, liquid level meters (LE) based on differential pressure measurements, and flow meters (FE) using an orifice, venturi or nozzle. There are many conduction probes (CP) distributed to indicate the presence of liquid.

Advanced two-phase flow instruments, which include drag discs (MF) and three-beam gamma densitometers (DE), are prepared in engineering units (RC). The break flow rate is measured by the Venturi-flow meter and drag-disks in the break unit. The primary fluid mass discharged into the catch tank (ST) is measured by the water level change with an average water density.

3. Test Conditions and Procedure for SB-PV-01 Test

The major initial conditions of the lower plenum break test (SB-PV-01) are shown in Table 3.1. The test procedures were determined to minimize the effect of following design compromizes as follows.

The most important design scaling compromise was the 10 MW maximum core power limitation, 14% of the scaled reference PWR rated power. Therefore, the steady-state core mass flow rate was restricted to 14% of the 1/48 scaled value to simulate the rated condition of the temperature distribution in the PWR primary loop. The desired primary coolant flow rate was established by reducing the pump speed with the flow control valves (FCVs) in the cross-over leg fully open. At the time of break initiation, the primary loop flow rate was increased to simulate the primary pump coastdown characteristics after the reactor scram for the reference PWR.

The primary to secondary heat transfer was initially maintained at 10 MW, i.e., 14% of the scaled value. Since the LSTF steam generators (SGs) are geometrically scaled to the reference PWR, the 14% primary to secondary heat transfer rate was established by raising the initial secondary temperature such that the primary pressure and temperatuere were representative of the reference PWR.

Major operational setpoints and conditions including ECCS actuation logic for this test are shown in Fig.3.1 and summarized in Table 3.2. At a pressure of 12.97 MPa, the reactor scram was designed to trip with a time delay of 3 s. As the loss-of-offsite power concurrent with the reactor scram was assumed, the primary coolant pumps were to trip for simulation of coastdown, the steam flow control valves in the SG secondary system were to close and the main feedwater was to stop immediately after the reactor scram trip. The auxiliary feedwater operation was assumed to fail in both SG-A and SG-B.

The ECCS conditions are summarized in Table 3.3. In the SB-PV-01 test, all of the ECCSs were assumed to actuate. However, the high pressure injection (HPI) system and a high pressure charging system were assumed to actuate manually after the core dryout was detected by operators. The core dryout detection was determined by a more than 10 K higher fluid temperature above the saturated fluid temperature at one of the hot legs. The accumulators, ACC and ACH, were injected into cold leg A and cold leg B, respectively. The low pressure injection (LPI) system

was available for both cold legs. However, the LPI system was not actuated in the SB-PV-01 test because of the primary system pressure higher than the LPI pump head (1.2 MPa) for all test period.

The core power decay was set to decrease along the pre-programmed decay curve after 29s from the scram trip. A core power decay curve, which takes into account of the actnides and the delayed neutron effect, gives higher value than the ANS standard. The core power decay curve used in the experiments is included in digitized form in Table 3.4. The experiment description summary is shown in Appendix B. After establishing the initial primary conditions, the break was initiated by opening the break initiation valve.

The SB-PV-01 test was performed on Dec. 17 in 1986 and it took approximately 12 hours to heat-up the primary and secondary systems and to establish the test conditions prior to the test initiation. The data recording system was initiated prior to the break initiation until 3620 s after the break.

4. Data Reduction and Qualification

4.1 Date Reduction

The instrument signals (unit in volt) recorded by the data logger, YEWCOM 7000, are converted to engineering units using appropriate conversion equations and factors. Some instruments employing a differential pressure transducer, such as a flow meter (FE) or liquid level meter (LE), require calculation of the density of the fluid (single-phase) from the local pressure and fluid temperature data using a steam table. A detailed description of the data acquisition and reduction processes is given in the report.(53)

The two-phase flow instruments such as gamma densitometers, drag disks and turbine flow meters use conversion equations unique to the model type. The conversion factors required for each instrument must be determined in a systematic manner. The constants used in preparation of this report are based on the results of calibration tests conducted well before the present experiment, and are reasonably accurate. However, some instruments seem to change their response characteristics from test to test and a need for more rigorous and systematic means of determining the values of constants has been identified as a result of the data qualification effort described below.

4.2 Data Qualification

The data qualification method employed to prepare this report consisted of both automatic data qualification (ADQ) and manual qualification.

The ADQ checks failed instruments by comparing the steady state readings obtained before the break in each test with those from previous test having almost the same initial conditions in order to verify that the signal level has not changed drastically from the previous tests. It also compares the steady state signals with the similar readings of the instruments of the same type in proximity to check the consistency of each instrument reading. The software for ADQ is still under development, but is completed for checking all of the thermocouple data which accounts for about 70% of the 2000 channels.

Manual qualification was employed to check the rest of the

instrumentation. The conduction probes, about 20% of the data channels, were relatively easy to check failure and abnormal behavior because of the simplicity of the instrument response. Of the remaining 10%, those that suffer little from zero-level drift, such as pressure transducers, power meters, pump speed and vibration meters, and valve position indicators were also relatively easy to check inconsistent readings.

The relatively few measurements that required extensive manual qualification effort include the flow meters, differential pressure transducers, gamma densitometers and drag disk transducers. Zero-level shift due to static pressure effect was studied in detail based on the results of the static pressure effect calibration tests conducted in late 1984. The validity of the flow rate and differential pressure data depends mosty on whether or not the reading is in the sensitive region of the measurement range. The data from these instruments are presented with some corrections based upon calibration tests of each transducer.

The details of the measurement, such as measurement range and measurement identification (ID) name are summarized in the measurement list given in Appendix C in addition to their data validity. Each instrument is assigned a tag name which appears in the system description report, and a Function ID with which the data are identified in the data plots. The alphabetical prefix of the Function ID is uniquely associated with a particular type of instrument as shown in chapter 2.

5. Experimental Results of 0.5% Lower Plenum Break Test, SB-PV-01

Findings on the pressure responses, flow pattern, mass distribution and heater rod temperature responses in the primary system are shown in sections 5.1 through 5.4. The break flow rate, discharged primary mass and mass balance for the primary system are shown in sections 5.5 and 5.6. An initial primary fluid mass is estimated from the experiment results of total discharged mass and remaining mass at the time of core dryout detection in section 5.7 and the major events are also related to a calculated transient primary mass inventory. Experimental results for the SG secondary systems and U-tubes are shown in section 5.8. Principal results of SB-PV-01 test are summarized in section 5.9. All kinds of experiment data are presented in a form of microfiche in Appendix C.

5.1 Major Events Related to Primary Pressure

Major events observed in the SB-PV-01 test are described in this section and related to the primary pressure responses. Shown in Fig.5.1 and Table 5.1 are the pressurizer pressure, a representative of the primary system pressure, and timings of the major events.

After the break initiation, the pressure started to decrease due to water level decrease in the pressurizer (see Fig.5.2). At the same time, the primary pump speeds were raised to 1500 rpm to simulate the PWR primary flow characteristics after the reactor scram. The reactor scram, which was tripped at 82 s on a PR pressure of 12.97 MPa with a time delay of 3 s, tripped the turbine flow control valve closure (steam line closure), the main feedwater system isolation and the primary pumps coast-down.

The core power was maintained at 10 MW for 30 s after the reactor scram trip and then decreased along a pre-programmed power curve as shown in Fig.5.3, simulating 1/48-scaled heat transfer rate of the PWR core after the reactor scram. The pressurizer heater power, of which maximum capacity is 120 kW, was initially 28 kW and increased up to 80 kW to recover the PR pressure (see Fig.5.4). Power supply to the PR heater was tripped off at 70 s due to the PR water level lower than 1.0 m.

The PR pressure showed a temporary recovery at 93 s due to a PR water

level recovery (see Fig.5.2) caused by thermal expansion of the primary coolant, which was larger at that time than the continuing mass depletion through the break area. The coolant thermal expansion was mainly a result of decreased heat exchange through the SG U-tubes because the SG secondary pressure and fluid temperature increased after the steam line closure (82 s) under the core power of 10 MW in addition to the decreased primary flow rate after the pump coast-down initiation. The SG secondary pressure was automatically maintained by the relief valve operation between 8.2 and 7.8 MPa from 95 s (see section 5.8). Actually, the cold leg temperature increased gradually and the hot leg temperature increased rapidly at 93 s (see Figs.5.7 and 5.8).

The PR pressure began to decrease again at 122 s (10 s after the core power decrease). As the primary pressure approached the secondary pressure, the former initiated pressure oscillation at approximately 400 s due to the influence of pressure oscillation in the latter. Moreover, the evaporation in the cold legs (at 495 s in cold leg A and 518 s in cold leg B as shown by fluid density data in Figs.5.11 and 5.13) contributed to lower the depressurization rate.

The PR pressure was maintained slightly above or almost the same as the SG secondary pressure for a long time and became lower than the secondary pressure at 8 s after the continuous core heat-up initiation (1498 s). This means that the SGs functioned as a heat sink for the primary system before the core dryout initiation and as a heat source after it. Thereafter the heat input for the core mainly contributed to heat up the heater rods and slightly to heat up the saturated steam in the core.

After the core dryout detection by the operaters, the HPI systems were actuated at 1676 s and caused a rapid depressurization. The depressurization in the primary system was also promoted by two-phase discharge (1700 s) through the break and core power trip (1775 s). The accumulator injection started at 4.4 MPa for both cold legs and caused a pressure spike due to a temporary water seal at the lower plenum break line (see break line fluid density in Fig.5.25). Thus the ACC and ACH were injected in two times according to the primary pressure history.

The LPI system was not actuated in this test because the primary pressure was kept higher than the LPI pump head of 1.2 MPa under the condition of core power trip. It is necessary to actuate the LPI system for long-term core cooling. In order to actuate the LPI systems, it would be necessary to lower the primary system pressure below the LPI pump head by

manually operating the SG relief valves and/or the pressurizer relief valve.

The break valve was closed at 3095 s and the small break LOCA test, SB-PV-01, was completed.

5.2 Flow Patterns and Temperature Distribution in Primary Loops

Flow patterns in the primary loops, fluid temperature distribution in all the primary system and the hot leg temperature detection for the manual HPI actuation are shown in this section.

The primary pump speed (see Fig.5.5) was raised immediately after the break upto 1500 rpm and controlled along the pre-determined pump coast-down curve. The forced circulation, which is defined here as primary flow related to the primary pump rotation, was terminated by the pump trips of PC-A at 331 s and of PC-B at 517 s for the loop A and loop B, respectively.

Shown in Fig.5.6 (a) and (b) are the primary flow rates in loop A and loop B, respectively. The initial flow rate of 24.3 kg/s in one loop was raised to 44 - 46 kg/s within 14 s after the break and kept constant until the reactor scram trip. After the pump coast-down, the primary flow decreased rapidly. The hot leg flow rates lower than the cold leg flow rates after 116 s is not correct due to an effect of two-phase flow in the hot legs. At 114 s, a clear phase separation or a water level formation was observed in hot legs in both loops (see three-beams density data in Figs.5.10 and 5.12). The cold leg flow rates became incorrect from 495 s in loop A and 518 s in loop B, respectively due to the similar two-phase conditions.

After termination of forced circulation, the primary fluid was driven by the two-phase natural circulation, which gradually decreased accoding to the water level decrease in the SG U-tubes (see Figs.5.14 (a) through (f)) and finally stopped at 568 s in loop A and at 648 s in loop B. Thereafter, the primary fluid was almost stagnant. As the generated steam in the core passed through the upper plenum and hot legs, and condensed in the U-tubes forming the reflux cooling mode as shown in the next section, there was a very small mass transfer from the core to the SG U-tubes. However, they were not detected by the primary flow meters in the cold

legs.

Shown in Figs.5.7 (a),(b),(c) and 5.8 are the fluid temperatures in the primary system. In the initial state, the temperature difference between the hot and cold legs was 35 K in both loops. The cold leg and loop-seal temperatures slightly increased after the pump speed-up at the break time, and on the contrary, the hot leg temperature decreased. The temperature difference between the hot and cold leg became approximately 21 K after the pump speed-up with core power still being kept at 10 MW.

The primary fluid temperatue distribution is clearly shown in Fig.5.9. It is shown that the temperatures at the top of the downcomer and in the upper head deviated from the distribution due to the flow stagnation in these regions. The increased recirculation flow after the break and the decreased flow after the pump coast-down resulted in larger temperature change in hot legs than in cold legs because the cold leg temperatures were mainly controlled by the SG secondary fluid temperatures. The hot leg temperature increase at 93 s (see Figs.5.7 (a),(b)) was results of decreased core flow rate due to pump coast-down and the temperature increase in the SG secondary systems. The hot leg temperature showed saturation temperature at 114 s and thereafter followed the depressurization process toward the secondary system temperature, which was approximately 568 ± 3 K.

The core dryout detection was performed by the operators by finding a hot leg temperature increase more than 10 K above the saturation temperature at 1670 s. The hot leg temperature increased up to 600 K in maximum before the ACC injection. On the other hand, the upper plenum tempeature showed increase at 1540 s due to arrival of the superheated steam from the heated core and increased up to 642 K in maximum before the ACC injection time. As the upper plenum temperature showed more than 10 K higher value than the saturated temperature at 1600 s, an early core dryout detection by more than 70 s could be possible by detecting this temperature instead of the hot leg temperature.

The fluid temperatures in downcomer were similar to the cold leg temperature before the HPI actuation and slightly higher than the clod leg temperature after the accumulators injection. The lower plenum fluid temperature was similar to or slightly higher than the downcomer temperature for all the test period. After initiation of HPI systems, the cold

leg B temperature showed subcooling (1713 s) indicating the HPI water arrival. At the last phase of this test, the lowest temperature was observed at the cold legs among the primary system temperatures.

5.3 Fluid Density and Water Level in Primary System

The fluid density data, which were measured by gamma densitometers, and collapsed water levels measured by differential pressure instruments are useful to investigate the water distribution or void formation in the primary system.

Shown in Figs.5.10 and 5.11 are the three-beam densitometer data for loop A hot and cold legs, respectively. Shown in Figs.5.12 and 5.13 are those for loop B. A steam phase was clearly observed at the top of hot legs in both loops after 114 s (Beam A) and two-phase fluid was in the lower region (Beams B and C). This clear phase separation was observed for a long time after 114 s. The oscillation observed in the hot leg density data with a long cyclic time period (approximately 90 － 100 s) was due to the primary pressure oscillation, which was caused by the secondary pressure cyclic operation.

Emptying in both hot legs started at 1290 s and almost completed at 1390 s. Mass recovery in hot legs was observed twice as shown in density (Beams B and C), i.e., once after the accumulators injection and then in the later phase (2648 s). However, the Beam A did not show any water mass recovery in both hot legs.

The cold leg density data were also similar in both loops. A steam phase was observed at the top of cold leg at 495 s in loop A and 518 s in loop B (Beam A). The density data at Beams B and C followed the response of Beam A. It is shown that water mass remaining in cold legs was lesser than in the hot legs between 800 and 1390 s.

Reason of the larger mass residual in the hot legs can be ascribed to the small two-phase natural circulation flow in the core toward the SGs, which contributed to maintain the mixture level inside the core shroud higher than the hot leg nozzle level. On the other hand, both the generated steam after flashing in the cold legs and income flow through the downcomer top spray nozzles were not discharged from the cold leg region, which was closed at both ends by water, i.e., loop-seal region and down-

comer with remaining water.

Shown in Figs.5.14 (a) through (f) are the collapsed water levels in instrumented U-tubes (tube numbers 1 through 6) at the SG-A. The collapsed levels in upflow and downflow sides of U-tubes were calculated from the corresponding differential pressure data between the SG inlet plenum and top of U-tubes, and between the SG outlet plenum and top of U-tubes, respecti- vely. Nos.1 and 6 tubes are the shortest U-tubes (9.49 m in height), No.2 and 5 are middle (10.22 m in height) and No.3 and 4 are the longest U-tubes (10.96 m in height) among the 141 tubes.

The upflow side levels are initially higher than the downflow side levels due to the contribution of positive frictional pressure loss to the upflow side differential pressure and negative frictional pressure loss to the downflow side differential pressure. The frictional contribution diminished following the primary flow stagnation. The differences of water levels between upflow and downflow sides after the flow stagnation are due to difference of water mass remaining in both sides of U-tubes. The level decrease in the U-tubes started initially at 312 s in No.4 (longest) and No.6 (shortest) U-tube and lastly at 514 s in the No.5 middle U-tube. In the SG-B U-tubes, the level decrease started at 312 s in the No.3 (longest) U-tube and at 470 s in the No.5 (middle) U-tube. These water level responses were, therefore, similar between SG-A and SG-B.

Responses of local mass inventory in the cross-over legs (loop-seal regions) are indicated in each corresponding differential pressure data of Figs.5.15 (a) and (b). The water level began to decrease in the loop-seal downflow side at 1090 s for loop A and at 1237 s for loop B, and both levels reached the bottom immediately after the ACC injection. Thus, the loop-seal clearing occured at 2060 s. At 2366 s (immediately after the accumulators termination), the loop-seal region was filled again by cold ECC water (loop-seal reformation). Therefore, the injected cold water through the HPI systems and accumulators was mainly flowed into the downcomer until the loop-seal reformation.

Shown in Fig.5.16 (a) are the PV collapsed water level reduced from the differential pressure data between the PV top and bottom, and the other differential pressure data in lower plenum, downcomer and upper plenum, of which measuring locations are shown in Fig.5.16 (b). The timings of six typical transient phases in the SB-PV-01 test are shown in

Fig.5.16 (a) for reference in the next section. These differential pressure data indicate responses of the mass inventory in each region, i.e., mass distribution in the primary system, except for a short time of the forced circulation.

It is shown in the downcomer data that the collapsed water level was at the cold leg nozzle (EL 5.50 m at the center) during 482 and 886 s and thereafter decreased below the cold leg nozzle. The downcomer level decreased rapidly at 1464 s (at the elevation of EL 2.60 m) and reached the minimum level (EL 0.0 m) at 1686 s. The downcomer level slightly increased due to accumulation of HPI water and was higher than the lower plenum level. After the accumulator injection, the downcomer level temporarily decreased and then recovered rapidly.

The PV collapsed water level and the differential pressure data for lower and upper plena showed consistent responses as shown below. The PV level and the upper plenum (UP) differential pressure were maintained above or at the hot leg nozzle (EL 5.50 m at the center) for a long time and started to decrease rapidly at 1420 s. The UP region was filled by steam at 1449 s (drainage) and by water at 2254 s. The PV level reached an approximately constant value at 1710 s and increased abruptly at 2075 s (18 s after the accumulator injection).

The lower plenum differential pressure was held for a long time at a constant value of 11.8 kPa, which meant that the lower plenum was filled by water. This is important for an estimation of remaining water mass in the section 5.7. The lower plenum differential pressure decreased abruptly at 1645 s and reached an approximately constant value of 4 kPa, which corresponded to the downcomer bottom (EL −1.26 m) or the lower end of the core barrel at 1710 s. The PV water level and the lower plenum mass recovery were observed at the same time of 2072 s.

In the PV upper head (UH) region, three differential pressure measurements were installed (see Fig.A.10 in Appendix A), i.e., DPE331 in the upper region between the UH top and EL 7.83 m, DPE330 for the whole UH region between the UH top and EL 6.14 m including the upper core support plate, and DPE332 (see Fig.5.45) between the UH (EL 7.83 m) and top of the downcomer. The DPE 331 data showed that the UH level started to decrease at 217 s and reached the EL 7.83 m at 400 s. However, the UH water level in the lower region, especially in the lower well (EL 6.47−7.37 m), could not be derived from the data of DPE 330 and DPE 332. Thus the water level in the UH well was remained uncertain.

5.4 Primary Mass Distribution and Core Thermal Responses

In this section, transient mass distribution in the primary system is illustrated first at six typical time phases (see Fig.5.16) by summarizing the experiment results shown in the previous sections, and the resulting core thermal responses are described next.

Shown in Figs.5.17 (a) through (f) are illustrations of the primary mass distribution at six time phases. The collapsed water level in each region is reduced from the corresponding differential pressure data or the fluid density data and is summarized in Table 5.2. The six time phases are typical in the 0.5% lower plenum break LOCA test.

The first phase (a) is the time of break initiation and the primary fluid was in a subcooled condition except for the pressurizer. The core power of 10 MW (14% of 1/48 rated PWR power) was transported by the forced circulation flow to the SG secondary sides as in the rated condition of the reference PWR. The second phase (b; t = 520 s) shows that the primary fluid was in a two-phase condition and was driven by the natural circulation after the primary pump coast-down at a degraded core power of 1.74 MW (2.4% power). A steam phase was observed at the top of cold legs in addition to the hot legs. The pressurizer was already empty at this time. The SG U-tubes were almost covered by two-phase mixture and the collapsed water level in the upflow side was slightly higher than in the downflow side.

The third phase (c; t = 1200 s) shows the reflux cooling mode for the primary system. Namely the degraded core power of 1.4 MW (2.0% power) was mainly transported by the steam flow through the hot leg upper region and transfered to the secondary sides as a latent heat of the condensed water at the U-tube surfaces. The condensed water fell down to both sides of SG plena. The primary pressure was maintained for a long time at the secondary pressure, which had been controlled between 7.8 and 8.2 MPa by the automatical relief valve operation after the steam line closure. The hot leg fluid level was maintained highly for a long time, whereas that in the cold leg was very low. As the loop-seal water level started to decrease gradually at the downflow side, the remaining water flowed into the downcomer.

At the fourth phase (d; t = 1500 s), most of the primary water lost through the break except for the loop-seal and lower PV regions, and the

core mixture level started to decrease resulting in the continuous heater rod temperature excursion at position 8 (EL 3.05 m). The core power was 1.32 MW (1.8% power) at this phase. There was a slight water level difference between the downflow side and the upflow side of the loop-seal regions indicating a slightly higher pressure in the hot leg than in the cold leg. Therefore, a collapsed core water level, which was not measured directly in the test, could be expected to be slightly lower than the downcomer level (EL 2.45 m). After this phase the primary pressure became lower than the secondary pressure. The core bottom was uncovered at 1638 s after the break. It took 1390 s for the hot leg to be almost empty and 1420 s for the upper plenum water level to decrease below the hot leg elevation. The core bottom was uncovered only 140 s after this phase. This time period of 140 s is approximately 1/10 of the upper plenum water level decrease time after the break. Consequently the whole core was uncovered early in this lower plenum break test due to the continuous water discharge through the lowest break location.

The core dryout was detected by the superheated steam temperature in the hot legs for the HPI systems actuation at the fifth phase (e; t = 1670 s), at which the primary mass depletion still continued at the break line and the core power was 1.27 MW (1.8% power). An apparent two-phase discharge was observed in the break fluid density at 30 s after this phase. The primary mass inventory was quantitatively estimated at this phase as shown in section 5.7 and Appendix D. The HPI and charging systems were actuated immediately after this phase.

The last phase (f; t = 2050 s) shows the lowest primary mass inventory despite the injection of HPI water at the cold legs. The ACC and ACH were actuated at 7 s after this phase. The high temperature core, of which power had already been tripped at 1775 s, was quenched completely at 2248 s (191 s after the ACC and ACH actuations). The upper plenum was filled by water at 2266 s. Total amount of the accumulator water was sufficient to fill the core and upper plenum but insufficient to fill completely the hot legs and SG U-tubes.

Next the core thermal responses are shown below with respect to the heater rod temperature excursion during the fourth through sixth time phases shown above, and dryout and quench characteristics of heater rods related with the water level responses in the upper and lower plena.

The three kinds of heater rod bundles are the eight high-power bundles

with radial peaking factor of 1.51, four middle-power bundles with factor of 1.00 and low-power peripheral bundles with factor of 0.66. Shown in Figs.5.18, 5.19, 5.20 and 5.21 are the representative heater rod surface temperatures along the rod axis in the high-power bundle (B15), middle-power bundle (B22), low-power bundle (B03) and outer region of the B03 bundle, respectively. The thermocouple positions 1 and 9 show bottom and top of the core region, respectively.

At the high-power rod (4,4) in the bundle B15 (abbreviated as B15(4,4) rod), the highest power region at the middle height (Pos.5) showed the first temperature excursion at 1537 s, the lowest power regions at top of the rod (Pos.9) at 1579 s and bottom of the rod (Pos.1) at 1638 s, respectively. At the low-power rod B03(4,3), the first temperature excursion was observed at Pos.3,5 and 7 at the same time of 1587 s, Pos.1 at 1638 s and Pos.9 at 1668 s. The middle-power rod B22(5,4) showed earlier temperature excursion at 1507 s at Pos.7. Thus the timings of heater rod temperature excursions were widely distributed in the upper core region. On the other hand, the timings of heater rod quenching were almost the same in the same height.

The heater rod surface temperatures depicted in Fig.5.18 are shown in a different manner in Fig.5.22. The dryout and quench behavior of the heater rod are closely related to the PV water level responses as shown below. The dryout or quench timings for all the instrumented heater rods are shown in Fig.5.23. It is shown that the dryout initiation timings are widely distributed in the top core region (between 270 s after 1505 s at Pos.9) and that the responses of the earlier dryout front or the quench front agreed well to the extraporated collapsed water levels in the upper and lower plena. This means that the heater rod thermal responses are clearly dependent on a core water level in this phase.

Shown in Table 5.3 are a time sequential list of the maximum heater rod temperature at each time between 1400 and 1800 s. The first continuous temperature excursion was observed at 1498 s at Pos.8 of B18(4,4) rod. However, some temporary temperature rises above the steady values (between 575 and 578 K) were observed in various locations prior to this time. For example, Pos.4 of the high-power rod B20(4,4) showed 593 K only at 1446 s, which was 15 K higher than the stable values. These temperature fluctuations are due to an unstable thermal conditions on the heater rod surfaces probably caused by fluctuation of local void fraction and two-phase natural circulation in the core.

The maximum heater rod surface temperature of the SB-PV-01 test was observed at the time of core power trip (1775 s) at the highest power region of Pos.5 of B17(4,4) rod, as 925 K as shown in Table 5.4. The increased temperature was 347 K from the initiation of excursion and an average increasing rate was 1.43 K/s. The temperature decrease after 1775 s are due to core power trip.

The effect of radial power distribution is clearly shown in the temperature increasing rates after core dryout shown in these figures. In addition to this, a difference of local cooling condition was observed among the heater rods in the same peripheral bundle (B-03) by comparing the results in Figs.5.20 and 5.21. The outer heater rod showed lower temperature than the middle rod.

It is interesting to estimate the heater rod surface temperature response in a case of continuous core power supply in this test. If the accumulators were actuated at the same time as the test result, the highest power region of the heater rod (see Pos.5 in Fig.5.18) would exceed 1100 K at the time of 2057 s. The water mass recovery inside the core shroud would be delayed due to pressure increase after the ACC and ACH actuations, larger steam generation in the core and larger break mass flow rate than in the test results. Thus the core quenching would be delayed. As the ACC and ACH were stopped at each setpoint water level in the test, following core cooling must be performed by the HPI systems. The LPI systems could not be actuated as the primary system pressure would be higher than the test results. Therefore some active depressurization techniques would be neccesary for the system cool-down and LPI actuation, for example by conducting the SG depressurization and/or PR relief valve operation.

It can be concluded that a continuous core power generation would result in more severe thermal conditions in the core than the actual test results due to the highly increased heater rod temperature, larger amount of steam generation in the core reflooding phase, and higher primary system pressure after the accumulator actuations.

5.5 Break Flow Rate and Discharged Primary Mass

Break flow rate and the primary mass balance are described in this section. A valid data range for the break flow data measured by the Venturi flow meter is also discussed.

Shown in Fig.5.24 is the break flow rate measured by the Venturi meter located at the upstream-side of the break orifice in the horizontal break unit (see Fig.A.5 in Appendix A). The Venturi meter gives accurate data for single-phase water flow within a nominal accuracy of 1.12% F.S. (± 0.1 kg/s in flow rate). In addition to this, a small zero-level shift existed in the differential pressure data and it affected the flow rate accuracy by + 0.1 kg/s for water flow rate higher than 2.0 kg/s. Thus, an uncertainty of the Venturi data is estimated between −0.1 and +0.2 kg/s for the single-phase water flow higher than 2.0 kg/s.

A time period of the single-phase water flow is checked by results of the three-beam densitometer (Fig.5.25) located at the downflow side of the Venturi meter, and also by the fluid temperatures at the lower plenum (see Fig.5.8). The lower plenum fluid temperature gradually increased after the break. The subcooling temperature for the lower plenum fluid reached 4 K at 400 s and less than 2 K after 500 s. Therefore a single-phase water with more than 4 K subcooling flowed out from the lower plenum during the initial 400 s, and thereafter almost saturated water flowed out. The break fluid density data showed almost saturated water density (720 ± 43 kg/m^3) between 300 and 1700 s. Moreover, the three chord averaged densities agreed completely with each other until 1700 s indicating no apparent phase separation in the break unit during the time period. Anyhow, it is expected that the break flow rate measured by the Venturi meter is valid in a initial time period shorter than 400 s within the accuracy mentioned above. The break flow data beyond the time period can be refered as a qualitative results of the break flow.

The break fluid density also shows that a steam phase appeared at the top of break unit at 1700 s and a complete steam phase appeared in two times after 2000 s. Between 2075 and 2150 s the break unit was covered temporarily by water resulting a temporary pressure increase in the primary system and break flow increase. The break unit was covered again by water at 2540 s.

Shown in Fig.5.26 is the integrated discharged mass, which was calculated from the water level data in the ST tank compared with a time-integrated value of the Venturi flow data. These two data agreed well in the first 300 s. This fact indicates that the discharged mass is similarly accurate during the time period as in the break flow data. The discrepancy between the discharged mass and the time-integrated break flow rate was within 8% for the former for all the test period.

An accuracy of the discharged mass data may consist of four terms, i.e., (1) an uncertainty of the net level rise data, which are obtained from a difference of two differential pressure data between the initial time and the measuring time, (2) mass reduction error including a time averaging error for both the oscillating differential pressure data and water temperature distribution beyond the two measured data, and (3) transient fluid mass change in the discharge line piping between the break unit and the ST tank, i.e., an increase due to steam condensation at the cold pipe wall especially in the early blowdown phase, and a decrease due to purge of water initially remained in the pipings.

It can be shown that an uncertainty of the net level rise data is smaller than that of the level data itself (0.32% F.S.; ± 0.038 m in height and ± 0.202 m^3 in water volume) because a possible systematic error including a zero level shift can be eliminated by using the same level meter in the same test conditions. Moreover, a relative accuracy for the level change data bocomes smaller in the later test phase because the total discharged mass becomes large. The second term for the time averaging method can be negligible except for a short time after the break. As the fluid temperature distribution is not measured yet all over the catch tank water except for the two thermo-couples (see Fig.A.5 in Appendix A), an accuracy of the reduced average fluid density can not be determined. The third term is also unknown due to lack of experiment data. Thus, an uncertainty was not quantitatively determinedd for the discharged mass during all the test period.

However, a gross reliability of the data, which was already confirmed at least for the initial 300 s through the comparison with the break flow data, can be applied beyond the first 300 s because these uncertain factors are expected to be smaller in the later blowdown phase than in the initial phase. As one of the uncertainties, a scattering error around a smoothed average value was observed for the discharged mass fluctuations shown in Fig.5.26 as ± 60 kg during the test period of 1700 s (before the

high-quality two-phase discharge) and ± 70 kg after 1700 s. This scattering error of ± 70 kg is used as a representative uncertainty for the discharged mass in the primary mass estimation (see section 5.7).

The discharged primary mass (M_D) at the time of core dryout detection (1670 s) was,

$$M_D = 4760 \pm 70 \text{ kg}.$$

This value is used for the estimation of an initial primary fluid mass in section 5.7. The discharged mass at the end of HPI actuation was 7250 kg. Therefore, a discharged primary mass during the ECCS actuation time period (1676 – 3086 s) was 2490 kg, which corresponded to 65% of all of the injected ECC water mass (3850 kg, see the next section).

Compared in Table 5.5 are an average break flow rate in each 200 s reduced from the Venturi data and that reduced from the discharged mass data. The discrepancy was very small in the first 400 s and within ± 0.31 kg/s for all the test period. These values are compared with the total ECC water injection flow rate in the next section for the primary mass balance.

5.6 Effect of ECCS on Primary Mass Balance

Total ECC flow rate is compared in this section with the break flow rate on a view point of mass balance in the primary system after initiation of the HPI systems.

Shown in Fig.5.27 (a) are the HPI flow rates injected into the cold legs A and B between 1676 and 3086 s. A shift from zero value prior to the break initiation was an measuring error. The HPI flow rate in the cold leg B was smaller than that in the cold leg A as shown in the figure. Shown in Fig.5.27 (b) are the accumulator injection flow rates for the cold leg A (ACC) and the cold leg B (ACH). The ACC and ACH were actuated during 2057 and 2360 s.

Their total amount of water injected into the primary system were obtained from the water level data for the RWST, ACC and ACH tanks (Fig.5.28) as 2700 kg in 1410 s, 630 kg in 303 s and 520 kg in 303 s, respectively. Their average injection flow rates were 1.915kg/s for the HPI systems, 2.052 kg/s for the ACC and 1.694 kg/s for the ACH during each

injection time period. An average HPI flow rate at transient time period was also derived from the tank (RWST, 3.65 m I.D.) level data as shown in Table 5.6. The RWST level data showed a little undershoot value after its actuation time and it was corrected in the table. The HPI flow rate measured by a flow meter (see Fig.5.27 (a)) was consistently lower than the average HPI flow rate measured from the RWST level by less than 13%.

The total injection flow rate of the HPI systems is compared with the break flow rates as shown in Fig.5.29 (a) and (b). The break flow rate was larger than the total HPI flow rate above the system pressure of 4.6 MPa (between 2100 and 2200 s) indicating that full mode actuation of the HPI systems was not sufficient for the primary mass recovery until 4.6 MPa. However, the HPI systems significantly contributed to decrease the primary system pressure and to early actuate the accumulators.

It is clear that the primary fluid mass continuously decreased even after actuation of the full mode HPI systems above the primary pressure of 4.6 MPa and it recovered only by the accumulator systems in this 0.5% lower plenum break LOCA test. This result is due to the large break mass flow rate related with the low break location, which was covered by water level. In order to perform further mass recovery in the primary system, it was necessary to decrease the primary pressure for the LPI systems actuation.

5.7 Estimation of Primary Mass Inventory

Primary fluid masses at the initial and transient conditions are experimentally derived in this section.

An initial fluid mass of 5429 kg for the primary system has been obtained from the designed data shown in the facility system description and from the updated vessel inventory data. It is clear that some pipe lines connected to the primary system, like as the ECCS pipings, has not been considered for the initial mass inventory data as a dead volume. However, a certain amount of water, which initially remained in these additional pipings, can affect the primary mass inventory in the transient blowdown process after the break initiation. And some amount of this remaining water would be heated up during the heat-up process prior to the test initiation. However, there was no data to determine the fluid tem-

peratures for these water regions. What is the content of the "active" dead volume ?

A primary fluid mass of 5848 kg[54] was obtained by measuring the cold water flow rate in the water filling process and the draining flow rate in the heatup process for the initial test condition. The uncertainty, which mainly depends on those of the filling and draining flow rates, was not yet determined. In order to determine the contribution of the "active" dead volume in the actual LOCA experiment, it is necessary to determine the discharged fluid mass and remaining fluid mass at the end phase of the LOCA experiment.

A new initial primary fluid mass is experimentally determined for this test by using the discharged primary mass and remaining primary mass at 1670 s after the break. At this timing the whole core was already uncovered. As the fluid temperatures in the loop-seal region, downcomer and lower plenum were raised slightly higher than their initial values at this timing (see Figs.5.7 (a) and (b) and Fig.5.8), there was no heat release into the fluid from the surrounding metal heat structures in these regions, where primary water mainly remained at this timing. Moreover, the primary system was almost stable and void formation due to depressurization was also negligible. The whole core dryout, negligible void fraction and the least primary water mass in the almost stable phase are the best conditions for estimation of the remaining primary fluid mass in this system. There was no other test with these best conditions in the LSTF integral LOCA tests except for this SB-PV-01 test.

The primary remaining fluid mass was estimated by using the experiment data of the fluid densities, collapsed water levels and thermal-hydraulic conditions in addition to the system design data for each primary region as shown in Table 5.7 (details are shown in Appendix D). As there was no experiment data for the upper head water volume in the lower well (EL 6.47-7.37 m), the water level was assumed to be at the middle height of the upper head well accompanying an uncertainty. It is clear that the primary water mass at 1670 s was mainly distributed in the regions of the lower plenum and downcomer (53%) and cross-over legs (40%). The total water mass was obtained as 708 kg. Most of the primary components (more than 88% of the primary-system free volume) were filled by the saturated steam or super-heated steam, of which total weight was 292 kg. Thus the total remaining fluid mass (M_r) at 1670 s was,

M_r = 1000 ± 68 kg.

The uncertainty is mainly due to the undetermined upper head water mass.

As the discharged primary fluid mass was already obtained in section 5.6 as 4760 kg at 1670 s, the initial primary fluid mass was obtained as a sum of these masses, i.e., 5760 kg. By using the scattering error of the discharged mass of ± 70 kg, an accuracy of the initial primary fluid mass (M_o) can be shown as ± 138 kg. Therefore, it was obtained as,

M_o = 5760 ± 138 kg.

A discrepancy of 331 kg from the previously used data is much larger than the accuracy range and is considered to be mainly due to the "active" dead volume.

Next, a transient primary fluid mass at any time is calculated by subtracting the discharged mass from the initial primary mass including the injected ECC water mass estimated above. Shown in Fig.5.30 and Table 5.8 are the transient primary mass inventory during all the test period and related major events with their timings (see Table 5.1). The transient primary mass inventory (M) is also represented by a primary mass ratio of M/M_o, where M_o is the initial fluid mass shown above.

Fig.5.30 shows that the primary fluid mass decreased linearly until manual actuation of the HPI systems. The mass decreasing rate was lowered by the HPI actuation at 1676 s and also promoted by the apparent two-phase break flow after 1700 s.

The clear phase separation in the hot legs occured at the mass ratio of 93%. The level formation at the top of SG U-tubes occured between the mass ratios (transient mass devided by the initial mass) of 83 and 73%. The two-phase natural circulation almost stopped at the mass ratio of 62%. The cross-over leg levels started to decrease at the mass ratio of 45% in loop-A and at 38% in loop-B. The PV water level started to decrease (after the hot leg emptying) at the mass ratio of 29%. The core dryout was initiated at the mass ratio of 25% for the core top and at 19% for the core bottom. The primary mass recovered to 34% after the ACC and ACH actuation. The whole core was quenched at the mass ratio of 21%. The loop-seal clearing and reformation occured at 14 and 34%, respectively.

Mass balance during the HPI injection time period was as follows. As the remaining mass ratio was 17% at the HPI actuation time and the total injected ECC water was 67% of the initial mass, a sum of these two was 84% mass ratio. However, as 41% mass ratio remained in the primary

system, 43% mass ratio discharged through the break during this period. The discharged mass corresponded to 65% of the total injected ECC water. Thus, an efficiency of the ECC water accumulation in the primary system can be shown as 35% for this SB-PV-01 test.

It can be shown that there would be no water mass in the primary system if the HPI were delayed more than 400 s than the test result. The least primary mass was 14% at 1800 s. Although the LPI system had a capability of the injection flow rate of 12 kg/s at 0.9 MPa, it was not actuated in this test. After termination of the accumulators, it becomes important to actuate the LPI systems, and therefore a further depressurization becomes necessary for this LPI actuation.

5.8 Fluid Behaviors in SG Secondary System and Other Data

System responses in the SG secondary systems and SG U-tubes are described in this section.

Shown in Figs.5.31 are the pressures in the steam dome of SG-A and SG-B compared with the primary system pressure. The pressure responses in SG-A and SG-B are almost the same. The SG pressure began to increase immediately after the break due to the increased heat transfer rate at the U-tubes, which was a result of increased primary flow rate, and then decreased toward a thermal steady condition. The SG pressure began toincrease again rapidly after the steam line valve closure at 82 s. Thereafter the SG pressure was automatically controlled by the relief valve operations between 8.2 and 7.8 MPa. The primary pressure became lower than the secondary pressure at 1506 s (immediately after the core heat-up initiation). After this time, the SG-A and SG-B became heat sources for the primary system.

Shown in Fig.5.32 are the wide-range water levels in SG-A and SG-B. The downcomer water flow rates in four pipings for SG-A and SG-B are shown in Figs.5.33 (a) and (b), respectively. It is clearly shown that the natural circulation in the SG secondary system rapidly decreased 6 s after the steam line closure due to void collapse in the boiling section, which was caused by the rapid pressure increase in the secondary system. The secondary flow almost stopped at approximately 200 s accompanying some flow oscillations. The secondary water mass decreased due to steam dis-

charge through the relief valves and the collapsed water level decreased as shown in Fig.5.32. After termination of relief valve operation (1475 s), the level was at 7.9 m in SG-A and 7.8 m in SG-B. The gradual level decrease after the relief valve termination was due to the thermal contraction of the secondary fluid under the cotinuing depressurization.

Shown in Figs.5.34 (a) and (b) are the steam and feedwater flow rates in SG-A and SG-B, respectively. These flows were stopped at the reactor scram trip at 82 s.

Shown in Figs.5.35 and 5.36 are the fluid temperatures in the secondary systems of SG-A and SG-B, respectively. There was a small temperature distribution less than 6 K during the test period in the SG secondary system including steam dome, downcomer and boiler section. The feedwater temperature showed continuous decrease after the reactor scram trip due to heat loss through the surrounding structures.

Next, fluid temperatures and differential pressures across the primary side of the SG U-tubes are presented to show influences of little flow distribution among the tubes, and other experiment data including the differential pressure and conduction probe data are presented as follows.

Shown in Figs.5.37 (a)(b), 5.38 (a)(b) and 5.39 are the fluid temperatures in 6 SG-A U-tubes at Position 1 (lowest elevation), Position 6 (middle) and Positions 10 and 11 (highest elevations), respectively. There was no temperature distribution among the downflow sides and top part of the U-tubes. Slight temperature distribution was observed in the decreased forced circulation phase at 245 s at the lower region of upflow side in in No.2 (middle length) and No.3 U-tubes (longest), of which temperatures were almost the U-tube exit temperature or the secondary fluid temperature. This means existence of flow stagnation or reverse flow in these tubes. This flow distribution was diminished later at 500 s.

After a short time from the HPI actuation (1676 s), the fluid temperatures in the SG U-tubes began to decrease. However, they soon recovered to the secondary fluid temperature indicating existence of the super-heated steam in the U-tubes under the condition of primary flow stagnation. Sharp increase and decrease of the fluid temperatures were observed at the nearest position to the hot leg (Position 1 up-flow side) after the ACC injection. The sharp increase is due to arrival of super-heated steam from the hot legs or upper plenum. The rapid decrease of fluid tempera-

tures is arrival of saturated steam from the quenched core. The fluid temperatures in SG U-tubes recovered again to the secondary temperature at 2400 s. Thereafter, the U-tube fluid temperature was principally controlled by the secondary temperature.

Figure 5.40 shows fluid temperatures at the ECC injection lines and in the tanks of ACC and RWST. The ECC injection line temperatures showed abrupt decrease at 1676 s due to cold HPI water arrival and recovered gradually after termination of HPI. The fluid temperatures for the ACC water and HPI water were 320 and 310 K, respectively.

Shown in Figs.5.41 (a),(b) and 5.42 (a),(b) are the differential pressure data in SG U-tubes. Shown in Figs.5.43, 5.44 and 5.45 are the differential pressure data across the lower core plate, upper core support plate, and between the upper head and downcomer top, respectively. Shown in Figs.5.46 and 5.47 are the differential pressure across the primary pumps of PC-A and PC-B, respectively. Conduction probe data in the U-tubes with short, middle and long length are shown in Figs.5.48 through 5.50. Some of the conduction tube data are bad due to failure.

5.9 Summary of 0.5% Lower Plenum Break Test Results

Characteristic results for the SB-PV-01 test are summarized below.

(1) The primary system cooling was performed as follows. The primary pressure was maintained higher than or almost the same as the secondary pressure for 1506 s after the break, and the heat generated in the core, which simulated the 1/48 scaled PWR decay power, was transported to the SG secondary system by the forced circulation flow (until the primary pump stop at 312 s for loop A and 514 s for loop B), subsequently two-phase natural circulation flow (until 495 s in loop A and 518 s in loop B), and also by reflux cooling in the later phase.

A short time after the core heatup initiation at 1498 s, the primary pressure began to decrease gradually due to the continuous mass discharge and decrease of steam generation in the core. The primary system depressurization was promoted by condensation effect of the HPI water (1676 s) and also by an apparent two-phase discharge at the break area (1700 s). The accumulators completely cooled the uncovered core.

Finally the primary pressure was above 2 MPa under the condition of core power trip.

(2) The secondary system pressure started to increase rapidly by the steam line closure at the reactor scram trip (82 s) and was controlled by the relief valve operation between 7.8 and 8.2 MPa. As the auxiliary feedwater was assumed to fail after the main feedwater stop at the time of reactor scram (82 s), the secondary fluid mass decreased due to the steam discharge through the relief valves until termination of heat transfer from the primary system.

The secondary system functioned as a heat sink for the primary system as long as the core was covered by the mixture level and turned to a heat source after the core dryout initiation. The lowest secondary level was 7.9 m in SG-A and 7.8 m in SG-B after the time of final relief valve opening at 1475 s.

(3) The break flow and primary mass balance were as follows. The break line, which was 1.74 m below the core bottom, was covered by the subcooled water for the first 400 s. The lower plenum subcooling was 4 K at 400 s and less than 2 K after 500 s. Thereafter almost saturated water flowed out from the lower plenum to the break unit for a long time even after the core bottom dryout (1638 s).

As the break mass flow rate was higher than the full mode HPI flow rate at the primary pressure above 4.6 MPa, the primary mass inventory actually did not recover until the accumulator actuation (4.4 MPa). The amount of injected ECC water was 2700 kg for the HPI systems during 1676 and 3086 s, 1150 kg for the ACC and ACH during 2057 and 2360 s, and the total amount was 3850 kg. The low pressure injection (LPI), which had a capability of 12 kg/s at 0.9 MPa, was not actuated in this test due to the primary pressure above the pump head of 1.2 MPa.

(4) A clear phase separation was observed in the hot legs between 114 and 1390 s indicating a continuous steam flow toward the SG U-tubes and remaining saturated water in the hot legs. On the other hand, the cold legs were almost filled by steam in a short time after the void formation (495 s in loop A and 518 s in loop B) because the steam mainly comming from the upper head accumulated in the upper downcomer and cold legs. The loop-seal downflow side water levels started to decrease

at 1090 s in loop A and 1237 s in loop B. The loop-seal clearing was observed only after the accumulator actuation, and the loop-seal was reformed immediately after the accumulator termination (2360 s).

(5) The PV water level response and core dryout detection were as follows. The PV level was maintained at the hot leg level until 1420 s after the break and thereafter rapidly decreased resulting the following heater rod temperature increase at 1498 s. After this core top dryout initiation, the whole core was uncovered within only 140 s, which is approximately 1/10 of the hot leg uncovery time after the break. This rapid PV level decrease is clearly due to the large break mass flow rate.

The core dryout was recognized at 1670 s by operators through the consistent fluid temperature excursion more than 10K above the saturation temperature in the hot legs. This timing was 172 s after the core dryout initiation. The fluid temperature in the upper plenum, however, showed the similar temperature excursion before 1600 s indicating a possibility of 70 s earlier core dryout detection than the test result.

(6) The core thermal responses were as follows. The heater rod temperature excursion started at the upper region (Pos.8, 80% of the core height) at 1498 s. Although there was a wide distribution of temperature excursion timings in the upper region (270 s for the top core), no distribution of the timings was observed in the lower core region. The dryout and quench timings were closely related to the PV water level responses.

As the maximum heater rod surface temperature exceeded a limit of 923 K, the core power was tripped off at 1775 s (99 s after the HPI actuation). The peak cladding temperature in this test was 925 K at the highest power region (Pos.5, middle core height) of the high-power rod B17(4,4). The heater rods were completely quenched at 2248 s (during the accumulator actuation).

(7) A fluid mass inventory remaining in the primary system was directly estimated at the time of core dryout detection (1670 s) by using the differential pressure data or fluid density data in each region. This time phase was the best condition for the remaining fluid mass estimation because of no umbiguity on the core fluid water mass, negligible

void fraction in the water phase due to negligible heat input from the metal structures under the stable thermal conditions, and the least remaining water mass among all the LSTF LOCA tests.

The primary water mainly remained in the cross-over legs (40% of the total remaining water of 708 kg) and in the bottom of downcomer and lower plenum (53% of the total). The remaining water in the lower well of the upper head was the largest uncertain mass (46 ± 45 kg). Most of the primary system was filled by saturated or super-heated steam, which was 292 kg in total weight. Thus, the remaining primary fluid mass was estimated as 1000 ± 68 kg at this phase.

(8) The discharged primary fluid mass was measured by the catch tank level change as 4760 kg at 1670 s. Although an uncertainty of the discharged primary mass was not directly determined, a good reliability for the discharged mass was expected from the good agreement with the single-phase water break flow data in the early blowdown phase during 400 s. A scattering error within ± 70 kg was observed for the data fluctuation around a smoothed average value during the all test period.

By adding this discharged mass onto the remaining fluid mass and also by adding their uncertain factors, an initial primary fluid mass (M_0) was obtained as 5760 ± 138 kg. Then a transient primary fluid mass (M) at any time was calculated by using this initial value, discharged mass and injected ECC water mass.

(9) Major events related to the primary mass inventory were as follows. The water level was formed at the top of hot legs at 93% of mass ratio to the initial value (M/M_0), and at the U-tubes top between 83 and 73% mass ratio. The forced circulation in the primary loop stopped at 82% mass ratio in loop-A and at 73% in loop-B, the two-phase natural circulation almost diminished at 62%, the loop-seal downflow side level began to decrease at 45% in loop-A and 38% in loop-B, respectively.

The PV water level began to decrease below the hot leg nozzle at 29% mass ratio and the whole core was uncovered from top to bottom during 25 and 19%. The final core quench was conducted by the accumulators at 21% mass ratio. The least mass ratio was 14.4% at 1800 s. Comparing a sum of the total amount of injected ECC water (3850 kg, 67% of the initial mass) and the remaining mass ratio of 17% at the HPI actuation time with the final remaining mass ratio of 41% at the end of HPI

injection, it was found that almost a half water mass discharged from the vessel during the HPI injection period.

In addition to these results, following discussion should be noted with respect to the core cooling conditions. If the core power were not tripped at 1775 s in the SB-PV-01 test, what consequences would be resulted thereafter ? The consequences were guessed on the extrapolation of the actual test results.

First, as the maximum heater rod surface temperature would exceed 1100 K at the time of accumulator actuation (2057 s), the final core quench would be delayed than in the test result. Second, the primary pressure would be considerably higher than the test result due to large steam generation in the core reflooding phase, and this would not only reduce the injection flow rates of HPI systems and accumulators, but also increase the break mass flow rate. Consequently the primary mass inventory would be considerably lower than the test results.

Finally, it would be important to ensure a long-term core cooling after the ACC termination by actuating the LPI systems. In order to actuate the LPI systems, it would be necessary to lower the primary pressure below the pump head of 1.2 MPa by operating some primary system cool-down methods, such as the SG cooling due to a manual relief valves operation and/or a steam discharge through the PR relief valve.

6. Effects of Break Locations on 0.5% Small Break LOCA Phenomena

Up to the present time, the break location effects on the PWR small break LOCA have been studied as in the references (38), (39) and (46). However, effects of the break elevations on the core cooling phenomena and transient primary mass inventory were not discussed in detail.

Major test results of six break location parameter tests with the same 0.5% break area are investigated in this chapter. Test conditions of six tests are shown in section 6.1 and the results of each test are briefly summarized in section 6.2 except for the lower plenum break test. Effects of the break locations on the key event timings, break flow rates, two-phase break flow conditions, primary mass inventory, ECC water accumulation, and consequent core thermal responses are investigated in sections 6.3 and 6.4.

6.1 Test Conditions for Six Break Location Parameter Tests

Six typical break locations are selected in the primary system at the lower plenum (the lowest location), cold leg B, hog leg B, PV upper head, SG U-tubes and the power-operated relief valve (PORV) at the top of PR (the highest location) for the tests of SB-PV-01, which was abbreviated as SP1, SB-CL-12 (SCC), SB-HL-03 (SH3), SB-PV-02 (SP2), SB-SG-01 (SS1) and AT-SB-03 (SB3), respectively. These break locations are shown in Figs.6.1 (a) through (c) and Table 6.1.

As already shown in chapter 3, the SP1 test simulated an instantaneous break of 24 instrument tubes out of 58 flush at the bottom of PV in the PWR. The SB3 test was conducted as a TMI-type small break LOCA initiated by a stuck-open PORV and failure of the auxiliary feedwater system. The SS1 test simulated an instantaneous (guilotine) break of 3.2 U-tubes at elevation of the SG-B tube-sheet and the primary fluid was lead to the secondary system after the break. The other tests simulated a small pipe break LOCA.

The break orifice for five tests have the same configuration and area of 4.07×10^{-5} m^2 (7.2 mm I.D.), which corresponds to 1/48 scaled 2 inch pipe or 0.5% of cold leg flow area in the reference PWR. The break orifice of the TMI-type test (SB3) slightly differed from others, i.e., 6.83 mm I.D. (0.45% break area). The break line pipings of each test between

the break unit and the catch tank nozzle are different one by one as shown in Table 6.2. These differences can affect the amounts of initially remaining water mass, the transient mass accumulation during the test period and therefore, the uncertainty of the primary discharged mass among the all tests. The initially remaining water mass in the SP2, SCC or SH3 test was purged out prior to the break initiation by using an air injection method at the break line pipings.

The initial test conditions for each test were almost the same as those of the SP1 test (see chapter 4). Failures were commonly assumed in six tests on the off-site AC power during each test period, the high pressure injection systems, which were actuated manually by operators in the tests, and on the auxiliary feedwater system (AFW). The transient test conditions for the components were almost the same as in the SP1 test except for the SB3 test, in which the primary pump speeds were maintained constant until the reactor scram trip and the different core power curve was used as shown in Figs.6.2 (a) and (b). In the later phase of the SP2, SCC, SH3 and SS1 tests, another plant recovery test or a natural circulation test was performed. These later phase tests are out of view in this report.

The core dryout detection was performed for the manual actuation of the HPI systems by the following way. In the SP1 and SP2 tests, the hot leg fluid temperatures were observed and the super-heated steam, which came from the heated core, was detected by approximately 10 K higher value than the saturated temperature on these thermo-couples. On the other hand, the heater rod surface temperatures higher than a setpoint (approximately 750 K) were used for the core dryout detection in SCC and SH3 tests. In the SB3 test, the heater rod temperatures were observed. These differences can slightly affect the core dryout detection delay times among the tests.

The ECC injection conditions differed slightly among the six tests. The high pressure charging water was injected in the cold leg A and the HPI water was injected in the cold leg B. The ECC water injection flow was distributed in the two cold legs by equal ratio for the SP1 test and by a ratio of 3 and 1 in the cold leg A and cold leg B, respectively for the other tests. Full ECCS mode was assumed in the SP1 test, whereas one of two HPI systems was assumed to actuate in the other four tests. In the SB3 test the HPI systems flow rates were degraded from these conditions.

The accumulators ACC and ACH were prepared to inject cold water into the cold leg A and cold leg B, respectively, at the actuation pressure of 4.5 MPa. The low pressure injection system (LPIS) was actuated by a SI trip signal, which was tripped on the PR pressure of 12.27 MPa with a time delay of 17s, and injected cold water into both cold legs at the system pressure of 1.29 MPa.

6.2 Brief Explanation of Five Tests Results

Major events observed in all tests except for the SP1 test are briefly summarized in this section with their chronologies shown in Table 6.3.

(1) A 0.5% Upper Head Break LOCA Test, SB-PV-02 (SP2)

The LOCA test was performed during 4342 s after the break and thereafter another plant recovery test was performed.

Shown in Figs.6.3 (a) through (d) are the representative results for SP2 test, i.e., the primary and secondary pressures, primary flow rates, break flow rate and break flow density (beam B), water level and differential pressures in PV, and representative heater rod surface temperatures at positions 1,3,5,7 and 9 of the high-power rods in bundle 15.

After break initiation at the PV top, the PR pressure started to decrease and the PC pump speeds were raised up to 1500 rpm. The reactor scram trip (87 s) initiated to close the steam and feedwater lines in the SG secondary system and to control the PC pump speeds along the pre-determined curve. After the steam line closure, the secondary pressure increased up to the relief valve setpoints as in the SP1 test. The core power began to decrease 32s after the reactor scram trip.

The hot leg temperature reached the saturated temperature at 123 s. The forced circulation in two primary loops were terminated by PC pumps stop (336 s) and followed the natural two-phase circulation accompanying some intermittent flow shown in Fig.6.3 (a). The natural circulation flow in the loop B was observed until 1821 s. Thereafter, the primary flow was almost stagnant. The SG-B relief valve was operated until 2245 s (49 s after the steam discharge at the break), whereas that of SG-A relief valve was operated until 3736 s (184 s after the core dryout initiation). After the HPI actuation the primary pressure began to decrease rapidly

resulting in the SG secondary system as a heat source for the primary system.

Shown in Fig.6.3 (b) is the break flow rate. Initially the subcooled water (15.4 MPa and 593 K) in the upper head discharged through the break orifice. The primary fluid flowed into the upper head through the upper plenum and downcomer (spray nozzle). The break density and upper head differential pressure showed rapid decrease at 164 s indicating initiation of two-phase fluid discharge and flashing in the region. Thereafter the break flow data was incorrect and the primary discharged mass can be used instead of this data. The break flow density showed steam discharge (break uncovery) at 2196 s.

The average break flow rate derived from the ST level data was 1.53 kg/s during the two-phase discharge period (from 600 to 2000 s) and was 0.54 kg/s during the steam discharge period (from 2200 to 3500 s).

The water levels in the cross-over leg (loop-seal region) downflow sides began to decrease at 1464 s in the loop-A and 1686 s in the loop-B. The loop-seal clearing did not occur until actuation of the HPI actuation. The upper head differential pressure in Fig.6.3(c) began to decrease at 2714 s indicating initiation of upper head drainage. The PV level began to decrease immediately after initiation of the upper head drainage and followed the downcomer water level decrease. The PV level showed rapid mass recovery at 3970 s (40 s after initiation of the HPI injection). The total HPI flow rate was 1.3 kg/s at 3930 s and 1.55 kg/s at 4200 s. As this total injection flow rate was much larger than the steam discharge flow rate, the PV mass inventory quickly recovered only by these high pressure systems.

The heater rod dryout started at 3552 s at position 9 in the top core as shown in Fig.6.3 (d). The core dryout was detected at 3930 s by a hot leg fluid temperature higher than the saturated temperature. The peak cladding temperature (PCT) was observed at 3974 s at Pos.8 of B14(4,4) high power rod as 658 K, which was slightly higher than the initial heater rod surface temperature. And the whole core was completely quenched only by the high pressure injection systems within 52 s from its actuation. Thus the accumulators were not necessary for core cooling in the SP2 test.

(2) A 0.5% Cold Leg Break LOCA Test, SB-CL-12 (SCC)

The LOCA test was performed during 2605 s after the break and thereafter another plant recovery test was performed. Shown in Figs.6.4 (a) through (d) are the representative test results of the SCC test.

The overall pressure responses for primary and secondary systems (Fig.6.4 (a)) were similar as in the SP1 test mentioned in the previous chapter. The reactor scram was tripped at 80 s and followed the steam line closure, feedwater line closure and the primary pump coast-down. The forced circulation flow was terminated by the PC pump stop (332 s for PC-A and 483 s for PC-B). The intermittent natural circulation flow lasted in the primary loops until 1260 s. The SG-B relief valve operated until 1750 s (66 s after the break uncovery), whereas that in the SG-A operated until 2018 s (37 s after the core dryout initiation). The primary pressure rapidly decreased at 2290 s (36 s after the HPI actuation).

Shown in Fig.6.4(b) are the discharged primary mass and break mass flow derived from the discharged mass data. After the cold leg density detected a steam phase at 507 s, two-phase flow started to discharge. Steam flow or a high-quality two-phase flow started to discharge at 1684 s. The average break flow rate during the two-phase flow time period (600 and 1600 s) was 2.29 kg/s and that during the steam flow time period (1800 and 2200 s) was 0.50 kg/s. Thus the break flow rate was significantly decreased (to less than one fourth of the former) after the steam discharge through the break.

Level decrease in the loop-seal downflow sides was observed approximately at 1000 s in loop A and 1240 s in loop B. The loop-seal upflow sides were filled by water until the loop-seal clearing occurrence. The downflow side level in loop A decreased below the cold leg elevation and reached the middle elevation of the downflow side region at 1318 s. Further level decrease in the loop-seal downflow sides were observed at 1470 s and reached the loop-seal bottom at 1680 s resulting the loop-seal clearing. A temporary core uncovery occurred during this loop-seal clearing process. Thereafter the loop-seal was reformed in the loop A, but no loopseal was observed in the loop B (reference (46)).

This phenomena, however, are not observed in other five 0.5% break tests as shown later. Main reason of this loop-seal clearing in the small cold leg break LOCA test is as follows. The cold leg water level was kept almost constant slightly above the cold leg middle elevation between 800 and 1400 s (reference (46)). It began to decrease linearly at 1400 s and

abruptly decreased after the loop-seal clearing. This gradual cold leg level decrease results in increase of steam quality in the two-phase break flow and consequently causes depressurization in the cold leg. This depressurization increases differential pressure between the hot leg and cold leg or loop-seal downflow region and cold leg, and supresses the loop-seal downflow side water level. Actually, the loop-seal downflow side levels began to decrease 70 s after the cold leg level decrease (1400 s) and the differential pressure between the hot leg and the cold leg began to increase 30 s after these loop-seal level decreases. The increased differential pressure between the hot and cold legs resulted in increased steam flow rate through the spray nozzles at top of the downcomer and caused the break flow quality increase as shown in the reference. However, the loop-seal level decrease prior to the steam flow increase (1500 s) is clearly a result of cold leg depressurization caused by the break quality increase, which is determined by the local fluid conditions near the break area.

Thus a major motive force of the further loop-seal level decrease is the further depressurization in the cold leg caused by increase of the break flow quality.

Shown in Fig.6.4 (c) are the collapsed water level and differential pressures in PV. The PV level decreased twice from the hot leg nozzle level. The first one occured temporarily at 1526 s due to manometric pressure balance between the loop-seal region and the core. The second level decrease at 1815 s was mainly due to boil-off of the remaining water and partly due to the loop-seal reformation in the loop A. And the PV level began to increase at 2271 s (17 s after the HPI actuation). The total HPI flow rate was 1.45 kg/s at 2400 s, which was approximately 3 times as large as the steam break flow rate.

Shown in Fig.6.4 (d) are the representative heater rod surface temperatures. The core dryout was observed twice corresponding to the PV level responses, i.e., the first one started at 1609 s and the second was at 1981 s. As the maximum heater rod surface temperature exceeded a setpoint, operators actuated the HPI systems at 2254 s. Thereafter the core was rapidly covered by water. The PCT was observed as 736 K at 2283 s at Pos.7 of B13(4,4) high-power rod. The whole core was quenched within 94 s from the HPI actuation.

(3) A 0.5% Hot Leg Break LOCA Test, SB-HL-03 (SH3)

The SH3 LOCA test was performed during 3250 s after the break and thereafter another natural circulation (reflux condensation) test was performed. Shown in Figs.6.5 (a) through (d) are the representative results of the SH3 test.

The system pressure responses (Fig.6.5 (a)) in SH3 test are almost similar as in the SCC test. The reactor scram signal was tripped at 81 s and followed closure of the steam and feedwater lines in the secondary systems, and primary pump coast-down. The core power began to decrease at 116 s (35 s after the scram signal). The PC pumps stopped at 340 s. The primary coolant flows in SH3 test are almost terminated at 900 s. The SG-B relief valve was operated until 2020 s (370 s after the break uncovery) and that of the SG-A was operated until 2480 s (110 s after the core dryout initiation). The primary pressure began to decrease rapidly immediately after the HPI actuation. A pressure spike was observed at 2829 s (immediately after the loop-seal clearing and core quench). Thereafter the primary pressure decreased again.

Shown in Fig.6.5 (b) is a break flow rate calculated from the catch tank level data. The two-phase discharge started at 123 s (at the time of steam phase formation at the hot leg top), and steam or high-quality two-phase flow started to discharge at 1650 s. The average two-phase break flow was 2.43 kg/s between 600 and 1600 s and the average steam flow was 0.48 kg/s between 1800 and 2600 s.

Shown in Fig.6.5 (c) are the collapsed water level and differential pressures in PV. The PV collapsed water level began to decrease below the primary loop nozzle at 2057 s. The upper plenum was emptized at 2225 s and the top core was uncovered at 2370 s. The loop-seal level began to decrease at 1100 s in loop B and at 1125 s in loop A. However, the water levels did not decrease below the middle height of the loop-seal downflow side region until occurrence of loop-seal clearing (2825 s, 43 s after the HPI injection). The PV mass recovered rapidly by the HPI water and loop-seal clearing. The total HPI flow rate was 1.39 kg/s at 2700 s and 1.47 kg/s at 3000 s.

The heater rod surface temperatures (Fig.6.5 (d)) began to continuously increase (2370 s) during the loop-seal level formation. The core dryout detection at 2782 s immediately initiated the HPI systems. The PCT was observed as 747 K at B17(4,4) rod Pos.7 at 2828 s (immediately after the

loop-seal clearing) and the whole core was quenched within 56 s from the HPI actuation.

(4) A PORV Stuck-Open LOCA Test, AT-SB-03 (SB3)

Shown in Figs.6.6 (a) through (d) are the representative test results in SB3 test. Due to the assumption of one PORV stuck-open, PR steam began to discharge at time zero. The primary pressure responses in SB3 test are different from that in the SP1 test. As the core power started to decrease immediately after the reactor scram trip (64 s), the depressurization rate was higher than other tests and showed no temporary pressure recovery. At 250 s, the primary pressure showed a slight recovery, which occured after the two-phase discharge at the PORV. The steam flow began to start after the PR water level decreased below the top level at 4340 s (break uncovery). Thereafter time intervals of the relief valve operation in two SGs became longer than the previous period, and the relief valves were not operated after the final operation at 5370 s. A gradual depressurization after 5770 s was mainly due to the decreased steam generation in the heated core and a rapid depressurization at 6700 s was due to the HPI actuation.

The primary coolant flow (Fig.6.6 (a)) began to decrease from the initial value at the reactor scram trip. The hot leg fluid reached the saturated condition at 100 s and the cold leg temperature reached it at 820 s. The forced circulation continued until 314 s and followed the natural circulation until 1500 s.

Primary discharged mass was estimated from the catch tank level rise data as shown below. The tank level (Fig.6.6(b)) began to oscillate at 40 s and showed a slight increase at 250 s (at the two-phase discharge time). Thus the amount of discharged steam during the initial 250 s may be condensed and accumulated in the long break line pipings, which were initially at room temperature. If the condensation and accumulation of steam were perfectly terminated in the pipings, the catch tank level increase would indicate the correct discharged mass.

Discharged mass during the first 250 s was estimated by using a preliminary analysis for the SB3 test by using the RELAP5/MOD1 code. The average break flow rate for the steam discharge time period was 0.47 kg/s, which corresponded to 0.52 kg/s for the same break area of the other tests, and the total discharged steam mass was 118 kg (131 kg for 0.5% break

area) during the initial 250 s. The discharged mass showed a constant increasing rate between 1000 and 4000 s, in which the steam condensation effect was expected to be very small, and the average two-phase break flow rate was 0.73 kg/s (0.81 kg/s for 0.5% break area). For the time period between 250 and 1000 s, this average break flow rate of 0.73 kg/s was assumed to be applicable. This value is, however, slightly lower than a true value because of the underestimated system pressure than the test result (between 8.4 and 9.5 MPa). The steam break flow rate after the break uncovery was obtained as 0.47 kg/s between 4500 and 6000 s.

Shown in Fig.6.6 (c) are the collapsed levels and differential pressures in PV and pressurizer (PR). The PR level started to increase at 135 s and reached the top level covering the break line at 250 s. Thereafter the PR level was kept constant until the level decrease at 4340 s. The PV level and differential pressures showed that the primary loop nozzles were covered by the two-phase fluid until 4800 s. The upper plenum level began to decrease at 4600s and reached the bottom at 5357 s (upper plenum drainage). The water levels in the downflow sides of the cross-over legs started to decrease at 3750 s in loop B and 4130 s in loop A. However, the cross-over leg levels were maintained almost constant at the primary loop nozzle level for a long time even after the core dryout initiation. And the loop-seal clearing was not observed until the HPI actuation at 6600 s. The total HPI injection flow rate was 0.68 kg/s at 6840 s and 0.76 kg/s at 7000 s. This HPI flow rate was diffrent from other tests with a single failure mode (approximately a half of them in the SB3 test) due to an acceptance test for the test facility.

The heater rod surface temperatures began to increase at 5510 s at position 8 (upper core region) and most of the core region (except for the lower part below position 3) became uncovered before the HPI actuation. The heater rods were finally quenched at 6943 s (343 s after the HPI actuation). The total electric core power was lowered by operators from 6057 s and became 0.2 MW between 6500 and 6843 s in order to prevent the over-excursion of the heater rod temperature. The power recovered to the predetermined decay heat simulation at 6957 s.

(5) An Instantaneous Break Test for 3.2 U-Tubes, SB-SG-01 (SS1)

Shown in Figs.6.7 (a) through (d) are the representative results of SS1

test. In this test, 3.2 U-tubes break was simulated at the SG-B during 1500 s and thereafter a system cool-down test was performed by opening the relief valve at the SG-A. Thus the primary fluid discharge was terminated because the primary pressure became lower than the SG-B secondary pressure.

The PR pressure (Fig.6.7 (a)) showed similar to but fairly delayed from the responses of the SP1 test. The reactor scram was tripped at 116 s and initiated to close the steam and feedwater lines and to trip the PC pumps. The core power began to decrease 30 s after the scram trip. A temporary pressure recovery was observed after the reactor trip time due to the secondary pressure increase. Thereafter the primary pressure approached gradually the the secondary pressure.

The forced circulation flow was terminated at 365 s and the natural circulation flow was maintained during the test period (1500 s). The break flow was measured by the Venturi flow meter but the flow data after the hot leg vaporization (211 s) was not correct. The primary flow in loop A increased after the SG-A cooling initiation, whereas that in loop B became almost stagnant after the SG-B pressure became higher than the primary pressure.

Shown in Fig. 6.7 (c) are the PV collapsed level and differential pressures in PV. The PV level was almost higher than the primary loop nozzle during the test period. Therefore, no core dryout was observed as shown in Fig.6.7 (d). In the lower core region, large subcooling was observed after the SG-A cooling operation indicating sufficiency of primary cool-down capacity by a half of all SGs.

6.3 Break Location Effects on Overall System Responses

(1) Primary Pressure Responses Related to Secondary System Operation, Core Cooling Condition and HPI Actuation

Shown in Figs.6.8 (a) and (b) are the primary system pressures for the six break location parameter tests both in a short and long time periods after the break, respectively. Major events relating to the primary pressure responses are refered in the previous section.

In the early subcooling decompression process, the primary pressure

was mainly controlled by primary mass depletion rate and thermal contraction or expansion of the coolant caused by changes of the primary circulation flow rate, SG secondary pressures and core heat generation rate.

As these transient conditions were almost the same among the lower plenum break (SP1), cold leg break (SCC), hot leg break (SH3) and upper head break (SP2) tests, the primary pressures of these tests were almost the same before initiation of hot leg vaporization. The increasing circulation flow in the initial 15 s resulted in a slightly faster depressurization for the four tests as shown in Fig.6.8 (a) due to the thermal contraction of the primary fluid in comparison with the depressurization rate in the next 80 s. And the scram trip timings of these four tests were within 80 and 87 s. Thereafter the primary pressures for these tests temporarily increased due to the thermal expansion of the primary fluid, which was caused by the decreased heat transfer rate through the SG U-tubes after the steam line closure and also by the decreased primary coolant flows under the continuous core power generation of 10 MW, and began to decrease again according to the rapid core power decrease approximately 30 s after the scram trip timings.

On the other hand, the primary pressure of the TMI-type (SB3) test showed different pressure responses from these tests due to steam discharge through the PORV (1/48 scaled 0.45% break area) during the initial 250 s and also by the earlier core power decrease immediately after the scram trip (68 s). The depressurization rate in the SB3 test became slightly lower after initiation of the PR water level increase at 135 s.

The primary pressure in the SG U-tubes break (SS1) test became slightly higher than the four tests at 15 s due to the smaller break mass flow rate. As the break upstream fluid conditions were almost the same between the SS1 and SH3 tests, this fact indicates that the SS1 break flow was affected by the break downstream fluid conditions (secondary system), and therefore, the break flow was not the critical choking flow but the inertia flow. Thus the difference of the primary pressure responses between the SS1 and SH3 tests became larger as the primary pressure approached the secondary pressure.

It is shown in Fig.6.8 (a) that the break locations in the cold water regions (SP1 and SCC tests) resulted in no meaningful difference not only in the early decompression process but also in the following saturation decompression process. A slight difference in the primary pressure was observed between these and the hot break location tests (SH3 and SP2).

Irrespective of the early two-phase discharge initiation in the SH3 and SP2 tests, their depressurization rate was slower than the cold break location tests after approximately 150 s. This slower depressurization is probably due to a smaller hot leg flow rate toward the SG U-tubes, which caused a smaller heat transfer through the U-tube wall.

After the subcooled decompression process, a long saturated decompression process started in the five tests except for the SB3 test. The primary system was continuously cooled by the SG secondary systems as long as the primary pressure was higher than the secondary pressure.

The steam discharge at the break (break uncovery) in SCC, SH3, SP2 and SB3 tests contributed to slightly decrease both the primary pressure and the heat transfer rate through the U-tubes, which resulted in termination of the SG relief valve operation in one of the two SGs or resulted in degraded relief valve operations in the two SGs (see Figs.6.3(a) through 6.7 (a)). In these four tests, the following core dryout initiations resulted in both the gradual decrease of the primary pressure and the complete termination of the SG relief valve operations. It should be noted that these were not caused by the HPI actuation but by the core dryout initiation.

The HPI actuation, which was initiated manually by the operators after detecting the core dryout initiation, resulted in rapid decrease of the primary pressure as shown in Fig.6.8 (b) and also resulted in complete core cooling within 94 s after the HPI actuation in the SCC, SH3 and SP2 tests. The saturated decompression process for the SB3 test was qualitatively the same but significantly delayed in comparison with other tests.

On the other hand, there was no steam discharge nor apparent two-phase discharge before the core dryout initiation (1498 s) in the SP1 test. And the two SG relief valves were operated to release the excess energy in the secondary system, which was transfered from the primary system until initiation of the gradual primary pressure decrease due to the core dryout initiation. The primary pressure began to decrease rapidly after the HPI actuation in the SP1 test as in the other tests. However, the heated core was not cooled by the HPI in the SP1 test.

It was common for these all 0.5% break LOCA tests that the primary system was cooled well by the SG relief valve operation(s) during the long saturated decompression process until the core dryout initiation. The core dryout initiation resulted in the gradual primary pressure decrease below

the secondary pressure without the SG relief valve operation(s). Namely this core dryout initiation changed the SG secondary systems to a heat source from a heat sink. It was also common that the break uncovery initiation resulted in degradation of the SG heat sink function (almost 1/2 of that in the two-phase discharge phase) for the four tests with the break location higher than the core.

(2) Key Event Timings Related with Break Elevations

As shown in section 6.1, the break locations for the five tests include the highest (SB3) and the lowest (SP1) elevations in the PWR primary system in addition to the typical primary loops (SCC and SH3) and the upper head (SP2) as a special location. The results of U-tube break test were excluded here due to its different break downstream conditions from the others.

Shown in Fig.6.9 are the timings of key events for each test such as the two-phase discharge, the water level decrease in the loop-seal downflow regions, the break uncovery, the core dryout initiation, the HPI actuation and the following final core quench, related with the break elevations in the primary system. It should be noted that the 0.45% break area of the SB3 test resulted in slightly later timings than in a 0.5% break area condition.

A time sequence of these events was the same in the four tests (SCC, SH3, SP2 and SB3). These timings were, of course, later in the higher break location test. Reasons of the later break uncovery timing for the higher break location tests are as follows. The break uncovery was closely related to the timing of primary loop emptization except for the loop-seal regions for each test. Therefore, the timing of the break uncovery was mainly determined by amount of primary fluid mass above the primary loop bottom elevation, and also by the break mass flow rate during the previous two-phase flow discharge process. As steam quality of the two-phase flow was higher in the higher break location test, the break uncovery timing became later (see next section). This break uncovery timing is, therefore, characteristic for each break elevation test and is important to know the following core dryout initiation in these four tests. As shown in Table 6.3, the core dryout time was 297 s after the break uncovery time in the SCC test, 720 s in the SH3 test, 1356 s in SP2 test and 1170 s in the SB3 test, respectively. As large amount of primary fluid mass remained

in the pressurizer at this time in the SB3 test, the break uncovery timing was relatively earlier than the SP2 test.

On the other hand, the time sequence of these key events in the SP1 test was different from the others by the earlier core dryout initiation before the apparent two-phase discharge and the break uncovery timings. This is also a result of the break elevation lower than the core bottom by 1.74 m in the SP1 test. If another break location was considered at the PV wall between the core bottom and the lower plenum bottom, its key event timings would be close to those of the SP1 test results.

The differences between the hot and cold leg breaks were not so large as those between the different break elevation tests such as the cold leg break and the upper head break. Namely, timings of the break uncovery, core dryout initiation and final core quench for the five tests compared with those in the cold leg break are in the following ratios (for SB3 test, timings are modified assuming an equivalent 0.5% break area condition by multiplying 0.9),

break uncov.; SP1 : SCC : SH3 : SP2 : SB3 = 1.2 : 1.0 : 1.0 : 1.3 : 2.3,
core dryout ; SP1 : SCC : SH3 : SP2 : SB3 = 0.8 : 1.0 : 1.2 : 1.8 : 2.5,
core quench ; SP1 : SCC : SH3 : SP2 : SB3 = 1.0 : 1.0 : 1.2 : 1.7 : 2.7.

This relatively smaller difference of key events timings between the SCC and SH3 tests can be expected in other break location tests with the similar break elevations.

Therefore it is concluded that these key events in the small break LOCA are controlled principally by the break elevation and slightly by the horizontal variations, as a result of gravity controlling phenomena in a small break LOCA. By using these relations between the key event timings and the break elevations for the five typical break location tests, key events in other small break LOCA with the similar break area but with different break location in the primary system can be predicted .

(3) Core Cooling Conditions for Five Break Tests

Core cooling phenomena related with the break location effects are shown below except for the SG U-tubes break test (SS1) because of its no core dryout occurrence in the LOCA test period. As already shown in section 6.2, the heater rods in the core were uncovered as the PV water level decreased below the core top region and finally quenched by the HPI systems in the four tests and by the accumulators in addition to the HPI sys-

tems in the SP1 test. The core thermal responses related both with the loop-seal level responses and the ECCS actuation are discussed below on the view point of break location effects.

The temporary core dryout before the break uncovery was observed only in the cold leg break (SCC) as one of the break location effects. This temporary core level decrease was due to the manometric pressure balance in the primary system especially across the loop-seal region, SG U-tubes and the PV internal regions. A further level decrease at approximately 1400 s after the break in the downflow sides of the loop-seal region principally contributed to the core level depression. The further level depression in the loop-seal down-flow sides was caused in the SCC test by the increasing steam flow rate through the break area (this can be confirmed by the decreasing fluid densities before the loop-seal clearing timing). The core level depression was finally terminated and recovered by the income fluid mass from the loop-seal region after the loop-seal clearing.

In the hot leg break test (also in the upper head and TMI-type tests), there was no motive force for the increasing steam flow from the loop-seal region toward the cold leg except for the continuous steam generation in the core. Most of these generated steam discharged through the break area at the hot leg (or in the upper head and pressurizer) or condensed at the SG U-tubes during the reflux cooling periods. Therefore the loop-seal clearing did not occur in these tests until the HPI actuation timings.

In the lower plenum break test (SP1), of which primary pressure responses were almost the same as those of the SCC test until the core dryout initiation, level decrease in the loop-seal downflow sides started at 1090 s as in the cold leg break test. However, the whole core was uncovered (between 1498 s and 1638 s) before the loop-seal clearing occurred. As the steam generation diminished in the heated core and there was no motive force to increase the steam flow through the cold legs until the apparent two-phase discharge, the loop-seal clearing did not occur during the core heat-up process in the SP1 test.

It is expected that the temporary loop-seal clearing could occur in other break case with break location close to the cold legs, i.e., pressure vessel wall in the higher downcomer region or cross-over legs, with the similar break area as in this case.

In other four tests the core was uncovered due to the decreased primary mass inventory (boil-off process) after the break uncovery timing. And therefore the core level decreasing speed was much smaller than in the SP1 test as shown previously. At the time of HPI actuation, the upper core region (approximately 1/3 of the whole core region) was uncovered in SCC, SH3 and SP2 tests and approximately 2/3 core region in the SB3 test, respectively. The heated core in these four tests was completely quenched only by the HPI system actuation. The completion of the core quench was within 74 s after the HPI actuation for the cold leg, hot leg and upper head break tests and within 394 s for the SB3 test, which was the result of smaller HPI flow rate than other tests. Thus the HPI system with a single failure assumption was sufficient for the core cooling in these 0.5% small break LOCA tests. On the other hand, the full mode HPI systems was sufficient neither for the primary mass recovery nor the core quench in the lower plenum break test.

The peak cladding temperatures (PCT) for the five tests are compared in Fig.6.10. The highest was the lower plenum break test (925 K) and it was expected to exceed more than 1100 K if the core power was continuously supplied even after the actual power trip time (1775 s). The PCT for the cold and hot leg breaks were similar as 736 and 747 K, respectively. The PCT of the upper head break was slightly lower than these as 658 K. This sequence of the PCT values is the same as the sequence of the break elevations.

In the TMI-type test (SB3), however, the PCT cannot be compared with others because of the different HPI actuation logic and different core power control process during the core dryout period. When the super-heated steam temperature was recorded in the hot legs (6171 s), the maximum heater rod surface temperature was 739 K at Pos.7 of the B20(4,4) rod. Thus the core dryout detection of the SB3 test, if it were assumed to perform either on the heater rod temperature above 750 K or the super-heated steam temperature in the hot legs, would result in the similar PCT as in the SH3 test.

It is concluded that the PCT was slightly affected by the break elevation above the core top and significantly affected by the break elevation below the core bottom as a result of HPI water accumulation ratio in the pressure vessel (see next section).

6.4 Break Location Effects on Break Flow and Primary Mass Inventory

(1) Discharged Primary Fluid Mass for Six Tests

Fluid mass discharged from the primary system was lead to the catch tank and measured by the level meter for five tests except for the SS1 test, in which the discharged mass was obtained from the Venturi flow meter with valid period of the initial 200 s. Shown in Fig.6.11 are the discharged primary mass for the five tests and that of SS1 test for comparison. A scattering data error of ± 80 kg was observed among the five tests during a initial 100 s. And the data fluctuation error around a smoothed average value was maximum as ± 100 kg in the SB3 test, ± 70 kg for the SP1 test (see section 5.5) and more less for the SCC, SH3 and SP2 tests. The discharged mass for each test was summarized in Table 6.4 including the data correction on the SB3 data (for the initial 250 s). The data fluctuation was smoothed in the Table for each test.

The discharged primary fluid mass was significantly affected by the break locations as shown in Fig.6.11. Namely, the higher break location tests resulted in smaller discharged mass due to initiation of earlier two-phase discharge timings and higher steam quality in the two-phase flow than in the lower plenum break test. Thus the break uncovery timings were later in the higher break location tests and were almost the same in the cold and hot leg break tests irrespective of the significant difference of their two-phase discharge timings.

In the SP1 test, the discharged mass almost linearly increased with time until the apparent two-phase discharge at 1700 s. So this was an extreme case with the fastest mass depletion among the six break locations, whereas the TMI-type break (SB3) was another extreme case with the latest mass depletion. It is expected that discharged primary mass of another location break except for these six tests would be intermediate of these two extreme cases because of its intermediate break elevation.

After the break uncovery timing, the mass depletion rate became significantly lower in the SCC, SH3 and SP2 tests, and became almost the same among these three test as a result of similar steam flow conditions. The core dryout started after the break uncovery timing by 297 s for the SCC test, 720 s for the SH3 test and 1356 s for the SP2 test. On the contrary, core dryout started 502 s before the break uncovery timing in the SP1 test. In the SB3 test, the core dryout started 1170 s after the break

uncovery timing.

(2) Average Break Flow Rate and Two-Phase Flow Conditions

By using the experiment data of the primary discharged mass, average break flow rates were obtained for each single-phase water flow, two-phase flow and steam flow as shown in Table 6.5. And two-phase flow conditions such as void frcation and steam quality are estimated for each test.

In the early subcooling decompression process for the initial 100 s, the average break flow rates for the four tests (SP1, SCC, SH3 and SP2) showed a discrepancy of 0.8 kg/s in maximum, i.e., a scattering error within ± 0.5 kg/s around their average value of 3.5 kg/s (relative error is ± 14%). This relatively large scattering is due to that of the discharged mass of ± 80 kg in the initial 100 s among them. Relative errors for the average break flow rates both for the two-phase and steam flow are expected to be smaller than this, because of the larger amount of dicharged mass during the longer time period for the two-phase flow, and later phase and longer time period for the steam flow in each test (ref. discussion on the uncertainty of the discharged mass data in section 5.5).

The average two-phase flow rate was obtained for the long saturated decompression process, in which the primary pressure was almost constant at 8 MPa for the five tests. The highest value was 2.78 kg/s in the lower plenum break test (SP1), next were hot and cold leg breaks (82-87% of the SP1 test data), the third was 55% of the SP1 data for the upper head break and the lowest was 29% of the SP1 data for the TMI-type test (on a 0.5% equivalent break area). Thus the break elevation effects on the two-phase break flow rate was clearly shown in this comparison. The average steam flow rates for the four tests (SCC, SH3, SP2 and SB3) slightly differed with each other. The lowest is the SH3 data of 0.48 kg/s and an average is 0.51 kg/s with a scattering error of ± 0.03 kg/s.

In order to clarify the two-phase flow conditions at the primary pressure of 8 MPa, an average void fraction (α) and an average steam quality (x) upstream the break orifice were derived for the five tests by assuming a saturated water break flow (W_{fc} at x = 0.0) on the SP1 two-phase flow rate of 2.78 kg/s, a saturated steam break flow (W_{gc} at x = 1.0) on the SH3 steam flow rate of 0.48 kg/s, and a constant slip ratio for any

two-phase flows. The first and second assumptions hold adequate as shown in section 5.5 for the SP1 test and in section 6.2 for the SH3 test. The third assumption, however, does not hold in general but holds for a special case, in which the constant slip ratio is equal to a velocity ratio between W_{gc} and W_{fc} (u_{gc}/u_{fc} = 5 at 8 MPa, where u_{gc} and u_{fc} are average velocities for the steam and water flows, respectively). A thermal equilibrium is assumed for both the water and steam phases in the two-phase flow. The void fraction and the steam quality are defined as,

$$\alpha = A_g / A,$$

$$x = W_g / W,$$

where A is a total flow area, A_g is steam flow area in the two-phase flow, W is the total break mass flow rate and W_g is the steam mass flow rate in the two-phase flow. As W is a sum of W_g and W_f (water mass flow rate in the two-phase flow), $W_g = \alpha W_{gc}$ and $W_f = (1 - \alpha)W_{fc}$,

$$W = \alpha W_{gc} + (1 - \alpha)W_{fc},$$

$$\alpha = (W_{fc} - W) / (W_{fc} - W_{gc}),$$

$$x = \alpha W_{gc} / W,$$

where W_{fc} = 2.78 kg/s and W_{gc} = 0.48 kg/s.

The calculated average void fraction and the steam quality are shown in Table 6.6, in which another value for the void fraction or the steam quality is also shown by the bracketed values corresponding to the average value of W_{gc} = 0.51 kg/s shown above (for the SB3 test, modified break flow data on the 0.5% break area are used for comparison). This variation of the steam flow rate (W_{gc}), however, resulted in little difference on the void fraction or steam quality indicating a small influence of the average flow rate data uncertainty on these calculations.

Figs.6.12 (a) and (b) show clear dependence of the two-phase flow rate, void fraction and steam quality on the break elevations for these five tests even if the apparent two-phase flow after 1700 s in the SP1 test was included in this comparison. In the SCC, SH3 and SP2 tests, the break uncovery significantly decreased the break flow rate such as 22% of the two-phase flow rate in the SCC test, 20% in the SH3 test and 35% in the SP2 test, respectively. In the SB3 test, the mass flow rate became 64% after the break uncovery compared with the previous time phase. On the other hand, these steam flow rates corresponded to 17 - 19% of the saturated water flow rate of the SP1 test before the core dryout initiation. Therefore, the break uncovery significantly delayed the core dryout timings due to the decreased primary mass depletion rate in the four tests com-

pared with the SP1 test.

It is also clearly shown that the void fraction in the upstream two-phase flow was higher in the higher break elevation test (the highest is more than 86% in the SB3 test, next is more than 54% in the SP2 test and 15-22% in the SCC and SCH tests according to the assumptions), and this contributed to the later break uncovery time. The differences of void fraction or steam quality between the cold and hot leg break tests were not so large as the effects of break elevation. Thus the later core dryout initiation in the higher break location test was caused both by the delayed break uncovery time and the following decreased mass depletion rate, as the prominent break elevation effect.

(3) Primary Mass Inventory and ECC Accumulation Efficiency

Transient fluid mass remaining in the primary system was calculated for each test by using the discharged primary mass data and the initial primary mass of 5760 kg as in the SP1 test (see section 5.7 and Fig.5.30). The effects of ECC water on the primary mass recovery was also described below for each test.

Shown in Table 6.7 are transient fluid mass remaining in the primary system calculated by subtracting the discharged mass (M_D) from the initial mass (M_o) with the injected ECC water mass (M_E) as,

$$M = M_o - M_D + M_E,$$

for five 0.5% break tests except for the U-tube break tests (SS1).

The results are compared in Fig.6.13. Overall responses were similar as those in the discharged mass shown in Fig.6.10 during the subcooling and saturated decompression processes. Each primary mass recovery process (refill and reflooding processes), however, is investigated quantitatively from this comparison. Transient mass ratios (M/M_o) for the key events are also shown in Fig.6.13 and Table 6.8.

The water level decrease in the loop-seal downflow regions started at slightly higher mass ratio in the SP2, SB3 and SH3 tests (during 49 - 54%) and at the lowest mass ratio in the SP1 test (during 38 - 45%). The break uncovery occurred at higher mass ratio in the higher and hotter break location tests, and at the lowest mass ratio in the SP1 test, indicating the largest influence of the break location effects.

On the other hand, the core dryout initiation occurred at the similar

mass ratios (22 - 25%) for the four tests (SP1, SCC, SH3 and SP2). In the SB3 test, the pressurizer water level was 3.53 m at this time, which corresponds to 720 kg of primary mass (M/M_0 = 13%). Thus remaining primary mass except for the pressurizer in SB3 test is 24% and agrees well with others. This is also a typical result of the gravity controlling phenomena in small break LOCAs.

The HPI was actuated at the mass ratio of 16 - 20% for the four tests and at 28% for the SB3 test. The HPI actuation contributed to the primary mass recovery except for the SP1 test. Difference of the ECC water accumulation in the PV between the SP1 and other tests is clearly the result of larger break mass flow rate for the former.

An accumulation efficiency of the ECC water (E_a) is defined to clear the effect of ECC water on the primary mass inventory as a ratio of remaining fluid mass to the injected ECC water mass (M_E). As the remaining fluid mass is obtained as ($M_E - M_D$), where M_D is the discharged fluid mass from the primary system, the efficiency for an arbitrary time period is defined as,

$$E_a = (M_E - M_D) / M_E.$$

Shown in Table 6.9 are the results of five tests with respect to the accumuration efficiency. For the SP1 test, the ECC injection time period was devided into three parts accoding to the early HPI injection period (phase I) at the higher primary pressure, the accumulator actuation period and the later HPI injection period (phase II) at lower primary pressure. For the four tests (SCC, SH3, SP2 and SB3), the accumulation efficiency was more than 57% even at the higher primary pressure above 5 MPa, whereas it was negative for the SP1 test at the same pressure range, i.e., more fluid mass discharged from the primary system than the injected ECC water mass. In the accumulator actuation period, the efficiency increased to 64% in the SP1 test. Thus, the effects of larger break mass flow rate on the ECC water mass depletion in the SP1 test was prominent as the result of lowest break location among the six break location parameter tests.

7. Conclusions

Typical thermal-hydraulic phenomena are clarified for the small lower plenum break LOCA test (SP1), which simulates 24 instrument tubes break at the PWR vessel bottom, with assumptions on manual actuation of the HPI systems and failure of the auxiliary feedwater system at the ROSA-IV/LSTF system as shown in chapter 5. In addition to these, the effects of break location on key event timings, primary mass inventory and core cooling conditions are clarified by comparing with five similar LOCA test results as shown in chapter 6. These are cold leg break (SCC), hot leg break (SH3), upper head break (SP2) and 3.2 U-tubes break (SS1) with the same 0.5% break area, and pressurizer top break with 0.45% break area (TMI-type, SB3).

Following are conclusions, which are useful not only to quantitatively estimate the key event timings in other LSTF LOCA test with the similar break area but also to qualitatively estimate the key events in small break LOCA in other full-height integral systems including the PWR by extending these experiment results on the break location parameters.

(1) Effects of break elevation in the primary system are significant on small break LOCA phenomena in comparison with effects of horizontal variation (such as cold leg and hot leg breaks) as a result of gravity controlling phenomena. Therefore, importance of the full-height modeling of the LSTF system is confirmed for simulation of the actual PWR system responses in a small break LOCA.

(1-1) Timings of the core dryout initiation, which are result of core water level depression (core uncovery) during the boil-off process in the five tests, are widely distributed depending on their break elevations. Ratios of their timings compared with the cold leg break (on the same 0.5% break area condition) are, as

SP1 : SCC : SH3 : SP2 : SB3 = 0.8 : 1.0 : 1.2 : 1.8 : 2.5,

and the longest in the highest break location test (SB3) is approximately 3 times as large as the shortest in the lowest break location test (SP1). The timings in the cold leg and hot leg breaks are included in these two extreme cases and their difference is very small compared with the effects of break elevations.

(1-2) Principal reason of the later core dryout is the lower discharge mass flow rate (higher steam quality) in the higher break location test

during their long two-phase discharge time periods. Actually, their average break flow rates on the same 0.5% break area condition were in the following ratios compared with that of the cold leg break, as

SP1 : SCC : SH3 : SP2 : SB3 = 1.2 : 1.0 : 1.1 : 0.6 : 0.4.

Additionally the earlier two-phase discharge initiation slightly delayed each core dryout timing. The higher break location above the core region significantly delayed the core dryout timing after the steam discharge (break uncovery) initiation. On the other hand, the break uncovery in the SP1 test occurred after the whole core dryout because of its break location lower than the core bottom.

(1-3) ECC water accumulation efficiency (E_a), which is defined as,

$$E_a = (M_E - M_D) / M_E,$$

where M_E is the injected ECC water mass and M_D is the discharged primary fluid mass during an arbitrary time period, is useful to estimate the effect of ECCS on primary mass inventory.

In the 0.5% lower plenum break test, this was negative for full-mode HPI systems at the primary system pressure above 4.6 MPa and 0.64 even in the accumulator actuation period due to the continuous water discharge. On the other hand, the efficiency was more than 0.57 for the other four tests (SCC, SH3, SP2 and SB3) for the HPI systems with single-failure assumption due to the steam discharge through the break. This efficiency clearly depends on whether the break location is at the PV wall or not in addition to the break elevation relative to the core region.

(2) Core thermal condition is the severest in the lower plenum break among the various break location tests due to the continuous water discharge through the break area, which results in the earlist core dryout initiation, the lowest ECC water accumulation efficiency and the lowest primary fluid mass inventory, and also due to no break uncovery before the core dryout initiation.

The PCT in the SP1 test was the highest (more than 1100 K if the core power were not tripped off) among them and the heated whole core was quenched by the accumulators under the condition of core power trip. Similar results can be obtained in other cases with break locations at the downcomer PV wall lower than the core region. On the other hand, the heated core was completely quenched by the HPI systems under the single-failure mode (within 74 s in SCC, SH3 and SP2 tests,

and within 394 s in SB3 test under the further degraded HPI flow rate).

(3) The SG U-tubes break with the same break srea as in the other tests results in the largest primary fluid mass inventory and no core dryout due to the low break mass flow rate, which depends on the secondary system pressure and terminates as the primary pressure approaches the secondary pressure. This is a special case among the break location tests.

(4) A temporary core dryout, which occurs in the loop-seal clearing process, also depends on the break locations in the primary system in addition to the break area dependence. This was observed in the cold leg break test and was not observed in four tests (SP1, SH3, SP2 and SB3) before their boil-off core dryout timings. Motive force of the loop-seal level depression to the bottom in the case of cold leg break was the increased steam flow in the two-phase break flow, which increased the differential pressure across the loop-seal region. Similar loop-seal clearing phenomena can be expected in other cases with break locations near the cold legs, i.e., loop-seal region and upper downcomer region.

(5) Following phenomena were commonly observed in the small 0.5% break LOCA tests irrespective of their different break locations.

(5-1) The core decay power was transferred to the SG secondary systems for a long time by the forced and natural primary circulation flows or the steam condensation cooling at the U-tubes (reflux cooling mode) as long as the core was covered by fluid mixture level.

(5-2) The break uncovery, which occurred after the long two-phase discharge process and before the core dryout initiation in the four tests (SCC, SH3, SP2 and SB3), decreased steam condensation at the U-tubes and resulted in termination of relief valve operation in one of two SGs or resulted in degraded relief valve operations in two SGs.

(5-3) Initiation of the boil-off core dryout approximately in 1/3 total region resulted in decrease of steam generation in the core, decrease of the primary pressure below the secondary pressures and therefore, no heat sink for the primary system. Thus, the SG function was changed into a heat source for the primary system by the core dryout initiation in these tests except for the SG U-tubes break test with no core uncovery.

(5-4) It was clarified that the boil-off core dryout started at the similar primary fluid mass condition (22 - 25% of the initial value) in five tests irrespective of their significantly different initiation timings. In the SB3 test, 13% additional primary mass remained in the pressurizer, in which no water remained at these timings in other four tests.

It was also clarified that water levels in the loop-seal downflow regions began to decrease at the primary mass ratios between 38 - 54% prior to the core uncovery in the five tests. These mass ratios are smaller in the lower break location tests.

(6) Other noteworthy findings derived from the SP1 test are:

(6-1) The primary fluid mass remaining at the time of core dryout detection (1670 s) was directly obtained by using differential pressure data for the water remaining regions such as cross-over legs, downcomer bottom and lower plenum. This condition was the best for estimation of remaining primary mass due to the smallest uncertainty. The remaining primary fluid mass including steam mass was obtained as 1000 ± 68 kg. Most of the uncertain factor is due to the unknown upper head mass.

(6-2) An intial fluid mass (M_0) for the LSTF primary system including active dead volumes (such as the ECCS pipings) was obtained by adding the remaining fluid mass shown above and the total discharged fluid mass at 1670 s (4760 kg) and by also adding their uncertain factors as,

$$M_0 = 5760 \pm 138 \text{ kg}.$$

This value including the steam mass can be used for estimation of the transient primary mass inventory in other LSTF tests.

Acknowledgment

The author is grateful to Dr.Y.KUKITA for his overall useful comments and discussions, Mr.K.HIRATA for his helpful cooperation on the data processing, other members in the ROSA-IV group for their useful comments on the report, Mr.K.Hiyama and Mr.E.Umeki for their data plots, and Miss M.Kikuchi and T.Kurosawa for typing the manuscripts.

(5-4) It was clarified that the boil-off core dryout started at the similar primary fluid mass condition (22 - 25% of the initial value) in five tests irrespective of their significantly different initiation timings. In the SB3 test, 13% additional primary mass remained in the pressurizer, in which no water remained at these timings in other four tests.

It was also clarified that water levels in the loop-seal downflow regions began to decrease at the primary mass ratios between 38 - 54% prior to the core uncovery in the five tests. These mass ratios are smaller in the lower break location tests.

(6) Other noteworthy findings derived from the SP1 test are:

(6-1) The primary fluid mass remaining at the time of core dryout detection (1670 s) was directly obtained by using differential pressure data for the water remaining regions such as cross-over legs, downcomer bottom and lower plenum. This condition was the best for estimation of remaining primary mass due to the smallest uncertainty. The remaining primary fluid mass including steam mass was obtained as 1000 ± 68 kg. Most of the uncertain factor is due to the unknown upper head mass.

(6-2) An intial fluid mass (M_0) for the LSTF primary system including active dead volumes (such as the ECCS pipings) was obtained by adding the remaining fluid mass shown above and the total discharged fluid mass at 1670 s (4760 kg) and by also adding their uncertain factors as,

$$M_0 = 5760 \pm 138 \text{ kg}.$$

This value including the steam mass can be used for estimation of the transient primary mass inventory in other LSTF tests.

Acknowledgment

The author is grateful to Dr.Y.KUKITA for his overall useful comments and discussions, Mr.K.HIRATA for his helpful cooperation on the data processing, other members in the ROSA-IV group for their useful comments on the report, Mr.K.Hiyama and Mr.E.Umeki for their data plots, and Miss M.Kikuchi and T.Kurosawa for typing the manuscripts.

References

(1) Task Force for Assessments of TMI-2 Accident, Reactor Safety Research Center, "Prompt Technical Assessments of the TMI-2 Accident by JAERI Task Force", JAERI-M 8373 (in Japanese), (May, 1979).

(2) M.TANAKA, "Radioactivity Release Pathways of TMI-2 Accident", J. Atomic Energy Soc. (in Japanese), (1980).

(3) M.TANAKA, "Present Status of TMI", "Genshiryoku-Kogyo" (in Japanese)(1981).

(4) K.TASAKA, M.TANAKA, H.ITOH, et. al., "Conceptional Design of Large Scale Test Facility (LSTF) of ROSA-IV Program for PWR Small Break LOCA Integral Experiment", JAERI-M 9849 (1981).

(5) K.TASAKA, "ROSA-IV Program for the Experimental Study on Small Break LOCA's and the Related Transients in a PWR", 10th WRSRIM (USA). (Oct., 1982).

(6) M.TANAKA, K.TASAKA, Y.KOIZUMI, et. al., "ROSA-IV/LSTF Program at JAERI for PWR Small Break LOCA and Operational Transient Experiments", ANS Topical Meeting (USA), (Sept., 1983).

(7) ROSA-IV Group, "ROSA-IV Large Scale Test Facility (LSTF) System Description", JAERI-M 84-237 (1984).

(8) M.TANAKA, K.KATADA and K.TASAKA, "Preanalysis of ROSA-IV LSTF for PWR Small-Break LOCA Test with RELAP5/MOD0", JAERI-M 9356 (in Japanese) (1981).

(9) M.TANAKA, K.KATADA and K.TASAKA, "Preanalysis of ROSA-IV LSTF for PWR Small-Break LOCA Test with RELAP5/MOD0 -- 2.5% Cold Leg Break with HPI Failure", JAERI-M 9676 (in Japanese) (1981).

(10) C.P.Fineman, M.TANAKA and K.TASAKA, "Comparison of Calculations for the ROSA-IV LSTF with RELAP5/MOD0 and RELAP5/MOD1 (Cycle 1) -- 10% and 2.5% Cold Leg Break -- ", JAERI-M 82-004 (1982).

(11) M.TANAKA, C.P.Fineman and K.TASAKA, "PORV Break Calculations for ROSA-IV LSTF and the Reference PWR with RELAP5/MOD1 (Cycle 1)", JAERI-M 83-067 (1983).

(12) M.TANAKA, K.TASAKA, H.ITOH, et. al., "Examination of TMI Accident Simulation Tests at LSTF in ROSA-IV Program", JAERI-M 83-105 (in Japanese) (1983).

(13) C.P.Fineman, M.TANAKA and K.TASAKA, "Loss-of-Feedwater Transient Calculations for the ROSA-IV LSTF and the Reference PWR with RELAP5/MOD1 (Cycle 1)", JAERI-M 83-088 (1983).

(14) C.P.Fineman, M.TANAKA and K.TASAKA, "Loss-of-Load Transient Calculations for the ROSA-IV LSTF and the Reference PWR with RELAP5/MOD1 (Cycle 1)", JAERI-M 83-097 (1983).

(15) R.R.Schultz, Y.KUKITA and K.TASAKA, "Simulation of a TMI-2 Type Scenario at the ROSA IV Program's Large Scale Test Facility : A First Look", JAERI-M 84-176 (1984).

(16) R.R.Schultz, Y.KUKITA and K.TASAKA, "A LSTF Simulation of the TMI-2 Scnario in a Westinghouse Type Four Loop PWR", 5th International Mtg on Thermal Nuclear Reactor Safety (Karsruhe), (Sept., 1984).

(17) M.TANAKA, Y.KUKITA, R.R.Schultz, et. al., " A 10% Cold Leg Break Test at ROSA-IV Large Scale Test Facility", Specialists Mtg. on Small Break LOCA Analysis in LWRs (Italy), (June, 1985).

(18) K.TASAKA, Y.KOIZUMI, Y.KUKITA, et. al., "The ROSA-IV Program TMI-2 Type Scenario Experiments : A Multi-Faceted Investigation", Specialists Mtg. on Small Break LOCA Analysis in LWRs (Italy), (June, 1985).

(19) Y.KOIZUMI and K.TASAKA, "ROSA-IV Large Scale Test Facility for PWR Small Break LOCA Integral Simulation Test", Specialists Mtg. on Small Break LOCA Analysis in LWRs, (Italy), (June, 1985).

(20) Y.KUKITA, M.OSAKABE, M.TANAKA, et. al., "Simulation of PWR Turbine Trip Transient in ROSA-IV Large Scale Test Facility", J. Nucl. Sci. and Technol. (1985).

(21) Y.KOIZUMI, H.KUMAMARU, Y.KUKITA, et. al., "Blind-Blind Prediction by RELAP5/MOD1 for a 0.1% Very Small Cold-Leg Break Experiment at ROSA-IV Large Scale Test Facility", J. Nucl. Technol. (1985).

(22) K.TASAKA, M.KAWAJI, M.OSAKABE, et. al., "The Results of the ROSA-IV LSTF Small-Break LOCA Experiments", 13th WRSRIM, (USA), (Oct., 1985).

(23) M.OSAKABE, M.KAWAJI, Y.KOIUMI, et. al., "Thermal-Hydraulic Mechanisms of Core Liquid Level Depression and Recovery during Small Break LOCA Experiment", International ANS/ENS Topical Mtg. on Thermal Reactor Safety (San Diago), (Feb., 1985).

(24) M.KAWAJI, M.OSAKABE, Y.KOIZUMI, et. al., "Three Key Indicators Useful for Emergency Operator Action during PWR SBLOCA", IAEA Seminar on Operating Procedures for Abnormal Conditions in Nuclear Power Plants (Munich), (June, 1986).

(25) H.ASAKA, M.OSAKABE, Y.KOIZUMI, et. al., "Analysis of LSTF 10% Cold Leg Break Experiment by RELAP5/MOD1 and MOD2", 2nd International Mtg. on Thermal-Hydraulics and Operations for Nuclear Power Plant, (Tokyo) (1986).

(26) H.KUMAMARU, Y.KOIZUMI, M.OSAKABE, et. al., "Effect of Steam Generator Secondary Inventory on Reflux Condensation", 1986 ASME Winter Annual Mtg., (California, USA), (Dec., 1986).

(27) M.TANAKA, Y.KUKITA, R.R.Schultz, et. al., "A 10% Cold Leg Break Test at ROSA-IV Large Scale Test Facility", Nucl. Eng. and Design (1986).

(28) K.TASAKA, Y.KUKITA, Y.KOIZUMI, et. al., "The Results of 5% Small Break LOCA Tests and Natural Circulation Tests at ROSA-IV LSTF", 14th WRSRIM (Maryland, USA), (Oct., 1986).

(29) K.TASAKA and Y.KOIZUMI, "The ROSA-IV Large Scale Test Facility (LSTF) -- Test Program and First Look of Test Results --", J. Atomic Energy Soc. Japan (in Japanese) (1986).

(30) M.OSAKABE, C.Chauliac, T.YONOMOTO, et. al., "Core Liquid Level Depression due to Manometric Effect during Small Break LOCA -- Effect of Break Area --", J. Nucl. Sci. Technol. (1986).

(31) K.TASAKA, Y.KUKITA, Y.KOIZUMI, et. al., "The Results of 5% Small Break LOCA Tests and Natural Circulation Tests at the ROSA-IV LSTF", Nucl. Eng. and Design (1987).

(32) Y.KOIZUMI, M.OSAKABE, H.KUMAMARU, et. al., "Investigation of Natural Circulation Heat Transfer in Primary and Secondary Sides of Pressurized Water Reactor Steam Generator", International Symposium on Natural Circulation at the ASME Winter Annual Mtg. (Boston, USA), (Dec., 1987).

(33) Y.KUKITA, H.NAKAMURA, C.Chauliac, et. al., "Nonuniform Steam Generator U-Tube Flow Distribution during Natural Circulation Tests in ROSA-IV Large Scale Test Facility", 24th U.S. National Heat Transfer Conference (USA), (1987).

(34) M.OSAKABE, T.YONOMOTO, Y.KUKITA, et. al., "Core Liquid Level Depression due to Matometric Effect during PWR Small Break LOCA -- Effect of Core Bypass --", J. Nucl. Sci. Tecnol. (1987).

(35) Y.KUKITA, M.OSAKABE, Y.ANODA, et. al., "Flooding at Steam Generator Inlet and Its Impacts on Simulated PWR Natural Circulation", International Symposium on Natural Circulation ASME Winter Annual Mtg. (Boston), (Dec., 1987).

(36) R.R.Schultz, J.Chapman, Y.KUKITA, et. al., "Single and Two-Phase Natural Circulation in Westinghouse (W) Pressurized Water Reactor (PWR) Simulators : Phenomena, Analysis and Scaling", International Symposium on Natural Circulation ASME Winter Annual Mtg. (Boston), (Dec., 1987).

(37) H.Stumpf, F.Motley, R.Schulz, et. al., "Reverse Primary-Side Flow in Steam Generators during Natural Circulation Cooling", International Symposium on Natural circulation ASME Winter Annual Mtg. (Boston), (Dec., 1987).

(38) M.SUZUKI and K.TASAKA, "Simulation Test of PWR Instrument Tube Break LOCA in ROSA-IV Program", J. Nucl. Sci. Technol (1987).

(39) K.TASAKA, Y.KUKITA, H.KUMAMARU, et. al., "The Results of 0.5% PWR Small Break LOCA Tests in ROSA-IV LSTF Break Location Parameter Test Series", 15th WRSRIM (Maryland, USA), (Oct., 1987).

(40) Y.KOIZUMI, H.ASAKA, H.KUMAMARU, et. al., "Investigation of Break Orientation Effect during Cold Leg Small Break LOCA at ROSA-IV LSTF", J. Nucl. Sci. Technol. (1987).

(41) Y.KUKITA, H.NAKAMURA, K.TASAKA, et. al., "Nonuniform Steam Generator U-Tube Flow Distribution during Natural Circulatin Tests in ROSA-IV Large Scale Test Facility", Nucl. Sci. Engin. (1987).

(42) Y.KUKITA, Y.ANODA, K.TASAKA, et. al.,"Assessment and Improvement of RELAP5/MOD2 Code7s Interphase Drag Models", AIChE Symposium, Pittsburgh (1987)

(43) Y.KOIZUMI, H.KUMAMARU, Y.MIMURA, et. al., "Heat Transfer and Thermal-Hydraulics of Westinghouse-Type Pressurized Water Reactor Steam Generator -- Assessment of RELAP5/MOD2 Code --", 1988 ASME Winter Annual Mtg., Session of Thermal-Hydraulics of Nuclear Steam Generator/Heat Exchangers (Chicago, USA), (Nov., 1988).

(44) Y.KUKITA, Y.ANODA, H.NAKAMURA, et. al., "Steam Generator Primary Side Voiding during a Small-Break Loss-of-Coolant Accident in a Westinghuse-Type Pressurized Water Reactor", 1988 ASME Winter Annual Mtg., Session of Thermal-Hydraulics of Nuclear Steam Generator/Heat Exchangers (Chicago, USA), (Nov., 1988).

(45) Y.KUKITA, H.KUMAMARU, H.NAKAMURA, et. al., "CATHARE Analysis of ROSA-IV Experiments", CATHARE International Seminar (France), (May, 1988).

(46) K.TASAKA, Y.KUKITA, H.ASAKA, et. al., "The Effects of Break Location on PWR Small Break LOCA", 3rd International Topical Mtg. on Nuclear Power Plant Thermal-Hydraulics and Operations, (Seoul, Korea), (Nov., 1988).

(47) Y.KUKITA, T.YONOMOTO, H.NAKAMUA, et. al., "Manometric Core Liquid Level Depression during a Small-Break Loss-of-Coolant Accident in a Westinghouse-Type Pressurized Water Reactor", International Conference or Thermal Reactor Safety, ENS/ANS Topical Mtg. (France), (Oct., 1988).

(48) C.Renault, Y.KUKITA and K.TASAKA, "CATHARE Analysis of Break Flow Through an Orifice and of Bypass Effects in the Scaled 2-Inch Hot Leg Break LSTF Run SB-HL-03", International Conference on Thermal Reactor Safety, ENS/ANS Topical Mtg. (France), (Oct., 1988).

(49) T.YONOMOTO and K.TASAKA, "Theoretical and Experimental Study on Two-Phase Discharge Flow from a Stratified Two-Phase Region through a Small Break", ENS/ANS Topical Meeting, Avignon, France (Oct. 1988).

(50) K.TASAKA, Y.KUKITA, J.KATAYAMA, et.al., "Loop Seal Clearing and Refilling during a PWR Small-Break LOCA: Results of ROSA-IV LSTF Experiments", 16th WRSRI Mtg., (1988).

(51) Y.ANODA, R.HOSOYAMADA, Y.SHIMANE, et. al., "An Intractive Graphics Processor -- ROPS 2.0 -- User's Manual", JAERI-M 88-030 (in Japanese), (1988).

(52) N.Zuber, "Problems in modeling of Small Break LOCA", NUREG-0727, (1980).

(53) M.FUJII, M.YOKOKAWA, M.KAWAJI, et.al., "ROSA-IV/LSTF Experimental Data Reduction and Management Software System (Version 1)", JAERI-M 85-121, (in Japanese) (1985).

(54) Y.KUKITA, private communication (Dec. 1988).

Table 2.1 Major design characteristics of LSTF and PWR

		LSTF	PWR	PWR/LSTF
Pressure	(MPa)	16	16	1
Temperature	(K)	598	598	1
No. of fuel rods		1064	50952	48
Core height	(m)	3.66	3.66	1
Fluid volume V	(m^3)	7.23	347	48
Core power P	(MW)	10	3423(t)	342
P/V	(MW/m^3)	1.4	9.9	7.1
Core inlet flow	(t/s)	0.0488	16.7	342
Downcomer gap	(m)	0.053	0.260	4.91
Hot leg D	(m)	0.207	0.737	3.56
L	(m)	3.69	6.99	1.89
$L/\sqrt{D}$	($m^{1/2}$)	8.15	8.15	1.0
$\frac{\pi}{4}D^2L$	(m^3)	0.124	2.98	24.0
No. of loops		2	4	2
No. of tubes in steam generator		141	3382	24
Length of steam generator tube (average)	(m)	20.2	20.2	1.0

Table 2.2 LSTF instruments list

SEQ. NO.	FUNC ID.	TAG NAME	SEQ. NO.	FUNC ID.	TAG NAME	SEQ. NO.	FUNC ID.	TAG NAME	SEQ. NO.	FUNC ID.	TAG NAME	SEQ. NO.	FUNC ID.	TAG NAME
1	TE 1	TE010A-HLA	51	TE 51	TE270C-PR	101	TE 101	TE770-LSB	151	TE 151	TE-EX040-B01-UCP	201	TE 201	TE-N036C-DC
2	TE 2	TE010B-HLA	52	TE 52	TE280C-PR	102	TE 102	TE780-CLB	152	TE 152	TE-EX040-B03-UCP	202	TE 202	TE-S036C-DC
3	TE 3	TE010C-HLA	53	TE 53	TE290-PR	103	TE 103	TE790-PV	153	TE 153	TE-EX040-B05-UCP	203	TE 203	TE-E036C-DC
4	TE 4	TE010D-HLA	54	TE 54	TE300-PR	104	TE 104	TE800-PV	154	TE 154	TE-EX040-B07-UCP	204	TE 204	TE-W036C-DC
5	TE 5	TE010E-HLA	55	TE 55	TE430-SGA	105	TE 105	TE810-PR	155	TE 155	TE-EX040-B21-UCP	205	TE 205	TE-N060C-DC
6	TE 6	TE020C-HLA	56	TE 56	TE440-SGA	106	TE 106	TE820-PL	156	TE 156	TE-EX040-B23-UCP	206	TE 206	TE-S060C-DC
7	TE 7	TE020D-HLA	57	TE 57	TE450-SGA	107	TE 107	TE830-PL	157	TE 157	TE-EX040-B02-UCP	207	TE 207	TE-E060C-DC
8	TE 8	TE030C-HLA	58	TE 58	TE460-SGA	108	TE 108	TE840-PL	158	TE 158	TE-EX040-B06-UCP	208	TE 208	TE-W060C-DC
9	TE 9	TE030D-HLA	59	TE 59	TE470-SGB	109	TE 109	TE850-PL	159	TE 159	TE-EX040-B14-UCP	209	TE 209	TE-N055C-DC
10	TE 10	TE040A-HLA	60	TE 60	TE480-SGB	110	TE 110	TE860-PL	160	TE 160	TE-EX040-B15-UCP	210	TE 210	TE-S055C-DC
11	TE 11	TE040B-HLA	61	TE 61	TE490-SGB	111	TE 111	TE870-PL	161	TE 161	TE-EX040-B18-UCP	211	TE 211	TE-C-021-LP
12	TE 12	TE040C-HLA	62	TE 62	TE500-SGB	112	TE 112	TE880-RWST	162	TE 162	TE-EX040-B19-UCP	212	TE 212	TE-C-018-LP
13	TE 13	TE040D-HLA	63	TE 63	TE510-SH	113	TE 113	TE890-RWST	163	TE 163	TE-EX040-B10-UCP	213	TE 213	TE-C-015-LP
14	TE 14	TE040E-HLA	64	TE 64	TE520-JC	114	TE 114	TE900-EX	164	TE 164	TE-EX040-B12-UCP	214	TE 214	TE-C-012-LP
15	TE 15	TE050C-LSA	65	TE 65	TE530-JC	115	TE 115	TE-E066F-PV	165	TE 165	TE-EX040-B04-UCP	215	TE 215	TE-C-009-LP
16	TE 16	TE070C-CLA	66	TE 66	TE540-JC	116	TE 116	TE-W066F-PV	166	TE 166	TE-EX040-B08-UCP	216	TE 216	TE-C-006-LP
17	TE 17	TE070D-CLA	67	TE 67	TE550-JC	117	TE 117	TE-E075F-PV	167	TE 167	TE-EX040-B22-UCP	217	TE 217	TE-C-005-LP
18	TE 18	TE080C-CLA	68	TE 68	TE431-SGA	118	TE 118	TE-W075F-PV	168	TE 168	TE-EX040-B24-UCP	218	TE 218	TE-C-003-LP
19	TE 19	TE080D-CLA	69	TE 69	TE432-SGA	119	TE 119	TE-E081F-PV	169	TE 169	TE-IN-002B02-LCPP	219	TE 219	TE-B18621
20	TE 20	TE090A-CLA	70	TE 70	TE433-SGA	120	TE 120	TE-W081F-PV	170	TE 170	TE-IN-002B03-LCPP	220	TE 220	TE-B18622
21	TE 21	TE090B-CLA	71	TE 71	TE434-SGA	121	TE 121	TE-E080H-PV	171	TE 171	TE-IN-002B06-LCPP	221	TE 221	TE-B18623
22	TE 22	TE090C-CLA	72	TE 72	TE471-SGB	122	TE 122	TE-W080H-PV	172	TE 172	TE-IN-002B07-LCPP	222	TE 222	TE-B18624
23	TE 23	TE090D-CLA	73	TE 73	TE472-SGB	123	TE 123	TE-E049F-PV	173	TE 173	TE-IN-002B09-LCPP	223	TE 223	TE-B18625
24	TE 24	TE090E-CLA	74	TE 74	TE473-SGB	124	TE 124	TE-W049F-PV	174	TE 174	TE-IN-002B11-LCPP	224	TE 224	TE-B18626
25	TE 25	TE100-HLA	75	TE 75	TE474-SGB	125	TE 125	TE-E055F-PV	175	TE 175	TE-IN-002B14-LCPP	225	TE 225	TE-B18627
26	TE 26	TE150A-HLB	76	TE 76	TE560C-BU	126	TE 126	TE-W055F-PV	176	TE 176	TE-IN-002B16-LCPP	226	TE 226	TE-B18628
27	TE 27	TE150B-HLB	77	TE 77	TE560D-BU	127	TE 127	TE-E060F-PV	177	TE 177	TE-IN-002B18-LCPP	227	TE 227	TE-B18629
28	TE 28	TE150C-HLB	78	TE 78	TE570C-BU	128	TE 128	TE-W060F-PV	178	TE 178	TE-IN-002B20-LCPP	228	TE 228	TE-B01221
29	TE 29	TE150D-HLB	79	TE 79	TE570D-BU	129	TE 129	TE-IN038-B09-UCP	179	TE 179	TE-IN-002B21-LCPP	229	TE 229	TE-B01223
30	TE 30	TE150E-HLB	80	TE 80	TE580C-BU	130	TE 130	TE-IN038-B11-UCP	180	TE 180	TE-IN-002B23-LCPP	230	TE 230	TE-B01225
31	TE 31	TE160C-HLB	81	TE 81	TE580D-BU	131	TE 131	TE-IN038-B01-UCP	181	TE 181	TE-EX-000B02-LCPP	231	TE 231	TE-B01226
32	TE 32	TE160D-HLB	82	TE 82	TE590C-BU	132	TE 132	TE-IN038-B03-UCP	182	TE 182	TE-EX-000B03-LCPP	232	TE 232	TE-B01227
33	TE 33	TE170C-HLB	83	TE 83	TE590D-BU	133	TE 133	TE-IN038-B05-UCP	183	TE 183	TE-EX-000B06-LCPP	233	TE 233	TE-B01229
34	TE 34	TE170D-HLB	84	TE 84	TE600-ST	134	TE 134	TE-IN038-B07-UCP	184	TE 184	TE-EX-000B07-LCPP	234	TE 234	TE-B14262
35	TE 35	TE180A-HLB	85	TE 85	TE610-ST	135	TE 135	TE-IN038-B21-UCP	185	TE 185	TE-EX-000B09-LCPP	235	TE 235	TE-B14264
36	TE 36	TE180B-HLB	86	TE 86	TE620-ST	136	TE 136	TE-IN038-B23-UCP	186	TE 186	TE-EX-000B11-LCPP	236	TE 236	TE-B14268
37	TE 37	TE180C-HLB	87	TE 87	TE630-ST	137	TE 137	TE-IN038-B02-UCP	187	TE 187	TE-EX-000B14-LCPP	237	TE 237	TE-B05261
38	TE 38	TE180D-HLB	88	TE 88	TE640-ST	138	TE 138	TE-IN038-B06-UCP	188	TE 188	TE-EX-000B16-LCPP	238	TE 238	TE-B05263
39	TE 39	TE180E-HLB	89	TE 89	TE650-ACC	139	TE 139	TE-IN038-B14-UCP	189	TE 189	TE-EX-000B18-LCPP	239	TE 239	TE-B05265
40	TE 40	TE190C-LSB	90	TE 90	TE660-ACC	140	TE 140	TE-IN038-B15-UCP	190	TE 190	TE-EX-000B20-LCPP	240	TE 240	TE-B05266
41	TE 41	TE210C-CLB	91	TE 91	TE670-ACC	141	TE 141	TE-IN038-B18-UCP	191	TE 191	TE-EX-000B21-LCPP	241	TE 241	TE-B05267
42	TE 42	TE210D-CLB	92	TE 92	TE680-ACC	142	TE 142	TE-IN038-B19-UCP	192	TE 192	TE-EX-000B23-LCPP	242	TE 242	TE-B05269
43	TE 43	TE220C-CLB	93	TE 93	TE690-ACH	143	TE 143	TE-IN038-B10-UCP	193	TE 193	TE-N000C-DC	243	TE 243	TE-B04221
44	TE 44	TE220D-CLB	94	TE 94	TE700-ACH	144	TE 144	TE-IN038-B12-UCP	194	TE 194	TE-S000C-DC	244	TE 244	TE-B04223
45	TE 45	TE230A-CLB	95	TE 95	TE710-ACH	145	TE 145	TE-IN038-B04-UCP	195	TE 195	TE-E000C-DC	245	TE 245	TE-B04225
46	TE 46	TE230B-CLB	96	TE 96	TE720-ACH	146	TE 146	TE-IN038-B08-UCP	196	TE 196	TE-W000C-DC	246	TE 246	TE-B04226
47	TE 47	TE230C-CLB	97	TE 97	TE730-HLA	147	TE 147	TE-IN038-B22-UCP	197	TE 197	TE-N018C-DC	247	TE 247	TE-B04227
48	TE 48	TE230D-CLB	98	TE 98	TE740-LSA	148	TE 148	TE-IN038-B24-UCP	198	TE 198	TE-S018C-DC	248	TE 248	TE-B04229
49	TE 49	TE230E-CLB	99	TE 99	TE750-CLA	149	TE 149	TE-EX040-B09-UCP	199	TE 199	TE-E018C-DC	249	TE 249	TE-B07621
50	TE 50	TE240-HLB	100	TE 100	TE760-HLB	150	TE 150	TE-EX040-B11-UCP	200	TE 200	TE-W018C-DC	250	TE 250	TE-B07623

Table 2.2 LSTF instruments list (Cont'd)

SEQ. NO.	FUNC ID.	TAG NAME	SEQ. NO.	FUNC ID.	TAG NAME	SEQ. NO.	FUNC ID.	TAG NAME	SEQ. NO.	FUNC ID.	TAG NAME	SEQ. NO.	FUNC ID.	TAG NAME
251	TE 251	TE-B07625	301	TE 301	TE-B20662	351	TE 351	TE-EX0992-SGA	401	TE 401	TE-EX1376-SGA	451	TE 451	TE-IN0863-SGB
252	TE 252	TE-B07626	302	TE 302	TE-B20663	352	TE 352	TE-IN0993-SGA	402	TE 402	TE-IN1501-SGA	452	TE 452	TE-IN0864-SGB
253	TE 253	TE-B07627	303	TE 303	TE-B20664	353	TE 353	TE-EX0993-SGA	403	TE 403	TE-EX1501-SGA	453	TE 453	TE-IN0865-SGB
254	TE 254	TE-B07629	304	TE 304	TE-B20665	354	TE 354	TE-IN0994-SGA	404	TE 404	TE-IN1502-SGA	454	TE 454	TE-IN0866-SGB
255	TE 255	TE-B09661	305	TE 305	TE-B20666	355	TE 355	TE-EX0994-SGA	405	TE 405	TE-EX1502-SGA	455	TE 455	TE-EX0861-SGB
256	TE 256	TE-B09663	306	TE 306	TE-B20667	356	TE 356	TE-IN0995-SGA	406	TE 406	TE-IN1503-SGA	456	TE 456	TE-EX0862-SGB
257	TE 257	TE-B09665	307	TE 307	TE-B20668	357	TE 357	TE-EX0995-SGA	407	TE 407	TE-EX1503-SGA	457	TE 457	TE-EX0863-SGB
258	TE 258	TE-B09666	308	TE 308	TE-B20669	358	TE 358	TE-IN0996-SGA	408	TE 408	TE-IN1504-SGA	458	TE 458	TE-EX0864-SGB
259	TE 259	TE-B09667	309	TE 309	TE-B22661	359	TE 359	TE-EX0996-SGA	409	TE 409	TE-EX1504-SGA	459	TE 459	TE-EX0865-SGB
260	TE 260	TE-B09669	310	TE 310	TE-B22662	360	TE 360	TE-IN1051-SGA	410	TE 410	TE-IN1505-SGA	460	TE 460	TE-EX0866-SGB
261	TE 261	TE-B10621	311	TE 311	TE-B22663	361	TE 361	TE-IN1052-SGA	411	TE 411	TE-EX1505-SGA	461	TE 461	TE-IN0931-SGB
262	TE 262	TE-B10623	312	TE 312	TE-B22664	362	TE 362	TE-IN1053-SGA	412	TE 412	TE-IN1506-SGA	462	TE 462	TE-IN0932-SGB
263	TE 263	TE-B10625	313	TE 313	TE-B22665	363	TE 363	TE-IN1054-SGA	413	TE 413	TE-EX1506-SGA	463	TE 463	TE-IN0933-SGB
264	TE 264	TE-B10626	314	TE 314	TE-B22666	364	TE 364	TE-IN1055-SGA	414	TE 414	TE-IN1632-SGA	464	TE 464	TE-IN0934-SGB
265	TE 265	TE-B10627	315	TE 315	TE-B22667	365	TE 365	TE-IN1056-SGA	415	TE 415	TE-EX1632-SGA	465	TE 465	TE-IN0935-SGB
266	TE 266	TE-B10629	316	TE 316	TE-B22668	366	TE 366	TE-IN1121-SGA	416	TE 416	TE-IN1633-SGA	466	TE 466	TE-IN0936-SGB
267	TE 267	TE-B11221	317	TE 317	TE-B22669	367	TE 367	TE-EX1121-SGA	417	TE 417	TE-EX1633-SGA	467	TE 467	TE-IN0991-SGB
268	TE 268	TE-B11223	318	TE 318	TE-B24621	368	TE 368	TE-IN1122-SGA	418	TE 418	TE-IN1634-SGA	468	TE 468	TE-EX0991-SGB
269	TE 269	TE-B11225	319	TE 319	TE-B24623	369	TE 369	TE-EX1122-SGA	419	TE 419	TE-EX1634-SGA	469	TE 469	TE-IN0992-SGB
270	TE 270	TE-B11226	320	TE 320	TE-B24625	370	TE 370	TE-IN1123-SGA	420	TE 420	TE-IN1635-SGA	470	TE 470	TE-EX0992-SGB
271	TE 271	TE-B11227	321	TE 321	TE-B24626	371	TE 371	TE-EX1123-SGA	421	TE 421	TE-EX1635-SGA	471	TE 471	TE-IN0993-SGB
272	TE 272	TE-B11229	322	TE 322	TE-B24627	372	TE 372	TE-IN1124-SGA	422	TE 422	TE-IN1701-SGA	472	TE 472	TE-EX0993-SGB
273	TE 273	TE-B14261	323	TE 323	TE-B24629	373	TE 373	TE-EX1124-SGA	423	TE 423	TE-IN1706-SGA	473	TE 473	TE-IN0994-SGB
274	TE 274	TE-B14263	324	TE 324	TE-IN0641-SGA	374	TE 374	TE-IN1125-SGA	424	TE 424	TE-IN1782-SGA	474	TE 474	TE-EX0994-SGB
275	TE 275	TE-B14265	325	TE 325	TE-IN0642-SGA	375	TE 375	TE-EX1125-SGA	425	TE 425	TE-IN1785-SGA	475	TE 475	TE-IN0995-SGB
276	TE 276	TE-B14266	326	TE 326	TE-IN0643-SGA	376	TE 376	TE-IN1126-SGA	426	TE 426	TE-IN1863-SGA	476	TE 476	TE-EX0995-SGB
277	TE 277	TE-B14267	327	TE 327	TE-EX0641-SGA	377	TE 377	TE-EX1126-SGA	427	TE 427	TE-IN1864-SGA	477	TE 477	TE-IN0996-SGB
278	TE 278	TE-B14269	328	TE 328	TE-EX0642-SGA	378	TE 378	TE-IN1251-SGA	428	TE 428	TE-223D-SGA	478	TE 478	TE-EX0996-SGB
279	TE 279	TE-B15261	329	TE 329	TE-EX0643-SGA	379	TE 379	TE-EX1251-SGA	429	TE 429	TE-086C-SGA	479	TE 479	TE-IN1051-SGB
280	TE 280	TE-B15263	330	TE 330	TE-IN0861-SGA	380	TE 380	TE-IN1252-SGA	430	TE 430	TE-099C-SGA	480	TE 480	TE-IN1052-SGB
281	TE 281	TE-B15265	331	TE 331	TE-IN0862-SGA	381	TE 381	TE-EX1252-SGA	431	TE 431	TE-112C-SGA	481	TE 481	TE-IN1053-SGB
282	TE 282	TE-B15266	332	TE 332	TE-IN0863-SGA	382	TE 382	TE-IN1253-SGA	432	TE 432	TE-125C-SGA	482	TE 482	TE-IN1054-SGB
283	TE 283	TE-B15267	333	TE 333	TE-IN0864-SGA	383	TE 383	TE-EX1253-SGA	433	TE 433	TE-137C-SGA	483	TE 483	TE-IN1055-SGB
284	TE 284	TE-B15269	334	TE 334	TE-IN0865-SGA	384	TE 384	TE-IN1254-SGA	434	TE 434	TE-150C-SGA	484	TE 484	TE-IN1056-SGB
285	TE 285	TE-B16221	335	TE 335	TE-IN0866-SGA	385	TE 385	TE-EX1254-SGA	435	TE 435	TE-163C-SGA	485	TE 485	TE-IN1121-SGB
286	TE 286	TE-B16223	336	TE 336	TE-EX0861-SGA	386	TE 386	TE-IN1255-SGA	436	TE 436	TE-178C-SGA	486	TE 486	TE-EX1121-SGB
287	TE 287	TE-B16225	337	TE 337	TE-EX0862-SGA	387	TE 387	TE-EX1255-SGA	437	TE 437	TE-192F-SGA	487	TE 487	TE-IN1122-SGB
288	TE 288	TE-B16226	338	TE 338	TE-EX0863-SGA	388	TE 388	TE-IN1256-SGA	438	TE 438	TE-208F-SGA	488	TE 488	TE-EX1122-SGB
289	TE 289	TE-B16227	339	TE 339	TE-EX0864-SGA	389	TE 389	TE-EX1256-SGA	439	TE 439	TE-192C-SGA	489	TE 489	TE-IN1123-SGB
290	TE 290	TE-B16229	340	TE 340	TE-EX0865-SGA	390	TE 390	TE-IN1371-SGA	440	TE 440	TE-208C-SGA	490	TE 490	TE-EX1123-SGB
291	TE 291	TE-B15262	341	TE 341	TE-EX0866-SGA	391	TE 391	TE-EX1371-SGA	441	TE 441	TE-223C-SGA	491	TE 491	TE-IN1124-SGB
292	TE 292	TE-B15264	342	TE 342	TE-IN0931-SGA	392	TE 392	TE-IN1372-SGA	442	TE 442	TE-245C-SGA	492	TE 492	TE-EX1124-SGB
293	TE 293	TE-B15268	343	TE 343	TE-IN0932-SGA	393	TE 393	TE-EX1372-SGA	443	TE 443	TE-IN0641-SGB	493	TE 493	TE-IN1125-SGB
294	TE 294	TE-B23221	344	TE 344	TE-IN0933-SGA	394	TE 394	TE-IN1373-SGA	444	TE 444	TE-IN0642-SGB	494	TE 494	TE-EX1125-SGB
295	TE 295	TE-B23223	345	TE 345	TE-IN0934-SGA	395	TE 395	TE-EX1373-SGA	445	TE 445	TE-IN0643-SGB	495	TE 495	TE-IN1126-SGB
296	TE 296	TE-B23225	346	TE 346	TE-IN0935-SGA	396	TE 396	TE-IN1374-SGA	446	TE 446	TE-EX0641-SGB	496	TE 496	TE-EX1126-SGB
297	TE 297	TE-B23226	347	TE 347	TE-IN0936-SGA	397	TE 397	TE-EX1374-SGA	447	TE 447	TE-EX0642-SGB	497	TE 497	TE-IN1251-SGB
298	TE 298	TE-B23227	348	TE 348	TE-IN0991-SGA	398	TE 398	TE-IN1375-SGA	448	TE 448	TE-EX0643-SGB	498	TE 498	TE-EX1251-SGB
299	TE 299	TE-B23229	349	TE 349	TE-EX0991-SGA	399	TE 399	TE-EX1375-SGA	449	TE 449	TE-IN0861-SGB	499	TE 499	TE-IN1252-SGB
300	TE 300	TE-B20661	350	TE 350	TE-IN0992-SGA	400	TE 400	TE-IN1376-SGA	450	TE 450	TE-IN0862-SGB	500	TE 500	TE-EX1252-SGB

Table 2.2 LSTF instruments list (Cont'd)

SEQ. NO.	FUNC ID.	TAG NAME	SEQ. NO.	FUNC ID.	TAG NAME	SEQ. NO.	FUNC ID.	TAG NAME	SEQ. NO.	FUNC ID.	TAG NAME	SEQ. NO.	FUNC ID.	TAG NAME
501	TE 501	TE-IN1253-SGB	551	TE 551	TE-125C-SGB	601	TE 617	TE071B-CLA	651	DT 16	DTE170B-HLB	701	DT 66	DTE-W000C-PV
502	TE 502	TE-EX1253-SGB	552	TE 552	TE-137C-SGB	602	TE 618	TE071C-CLA	652	DT 17	DTE190A-LSB	702	DT 67	DTE-N018C-PV
503	TE 503	TE-IN1254-SGB	553	TE 553	TE-150C-SGB	603	TE 619	TE072C-CLA	653	DT 18	DTE190B-LSB	703	DT 68	DTE-S018C-PV
504	TE 504	TE-EX1254-SGB	554	TE 554	TE-163C-SGB	604	TE 620	TE072D-CLA	654	DT 19	DTE200A-PCB	704	DT 69	DTE-E018C-PV
505	TE 505	TE-IN1255-SGB	555	TE 555	TE-178C-SGB	605	TE 621	TE151A-HLB	655	DT 20	DTE210A-CLB	705	DT 70	DTE-W018C-PV
506	TE 506	TE-EX1255-SGB	556	TE 556	TE-192F-SGB	606	TE 622	TE151B-HLB	656	DT 21	DTE210B-CLB	706	DT 71	DTE-N036C-PV
507	TE 507	TE-IN1256-SGB	557	TE 557	TE-208F-SGB	607	TE 623	TE151C-HLB	657	DT 22	DTE220A-CLB	707	DT 72	DTE-S036C-PV
508	TE 508	TE-EX1256-SGB	558	TE 558	TE-192C-SGB	608	TE 624	TE152C-HLB	658	DT 23	DTE220B-CLB	708	DT 73	DTE-E036C-PV
509	TE 509	TE-IN1371-SGB	559	TE 559	TE-208C-SGB	609	TE 625	TE152D-HLB	659	DT 24	DTE240-HLB	709	DT 74	DTE-W036C-PV
510	TE 510	TE-EX1371-SGB	560	TE 560	TE-223C-SGB	610	TE 626	TE191A-LSB	660	DT 25	DTE270A-PR	710	DT 75	DTE-N060C-PV
511	TE 511	TE-IN1372-SGB	561	TE 561	TE-245C-SGB	611	TE 627	TE191B-LSB	661	DT 26	DTE280A-PR	711	DT 76	DTE-S060C-PV
512	TE 512	TE-EX1372-SGB	562	TE 562	TE-211C-PR	612	TE 628	TE191C-LSB	662	DT 27	DTE-E-015A-PV	712	DT 77	DTE-E060C-PV
513	TE 513	TE-IN1373-SGB	563	TE 563	TE-194C-PR	613	TE 629	TE191D-LSB	663	DT 28	DTE-W-015A-PV	713	DT 78	DTE-W060C-PV
514	TE 514	TE-EX1373-SGB	564	TE 564	TE-177C-PR	614	TE 630	TE192-LSB	664	DT 29	DTE-N000A-PV	714	DT 79	DTE-N000E-PV
515	TE 515	TE-IN1374-SGB	565	TE 565	TE-980	615	TE 631	TE211A-CLB	665	DT 30	DTE-S000A-PV	715	DT 80	DTE-S000E-PV
516	TE 516	TE-EX1374-SGB	566	TE 566	TE-981	616	TE 632	TE211B-CLB	666	DT 31	DTE-E000A-PV	716	DT 81	DTE-E000E-PV
517	TE 517	TE-IN1375-SGB	567	TE 567	TE-982	617	TE 633	TE211C-CLB	667	DT 32	DTE-W000A-PV	717	DT 82	DTE-W000E-PV
518	TE 518	TE-EX1375-SGB	568	TE 568	TE-983	618	TE 634	TE212C-CLB	668	DT 33	DTE-N018A-PV	718	DT 83	DTE-N010E-PV
519	TE 519	TE-IN1376-SGB	569	TE 569	TE-984	619	TE 635	TE212D-CLB	669	DT 34	DTE-S018A-PV	719	DT 84	DTE-S010E-PV
520	TE 520	TE-EX1376-SGB	570	TE 570	TE-985	620	TE 636	TE291C-PR	670	DT 35	DTE-E018A-PV	720	DT 85	DTE-E010E-PV
521	TE 521	TE-IN1501-SGB	571	TE 571	TE986	621	TE 637	TE291D-PR	671	DT 36	DTE-W018A-PV	721	DT 86	DTE-W010E-PV
522	TE 522	TE-EX1501-SGB	572	TE 572	TE-990	622	TE 638	TE301C-PR	672	DT 37	DTE-N036A-PV	722	DT 87	DTE-N018E-PV
523	TE 523	TE-IN1502-SGB	573	TE 573	TE-991	623	TE 639	TE301D-PR	673	DT 38	DTE-S036A-PV	723	DT 88	DTE-S018E-PV
524	TE 524	TE-EX1502-SGB	574	TE 574	TE-992	624	TE 640	TE311C-PR	674	DT 39	DTE-E036A-PV	724	DT 89	DTE-E018E-PV
525	TE 525	TE-IN1503-SGB	575	TE 575	TE-993	625	TE 641	TE311D-PR	675	DT 40	DTE-W036A-PV	725	DT 90	DTE-W018E-PV
526	TE 526	TE-EX1503-SGB	576	TE 576	TE-994	626	TE 644	TE571C-BU	676	DT 41	DTE-N060A-PV	726	DT 91	DTE-N026E-PV
527	TE 527	TE-IN1504-SGB	577	TE 577	TE-995	627	TE 645	TE571D-BU	677	DT 42	DTE-S060A-PV	727	DT 92	DTE-S026E-PV
528	TE 528	TE-EX1504-SGB	578	TE 578	TE-996	628	TE 651	TE591C-BU	678	DT 43	DTE-E060A-PV	728	DT 93	DTE-E026E-PV
529	TE 529	TE-IN1505-SGB	579	TE 579	TE-997	629	TE 652	TE591D-BU	679	DT 44	DTE-W060A-PV	729	DT 94	DTE-W026E-PV
530	TE 530	TE-EX1505-SGB	580	TE 596	TE-177D-PR	630	TE 662	TE-N-006-DC	680	DT 45	DTE-E080A-PV	730	DT 95	DTE-N036E-PV
531	TE 531	TE-IN1506-SGB	581	TE 597	TE-181D-PR	631	TE 663	TE-S-006-DC	681	DT 46	DTE-W080A-PV	731	DT 96	DTE-S036E-PV
532	TE 532	TE-EX1506-SGB	582	TE 598	TE-185D-PR	632	TE 664	TE-E-006-DC	682	DT 47	DTE-N000B-PV	732	DT 97	DTE-E036E-PV
533	TE 533	TE-IN1632-SGB	583	TE 599	TE-189D-PR	633	TE 665	TE-W-006-DC	683	DT 48	DTE-S000B-PV	733	DT 98	DTE-W036E-PV
534	TE 534	TE-EX1632-SGB	584	TE 600	TE-192D-PR	634	TE 666	TE451C-SGA	684	DT 49	DTE-E000B-PV	734	DT 99	DTE-N049E-PV
535	TE 535	TE-IN1633-SGB	585	TE 601	TE-196D-PR	635	TE 667	TE451D-SGA	685	DT 50	DTE-W000B-PV	735	DT 100	DTE-S049E-PV
536	TE 536	TE-EX1633-SGB	586	TE 602	TE-200D-PR	636	DT 1	DTE020A-HLA	686	DT 51	DTE-N018B-PV	736	DT 101	DTE-E049E-PV
537	TE 537	TE-IN1634-SGB	587	TE 603	TE-204D-PR	637	DT 2	DTE020B-HLA	687	DT 52	DTE-S018B-PV	737	DT 102	DTE-W049E-PV
538	TE 538	TE-EX1634-SGB	588	TE 604	TE-207D-PR	638	DT 3	DTE030A-HLA	688	DT 53	DTE-E018B-PV	738	DT 103	DTE-N060E-PV
539	TE 539	TE-IN1635-SGB	589	TE 605	TE-211D-PR	639	DT 4	DTE030B-HLA	689	DT 54	DTE-W018B-PV	739	DT 104	DTE-S060E-PV
540	TE 540	TE-EX1635-SGB	590	TE 606	TE011A-HLA	640	DT 5	DTE050A-LSA	690	DT 55	DTE-N036B-PV	740	DT 105	DTE-E060E-PV
541	TE 541	TE-IN1701-SGB	591	TE 607	TE011B-HLA	641	DT 6	DTE050B-LSA	691	DT 56	DTE-S036B-PV	741	DT 106	DTE-W060E-PV
542	TE 542	TE-IN1706-SGB	592	TE 608	TE011C-HLA	642	DT 7	DTE060A-PCA	692	DT 57	DTE-E036B-PV	742	DT 107	DTE-040-B09-UCP
543	TE 543	TE-IN1782-SGB	593	TE 609	TE012C-HLA	643	DT 8	DTE070A-CLA	693	DT 58	DTE-W036B-PV	743	DT 108	DTE-040-B11-UCP
544	TE 544	TE-IN1785-SGB	594	TE 610	TE012D-HLA	644	DT 9	DTE070B-CLA	694	DT 59	DTE-N060B-PV	744	DT 109	DTE-040-B01-UCP
545	TE 545	TE-IN1863-SGB	595	TE 611	TE051A-LSA	645	DT 10	DTE080A-CLA	695	DT 60	DTE-S060B-PV	745	DT 110	DTE-040-B03-UCP
546	TE 546	TE-IN1864-SGB	596	TE 612	TE051B-LSA	646	DT 11	DTE080B-CLA	696	DT 61	DTE-E060B-PV	746	DT 111	DTE-040-B05-UCP
547	TE 547	TE-223D-SGB	597	TE 613	TE051C-LSA	647	DT 12	DTE100-HLA	697	DT 62	DTE-W060B-PV	747	DT 112	DTE-040-B07-UCP
548	TE 548	TE-086C-SGB	598	TE 614	TE051D-LSA	648	DT 13	DTE160A-HLB	698	DT 63	DTE-N000C-PV	748	DT 113	DTE-040-B21-UCP
549	TE 549	TE-099C-SGB	599	TE 615	TE052-LSA	649	DT 14	DTE160B-HLB	699	DT 64	DTE-S000C-PV	749	DT 114	DTE-040-B23-UCP
550	TE 550	TE-112C-SGB	600	TE 616	TE071A-CLA	650	DT 15	DTE170A-HLB	700	DT 65	DTE-E000C-PV	750	DT 115	DTE-040-B02-UCP

Table 2.2 LSTF instruments list (Cont'd)

SEQ. NO.	FUNC ID.	TAG NAME	SEQ. NO.	FUNC ID.	TAG NAME	SEQ. NO.	FUNC ID.	TAG NAME	SEQ. NO.	FUNC ID.	TAG NAME	SEQ. NO.	FUNC ID.	TAG NAME
751	DT 116	DTE-040-B15-UCP	801	DT 166	DTE-EX1373-SGA	851	TW 8	TWE170B-HLB	901	TW 58	TWE-N036D-CB	951	TW 108	TWE-063-B09-UCSP
752	DT 117	DTE-040-B06-UCP	802	DT 167	DTE-IN1632-SGA	852	TW 9	TWE190B-LSB	902	TW 59	TWE-S036D-CB	952	TW 109	TWE-065-B09-UCSP
753	DT 118	DTE-040-B14-UCP	803	DT 168	DTE-EX1632-SGA	853	TW 10	TWE200B-PCB	903	TW 60	TWE-E036D-CB	953	TW 110	TWE-E047G-UP
754	DT 119	DTE-040-B18-UCP	804	DT 169	DTE-IN1633-SGA	854	TW 11	TWE210B-CLB	904	TW 61	TWE-W036D-CB	954	TW 111	TWE-W047G-UP
755	DT 120	DTE-040-B19-UCP	805	DT 170	DTE-EX1633-SGA	855	TW 12	TWE220B-CLB	905	TW 62	TWE-N049D-CB	955	TW 112	TWE-E056G-UP
756	DT 121	DTE-040-B10-UCP	806	DT 171	DTE-IN1701-SGA	856	TW 13	TWE280B-PR	906	TW 63	TWE-S049D-CB	956	TW 113	TWE-W056G-UP
757	DT 122	DTE-040-B12-UCP	807	DT 172	DTE-IN1782-SGA	857	TW 14	TWE431A-SGA	907	TW 64	TWE-E049D-CB	957	TW 114	TWE-080G-UH
758	DT 123	DTE-040-B04-UCP	808	DT 173	DTE-IN1863-SGA	858	TW 15	TWE432A-SGA	908	TW 65	TWE-W049D-CB	958	TW 115	TWE-B01342
759	DT 124	DTE-040-B08-UCP	809	DT 174	DTE-086A-SGB	859	TW 16	TWE433A-SGA	909	TW 66	TWE-N060D-CB	959	TW 116	TWE-B01344
760	DT 125	DTE-040-B22-UCP	810	DT 175	DTE-137A-SGB	860	TW 17	TWE434A-SGA	910	TW 67	TWE-S060D-CB	960	TW 117	TWE-B01345
761	DT 126	DTE-040-B24-UCP	811	DT 176	DTE-178A-SGB	861	TW 18	TWE471A-SGB	911	TW 68	TWE-E060D-CB	961	TW 118	TWE-B01346
762	DT 127	DTE-000-B02-LCP	812	DT 177	DTE-223A-SGB	862	TW 19	TWE472A-SGB	912	TW 69	TWE-W060D-CB	962	TW 119	TWE-B01347
763	DT 128	DTE-000-B03-LCP	813	DT 178	DTE-IN0861-SGB	863	TW 20	TWE473A-SGB	913	TW 70	TWE-N000E-CB	963	TW 120	TWE-B01348
764	DT 129	DTE-000-B06-LCP	814	DT 179	DTE-EX0861-SGB	864	TW 21	TWE474A-SGB	914	TW 71	TWE-S000E-CB	964	TW 121	TWE-B20431
765	DT 130	DTE-000-B07-LCP	815	DT 180	DTE-IN0862-SGB	865	TW 22	TWE-E-015B-PV	915	TW 72	TWE-E000E-CB	965	TW 122	TWE-B20433
766	DT 131	DTE-000-B09-LCP	816	DT 181	DTE-EX0862-SGB	866	TW 23	TWE-W-015B-PV	916	TW 73	TWE-W000E-CB	966	TW 123	TWE-B20435
767	DT 132	DTE-000-B11-LCP	817	DT 182	DTE-IN0863-SGB	867	TW 24	TWE-N000B-PV	917	TW 74	TWE-N010E-CB	967	TW 124	TWE-B20436
768	DT 133	DTE-000-B14-LCP	818	DT 183	DTE-EX0863-SGB	868	TW 25	TWE-S000B-PV	918	TW 75	TWE-S010E-CB	968	TW 125	TWE-B20438
769	DT 134	DTE-000-B16-LCP	819	DT 184	DTE-IN0991-SGB	869	TW 26	TWE-E000B-PV	919	TW 76	TWE-E010E-CB	969	TW 126	TWE-B20439
770	DT 135	DTE-000-B18-LCP	820	DT 185	DTE-EX0991-SGB	870	TW 27	TWE-W000B-PV	920	TW 77	TWE-W010E-CB	970	TW 127	TWE-B02241
771	DT 136	DTE-000-B20-LCP	821	DT 186	DTE-IN0992-SGB	871	TW 28	TWE-N018B-PV	921	TW 78	TWE-N018E-CB	971	TW 128	TWE-B02242
772	DT 137	DTE-000-B21-LCP	822	DT 187	DTE-EX0992-SGB	872	TW 29	TWE-S018B-PV	922	TW 79	TWE-S018E-CB	972	TW 129	TWE-B02244
773	DT 138	DTE-000-B23-LCP	823	DT 188	DTE-IN0993-SGB	873	TW 30	TWE-E018B-PV	923	TW 80	TWE-E018E-CB	973	TW 130	TWE-B02245
774	DT 139	DTE-086A-SGA	824	DT 189	DTE-EX0993-SGB	874	TW 31	TWE-W018B-PV	924	TW 81	TWE-W018E-CB	974	TW 131	TWE-B02247
775	DT 140	DTE-137A-SGA	825	DT 190	DTE-IN1121-SGB	875	TW 32	TWE-N036B-PV	925	TW 82	TWE-N026E-CB	975	TW 132	TWE-B02249
776	DT 141	DTE-178A-SGA	826	DT 191	DTE-EX1121-SGB	876	TW 33	TWE-S036B-PV	926	TW 83	TWE-S026E-CB	976	TW 133	TWE-B02341
777	DT 142	DTE-223A-SGA	827	DT 192	DTE-IN1122-SGB	877	TW 34	TWE-E036B-PV	927	TW 84	TWE-E026E-CB	977	TW 134	TWE-B02343
778	DT 143	DTE-IN0861-SGA	828	DT 193	DTE-EX1122-SGB	878	TW 35	TWE-W036B-PV	928	TW 85	TWE-W026E-CB	978	TW 135	TWE-B02345
779	DT 144	DTE-EX0861-SGA	829	DT 194	DTE-IN1123-SGB	879	TW 36	TWE-N060B-PV	929	TW 86	TWE-N036E-CB	979	TW 136	TWE-B02346
780	DT 145	DTE-IN0862-SGA	830	DT 195	DTE-EX1123-SGB	880	TW 37	TWE-S060B-PV	930	TW 87	TWE-S036E-CB	980	TW 137	TWE-B02348
781	DT 146	DTE-EX0862-SGA	831	DT 196	DTE-IN1371-SGB	881	TW 38	TWE-E060B-PV	931	TW 88	TWE-E036E-CB	981	TW 138	TWE-B02349
782	DT 147	DTE-IN0863-SGA	832	DT 197	DTE-EX1371-SGB	882	TW 39	TWE-W060B-PV	932	TW 89	TWE-W036E-CB	982	TW 139	TWE-B02482
783	DT 148	DTE-EX0863-SGA	833	DT 198	DTE-IN1372-SGB	883	TW 40	TWE-E080B-PV	933	TW 90	TWE-N049E-CB	983	TW 140	TWE-B02484
784	DT 149	DTE-IN0991-SGA	834	DT 199	DTE-EX1372-SGB	884	TW 41	TWE-W080B-PV	934	TW 91	TWE-S049E-CB	984	TW 141	TWE-B02485
785	DT 150	DTE-EX0991-SGA	835	DT 200	DTE-IN1373-SGB	885	TW 42	TWE-N000D-CB	935	TW 92	TWE-E049E-CB	985	TW 142	TWE-B02486
786	DT 151	DTE-IN0992-SGA	836	DT 201	DTE-EX1373-SGB	886	TW 43	TWE-S000D-CB	936	TW 93	TWE-W049E-CB	986	TW 143	TWE-B02487
787	DT 152	DTE-EX0992-SGA	837	DT 202	DTE-IN1632-SGB	887	TW 44	TWE-E000D-CB	937	TW 94	TWE-N060E-CB	987	TW 144	TWE-B02488
788	DT 153	DTE-IN0993-SGA	838	DT 203	DTE-EX1632-SGB	888	TW 45	TWE-W000D-CB	938	TW 95	TWE-S060E-CB	988	TW 145	TWE-B03421
789	DT 154	DTE-EX0993-SGA	839	DT 204	DTE-IN1633-SGB	889	TW 46	TWE-N010D-CB	939	TW 96	TWE-E060E-CB	989	TW 146	TWE-B03422
790	DT 155	DTE-IN1121-SGA	840	DT 205	DTE-EX1633-SGB	890	TW 47	TWE-S010D-CB	940	TW 97	TWE-W060E-CB	990	TW 147	TWE-B03424
791	DT 156	DTE-EX1121-SGA	841	DT 206	DTE-IN1701-SGB	891	TW 48	TWE-E010D-CB	941	TW 98	TWE-IN038B02-UCP	991	TW 148	TWE-B03425
792	DT 157	DTE-IN1122-SGA	842	DT 207	DTE-IN1782-SGB	892	TW 49	TWE-W010D-CB	942	TW 99	TWE-IN038B04-UCP	992	TW 149	TWE-B03427
793	DT 158	DTE-EX1122-SGA	843	DT 208	DTE-IN1863-SGB	893	TW 50	TWE-N018D-CB	943	TW 100	TWE-IN038B06-UCP	993	TW 150	TWE-B03429
794	DT 159	DTE-IN1123-SGA	844	TW 1	TWE020B-HLA	894	TW 51	TWE-S018D-CB	944	TW 101	TWE-IN038B08-UCP	994	TW 151	TWE-B03431
795	DT 160	DTE-EX1123-SGA	845	TW 2	TWE030B-HLA	895	TW 52	TWE-E018D-CB	945	TW 102	TWE-IN038B21-UCP	995	TW 152	TWE-B03433
796	DT 161	DTE-IN1371-SGA	846	TW 3	TWE050B-LSA	896	TW 53	TWE-W018D-CB	946	TW 103	TWE-EX040B02-UCP	996	TW 153	TWE-B03435
797	DT 162	DTE-EX1371-SGA	847	TW 4	TWE060B-PCA	897	TW 54	TWE-N026D-CB	947	TW 104	TWE-EX040B04-UCP	997	TW 154	TWE-B03436
798	DT 163	DTE-IN1372-SGA	848	TW 5	TWE070B-CLA	898	TW 55	TWE-S026D-CB	948	TW 105	TWE-EX040B06-UCP	998	TW 155	TWE-B03438
799	DT 164	DTE-EX1372-SGA	849	TW 6	TWE080B-CLA	899	TW 56	TWE-E026D-CB	949	TW 106	TWE-EX040B08-UCP	999	TW 156	TWE-B03439
800	DT 165	DTE-IN1373-SGA	850	TW 7	TWE160B-HLB	900	TW 57	TWE-W026D-CB	950	TW 107	TWE-EX040B21-UCP	1000	TW 157	TWE-B03842

Table 2.2 LSTF instruments list (Cont'd)

SEQ. NO.	FUNC ID.	TAG NAME	SEQ. NO.	FUNC ID.	TAG NAME	SEQ. NO.	FUNC ID.	TAG NAME	SEQ. NO.	FUNC ID.	TAG NAME	SEQ. NO.	FUNC ID.	TAG NAME
1001	TW 158	TWE-B03844	1051	TW 208	TWE-B07436	1101	TW 258	TWE-B11178	1151	TW 308	TWE-B15442	1201	TW 358	TWE-B18446
1002	TW 159	TWE-B03845	1052	TW 209	TWE-B07438	1102	TW 259	TWE-B12262	1152	TW 309	TWE-B15444	1202	TW 359	TWE-B18448
1003	TW 160	TWE-B03846	1053	TW 210	TWE-B07439	1103	TW 260	TWE-B12264	1153	TW 310	TWE-B15445	1203	TW 360	TWE-B18449
1004	TW 161	TWE-B03847	1054	TW 211	TWE-B07842	1104	TW 261	TWE-B12265	1154	TW 311	TWE-B15447	1204	TW 361	TWE-B19451
1005	TW 162	TWE-B03848	1055	TW 212	TWE-B07844	1105	TW 262	TWE-B12266	1155	TW 312	TWE-B15449	1205	TW 362	TWE-B19452
1006	TW 163	TWE-B04432	1056	TW 213	TWE-B07845	1106	TW 263	TWE-B12267	1156	TW 313	TWE-B15451	1206	TW 363	TWE-B19454
1007	TW 164	TWE-B04434	1057	TW 214	TWE-B07846	1107	TW 264	TWE-B12268	1157	TW 314	TWE-B15453	1207	TW 364	TWE-B19455
1008	TW 165	TWE-B04435	1058	TW 215	TWE-B07847	1108	TW 265	TWE-B12441	1158	TW 315	TWE-B15455	1208	TW 365	TWE-B19457
1009	TW 166	TWE-B04436	1059	TW 216	TWE-B07848	1109	TW 266	TWE-B12442	1159	TW 316	TWE-B15456	1209	TW 366	TWE-B19459
1010	TW 167	TWE-B04437	1060	TW 217	TWE-B08222	1110	TW 267	TWE-B12444	1160	TW 317	TWE-B15458	1210	TW 367	TWE-B19441
1011	TW 168	TWE-B04438	1061	TW 218	TWE-B08224	1111	TW 268	TWE-B12445	1161	TW 318	TWE-B15459	1211	TW 368	TWE-B19443
1012	TW 169	TWE-B05342	1062	TW 219	TWE-B08225	1112	TW 269	TWE-B12447	1162	TW 319	TWE-B15172	1212	TW 369	TWE-B19445
1013	TW 170	TWE-B05344	1063	TW 220	TWE-B08226	1113	TW 270	TWE-B12449	1163	TW 320	TWE-B15174	1213	TW 370	TWE-B19446
1014	TW 171	TWE-B05345	1064	TW 221	TWE-B08227	1114	TW 271	TWE-B12431	1164	TW 321	TWE-B15175	1214	TW 371	TWE-B19448
1015	TW 172	TWE-B05346	1065	TW 222	TWE-B08228	1115	TW 272	TWE-B12433	1165	TW 322	TWE-B15176	1215	TW 372	TWE-B19449
1016	TW 173	TWE-B05347	1066	TW 223	TWE-B08432	1116	TW 273	TWE-B12435	1166	TW 323	TWE-B15177	1216	TW 373	TWE-B20441
1017	TW 174	TWE-B05348	1067	TW 224	TWE-B08434	1117	TW 274	TWE-B12436	1167	TW 324	TWE-B15178	1217	TW 374	TWE-B20442
1018	TW 175	TWE-B05172	1068	TW 225	TWE-B08435	1118	TW 275	TWE-B12438	1168	TW 325	TWE-B16442	1218	TW 375	TWE-B20444
1019	TW 176	TWE-B05174	1069	TW 226	TWE-B08436	1119	TW 276	TWE-B12439	1169	TW 326	TWE-B16444	1219	TW 376	TWE-B20445
1020	TW 177	TWE-B05175	1070	TW 227	TWE-B08437	1120	TW 277	TWE-B13662	1170	TW 327	TWE-B16445	1220	TW 377	TWE-B20447
1021	TW 178	TWE-B05176	1071	TW 228	TWE-B08438	1121	TW 278	TWE-B13664	1171	TW 328	TWE-B16446	1221	TW 378	TWE-B20449
1022	TW 179	TWE-B05177	1072	TW 229	TWE-B09442	1122	TW 279	TWE-B13665	1172	TW 329	TWE-B16447	1222	TW 379	TWE-B21441
1023	TW 180	TWE-B05178	1073	TW 230	TWE-B09444	1123	TW 280	TWE-B13666	1173	TW 330	TWE-B16448	1223	TW 380	TWE-B21442
1024	TW 181	TWE-B06241	1074	TW 231	TWE-B09445	1124	TW 281	TWE-B13667	1174	TW 331	TWE-B16172	1224	TW 381	TWE-B21444
1025	TW 182	TWE-B06242	1075	TW 232	TWE-B09446	1125	TW 282	TWE-B13668	1175	TW 332	TWE-B16174	1225	TW 382	TWE-B21445
1026	TW 183	TWE-B06244	1076	TW 233	TWE-B09447	1126	TW 283	TWE-B13442	1176	TW 333	TWE-B16175	1226	TW 383	TWE-B21447
1027	TW 184	TWE-B06245	1077	TW 234	TWE-B09448	1127	TW 284	TWE-B13444	1177	TW 334	TWE-B16176	1227	TW 384	TWE-B21449
1028	TW 185	TWE-B06247	1078	TW 235	TWE-B10441	1128	TW 285	TWE-B13445	1178	TW 335	TWE-B16177	1228	TW 385	TWE-B21541
1029	TW 186	TWE-B06249	1079	TW 236	TWE-B10442	1129	TW 286	TWE-B13446	1179	TW 336	TWE-B16178	1229	TW 386	TWE-B21543
1030	TW 187	TWE-B06341	1080	TW 237	TWE-B10444	1130	TW 287	TWE-B13447	1180	TW 337	TWE-B17442	1230	TW 387	TWE-B21545
1031	TW 188	TWE-B06343	1081	TW 238	TWE-B10445	1131	TW 288	TWE-B13448	1181	TW 338	TWE-B17444	1231	TW 388	TWE-B21546
1032	TW 189	TWE-B06345	1082	TW 239	TWE-B10447	1132	TW 289	TWE-B14541	1182	TW 339	TWE-B17445	1232	TW 389	TWE-B21548
1033	TW 190	TWE-B06346	1083	TW 240	TWE-B10449	1133	TW 290	TWE-B14542	1183	TW 340	TWE-B17446	1233	TW 390	TWE-B21549
1034	TW 191	TWE-B06348	1084	TW 241	TWE-B10451	1134	TW 291	TWE-B14544	1184	TW 341	TWE-B17447	1234	TW 391	TWE-B21662
1035	TW 192	TWE-B06349	1085	TW 242	TWE-B10453	1135	TW 292	TWE-B14545	1185	TW 342	TWE-B17448	1235	TW 392	TWE-B21664
1036	TW 193	TWE-B06482	1086	TW 243	TWE-B10455	1136	TW 293	TWE-B14547	1186	TW 343	TWE-B17172	1236	TW 393	TWE-B21665
1037	TW 194	TWE-B06484	1087	TW 244	TWE-B10456	1137	TW 294	TWE-B14549	1187	TW 344	TWE-B17174	1237	TW 394	TWE-B21666
1038	TW 195	TWE-B06485	1088	TW 245	TWE-B10458	1138	TW 295	TWE-B14441	1188	TW 345	TWE-B17175	1238	TW 395	TWE-B21667
1039	TW 196	TWE-B06486	1089	TW 246	TWE-B10459	1139	TW 296	TWE-B14443	1189	TW 346	TWE-B17176	1239	TW 396	TWE-B21668
1040	TW 197	TWE-B06487	1090	TW 247	TWE-B11442	1140	TW 297	TWE-B14445	1190	TW 347	TWE-B17177	1240	TW 397	TWE-B21112
1041	TW 198	TWE-B06488	1091	TW 248	TWE-B11444	1141	TW 298	TWE-B14446	1191	TW 348	TWE-B17178	1241	TW 398	TWE-B21114
1042	TW 199	TWE-B07421	1092	TW 249	TWE-B11445	1142	TW 299	TWE-B14448	1192	TW 349	TWE-B18341	1242	TW 399	TWE-B21115
1043	TW 200	TWE-B07422	1093	TW 250	TWE-B11446	1143	TW 300	TWE-B14449	1193	TW 350	TWE-B18342	1243	TW 400	TWE-B21116
1044	TW 201	TWE-B07424	1094	TW 251	TWE-B11447	1144	TW 301	TWE-B14172	1194	TW 351	TWE-B18344	1244	TW 401	TWE-B21117
1045	TW 202	TWE-B07425	1095	TW 252	TWE-B11448	1145	TW 302	TWE-B14174	1195	TW 352	TWE-B18345	1245	TW 402	TWE-B21118
1046	TW 203	TWE-B07427	1096	TW 253	TWE-B11172	1146	TW 303	TWE-B14175	1196	TW 353	TWE-B18347	1246	TW 403	TWE-B22541
1047	TW 204	TWE-B07429	1097	TW 254	TWE-B11174	1147	TW 304	TWE-B14176	1197	TW 354	TWE-B18349	1247	TW 404	TWE-B22542
1048	TW 205	TWE-B07431	1098	TW 255	TWE-B11175	1148	TW 305	TWE-B14177	1198	TW 355	TWE-B18441	1248	TW 405	TWE-B22544
1049	TW 206	TWE-B07433	1099	TW 256	TWE-B11176	1149	TW 306	TWE-B14178	1199	TW 356	TWE-B18443	1249	TW 406	TWE-B22545
1050	TW 207	TWE-B07435	1100	TW 257	TWE-B11177	1150	TW 307	TWE-B15441	1200	TW 357	TWE-B18445	1250	TW 407	TWE-B22547

Table 2.2 LSTF instruments list (Cont'd)

SEQ. NO.	FUNC ID.	TAG NAME	SEQ. NO.	FUNC ID.	TAG NAME	SEQ. NO.	FUNC ID.	TAG NAME	SEQ. NO.	FUNC ID.	TAG NAME	SEQ. NO.	FUNC ID.	TAG NAME
1251	TW 408	TWE-B22549	1301	TW 458	TWE-IN0642-SGA	1351	TW 508	TWE-IN0861-SGB	1401	TW 558	TWE151B-HLB	1451	FE 27	FE490-SGB
1252	TW 409	TWE-B22441	1302	TW 459	TWE-IN0643-SGA	1352	TW 509	TWE-EX0861-SGB	1402	TW 559	TWE151C-HLB	1452	FE 28	FE500-SGB
1253	TW 410	TWE-B22443	1303	TW 460	TWE-EX0641-SGA	1353	TW 510	TWE-IN0862-SGB	1403	TW 560	TWE161-HLB	1453	FE 29	FE510-SH
1254	TW 411	TWE-B22445	1304	TW 461	TWE-EX0642-SGA	1354	TW 511	TWE-EX0862-SGB	1404	TW 561	TWE191A-LSB	1454	FE 30	FE520-PA
1255	TW 412	TWE-B22446	1305	TW 462	TWE-EX0643-SGA	1355	TW 512	TWE-IN0863-SGB	1405	TW 562	TWE191B-LSB	1455	FE 31	FE560A-BU
1256	TW 413	TWE-B22448	1306	TW 463	TWE-086B-SGA	1356	TW 513	TWE-EX0863-SGB	1406	TW 563	TWE191C-LSB	1456	FE 32	FE560B-BU
1257	TW 414	TWE-B22449	1307	TW 464	TWE-137B-SGA	1357	TW 514	TWE-IN0991-SGB	1407	TW 564	TWE191D-LSB	1457	FE 33	FE570A-BU
1258	TW 415	TWE-B22172	1308	TW 465	TWE-178B-SGA	1358	TW 515	TWE-EX0991-SGB	1408	TW 565	TWE211A-CLB	1458	FE 34	FE570B-BU
1259	TW 416	TWE-B22174	1309	TW 466	TWE-223B-SGA	1359	TW 516	TWE-IN0992-SGB	1409	TW 566	TWE211B-CLB	1459	FE 35	FE580-ST
1260	TW 417	TWE-B22175	1310	TW 467	TWE-IN0861-SGA	1360	TW 517	TWE-EX0992-SGB	1410	TW 567	TWE211C-CLB	1460	FE 36	FE590-ST
1261	TW 418	TWE-B22176	1311	TW 468	TWE-EX0861-SGA	1361	TW 518	TWE-IN0993-SGB	1411	TW 568	TWE291A-PR	1461	FE 37	FE650-ACC
1262	TW 419	TWE-B22177	1312	TW 469	TWE-IN0862-SGA	1362	TW 519	TWE-EX0993-SGB	1412	TW 569	TWE291B-PR	1462	FE 38	FE660-ACC
1263	TW 420	TWE-B22178	1313	TW 470	TWE-EX0862-SGA	1363	TW 520	TWE-IN1121-SGB	1413	TW 570	TWE301A-PR	1463	FE 39	FE670-ACH
1264	TW 421	TWE-B23441	1314	TW 471	TWE-IN0863-SGA	1364	TW 521	TWE-EX1121-SGB	1414	TW 571	TWE301B-PR	1464	FE 40	FE680-ACH
1265	TW 422	TWE-B23442	1315	TW 472	TWE-EX0863-SGA	1365	TW 522	TWE-IN1122-SGB	1415	TW 573	TWE571A-BU	1465	FE 41	FE730-PJ
1266	TW 423	TWE-B23444	1316	TW 473	TWE-IN0991-SGA	1366	TW 523	TWE-EX1122-SGB	1416	TW 574	TWE571B-BU	1466	FE 42	FE740-PJ
1267	TW 424	TWE-B23445	1317	TW 474	TWE-EX0991-SGA	1367	TW 524	TWE-IN1123-SGB	1417	TW 575	TWE591A-BU	1467	FE 43	FE750-PJ
1268	TW 425	TWE-B23447	1318	TW 475	TWE-IN0992-SGA	1368	TW 525	TWE-EX1123-SGB	1418	TW 576	TWE591B-BU	1468	FE 44	FE760-PH
1269	TW 426	TWE-B23449	1319	TW 476	TWE-EX0992-SGA	1369	TW 526	TWE-IN1371-SGB	1419	TW 581	TWE061A-LSA	1469	FE 45	FE770-PH
1270	TW 427	TWE-B23451	1320	TW 477	TWE-IN0993-SGA	1370	TW 527	TWE-EX1371-SGB	1420	TW 582	TWE061B-LSA	1470	FE 46	FE780-PH
1271	TW 428	TWE-B23453	1321	TW 478	TWE-EX0993-SGA	1371	TW 528	TWE-IN1372-SGB	1421	TW 583	TWE201A-LSB	1471	FE 47	FE790-PJ
1272	TW 429	TWE-B23455	1322	TW 479	TWE-IN1121-SGA	1372	TW 529	TWE-EX1372-SGB	1422	TW 584	TWE201B-LSB	1472	FE 48	FE820-PL
1273	TW 430	TWE-B23456	1323	TW 480	TWE-EX1121-SGA	1373	TW 530	TWE-IN1373-SGB	1423	TW 585	TWE311A-PR	1473	FE 49	FE830-PL
1274	TW 431	TWE-B23458	1324	TW 481	TWE-IN1122-SGA	1374	TW 531	TWE-EX1373-SGB	1424	TW 586	TWE311B-PR	1474	FE 50	FE840-PL
1275	TW 432	TWE-B23459	1325	TW 482	TWE-EX1122-SGA	1375	TW 532	TWE-IN1632-SGB	1425	FE 1	FE010-HLA	1475	FE 51	FE900-EX
1276	TW 433	TWE-B20112	1326	TW 483	TWE-IN1123-SGA	1376	TW 533	TWE-EX1632-SGB	1426	FE 2	FE020A-LSA	1476	FE 52	FE011-HLA
1277	TW 434	TWE-B20114	1327	TW 484	TWE-EX1123-SGA	1377	TW 534	TWE-IN1633-SGB	1427	FE 3	FE020B-LSA	1477	FE 53	FE151-HLB
1278	TW 435	TWE-B20115	1328	TW 485	TWE-IN1371-SGA	1378	TW 535	TWE-EX1633-SGB	1428	FE 4	FE150-HLB	1478	FE 54	FE320-PV
1279	TW 436	TWE-B20116	1329	TW 486	TWE-EX1371-SGA	1379	TW 536	TWE-IN1701-SGB	1429	FE 5	FE160A-LSB	1479	FE 55	FE781-PH
1280	TW 437	TWE-B20117	1330	TW 487	TWE-IN1372-SGA	1380	TW 537	TWE-IN1782-SGB	1430	FE 6	FE160B-LSB	1480	FE 56	FE782-PH
1281	TW 438	TWE-B20118	1331	TW 488	TWE-EX1372-SGA	1381	TW 538	TWE-IN1863-SGB	1431	FE 7	FE270-PR	1481	FE 57	FE783-PH
1282	TW 439	TWE-B24341	1332	TW 489	TWE-IN1373-SGA	1382	TW 539	TWE-211A-PR	1432	FE 8	FE280A-PR	1482	FE 58	FE784-PH
1283	TW 440	TWE-B24342	1333	TW 490	TWE-EX1373-SGA	1383	TW 540	TWE-211B-PR	1433	FE 9	FE280B-PR	1483	FE 59	FE785-PH
1284	TW 441	TWE-B24344	1334	TW 491	TWE-IN1632-SGA	1384	TW 541	TWE-194A-PR	1434	FE 10	FE290-PR	1484	FE 60	FE831-PL
1285	TW 442	TWE-B24345	1335	TW 492	TWE-EX1632-SGA	1385	TW 542	TWE-194B-PR	1435	FE 11	FE300-PR	1485	FE 61	FE841-PL
1286	TW 443	TWE-B24347	1336	TW 493	TWE-IN1633-SGA	1386	TW 543	TWE-177A-PR	1436	FE 12	FE310-PV	1486	FE 62	FE010B-HLA
1287	TW 444	TWE-B24349	1337	TW 494	TWE-EX1633-SGA	1387	TW 544	TWE-177B-PR	1437	FE 13	FE430-SGA	1487	FE 63	FE150B-HLB
1288	TW 445	TWE-B24441	1338	TW 495	TWE-IN1701-SGA	1388	TW 545	TWE270A-PR	1438	FE 14	FE431-SGA	1488	FE 64	FE280C-PR
1289	TW 446	TWE-B24443	1339	TW 496	TWE-IN1782-SGA	1389	TW 546	TWE011A-HLA	1439	FE 15	FE432-SGA	1489	FE 65	FE440B-SGA
1290	TW 447	TWE-B24445	1340	TW 497	TWE-IN1863-SGA	1390	TW 547	TWE011B-HLA	1440	FE 16	FE433-SGA	1490	FE 66	FE451-SGA
1291	TW 448	TWE-B24446	1341	TW 498	TWE-IN0641-SGB	1391	TW 548	TWE011C-HLA	1441	FE 17	FE434-SGA	1491	FE 67	FE480B-SGB
1292	TW 449	TWE-B24448	1342	TW 499	TWE-IN0642-SGB	1392	TW 549	TWE021-HLA	1442	FE 18	FE440-SGA	1492	FE 68	FE491-SGB
1293	TW 450	TWE-B24449	1343	TW 500	TWE-IN0643-SGB	1393	TW 550	TWE051A-LSA	1443	FE 19	FE450-SGA	1493	PE 1	PE561-BU
1294	TW 451	TWE-B24712	1344	TW 501	TWE-EX0641-SGB	1394	TW 551	TWE051B-LSA	1444	FE 20	FE460-SGA	1494	PE 2	PE581-BU
1295	TW 452	TWE-B24714	1345	TW 502	TWE-EX0642-SGB	1395	TW 552	TWE051C-LSA	1445	FE 21	FE470-SGB	1495	PE 3	PE010-SGA
1296	TW 453	TWE-B24715	1346	TW 503	TWE-EX0643-SGB	1396	TW 553	TWE051D-LSA	1446	FE 22	FE471-SGB	1496	PE 4	PE020-LSA
1297	TW 454	TWE-B24716	1347	TW 504	TWE-086B-SGB	1397	TW 554	TWE071A-CLA	1447	FE 23	FE472-SGB	1497	PE 5	PE030-CLA
1298	TW 455	TWE-B24717	1348	TW 505	TWE-137B-SGB	1398	TW 555	TWE071B-CLA	1448	FE 24	FE473-SGB	1498	PE 6	PE150-SGB
1299	TW 456	TWE-B24718	1349	TW 506	TWE-178B-SGB	1399	TW 556	TWE071C-CLA	1449	FE 25	FE474-SGB	1499	PE 7	PE160-LSB
1300	TW 457	TWE-IN0641-SGA	1350	TW 507	TWE-223B-SGB	1400	TW 557	TWE151A-HLB	1450	FE 26	FE480-SGB	1500	PE 8	PE170-CLB

Table 2.2 LSTF instruments list (Cont'd)

SEQ. NO.	FUNC ID.		TAG NAME	SEQ. NO.	FUNC ID.		TAG NAME	SEQ. NO.	FUNC ID.		TAG NAME	SEQ. NO.	FUNC ID.		TAG NAME	SEQ. NO.	FUNC ID.		TAG NAME
1501	PE	9	PE290-PV	1551	MI	15	AE010-PCA	1601	MI	98	VE030A-CLA	1651	DP	24	DPE140-HLA	1701	DP	74	DPE075-LSA
1502	PE	10	PE280A-PV	1552	MI	16	AE150-PCB	1602	MI	99	VE030B-CLA	1652	DP	25	DPE150-HLB	1702	DP	75	DPE076-LSA
1503	PE	11	PE280B-PV	1553	MI	17	WE270A-T	1603	MI	100	VE030-CLA	1653	DP	26	DPE160-HLB	1703	DP	76	DPE212-LSB
1504	PE	12	PE270-PV	1554	MI	18	WE270B-M	1604	MI	101	VE010A-HLA	1654	DP	27	DPE170-HLB	1704	DP	77	DPE213-LSB
1505	PE	13	PE300A-PR	1555	MI	19	WE270C-H1	1605	MI	102	VE010B-HLA	1655	DP	28	DPE180-HLB	1705	DP	78	DPE214-LSB
1506	PE	14	PE300B-PR	1556	MI	20	WE270D-H2	1606	MI	103	VE020A-LSA	1656	DP	29	DPE190A-SGB	1706	DP	79	DPE215-LSB
1507	PE	15	PE310-PR	1557	MI	21	WE270E-L1	1607	MI	104	VE020B-LSA	1657	DP	30	DPE190B-SGB	1707	DP	80	DPE216-LSB
1508	PE	16	PE320-PR	1558	MI	22	WE270F-L2	1608	MI	105	VE020-LSA	1658	DP	31	DPE190C-SGB	1708	DP	81	DPE430-SGA
1509	PE	17	PE330-PR	1559	MI	23	WE270G-L3	1609	LE	1	LE270-PV	1659	DP	32	DPE190D-SGB	1709	DP	82	DPE431-SGA
1510	PE	18	PE340-PR	1560	MI	24	WE280A-PR	1610	LE	2	LE280-PR	1660	DP	33	DPE190E-SGB	1710	DP	83	DPE432-SGA
1511	PE	19	PE430-SGA	1561	MI	25	WE280B-PR	1611	LE	3	LE430-SGA	1661	DP	34	DPE190F-SGB	1711	DP	84	DPE433-SGA
1512	PE	20	PE440-SGA	1562	MI	26	WE010-PCA	1612	LE	4	LE440-SGA	1662	DP	35	DPE200A-SGB	1712	DP	85	DPE434-SGA
1513	PE	21	PE450-SGB	1563	MI	27	WE150-PCB	1613	LE	5	LE441-SGA	1663	DP	36	DPE200B-SGB	1713	DP	86	DPE435-SGA
1514	PE	22	PE460-SGB	1564	MI	29	WE020-HLA	1614	LE	6	LE450-SGB	1664	DP	37	DPE200C-SGB	1714	DP	87	DPE436-SGA
1515	PE	23	PE470-SH	1565	MI	30	WE030-LSA	1615	LE	7	LE460-SGB	1665	DP	38	DPE200D-SGB	1715	DP	88	DPE437-SGA
1516	PE	24	PE480-JC	1566	MI	31	WE040-CLA	1616	LE	8	LE461-SGB	1666	DP	39	DPE200E-SGB	1716	DP	89	DPE438-SGA
1517	PE	25	PE610-ST	1567	MI	32	WE160-HLB	1617	LE	9	LE470-JC	1667	DP	40	DPE200F-SGB	1717	DP	90	DPE439-SGA
1518	PE	26	PE560-BU	1568	MI	33	WE170-LSB	1618	LE	10	LE560-ST	1668	DP	41	DPE210-LSB	1718	DP	91	DPE440-SGA
1519	PE	27	PE570-BU	1569	MI	34	WE180-CLB	1619	LE	11	LE570-ST	1669	DP	42	DPE220-LSB	1719	DP	92	DPE450-SGB
1520	PE	28	PE580-BU	1570	MI	35	WE271A-PV	1620	LE	12	LE580-ST	1670	DP	43	DPE230-PCB	1720	DP	93	DPE451-SGB
1521	PE	29	PE590-BU	1571	MI	36	WE271B-PV	1621	LE	13	LE590-ST	1671	DP	44	DPE240-CLB	1721	DP	94	DPE452-SGB
1522	PE	30	PE600-ST	1572	MI	37	WE271C-PV	1622	LE	14	LE650-ACC	1672	DP	45	DPE250-CLB	1722	DP	95	DPE453-SGB
1523	PE	31	PE650-ACC	1573	MI	38	WE271D-PV	1623	LE	15	LE660-ACH	1673	DP	46	DPE260-CLB	1723	DP	96	DPE454-SGB
1524	PE	32	PE660-ACH	1574	MI	39	WE430A-SGA	1624	LE	16	LE820-PL	1674	DP	47	DPE270-PV	1724	DP	97	DPE455-SGB
1525	PE	34	PE900-EX	1575	MI	40	WE430B-SGA	1625	LE	17	LE830-RWST	1675	DP	48	DPE280-PV	1725	DP	98	DPE456-SGB
1526	PE	35	PE011-HLA	1576	MI	41	WE430C-SGA	1626	LE	18	LE442-SGA	1676	DP	49	DPE290-PV	1726	DP	99	DPE457-SGB
1527	PE	36	PE071-CLA	1577	MI	42	WE430D-SGA	1627	LE	19	LE462-SGB	1677	DP	50	DPE300-PV	1727	DP	100	DPE458-SGB
1528	PE	37	PE151-HLB	1578	MI	43	WE440A-SGA	1628	DP	1	DPE010-HLA	1678	DP	51	DPE320-PV	1728	DP	101	DPE459-SGB
1529	PE	38	PE211-CLB	1579	MI	44	WE440B-SGA	1629	DP	2	DPE020-HLA	1679	DP	52	DPE330-PV	1729	DP	102	DPE460-SGB
1530	PE	39	PE291-PR	1580	MI	45	WE440C-SGA	1630	DP	3	DPE030A-HLA	1680	DP	53	DPE310-PV	1730	DP	103	DPE011-HLA
1531	PE	40	PE301-PR	1581	MI	46	WE440D-SGA	1631	DP	4	DPE040-HLA	1681	DP	54	DPE350A-PV	1731	DP	104	DPE071-CLA
1532	PE	41	PE311-PR	1582	MI	47	WE290-PR	1632	DP	5	DPE050A-SGA	1682	DP	55	DPE350B-PV	1732	DP	105	DPE151-HLB
1533	PE	43	PE571-BU	1583	MI	48	WE300-PR	1633	DP	6	DPE050B-SGA	1683	DP	56	DPE360-PV	1733	DP	106	DPE211-CLB
1534	PE	44	PE591-BU	1584	MI	49	WE450A-SGB	1634	DP	7	DPE050C-SGA	1684	DP	57	DPE370-PV	1734	DP	107	DPE571-BU
1535	PE	45	PE451-SGA	1585	MI	50	WE450B-SGB	1635	DP	8	DPE050D-SGA	1685	DP	58	DPE380-PV	1735	DP	108	DPE591-BU
1536	PE	46	PE820-RHR	1586	MI	51	WE450C-SGB	1636	DP	9	DPE050E-SGA	1686	DP	59	DPE390-PV	1736	DP	109	DPE041-PR
1537	MI	1	RE010-PCA	1587	MI	52	WE450D-SGB	1637	DP	10	DPE050F-SGA	1687	DP	60	DPE400-PV	1737	DP	110	DPE042-PR
1538	MI	2	RE150-PCB	1588	MI	53	WE460A-SGB	1638	DP	11	DPE060A-SGA	1688	DP	61	DPE410-PV	1738	DP	111	DPE043-PR
1539	MI	3	OPE270-PR	1589	MI	54	WE460B-SGB	1639	DP	12	DPE060B-SGA	1689	DP	62	DPE332-PV	1739	DP	112	DPE044-PR
1540	MI	4	OPE300A-PR	1590	MI	55	WE460C-SGB	1640	DP	13	DPE060C-SGA	1690	DP	63	DPE331-PV	1740	DP	113	DPE045-PR
1541	MI	5	OPE430-SGA	1591	MI	56	WE460D-SGB	1641	DP	14	DPE060D-SGA	1691	DP	64	DPE560A-BU	1741	DP	114	DPE046-PR
1542	MI	6	OPE470-SGB	1592	MI	57	WE650A-ACC	1642	DP	15	DPE060E-SGA	1692	DP	65	DPE560B-BU	1742	DP	115	DPE101-PR
1543	MI	7	OPE440-SGA	1593	MI	58	WE650B-ACC	1643	DP	16	DPE060F-SGA	1693	DP	66	DPE570-BU	1743	MF	1	MFE011A-HLA
1544	MI	8	OPE510-SH	1594	MI	59	WE660A-ACH	1644	DP	17	DPE070-LSA	1694	DP	67	DPE580A-BU	1744	MF	2	MFE011B-HLA
1545	MI	9	OPE820-PL	1595	MI	60	WE660B-ACH	1645	DP	18	DPE080-LSA	1695	DP	68	DPE580B-BU	1745	MF	3	MFE011C-HLA
1546	MI	10	OPE840-PL	1596	MI	86	VE010-HLA	1646	DP	19	DPE090-PCA	1696	DP	69	DPE590-BU	1746	MF	4	MFE051A-LSA
1547	MI	11	VBE010-PCA	1597	MI	92	VE-N-006-DC	1647	DP	20	DPE100-CLA	1697	DP	70	DPE030B-HLA	1747	MF	5	MFE051B-LSA
1548	MI	12	VBE150-PCB	1598	MI	93	VE-S-006-DC	1648	DP	21	DPE110-CLA	1698	DP	71	DPE072-LSA	1748	MF	6	MFE051C-LSA
1549	MI	13	TQE010-PCA	1599	MI	94	VE-E-006-DC	1649	DP	22	DPE120-CLA	1699	DP	72	DPE073-LSA	1749	MF	7	MFE071A-CLA
1550	MI	14	TQE150-PCB	1600	MI	95	VE-W-006-DC	1650	DP	23	DPE130-CLA	1700	DP	73	DPE074-LSA	1750	MF	8	MFE071B-CLA

Table 2.2 LSTF instruments list (Cont'd)

SEQ. NO.	FUNC ID.	TAG NAME	SEQ. NO.	FUNC ID.	TAG NAME	SEQ. NO.	FUNC ID.	TAG NAME	SEQ. NO.	FUNC ID.	TAG NAME	SEQ. NO.	FUNC ID.	TAG NAME
1751	MF 9	MFE071C-CLA	1801	MF 59	MFT191A-LSB	1851	CP 12	CPE-E055C-DC	1901	CP 62	CPE-C-012-LP	1951	CP 112	CPE-B22629
1752	MF 10	MFE151A-HLB	1802	MF 60	MFT191B-LSB	1852	CP 13	CPE-E061C-DC	1902	CP 63	CPE-C-009-LP	1952	CP 113	CPE-211-PR
1753	MF 11	MFE151B-HLB	1803	MF 61	MFT191C-LSB	1853	CP 14	CPE-E067C-DC	1903	CP 64	CPE-C-006-LP	1953	CP 114	CPE-207-PR
1754	MF 12	MFE151C-HLB	1804	MF 62	MFT191D-LSB	1854	CP 15	CPE-E066F-UH	1904	CP 65	CPE-C-005-LP	1954	CP 115	CPE-204-PR
1755	MF 13	MFE191A-LSB	1805	DE 1	DE011A-HLA	1855	CP 16	CPE-W066F-UH	1905	CP 66	CPE-C-003-LP	1955	CP 116	CPE-200-PR
1756	MF 14	MFE191B-LSB	1806	DE 2	DE011B-HLA	1856	CP 17	CPE-E069F-UH	1906	CP 67	CPE-C-002-LP	1956	CP 117	CPE-196-PR
1757	MF 15	MFE191C-LSB	1807	DE 3	DE011C-HLA	1857	CP 18	CPE-W069F-UH	1907	CP 68	CPE-B08001	1957	CP 118	CPE-192-PR
1758	MF 16	MFE211A-CLB	1808	DE 4	DE051A-LSA	1858	CP 19	CPE-E072F-UH	1908	CP 69	CPE-B08002	1958	CP 119	CPE-189-PR
1759	MF 17	MFE211B-CLB	1809	DE 5	DE051B-LSA	1859	CP 20	CPE-W072F-UH	1909	CP 70	CPE-B08003	1959	CP 120	CPE-185-PR
1760	MF 18	MFE211C-CLB	1810	DE 6	DE051C-LSA	1860	CP 21	CPE-E075F-UH	1910	CP 71	CPE-B08004	1960	CP 121	CPE-181-PR
1761	MF 19	MFE291A-PR	1811	DE 7	DE071A-CLA	1861	CP 22	CPE-W075F-UH	1911	CP 72	CPE-B08005	1961	CP 122	CPE-177-PR
1762	MF 20	MFE291B-PR	1812	DE 8	DE071B-CLA	1862	CP 23	CPE-E078F-UH	1912	CP 73	CPE-B08006	1962	CP 123	CPE-086C-SGA
1763	MF 21	MFE021-HLA	1813	DE 9	DE071C-CLA	1863	CP 24	CPE-W078F-UH	1913	CP 74	CPE-B08007	1963	CP 124	CPE-099C-SGA
1764	MF 22	MFE051D-LSA	1814	DE 10	DE151A-HLB	1864	CP 25	CPE-E081F-UH	1914	CP 75	CPE-B08008	1964	CP 125	CPE-112C-SGA
1765	MF 23	MFE161-HLB	1815	DE 11	DE151B-HLB	1865	CP 26	CPE-W081F-UH	1915	CP 76	CPE-B08009	1965	CP 126	CPE-125C-SGA
1766	MF 24	MFE191D-LSB	1816	DE 12	DE151C-HLB	1866	CP 27	CPE-E066H-GT	1916	CP 77	CPE-B15661	1966	CP 127	CPE-137C-SGA
1767	MF 25	MFE-N-006-DC	1817	DE 13	DE191A-LSB	1867	CP 28	CPE-W066H-GT	1917	CP 78	CPE-B15662	1967	CP 128	CPE-150C-SGA
1768	MF 26	MFE-S-006-DC	1818	DE 14	DE191B-LSB	1868	CP 29	CPE-E072H-GT	1918	CP 79	CPE-B15663	1968	CP 129	CPE-163C-SGA
1769	MF 27	MFE-E-006-DC	1819	DE 15	DE191C-LSB	1869	CP 30	CPE-W072H-GT	1919	CP 80	CPE-B15664	1969	CP 130	CPE-178C-SGA
1770	MF 28	MFE-W-006-DC	1820	DE 16	DE211A-CLB	1870	CP 31	CPE-E078H-GT	1920	CP 81	CPE-B15665	1970	CP 131	CPE-192F-SGA
1771	MF 29	MFE301B-PR	1821	DE 17	DE211B-CLB	1871	CP 32	CPE-W078H-GT	1921	CP 82	CPE-B15666	1971	CP 132	CPE-208F-SGA
1772	MF 30	MFT161-HLB	1822	DE 18	DE211C-CLB	1872	CP 33	CPE-E043H-GT	1922	CP 83	CPE-B15667	1972	CP 133	CPE-192C-SGA
1773	MF 31	MFE571A-BU	1823	DE 19	DE052-LSA	1873	CP 34	CPE-W043H-GT	1923	CP 84	CPE-B15668	1973	CP 134	CPE-208C-SGA
1774	MF 32	MFE571B-BU	1824	DE 20	DE192-LSB	1874	CP 35	CPE-E044H-GT	1924	CP 85	CPE-B15669	1974	CP 135	CPE-223C-SGA
1775	MF 33	MFE591A-BU	1825	DE 21	DE281-PR	1875	CP 36	CPE-W044H-GT	1925	CP 86	CPE-B04001	1975	CP 136	CPE-245C-SGA
1776	MF 34	MFE591B-BU	1826	DE 22	DE291-PR	1876	CP 37	CPE-E048H-GT	1926	CP 87	CPE-B04002	1976	CP 137	CPE-IN0861-SGA
1777	MF 35	MFE061A-LSA	1827	DE 23	DE301-PR	1877	CP 38	CPE-W048H-GT	1927	CP 88	CPE-B04003	1977	CP 138	CPE-EX0861-SGA
1778	MF 36	MFE061B-LSA	1828	DE 24	DE311-PR	1878	CP 39	CPE-E054H-GT	1928	CP 89	CPE-B04004	1978	CP 139	CPE-IN0862-SGA
1779	MF 37	MFE201A-LSB	1829	DE 25	DE431-SGA	1879	CP 40	CPE-W054H-GT	1929	CP 90	CPE-B04005	1979	CP 140	CPE-EX0862-SGA
1780	MF 38	MFE201B-LSB	1830	DE 26	DE471-SGB	1880	CP 41	CPE-E060H-GT	1930	CP 91	CPE-B04006	1980	CP 141	CPE-IN0863-SGA
1781	MF 39	MFE301A-PR	1831	DE 27	DE451A-SGA	1881	CP 42	CPE-W060H-GT	1931	CP 92	CPE-B04007	1981	CP 142	CPE-EX0863-SGA
1782	MF 40	MFT211A-CLB	1832	DE 28	DE451B-SGA	1882	CP 43	CPE-E042-UP	1932	CP 93	CPE-B04008	1982	CP 143	CPE-IN0864-SGA
1783	MF 41	MFT211B-CLB	1833	DE 29	DE451C-SGA	1883	CP 44	CPE-W042-UP	1933	CP 94	CPE-B04009	1983	CP 144	CPE-EX0864-SGA
1784	MF 42	MFT211C-CLB	1834	DE 30	DE571A-BU	1884	CP 45	CPE-E043-UP	1934	CP 95	CPE-B20621	1984	CP 145	CPE-IN0865-SGA
1785	MF 43	MFE311A-PR	1835	DE 31	DE571B-BU	1885	CP 46	CPE-W043-UP	1935	CP 96	CPE-B20622	1985	CP 146	CPE-EX0865-SGA
1786	MF 44	MFE311B-PR	1836	DE 32	DE571C-BU	1886	CP 47	CPE-E044-UP	1936	CP 97	CPE-B20623	1986	CP 147	CPE-IN0866-SGA
1787	MF 45	MFT011A-HLA	1837	DE 33	DE591A-BU	1887	CP 48	CPE-W044-UP	1937	CP 98	CPE-B20624	1987	CP 148	CPE-EX0866-SGA
1788	MF 46	MFT011B-HLA	1838	DE 34	DE591B-BU	1888	CP 49	CPE-E048-UP	1938	CP 99	CPE-B20625	1988	CP 149	CPE-IN0931-SGA
1789	MF 47	MFT011C-HLA	1839	DE 35	DE591C-BU	1889	CP 50	CPE-W048-UP	1939	CP 100	CPE-B20626	1989	CP 150	CPE-IN0932-SGA
1790	MF 48	MFT021-HLA	1840	CP 1	CPE-E-012C-DC	1890	CP 51	CPE-E051-UP	1940	CP 101	CPE-B20627	1990	CP 151	CPE-IN0933-SGA
1791	MF 49	MFT051A-LSA	1841	CP 2	CPE-E-006C-DC	1891	CP 52	CPE-W051-UP	1941	CP 102	CPE-B20628	1991	CP 152	CPE-IN0934-SGA
1792	MF 50	MFT051B-LSA	1842	CP 3	CPE-E000C-DC	1892	CP 53	CPE-E054-UP	1942	CP 103	CPE-B20629	1992	CP 153	CPE-IN0935-SGA
1793	MF 51	MFT051C-LSA	1843	CP 4	CPE-E006C-DC	1893	CP 54	CPE-W054-UP	1943	CP 104	CPE-B22621	1993	CP 154	CPE-IN0936-SGA
1794	MF 52	MFT051D-LSA	1844	CP 5	CPE-E012C-DC	1894	CP 55	CPE-E057-UP	1944	CP 105	CPE-B22622	1994	CP 155	CPE-IN0991-SGA
1795	MF 53	MFT071A-CLA	1845	CP 6	CPE-E018C-DC	1895	CP 56	CPE-W057-UP	1945	CP 106	CPE-B22623	1995	CP 156	CPE-EX0991-SGA
1796	MF 54	MFT071B-CLA	1846	CP 7	CPE-E024C-DC	1896	CP 57	CPE-E060-UP	1946	CP 107	CPE-B22624	1996	CP 157	CPE-IN0992-SGA
1797	MF 55	MFT071C-CLA	1847	CP 8	CPE-E031C-DC	1897	CP 58	CPE-W060-UP	1947	CP 108	CPE-B22625	1997	CP 158	CPE-EX0992-SGA
1798	MF 56	MFT151A-HLB	1848	CP 9	CPE-E037C-DC	1898	CP 59	CPE-C-021-LP	1948	CP 109	CPE-B22626	1998	CP 159	CPE-IN0993-SGA
1799	MF 57	MFT151B-HLB	1849	CP 10	CPE-E043C-DC	1899	CP 60	CPE-C-018-LP	1949	CP 110	CPE-B22627	1999	CP 160	CPE-EX0993-SGA
1800	MF 58	MFT151C-HLB	1850	CP 11	CPE-E049C-DC	1900	CP 61	CPE-C-015-LP	1950	CP 111	CPE-B22628	2000	CP 161	CPE-IN0994-SGA

Table 2.2 LSTF instruments list (Cont'd)

SEQ. NO.	FUNC ID.	TAG NAME	SEQ. NO.	FUNC ID.	TAG NAME	SEQ. NO.	FUNC ID.	TAG NAME	SEQ. NO.	FUNC ID.	TAG NAME	SEQ. NO.	FUNC ID.	TAG NAME
2001	CP 162	CPE-EX0994-SGA	2051	CP 212	CPE-EX1502-SGA	2101	CP 262	CPE-IN0932-SGB	2151	CP 312	CPE-EX1372-SGB	2201	CP 363	CPE-150B-HLB
2002	CP 163	CPE-IN0995-SGA	2052	CP 213	CPE-IN1503-SGA	2102	CP 263	CPE-IN0933-SGB	2152	CP 313	CPE-IN1373-SGB	2202	CP 364	CPE-150C-HLB
2003	CP 164	CPE-EX0995-SGA	2053	CP 214	CPE-EX1503-SGA	2103	CP 264	CPE-IN0934-SGB	2153	CP 314	CPE-EX1373-SGB	2203	CP 365	CPE-150D-HLB
2004	CP 165	CPE-IN0996-SGA	2054	CP 215	CPE-IN1504-SGA	2104	CP 265	CPE-IN0935-SGB	2154	CP 315	CPE-IN1374-SGB	2204	CP 366	CPE-150E-HLB
2005	CP 166	CPE-EX0996-SGA	2055	CP 216	CPE-EX1504-SGA	2105	CP 266	CPE-IN0936-SGB	2155	CP 316	CPE-EX1374-SGB	2205	CP 367	CPE-180A-HLB
2006	CP 167	CPE-IN1051-SGA	2056	CP 217	CPE-IN1505-SGA	2106	CP 267	CPE-IN0991-SGB	2156	CP 317	CPE-IN1375-SGB	2206	CP 368	CPE-180B-HLB
2007	CP 168	CPE-IN1052-SGA	2057	CP 218	CPE-EX1505-SGA	2107	CP 268	CPE-EX0991-SGB	2157	CP 318	CPE-EX1375-SGB	2207	CP 369	CPE-180C-HLB
2008	CP 169	CPE-IN1053-SGA	2058	CP 219	CPE-IN1506-SGA	2108	CP 269	CPE-IN0992-SGB	2158	CP 319	CPE-IN1376-SGB	2208	CP 370	CPE-180D-HLB
2009	CP 170	CPE-IN1054-SGA	2059	CP 220	CPE-EX1506-SGA	2109	CP 270	CPE-EX0992-SGB	2159	CP 320	CPE-EX1376-SGB	2209	CP 371	CPE-180E-HLB
2010	CP 171	CPE-IN1055-SGA	2060	CP 221	CPE-IN1632-SGA	2110	CP 271	CPE-IN0993-SGB	2160	CP 321	CPE-IN1501-SGB	2210	CP 372	CPE-230A-CLB
2011	CP 172	CPE-IN1056-SGA	2061	CP 222	CPE-EX1632-SGA	2111	CP 272	CPE-EX0993-SGB	2161	CP 322	CPE-EX1501-SGB	2211	CP 373	CPE-230B-CLB
2012	CP 173	CPE-IN1121-SGA	2062	CP 223	CPE-IN1633-SGA	2112	CP 273	CPE-IN0994-SGB	2162	CP 323	CPE-IN1502-SGB	2212	CP 374	CPE-230C-CLB
2013	CP 174	CPE-EX1121-SGA	2063	CP 224	CPE-EX1633-SGA	2113	CP 274	CPE-EX0994-SGB	2163	CP 324	CPE-EX1502-SGB	2213	CP 375	CPE-230D-CLB
2014	CP 175	CPE-IN1122-SGA	2064	CP 225	CPE-IN1634-SGA	2114	CP 275	CPE-IN0995-SGB	2164	CP 325	CPE-IN1503-SGB	2214	CP 376	CPE-230E-CLB
2015	CP 176	CPE-EX1122-SGA	2065	CP 226	CPE-EX1634-SGA	2115	CP 276	CPE-EX0995-SGB	2165	CP 326	CPE-EX1503-SGB	2215	CP 377	CPE-560-ST
2016	CP 177	CPE-IN1123-SGA	2066	CP 227	CPE-IN1635-SGA	2116	CP 277	CPE-IN0996-SGB	2166	CP 327	CPE-IN1504-SGB	2216	CP 378	CPE051A-LSA
2017	CP 178	CPE-EX1123-SGA	2067	CP 228	CPE-EX1635-SGA	2117	CP 278	CPE-EX0996-SGB	2167	CP 328	CPE-EX1504-SGB	2217	CP 379	CPE051B-LSA
2018	CP 179	CPE-IN1124-SGA	2068	CP 229	CPE-IN1701-SGA	2118	CP 279	CPE-IN1051-SGB	2168	CP 329	CPE-IN1505-SGB	2218	CP 380	CPE051C-LSA
2019	CP 180	CPE-EX1124-SGA	2069	CP 230	CPE-IN1706-SGA	2119	CP 280	CPE-IN1052-SGB	2169	CP 330	CPE-EX1505-SGB	2219	CP 381	CPE051D-LSA
2020	CP 181	CPE-IN1125-SGA	2070	CP 231	CPE-IN1782-SGA	2120	CP 281	CPE-IN1053-SGB	2170	CP 331	CPE-IN1506-SGB	2220	CP 382	CPE051E-LSA
2021	CP 182	CPE-EX1125-SGA	2071	CP 232	CPE-IN1785-SGA	2121	CP 282	CPE-IN1054-SGB	2171	CP 332	CPE-EX1506-SGB	2221	CP 383	CPE051F-LSA
2022	CP 183	CPE-IN1126-SGA	2072	CP 233	CPE-IN1863-SGA	2122	CP 283	CPE-IN1055-SGB	2172	CP 333	CPE-IN1632-SGB	2222	CP 384	CPE051G-LSA
2023	CP 184	CPE-EX1126-SGA	2073	CP 234	CPE-IN1864-SGA	2123	CP 284	CPE-IN1056-SGB	2173	CP 334	CPE-EX1632-SGB	2223	CP 385	CPE051H-LSA
2024	CP 185	CPE-IN1251-SGA	2074	CP 235	CPE-086C-SGB	2124	CP 285	CPE-IN1121-SGB	2174	CP 335	CPE-IN1633-SGB	2224	CP 386	CPE051I-LSA
2025	CP 186	CPE-EX1251-SGA	2075	CP 236	CPE-099C-SGB	2125	CP 286	CPE-EX1121-SGB	2175	CP 336	CPE-EX1633-SGB	2225	CP 387	CPE051J-LSA
2026	CP 187	CPE-IN1252-SGA	2076	CP 237	CPE-112C-SGB	2126	CP 287	CPE-IN1122-SGB	2176	CP 337	CPE-IN1634-SGB	2226	CP 388	CPE191A-LSB
2027	CP 188	CPE-EX1252-SGA	2077	CP 238	CPE-125C-SGB	2127	CP 288	CPE-EX1122-SGB	2177	CP 338	CPE-EX1634-SGB	2227	CP 389	CPE191B-LSB
2028	CP 189	CPE-IN1253-SGA	2078	CP 239	CPE-137C-SGB	2128	CP 289	CPE-IN1123-SGB	2178	CP 339	CPE-IN1635-SGB	2228	CP 390	CPE191C-LSB
2029	CP 190	CPE-EX1253-SGA	2079	CP 240	CPE-150C-SGB	2129	CP 290	CPE-EX1123-SGB	2179	CP 340	CPE-EX1635-SGB	2229	CP 391	CPE191D-LSB
2030	CP 191	CPE-IN1254-SGA	2080	CP 241	CPE-163C-SGB	2130	CP 291	CPE-IN1124-SGB	2180	CP 341	CPE-IN1701-SGB	2230	CP 392	CPE191E-LSB
2031	CP 192	CPE-EX1254-SGA	2081	CP 242	CPE-178C-SGB	2131	CP 292	CPE-EX1124-SGB	2181	CP 342	CPE-IN1706-SGB	2231	CP 393	CPE191F-LSB
2032	CP 193	CPE-IN1255-SGA	2082	CP 243	CPE-192F-SGB	2132	CP 293	CPE-IN1125-SGB	2182	CP 343	CPE-IN1782-SGB	2232	CP 394	CPE191G-LSB
2033	CP 194	CPE-EX1255-SGA	2083	CP 244	CPE-208F-SGB	2133	CP 294	CPE-EX1125-SGB	2183	CP 344	CPE-IN1785-SGB	2233	CP 395	CPE191H-LSB
2034	CP 195	CPE-IN1256-SGA	2084	CP 245	CPE-192C-SGB	2134	CP 295	CPE-IN1126-SGB	2184	CP 345	CPE-IN1863-SGB	2234	CP 396	CPE191I-LSB
2035	CP 196	CPE-EX1256-SGA	2085	CP 246	CPE-208C-SGB	2135	CP 296	CPE-EX1126-SGB	2185	CP 346	CPE-IN1864-SGB	2235	CP 397	CPE191J-LSB
2036	CP 197	CPE-IN1371-SGA	2086	CP 247	CPE-223C-SGB	2136	CP 297	CPE-IN1251-SGB	2186	CP 347	CPE-010A-HLA	2236	CP 408	CE270-PV
2037	CP 198	CPE-EX1371-SGA	2087	CP 248	CPE-245C-SGB	2137	CP 298	CPE-EX1251-SGB	2187	CP 348	CPE-010B-HLA	2237	CP 409	CP-VALVE-Y
2038	CP 199	CPE-IN1372-SGA	2088	CP 249	CPE-IN0861-SGB	2138	CP 299	CPE-IN1252-SGB	2188	CP 349	CPE-010C-HLA	2238	CP 410	CP-VALVE-S
2039	CP 200	CPE-EX1372-SGA	2089	CP 250	CPE-EX0861-SGB	2139	CP 300	CPE-EX1252-SGB	2189	CP 350	CPE-010D-HLA	2239	RC 1	MFE011A-HLA-EU
2040	CP 201	CPE-IN1373-SGA	2090	CP 251	CPE-IN0862-SGB	2140	CP 301	CPE-IN1253-SGB	2190	CP 351	CPE-010E-HLA	2240	RC 2	MFE011B-HLA-EU
2041	CP 202	CPE-EX1373-SGA	2091	CP 252	CPE-EX0862-SGB	2141	CP 302	CPE-EX1253-SGB	2191	CP 353	CPE-040B-HLA	2241	RC 3	MFE011C-HLA-EU
2042	CP 203	CPE-IN1374-SGA	2092	CP 253	CPE-IN0863-SGB	2142	CP 303	CPE-IN1254-SGB	2192	CP 354	CPE-040C-HLA	2242	RC 4	MFE051A-LSA-EU
2043	CP 204	CPE-EX1374-SGA	2093	CP 254	CPE-EX0863-SGB	2143	CP 304	CPE-EX1254-SGB	2193	CP 355	CPE-040D-HLA	2243	RC 5	MFE051B-LSA-EU
2044	CP 205	CPE-IN1375-SGA	2094	CP 255	CPE-IN0864-SGB	2144	CP 305	CPE-IN1255-SGB	2194	CP 356	CPE-040E-HLA	2244	RC 6	MFE051C-LSA-EU
2045	CP 206	CPE-EX1375-SGA	2095	CP 256	CPE-EX0864-SGB	2145	CP 306	CPE-EX1255-SGB	2195	CP 357	CPE-090A-CLA	2245	RC 7	MFE071A-CLA-EU
2046	CP 207	CPE-IN1376-SGA	2096	CP 257	CPE-IN0865-SGB	2146	CP 307	CPE-IN1256-SGB	2196	CP 358	CPE-090B-CLA	2246	RC 8	MFE071B-CLA-EU
2047	CP 208	CPE-EX1376-SGA	2097	CP 258	CPE-EX0865-SGB	2147	CP 308	CPE-EX1256-SGB	2197	CP 359	CPE-090C-CLA	2247	RC 9	MFE071C-CLA-EU
2048	CP 209	CPE-IN1501-SGA	2098	CP 259	CPE-IN0866-SGB	2148	CP 309	CPE-IN1371-SGB	2198	CP 360	CPE-090D-CLA	2248	RC 10	MFE151A-HLB-EU
2049	CP 210	CPE-EX1501-SGA	2099	CP 260	CPE-EX0866-SGB	2149	CP 310	CPE-EX1371-SGB	2199	CP 361	CPE-090E-CLA	2249	RC 11	MFE151B-HLB-EU
2050	CP 211	CPE-IN1502-SGA	2100	CP 261	CPE-IN0931-SGB	2150	CP 311	CPE-IN1372-SGB	2200	CP 362	CPE-150A-HLB	2250	RC 12	MFE151C-HLB-EU

Table 2.2 LSTF instruments list (Cont'd)

SEQ. NO.	FUNC ID.		TAG NAME	SEQ. NO.	FUNC ID.		TAG NAME
2251	RC	13	MFE191A-LSB-EU	2301	RC	63	DE192-LSB-EU
2252	RC	14	MFE191B-LSB-EU	2302	RC	64	DE281-PR-EU
2253	RC	15	MFE191C-LSB-EU	2303	RC	65	DE291-PR-EU
2254	RC	16	MFE211A-CLB-EU	2304	RC	66	DE301-PR-EU
2255	RC	17	MFE211B-CLB-EU	2305	RC	67	DE311-PR-EU
2256	RC	18	MFE211C-CLB-EU	2306	RC	68	DE431-SGA-EU
2257	RC	19	MFE021-HLA-EU	2307	RC	69	DE471-SGB-EU
2258	RC	20	MFE051D-LSA-EU	2308	RC	70	DE451A-SGA-EU
2259	RC	21	MFE161-HLB-EU	2309	RC	71	DE451B-SGA-EU
2260	RC	22	MFE191D-LSB-EU	2310	RC	72	DE451C-SGA-EU
2261	RC	23	MFE-E-006-DC-EU	2311	RC	76	MFE061A-LSA-EU
2262	RC	24	MFE-S-006-DC-EU	2312	RC	77	MFE061B-LSA-EU
2263	RC	25	MFE-W-006-DC-EU	2313	RC	78	MFE201A-LSB-EU
2264	RC	26	MFE-N-006-DC-EU	2314	RC	79	MFE201B-LSB-EU
2265	RC	27	VE-E-006-DC-EU	2315	RC	88	VE030A-CLA-EU
2266	RC	28	VE-S-006-DC-EU	2316	RC	89	VE030B-CLA-EU
2267	RC	29	VE-W-006-DC-EU	2317	RC	90	VE030-CLA-EU
2268	RC	30	VE-N-006-DC-EU	2318	RC	91	VE010A-HLA-EU
2269	RC	31	DE011A-HLA-EU	2319	RC	92	VE010B-HLA-EU
2270	RC	32	DE011B-HLA-EU	2320	RC	93	VE010-HLA-EU
2271	RC	33	DE011C-HLA-EU	2321	RC	94	VE020A-LSA-EU
2272	RC	34	DE151A-HLB-EU	2322	RC	95	VE020B-LSA-EU
2273	RC	35	DE151B-HLB-EU	2323	RC	96	VE020-LSA-EU
2274	RC	36	DE151C-HLB-EU	2324	RC	103	FE571A-AVG
2275	RC	37	DE071A-CLA-EU	2325	RC	104	FE571B-AVG
2276	RC	38	DE071B-CLA-EU	2326	RC	105	DE451-AVG
2277	RC	39	DE071C-CLA-EU	2327	RC	106	DE571-AVG
2278	RC	40	DE211A-CLB-EU	2328	RC	107	FRE590-ST
2279	RC	41	DE211B-CLB-EU	2329	RC	108	FRE675-ACH
2280	RC	42	DE211C-CLB-EU	2330	RC	109	FRE655-ACC
2281	RC	43	DE571A-BU-EU	2331	RC	110	FRE-051-LSA
2282	RC	44	DE571B-BU-EU	2332	RC	111	FRE-191-LSB
2283	RC	45	DE571C-BU-EU	2333	RC	112	DAE-051-LSA
2284	RC	46	FRE-011-HLA	2334	RC	113	DAE-191-LSB
2285	RC	47	DAE-011-HLA	2335	RC	114	FRE-061-LSA
2286	RC	48	FRE-151-HLB	2336	RC	115	FRE-201-LSB
2287	RC	49	DAE-151-HLB	2337	RC	116	FRE-571A-BU
2288	RC	50	FRE-071-CLA	2338	RC	117	FRE-571B-BU
2289	RC	51	FRE-211-CLB	2339	RC	120	DAE-051-LSA-TY
2290	RC	52	DAE-071-CLA	2340	RC	121	DAE-191-LSB-TY
2291	RC	53	DAE-211-CLB	2341	RC	122	DAE-571A-BU
2292	RC	54	MFE571A-BU-EU	2342	RC	123	DAE-571B-BU
2293	RC	55	MFE571B-BU-EU				
2294	RC	56	DE051A-LSA-EU				
2295	RC	57	DE051B-LSA-EU				
2296	RC	58	DE051C-LSA-EU				
2297	RC	59	DE191A-LSB-EU				
2298	RC	60	DE191B-LSB-EU				
2299	RC	61	DE191C-LSB-EU				
2300	RC	62	DE052-LSA-EU				

Table 3.1 Initial conditions for RUN SB-PV-01

Items	Unit	Specified	Measured
Pressurizer pressure	MPa	15.52	15.43
Hot leg fluid temperature (A/B)	K	598.1	598.5/598.7
Cold leg fluid temperature (A/B)	K	562.4	563.6/563.6
Total core power	MW	10.0	10.0
Core inlet flow rate	kg/s	48.6	48.6
Pressurizer water level	m	2.7	2.68
Primary coolant pump speed	rpm	800	750/782
SG secondary pressure (A/B)	MPa	7.3	7.34/7.37
SG secondary water level (A/B)	m	10.3	10.7/10.5
SG feedwater temperature (A/B)	K	495	495.1/495.1
SG feedwater flow rate (A/B)	kg/s	2.74	2.50/2.66
SG steam flow rate (A/B)	kg/s	2.74	2.59/2.68

Table 3.2 Operational setpoints and conditions for RUN SB-PV-01

Items	Unit	Specified	Measured
PR heater trip on PR level	m	1.0	1.0
Reactor scram on PR pressure	MPa	12.97	12.97
PC pumps coastdown	-	Reactor scram	Reactor scram
MSIV closure in SG	-	Reactor scram	Reactor scram
Main feedwater stop in SG	-	Reactor scram	Reactor scram
Turbine throttle valve closure	-	Reactor scram	Reactor scram
Auxiliary feedwater initiation	-	not available	not availabel
HPI and charging system	-	manual	manual
Accumulator pressure setpoint	MPa	4.51	4.4
Low pressure injection pressure	MPa	1.29	not used

Table 3.3 ECCS conditions for RUN SB-PV-01

ECCS	Unit	Specification
High pressure charging system		
Pump shut-off head	MPa	18.1
Actuation logic	-	Manual*1
Flow rate	-	Full mode flow
Fluid temperature	K	310
Injection location	-	cold leg A
High pressure injection system		
Pump shut-off head	MPa	10.7
Actuation logic	-	Manual*1
Flow rate	-	Full mode flow
Fluid temperature	K	310
Injection location	-	cold leg B
Accumulator system		
Tank pressure	MPa	4.51
Water temperature	K	320
Injection locations (ACC/ACH)	-	CL-A/CL-B
Low pressure injection system		
Pump shut-off head	MPa	1.29
Delay time from SI signal*2	s	17
Flow rate	-	Full mode flow
Fluid temperature	K	310
Injection locations		CL-A/CL-B

*1 Charging and HPI systems are actuated manually by operator's core dryout detection on account of the higher hot leg fluid temperature than the saturated temperature by more than 10 K.

*2 SI signal is tripped on the PR pressure lower than 12.27 MPa.

Table 3.4 Core power decay curve

Time s	Power MW	Time s	Power MW
0.000	10.000	100.000	5.200
1.000	10.000	150.000	3.632
2.000	10.000	200.000	2.848
3.000	10.000	400.000	1.776
4.000	10.000	600.000	1.568
5.000	10.000	800.000	1.488
6.000	10.000	1000.000	1.424
7.000	10.000	1500.000	1.280
8.000	10.000	2000.000	1.200
10.000	10.000	4000.000	.992
15.000	10.000	6000.000	.848
20.000	10.000	7980.000	.784
29.000	10.000	10020.000	.784
40.000	8.912	19980.000	.592
60.000	7.344	60000.000	.464
80.000	6.128	100020.000	.368

Table 5.1 Chronology of events for RUN SB-PV-01

Time (s)	Events
0	• Break initiation
	• PC-A,B Pumps speed up to 1500 rpm
79	• PR pressure at 12.97 MPa
82	• Reactor Scram on PR trip signal
	• MSIV closure and main feedwater stop
	• PC-A,B pumps coast-down
112	• Core power decrease
312	• Level formation at SGA U-tube top (～514s)
331	• PC-A pump stop (517s for PC-B)
495	• CL-A phase separation (518s for CL-B)
568	• CL-A flow stop (648s for CL-B)
1090	• Loopseal A (SG-side) level decrease
1237	• Loopseal B (SG-side) level decrease
1390	• Hot leg emptized
1420	• Upper plenum level decrease below loop nozzle
1498	• Core dryout initiation at top side
1638	• Core dryout at bottom side
1670	• Core dryout detection by operators
1676	• Actuation of charging and HPI
1700	• Highquality Two-phase break flow
1775	• Core electric power trip (923 K)
2000	• Steam flow discharge at break (～2377s)
2057	• Accumulators (ACC,ACH) injection (～2360s)
2248	• Final quench of heater rods
3086	• Termination of charging and HPI
3095	• Break valve closure

Table 5.2 Collapsed water levels in primary system in SB-PV-01 test

Primary Components	Reference Elevation(m)	Measuring Height(m)	Transient Water Level at Six Time Phases (m)					
			t = 0 s	t = 520 s	t = 1200 s	t = 1500 s	t = 1670 s	t = 2050 s
Pressurizer	EL 17.74	3.75	2.68	0	0	0	0	0
SG-A U-Tubes (Up-Flow)	EL 6.26	10.22*1	10.22	9.6	0	0	0	0
SG-A U-Tubes (Down-Flow)	EL 6.26	10.22*1	10.22	9.0	0	0	0	0
SGB U-Tubes (Up-Flow)	EL 6.26	10.22*1	10.22	9.6	0	0	0	0
SGB U-Tubes (Down-Flow)	EL 6.26	10.22*1	10.22	9.0	0	0	0	0
Hot Leg A*2	EL 5.40	0.21	0.21	0.15	0.15	0.03	0.01	0
Hot Leg B*2	EL 5.40	0.21	0.21	0.15	0.15	0.03	0.01	0
Cold Leg A*2	EL 5.40	0.21	0.21	0.20	0.03	0.03	0	0.05
Cold Leg B*2	EL 5.40	0.21	0.21	0.20	0.03	0.03	0	0.05
Cross-Over Leg A (Down-Flow)	EL 1.79	4.48	4.48	4.48	4.05	2.86	2.72	0.40
Cross-Over Leg A (Up-Flow)	EL 1.79	3.72	3.72	3.72	3.72	3.72	3.72	3.05
Cross-Over Leg B (Down-Flow)	EL 1.79	4.48	4.48	4.48	4.48	2.77	2.59	0.40
Cross-Over Leg B (Up-Flow)	EL 1.79	3.72	3.72	3.72	3.72	3.72	3.72	3.05
Upper Head	EL 6.47	2.13	2.13	1.23	< 1.23	< 1.23	< 1.23	0 ≦
Upper Plenum	EL 4.06	2.08	2.08	1.21	1.02	0.04	0	0
Lower Plenum	EL -1.80	1.65	1.65	1.65	1.65	1.65	1.37	0.47
Downcomer	EL -1.80	8.65	8.65	6.40	5.65	4.25	1.59	2.57
PV (Top-Bottom)	EL -2.36	10.30	10.30	7.92	7.19	6.04	3.03	2.10

*1 Average height for middle length tubes

*2 Estimated from fluid density data

Table 5.3 A time sequential list of transient maximum heater rod surface temperature during 1400 and 1800 s

TIME	TEMP.	FUNCID	TAG NAME
1.401E+03	5.755E+02	TW 309	TWE-B15444
1.402E+03	5.818E+02	TW 283	TWE-B13442
1.403E+03	5.826E+02	TW 178	TWE-B05176
1.404E+03	5.800E+02	TW 448	TWE-B24446
1.405E+03	5.757E+02	TW 309	TWE-B15444
1.406E+03	5.760E+02	TW 366	TWE-B19459
1.407E+03	5.779E+02	TW 374	TWE-B20442
1.408E+03	5.770E+02	TW 139	TWE-B02482
1.409E+03	5.778E+02	TW 333	TWE-B16175
1.410E+03	5.813E+02	TW 273	TWE-B12435
1.411E+03	5.844E+02	TW 445	TWE-B24441
1.412E+03	5.802E+02	TW 146	TWE-B03422
1.413E+03	5.759E+02	TW 309	TWE-B15444
1.414E+03	5.781E+02	TW 433	TWE-B20112
1.415E+03	5.760E+02	TW 309	TWE-B15444
1.416E+03	5.797E+02	TW 273	TWE-B12435
1.417E+03	5.760E+02	TW 309	TWE-B15444
1.418E+03	5.762E+02	TW 309	TWE-B15444
1.419E+03	5.763E+02	TW 309	TWE-B15444
1.420E+03	5.791E+02	TW 395	TWE-B21667
1.421E+03	5.761E+02	TW 309	TWE-B15444
1.422E+03	5.780E+02	TW 178	TWE-B05176
1.423E+03	5.762E+02	TW 258	TWE-B11178
1.424E+03	5.759E+02	TW 309	TWE-B15444
1.425E+03	5.809E+02	TW 359	TWE-B18448
1.426E+03	5.761E+02	TW 309	TWE-B15444
1.427E+03	5.763E+02	TW 309	TWE-B15444
1.428E+03	5.763E+02	TW 309	TWE-B15444
1.429E+03	5.763E+02	TW 309	TWE-B15444
1.430E+03	5.827E+02	TW 376	TWE-B20445
1.431E+03	5.808E+02	TW 165	TWE-B04435
1.432E+03	5.804E+02	TW 237	TWE-B10444
1.433E+03	5.762E+02	TW 309	TWE-B15444
1.434E+03	5.762E+02	TW 309	TWE-B15444
1.435E+03	5.763E+02	TW 309	TWE-B15444
1.436E+03	5.762E+02	TW 309	TWE-B15444
1.437E+03	5.817E+02	TW 360	TWE-B18449
1.438E+03	5.820E+02	TW 438	TWE-B20118
1.439E+03	5.777E+02	TW 152	TWE-B03433
1.440E+03	5.776E+02	TW 301	TWE-B14172
1.441E+03	5.767E+02	TW 456	TWE-B24718
1.442E+03	5.877E+02	TW 378	TWE-B20449
1.443E+03	5.765E+02	TW 309	TWE-B15444
1.444E+03	5.762E+02	TW 309	TWE-B15444
1.445E+03	5.810E+02	TW 225	TWE-B08435
1.446E+03	5.925E+02	TW 375	TWE-B20444
1.447E+03	5.765E+02	TW 309	TWE-B15444
1.448E+03	5.783E+02	TW 296	TWE-B14443
1.449E+03	5.784E+02	TW 128	TWE-B02242
1.450E+03	5.768E+02	TW 317	TWE-B15458
1.451E+03	5.765E+02	TW 309	TWE-B15444
1.452E+03	5.770E+02	TW 231	TWE-B09445
1.453E+03	5.813E+02	TW 285	TWE-B13445
1.454E+03	5.768E+02	TW 309	TWE-B15444
1.455E+03	5.773E+02	TW 236	TWE-B10442
1.456E+03	5.796E+02	TW 165	TWE-B04435
1.457E+03	5.762E+02	TW 309	TWE-B15444
1.458E+03	5.871E+02	TW 272	TWE-B12433
1.459E+03	5.771E+02	TW 309	TWE-B15444
1.460E+03	5.776E+02	TW 343	TWE-B17172
1.461E+03	5.765E+02	TW 309	TWE-B15444
1.462E+03	5.765E+02	TW 309	TWE-B15444
1.463E+03	5.858E+02	TW 250	TWE-B11446
1.464E+03	5.777E+02	TW 352	TWE-B18345
1.465E+03	5.812E+02	TW 456	TWE-B24718
1.466E+03	5.764E+02	TW 309	TWE-B15444
1.467E+03	5.762E+02	TW 309	TWE-B15444
1.468E+03	5.778E+02	TW 205	TWE-B07431
1.469E+03	5.758E+02	TW 309	TWE-B15444
1.470E+03	5.869E+02	TW 376	TWE-B20445
1.471E+03	5.764E+02	TW 335	TWE-B16177
1.472E+03	5.763E+02	TW 309	TWE-B15444
1.473E+03	5.766E+02	TW 450	TWE-B24449
1.474E+03	5.771E+02	TW 430	TWE-B23456
1.475E+03	5.780E+02	TW 129	TWE-B02244
1.476E+03	5.843E+02	TW 373	TWE-B20441
1.477E+03	5.772E+02	TW 423	TWE-B23444
1.478E+03	5.816E+02	TW 443	TWE-B24347
1.479E+03	5.766E+02	TW 219	TWE-B08225
1.480E+03	5.909E+02	TW 442	TWE-B24345
1.481E+03	5.752E+02	TW 207	TWE-B07435
1.482E+03	5.753E+02	TW 309	TWE-B15444
1.483E+03	5.766E+02	TW 357	TWE-B18445
1.484E+03	5.746E+02	TW 299	TWE-B14448
1.485E+03	5.752E+02	TW 309	TWE-B15444
1.486E+03	5.782E+02	TW 435	TWE-B20115
1.487E+03	5.752E+02	TW 309	TWE-B15444
1.488E+03	5.860E+02	TW 370	TWE-B19446
1.489E+03	5.752E+02	TW 309	TWE-B15444
1.490E+03	5.754E+02	TW 259	TWE-B12262
1.491E+03	5.779E+02	TW 274	TWE-B12436
1.492E+03	5.768E+02	TW 341	TWE-B17447
1.493E+03	5.789E+02	TW 117	TWE-B01345
1.494E+03	5.758E+02	TW 309	TWE-B15444
1.495E+03	5.865E+02	TW 309	TWE-B15444
1.496E+03	5.824E+02	TW 441	TWE-B24344
1.497E+03	5.780E+02	TW 320	TWE-B15174
1.498E+03	5.783E+02	TW 359	TWE-B18448
1.499E+03	5.792E+02	TW 359	TWE-B18448
1.500E+03	5.813E+02	TW 359	TWE-B18448

core dryout

Table 5.3 A time sequential list of transient maximum heater rod surface temperature during 1400 and 1800 s (Cont'd)

TIME	TEMP.	FUNCID	TAG NAME
1.501E+03	5.820E+02	TW 359	TWE-B18448
1.502E+03	5.835E+02	TW 359	TWE-B18448
1.503E+03	5.846E+02	TW 359	TWE-B18448
1.504E+03	5.861E+02	TW 359	TWE-B18448
1.505E+03	5.874E+02	TW 359	TWE-B18448
1.506E+03	5.883E+02	TW 359	TWE-B18448
1.507E+03	5.896E+02	TW 359	TWE-B18448
1.508E+03	5.908E+02	TW 359	TWE-B18448
1.509E+03	5.917E+02	TW 342	TWE-B17448
1.510E+03	5.928E+02	TW 359	TWE-B18448
1.511E+03	5.938E+02	TW 342	TWE-B17448
1.512E+03	5.952E+02	TW 342	TWE-B17448
1.513E+03	5.963E+02	TW 342	TWE-B17448
1.514E+03	5.975E+02	TW 342	TWE-B17448
1.515E+03	5.988E+02	TW 342	TWE-B17448
1.516E+03	5.996E+02	TW 342	TWE-B17448
1.517E+03	6.012E+02	TW 342	TWE-B17448
1.518E+03	6.020E+02	TW 342	TWE-B17448
1.519E+03	6.031E+02	TW 342	TWE-B17448
1.520E+03	6.041E+02	TW 342	TWE-B17448
1.521E+03	6.158E+02	TW 288	TWE-B13448
1.522E+03	6.066E+02	TW 342	TWE-B17448
1.523E+03	6.073E+02	TW 341	TWE-B17447
1.524E+03	6.091E+02	TW 341	TWE-B17447
1.525E+03	6.106E+02	TW 341	TWE-B17447
1.526E+03	6.123E+02	TW 341	TWE-B17447
1.527E+03	6.133E+02	TW 341	TWE-B17447
1.528E+03	6.149E+02	TW 341	TWE-B17447
1.529E+03	6.166E+02	TW 341	TWE-B17447
1.530E+03	6.186E+02	TW 341	TWE-B17447
1.531E+03	6.200E+02	TW 341	TWE-B17447
1.532E+03	6.214E+02	TW 341	TWE-B17447
1.533E+03	6.227E+02	TW 341	TWE-B17447
1.534E+03	6.245E+02	TW 341	TWE-B17447
1.535E+03	6.261E+02	TW 341	TWE-B17447
1.536E+03	6.274E+02	TW 341	TWE-B17447
1.537E+03	6.287E+02	TW 341	TWE-B17447
1.538E+03	6.304E+02	TW 341	TWE-B17447
1.539E+03	6.317E+02	TW 341	TWE-B17447
1.540E+03	6.328E+02	TW 341	TWE-B17447
1.541E+03	6.346E+02	TW 341	TWE-B17447
1.542E+03	6.357E+02	TW 341	TWE-B17447
1.543E+03	6.369E+02	TW 341	TWE-B17447
1.544E+03	6.380E+02	TW 341	TWE-B17447
1.545E+03	6.392E+02	TW 341	TWE-B17447
1.546E+03	6.408E+02	TW 341	TWE-B17447
1.547E+03	6.415E+02	TW 341	TWE-B17447
1.548E+03	6.431E+02	TW 341	TWE-B17447
1.549E+03	6.441E+02	TW 341	TWE-B17447
1.550E+03	6.453E+02	TW 341	TWE-B17447
1.551E+03	6.462E+02	TW 341	TWE-B17447
1.552E+03	6.472E+02	TW 341	TWE-B17447
1.553E+03	6.485E+02	TW 341	TWE-B17447
1.554E+03	6.496E+02	TW 340	TWE-B17446
1.555E+03	6.511E+02	TW 340	TWE-B17446
1.556E+03	6.532E+02	TW 340	TWE-B17446
1.557E+03	6.543E+02	TW 340	TWE-B17446
1.558E+03	6.560E+02	TW 340	TWE-B17446
1.559E+03	6.576E+02	TW 340	TWE-B17446
1.560E+03	6.591E+02	TW 340	TWE-B17446
1.561E+03	6.612E+02	TW 340	TWE-B17446
1.562E+03	6.622E+02	TW 340	TWE-B17446
1.563E+03	6.641E+02	TW 340	TWE-B17446
1.564E+03	6.655E+02	TW 340	TWE-B17446
1.565E+03	6.672E+02	TW 340	TWE-B17446
1.566E+03	6.690E+02	TW 340	TWE-B17446
1.567E+03	6.683E+02	TW 340	TWE-B17446
1.568E+03	6.717E+02	TW 340	TWE-B17446
1.569E+03	6.732E+02	TW 340	TWE-B17446
1.570E+03	6.748E+02	TW 340	TWE-B17446
1.571E+03	6.760E+02	TW 340	TWE-B17446
1.572E+03	6.779E+02	TW 340	TWE-B17446
1.573E+03	6.792E+02	TW 340	TWE-B17446
1.574E+03	6.805E+02	TW 340	TWE-B17446
1.575E+03	6.822E+02	TW 340	TWE-B17446
1.576E+03	6.833E+02	TW 340	TWE-B17446
1.577E+03	6.847E+02	TW 340	TWE-B17446
1.578E+03	6.862E+02	TW 340	TWE-B17446
1.579E+03	6.873E+02	TW 340	TWE-B17446
1.580E+03	6.888E+02	TW 340	TWE-B17446
1.581E+03	6.896E+02	TW 340	TWE-B17446
1.582E+03	6.918E+02	TW 340	TWE-B17446
1.583E+03	6.934E+02	TW 340	TWE-B17446
1.584E+03	6.946E+02	TW 340	TWE-B17446
1.585E+03	6.959E+02	TW 340	TWE-B17446
1.586E+03	6.971E+02	TW 340	TWE-B17446
1.587E+03	6.986E+02	TW 340	TWE-B17446
1.588E+03	6.999E+02	TW 340	TWE-B17446
1.589E+03	7.010E+02	TW 340	TWE-B17446
1.590E+03	7.029E+02	TW 340	TWE-B17446
1.591E+03	7.041E+02	TW 340	TWE-B17446
1.592E+03	7.055E+02	TW 340	TWE-B17446
1.593E+03	7.067E+02	TW 340	TWE-B17446
1.594E+03	7.074E+02	TW 340	TWE-B17446
1.595E+03	7.089E+02	TW 340	TWE-B17446
1.596E+03	7.097E+02	TW 340	TWE-B17446
1.597E+03	7.112E+02	TW 340	TWE-B17446
1.598E+03	7.130E+02	TW 340	TWE-B17446
1.599E+03	7.143E+02	TW 340	TWE-B17446
1.600E+03	7.156E+02	TW 340	TWE-B17446

Table 5.3 A time sequential list of transient maximum heater rod surface temperature during 1400 and 1800 s (Cont'd)

TIME	TEMP.	FUNCID	TAG NAME
1.601E+03	7.167E+02	TW 340	TWE-B17446
1.602E+03	7.179E+02	TW 340	TWE-B17446
1.603E+03	7.194E+02	TW 340	TWE-B17446
1.604E+03	7.203E+02	TW 340	TWE-B17446
1.605E+03	7.219E+02	TW 340	TWE-B17446
1.606E+03	7.229E+02	TW 340	TWE-B17446
1.607E+03	7.245E+02	TW 340	TWE-B17446
1.608E+03	7.264E+02	TW 340	TWE-B17446
1.609E+03	7.271E+02	TW 340	TWE-B17446
1.610E+03	7.289E+02	TW 340	TWE-B17446
1.611E+03	7.297E+02	TW 340	TWE-B17446
1.612E+03	7.312E+02	TW 340	TWE-B17446
1.613E+03	7.320E+02	TW 340	TWE-B17446
1.614E+03	7.334E+02	TW 340	TWE-B17446
1.615E+03	7.387E+02	TW 286	TWE-B13446
1.616E+03	7.359E+02	TW 340	TWE-B17446
1.617E+03	7.375E+02	TW 340	TWE-B17446
1.618E+03	7.384E+02	TW 340	TWE-B17446
1.619E+03	7.406E+02	TW 340	TWE-B17446
1.620E+03	7.410E+02	TW 340	TWE-B17446
1.621E+03	7.418E+02	TW 340	TWE-B17446
1.622E+03	7.435E+02	TW 340	TWE-B17446
1.623E+03	7.445E+02	TW 340	TWE-B17446
1.624E+03	7.457E+02	TW 340	TWE-B17446
1.625E+03	7.469E+02	TW 340	TWE-B17446
1.626E+03	7.485E+02	TW 340	TWE-B17446
1.627E+03	7.500E+02	TW 340	TWE-B17446
1.628E+03	7.508E+02	TW 340	TWE-B17446
1.629E+03	7.523E+02	TW 340	TWE-B17446
1.630E+03	7.536E+02	TW 340	TWE-B17446
1.631E+03	7.547E+02	TW 340	TWE-B17446
1.632E+03	7.559E+02	TW 340	TWE-B17446
1.633E+03	7.571E+02	TW 376	TWE-B20445
1.634E+03	7.585E+02	TW 340	TWE-B17446
1.635E+03	7.597E+02	TW 376	TWE-B20445
1.636E+03	7.615E+02	TW 376	TWE-B20445
1.637E+03	7.620E+02	TW 340	TWE-B17446
1.638E+03	7.635E+02	TW 376	TWE-B20445
1.639E+03	7.649E+02	TW 376	TWE-B20445
1.640E+03	7.696E+02	TW 369	TWE-B19445
1.641E+03	7.668E+02	TW 340	TWE-B17446
1.642E+03	7.688E+02	TW 376	TWE-B20445
1.643E+03	7.701E+02	TW 376	TWE-B20445
1.644E+03	7.712E+02	TW 376	TWE-B20445
1.645E+03	7.727E+02	TW 376	TWE-B20445
1.646E+03	7.737E+02	TW 376	TWE-B20445
1.647E+03	7.752E+02	TW 376	TWE-B20445
1.648E+03	7.759E+02	TW 376	TWE-B20445
1.649E+03	7.776E+02	TW 376	TWE-B20445
1.650E+03	7.787E+02	TW 376	TWE-B20445
1.651E+03	7.807E+02	TW 376	TWE-B20445
1.652E+03	7.813E+02	TW 376	TWE-B20445
1.653E+03	7.825E+02	TW 376	TWE-B20445
1.654E+03	7.842E+02	TW 376	TWE-B20445
1.655E+03	7.854E+02	TW 376	TWE-B20445
1.656E+03	7.896E+02	TW 285	TWE-B13445
1.657E+03	7.854E+02	TW 369	TWE-B19445
1.658E+03	7.885E+02	TW 376	TWE-B20445
1.659E+03	7.904E+02	TW 376	TWE-B20445
1.660E+03	7.911E+02	TW 376	TWE-B20445
1.661E+03	7.925E+02	TW 376	TWE-B20445
1.662E+03	8.002E+02	TW 376	TWE-B20445
1.663E+03	7.953E+02	TW 376	TWE-B20445
1.664E+03	7.958E+02	TW 376	TWE-B20445
1.665E+03	7.977E+02	TW 376	TWE-B20445
1.666E+03	7.984E+02	TW 376	TWE-B20445
1.667E+03	7.993E+02	TW 376	TWE-B20445
1.668E+03	8.012E+02	TW 376	TWE-B20445
1.669E+03	8.021E+02	TW 376	TWE-B20445
1.670E+03	8.030E+02	TW 376	TWE-B20445
1.671E+03	8.046E+02	TW 376	TWE-B20445
1.672E+03	8.059E+02	TW 376	TWE-B20445
1.673E+03	8.068E+02	TW 376	TWE-B20445
1.674E+03	8.080E+02	TW 376	TWE-B20445
1.675E+03	8.091E+02	TW 376	TWE-B20445
1.676E+03	8.103E+02	TW 376	TWE-B20445
1.677E+03	8.115E+02	TW 376	TWE-B20445
1.678E+03	8.126E+02	TW 339	TWE-B17445
1.679E+03	8.141E+02	TW 376	TWE-B20445
1.680E+03	8.151E+02	TW 376	TWE-B20445
1.681E+03	8.162E+02	TW 339	TWE-B17445
1.682E+03	8.174E+02	TW 339	TWE-B17445
1.683E+03	8.186E+02	TW 376	TWE-B20445
1.684E+03	8.194E+02	TW 376	TWE-B20445
1.685E+03	8.206E+02	TW 339	TWE-B17445
1.686E+03	8.223E+02	TW 339	TWE-B17445
1.687E+03	8.241E+02	TW 339	TWE-B17445
1.688E+03	8.251E+02	TW 376	TWE-B20445
1.689E+03	8.261E+02	TW 339	TWE-B17445
1.690E+03	8.273E+02	TW 339	TWE-B17445
1.691E+03	8.284E+02	TW 339	TWE-B17445
1.692E+03	8.297E+02	TW 339	TWE-B17445
1.693E+03	8.305E+02	TW 339	TWE-B17445
1.694E+03	8.319E+02	TW 339	TWE-B17445
1.695E+03	8.331E+02	TW 339	TWE-B17445
1.696E+03	8.345E+02	TW 339	TWE-B17445
1.697E+03	8.352E+02	TW 339	TWE-B17445
1.698E+03	8.367E+02	TW 339	TWE-B17445
1.699E+03	8.377E+02	TW 339	TWE-B17445
1.700E+03	8.391E+02	TW 339	TWE-B17445

Table 5.3 A time sequential list of transient maximum heater rod surface temperature during 1400 and 1800 s (Cont'd)

TIME	TEMP.	FUNCID		TAG NAME
1.701E+03	8.399E+02	TW	339	TWE-B17445
1.702E+03	8.412E+02	TW	339	TWE-B17445
1.703E+03	8.420E+02	TW	339	TWE-B17445
1.704E+03	8.438E+02	TW	339	TWE-B17445
1.705E+03	8.446E+02	TW	339	TWE-B17445
1.706E+03	8.451E+02	TW	376	TWE-B20445
1.707E+03	8.465E+02	TW	339	TWE-B17445
1.708E+03	8.483E+02	TW	339	TWE-B17445
1.709E+03	8.492E+02	TW	339	TWE-B17445
1.710E+03	8.510E+02	TW	339	TWE-B17445
1.711E+03	8.518E+02	TW	339	TWE-B17445
1.712E+03	8.530E+02	TW	339	TWE-B17445
1.713E+03	8.545E+02	TW	339	TWE-B17445
1.714E+03	8.606E+02	TW	339	TWE-B17445
1.715E+03	8.566E+02	TW	339	TWE-B17445
1.716E+03	8.580E+02	TW	339	TWE-B17445
1.717E+03	8.594E+02	TW	339	TWE-B17445
1.718E+03	8.607E+02	TW	339	TWE-B17445
1.719E+03	8.613E+02	TW	339	TWE-B17445
1.720E+03	8.627E+02	TW	339	TWE-B17445
1.721E+03	8.640E+02	TW	339	TWE-B17445
1.722E+03	8.652E+02	TW	339	TWE-B17445
1.723E+03	8.672E+02	TW	339	TWE-B17445
1.724E+03	8.765E+02	TW	357	TWE-B18445
1.725E+03	8.690E+02	TW	339	TWE-B17445
1.726E+03	8.706E+02	TW	339	TWE-B17445
1.727E+03	8.718E+02	TW	339	TWE-B17445
1.728E+03	8.727E+02	TW	339	TWE-B17445
1.729E+03	8.741E+02	TW	339	TWE-B17445
1.730E+03	8.751E+02	TW	339	TWE-B17445
1.731E+03	8.765E+02	TW	339	TWE-B17445
1.732E+03	8.777E+02	TW	339	TWE-B17445
1.733E+03	8.801E+02	TW	357	TWE-B18445
1.734E+03	8.801E+02	TW	339	TWE-B17445
1.735E+03	8.816E+02	TW	339	TWE-B17445
1.736E+03	8.829E+02	TW	339	TWE-B17445
1.737E+03	8.840E+02	TW	339	TWE-B17445
1.738E+03	8.856E+02	TW	339	TWE-B17445
1.739E+03	8.864E+02	TW	339	TWE-B17445
1.740E+03	8.894E+02	TW	339	TWE-B17445
1.741E+03	8.937E+02	TW	376	TWE-B20445
1.742E+03	8.918E+02	TW	339	TWE-B17445
1.743E+03	8.919E+02	TW	339	TWE-B17445
1.744E+03	8.952E+02	TW	339	TWE-B17445
1.745E+03	8.950E+02	TW	339	TWE-B17445
1.746E+03	8.967E+02	TW	339	TWE-B17445
1.747E+03	8.981E+02	TW	339	TWE-B17445
1.748E+03	8.991E+02	TW	339	TWE-B17445
1.749E+03	9.014E+02	TW	339	TWE-B17445
1.750E+03	9.014E+02	TW	339	TWE-B17445
1.751E+03	9.028E+02	TW	339	TWE-B17445
1.752E+03	9.036E+02	TW	339	TWE-B17445
1.753E+03	9.050E+02	TW	339	TWE-B17445
1.754E+03	9.059E+02	TW	339	TWE-B17445
1.755E+03	9.071E+02	TW	339	TWE-B17445
1.756E+03	9.084E+02	TW	339	TWE-B17445
1.757E+03	9.096E+02	TW	339	TWE-B17445
1.758E+03	9.113E+02	TW	339	TWE-B17445
1.759E+03	9.123E+02	TW	339	TWE-B17445
1.760E+03	9.132E+02	TW	339	TWE-B17445
1.761E+03	9.143E+02	TW	339	TWE-B17445
1.762E+03	9.166E+02	TW	339	TWE-B17445
1.763E+03	9.167E+02	TW	339	TWE-B17445
1.764E+03	9.178E+02	TW	339	TWE-B17445
1.765E+03	9.191E+02	TW	339	TWE-B17445
1.766E+03	9.195E+02	TW	339	TWE-B17445
1.767E+03	9.203E+02	TW	339	TWE-B17445
1.768E+03	9.211E+02	TW	339	TWE-B17445
1.769E+03	9.218E+02	TW	339	TWE-B17445
1.770E+03	9.225E+02	TW	339	TWE-B17445
1.771E+03	9.229E+02	TW	339	TWE-B17445
1.772E+03	9.235E+02	TW	339	TWE-B17445
1.773E+03	9.238E+02	TW	339	TWE-B17445
1.774E+03	9.228E+02	TW	376	TWE-B20445
1.775E+03	9.245E+02	TW	339	TWE-B17445
1.776E+03	9.243E+02	TW	339	TWE-B17445
1.777E+03	9.238E+02	TW	339	TWE-B17445
1.778E+03	9.231E+02	TW	339	TWE-B17445
1.779E+03	9.228E+02	TW	339	TWE-B17445
1.780E+03	9.218E+02	TW	339	TWE-B17445
1.781E+03	9.209E+02	TW	339	TWE-B17445
1.782E+03	9.196E+02	TW	339	TWE-B17445
1.783E+03	9.187E+02	TW	339	TWE-B17445
1.784E+03	9.173E+02	TW	339	TWE-B17445
1.785E+03	9.164E+02	TW	339	TWE-B17445
1.786E+03	9.150E+02	TW	339	TWE-B17445
1.787E+03	9.141E+02	TW	339	TWE-B17445
1.788E+03	9.128E+02	TW	339	TWE-B17445
1.789E+03	9.117E+02	TW	339	TWE-B17445
1.790E+03	9.108E+02	TW	339	TWE-B17445
1.791E+03	9.098E+02	TW	339	TWE-B17445
1.792E+03	9.083E+02	TW	339	TWE-B17445
1.793E+03	9.070E+02	TW	339	TWE-B17445
1.794E+03	9.062E+02	TW	339	TWE-B17445
1.795E+03	9.057E+02	TW	339	TWE-B17445
1.796E+03	9.037E+02	TW	339	TWE-B17445
1.797E+03	9.027E+02	TW	339	TWE-B17445
1.798E+03	9.023E+02	TW	339	TWE-B17445
1.799E+03	9.005E+02	TW	364	TWE-B19455
1.800E+03	8.997E+02	TW	364	TWE-B19455

core power trip

Table 5.4 Maximum heater rod surface temperature during all test period in SB-PV-01 test

NO.	FUNC	ID	TAG NAME	TIME	TEMP.
1	TW	339	TWE-B17445	1.775E+03	9.245E+02
2	TW	339	TWE-B17445	1.776E+03	9.243E+02
3	TW	339	TWE-B17445	1.773E+03	9.238E+02
4	TW	339	TWE-B17445	1.777E+03	9.238E+02
5	TW	339	TWE-B17445	1.772E+03	9.235E+02
6	TW	339	TWE-B17445	1.778E+03	9.231E+02
7	TW	339	TWE-B17445	1.771E+03	9.229E+02
8	TW	376	TWE-B20445	1.774E+03	9.228E+02
9	TW	339	TWE-B17445	1.779E+03	9.228E+02
10	TW	339	TWE-B17445	1.770E+03	9.225E+02
11	TW	339	TWE-B17445	1.769E+03	9.218E+02
12	TW	339	TWE-B17445	1.780E+03	9.218E+02
13	TW	339	TWE-B17445	1.768E+03	9.211E+02
14	TW	339	TWE-B17445	1.781E+03	9.209E+02
15	TW	339	TWE-B17445	1.767E+03	9.203E+02
16	TW	339	TWE-B17445	1.782E+03	9.196E+02
17	TW	339	TWE-B17445	1.766E+03	9.195E+02
18	TW	339	TWE-B17445	1.765E+03	9.191E+02
19	TW	339	TWE-B17445	1.783E+03	9.187E+02
20	TW	339	TWE-B17445	1.764E+03	9.178E+02
21	TW	339	TWE-B17445	1.784E+03	9.173E+02
22	TW	339	TWE-B17445	1.763E+03	9.167E+02
23	TW	339	TWE-B17445	1.762E+03	9.166E+02
24	TW	339	TWE-B17445	1.785E+03	9.164E+02
25	TW	339	TWE-B17445	1.786E+03	9.150E+02
26	TW	339	TWE-B17445	1.761E+03	9.143E+02
27	TW	339	TWE-B17445	1.787E+03	9.141E+02
28	TW	339	TWE-B17445	1.760E+03	9.132E+02
29	TW	339	TWE-B17445	1.788E+03	9.128E+02
30	TW	339	TWE-B17445	1.759E+03	9.123E+02
31	TW	339	TWE-B17445	1.789E+03	9.117E+02
32	TW	339	TWE-B17445	1.758E+03	9.113E+02
33	TW	339	TWE-B17445	1.790E+03	9.108E+02
34	TW	339	TWE-B17445	1.791E+03	9.098E+02
35	TW	339	TWE-B17445	1.757E+03	9.096E+02
36	TW	339	TWE-B17445	1.756E+03	9.084E+02
37	TW	339	TWE-B17445	1.792E+03	9.083E+02
38	TW	339	TWE-B17445	1.755E+03	9.071E+02
39	TW	339	TWE-B17445	1.793E+03	9.070E+02
40	TW	339	TWE-B17445	1.794E+03	9.062E+02
41	TW	339	TWE-B17445	1.754E+03	9.059E+02
42	TW	339	TWE-B17445	1.795E+03	9.057E+02
43	TW	339	TWE-B17445	1.753E+03	9.050E+02
44	TW	339	TWE-B17445	1.796E+03	9.037E+02
45	TW	339	TWE-B17445	1.752E+03	9.036E+02
46	TW	339	TWE-B17445	1.751E+03	9.028E+02
47	TW	339	TWE-B17445	1.797E+03	9.027E+02
48	TW	339	TWE-B17445	1.798E+03	9.023E+02
49	TW	339	TWE-B17445	1.750E+03	9.014E+02
50	TW	339	TWE-B17445	1.749E+03	9.014E+02

Table 5.5 Average break flow rates measured by Venturi meter and calculated from catch tank level change

Time Range (s)	Pressure Range (MPa)	Average Break Flow Rate		Difference
		W_v^{*1} (kg/s)	W_l^{*2} (kg/s)	(W_l-W_v) (kg/s)
0 - 200	15.43 - 11.73	3.35	3.39	0.04
200 - 400	11.73 - 8.52	2.80	2.86	0.06
400 - 600	8.52 - 8.13	2.60	2.77	0.17
600 - 800	8.25 - 8.04	2.55	2.80	0.25
800 - 1000	8.17 - 7.99	2.50	2.75	0.25
1000 - 1200	8.14 - 7.97	2.50	2.80	0.30
1200 - 1400	8.12 - 7.96	2.50	2.79	0.29
1400 - 1600	8.11 - 7.95	2.50	2.81	0.31
1600 - 1800	8.00 - 6.76	2.35	2.56	0.21
1800 - 2000	6.76 - 4.95	2.05	1.97	-0.08
2000 - 2200	4.95 - 3.78	1.90	1.92	0.02
2200 - 2400	3.78 - 2.00	1.50	1.57	0.07
2400 - 2600	2.00 - 2.03	1.55	1.39	-0.16
2600 - 2800	2.03 - 2.11	1.60	1.62	0.02
2800 - 3000	2.11 - 2.14	1.70	1.54	-0.16

*1 Measured by Venturi-meter.

*2 Estimated from catch tank level change.

Table 5.6 Injected HPI water calculated from RWST level data

Time (s)	RWST Level L (m)*1	Level Change L (m)	Injected Water M (kg)*2	Average HPI Flow during Each Time Period (kg/s)
1676	7.461	0	0	0.
1800	7.444	0.017	177	1.42
2000	7.411	0.050	520	1.72
2200	7.376	0.085	883	1.82
2400	7.338	0.123	1278	1.98
2600	7.299	0.162	1683	2.03
2800	7.259	0.202	2099	2.08
3000	7.219	0.242	2514	2.08
3086	7.201	0.260	2700	2.17

*1 Undershoot observed in level data (0.005-0.008 m) was corrected in each value.

*2 Uncertainty of the mass is not estimated.

Table 5.7 Estimation of primary remaining mass in SB-PV-01 test
(t = 1670 s)

Primary Components	Free Volume*1 (m^3)	Water Volume (m^3)		Water Mass (kg)	Steam Phase		Total Fluid Mass (kg)
		Data	Accuracy		T (K)	Mass (kg)	
Pressurizer & Pipes	1.241	0.0	-	0.0	Tsat.*4	52.2	52.2
SG Primary-Sides*2	3.150	0.002	-	1.4	Tsat.	132.5	133.9
Upper Head*3	0.514	0.063	±0.062	45.6	Tsat.	19.0	64.6
Upper Plenum	0.472	0.0	-	0.0	600.	17.4	17.4
Core	0.352	0.0	-	0.0	600.	13.0	13.0
Hot Legs	0.248	0.005	-	3.6	590.	9.4	13.0
Cold Legs & Pumps	0.279	0.0	-	0.0	Tsat.	11.7	11.7
Cross-Over Legs	0.424	0.392	±0.002	283.6	Tsat.	1.3	284.9
Downcomer & Lower Plenum	1.365	0.516	±0.036	373.3	Tsat.	35.7	409.0
Total Primary System	8.045	0.978	±0.100	707.5	-	292.2	999.7

*1 Free volumes for the connecting pipings like as ECCS lines are excluded.

*2 Filler blocks in plenums have been removed.

*3 Water level is assumed at the middle of the well (EL 6.47 - 7.37 m).

*4 Saturated temperature for the primary pressure of 7.93 MPa.
Densities for saturated steam and water are 42.1 and 723.5 kg/m^3, respectively.

Table 5.8 Discharged and remaining masses for primary system in SB-PV-01 test

Time (s)	Total Discharged Mass, M_D^{*1}(kg)	Injected ECC Mass*2		Remaining Mass M^{*1}	Mass Inventory Ratio M^{*1}/M_o
		M_{HP}(kg)	M_{ACC}(kg)		
0	0	0	0	5760	1.000
200	677	0	0	5083	0.882
400	1249	0	0	4511	0.783
600	1807	0	0	3953	0.686
800	2361	0	0	3399	0.590
1000	2911	0	0	2849	0.495
1200	3470	0	0	2290	0.398
1400	4028	0	0	1732	0.301
1600	4589	0	0	1171	0.203
1670	4760	0	0	1000	0.174
1800	5101	177	0	836	0.145
2000	5495	520	0	785	0.136
2200	5879	883	150	914	0.159
2400	6192	1278	1150	1996	0.347
2600	6470	1683	1150	2123	0.369
2800	6793	2099	1150	2216	0.385
3000	7101	2514	1150	2323	0.403
3086	7250	2700	1150	2360	0.410

*1 Reduced from catch tank level change. *2 Reduced from corrected tank levels.

Table 6.1 Major test conditions for six break location parameter tests

Items	Unit	SB-PV-01	SB-PV-02	SB-CL-12	SB-HL-03	AT-SB-03	SB-SG-01
Break Conditions							
·Break Location	-	Lower Plenum	Upper Head	Cold Leg B	Hot Leg B	Pressurizer	U-tube
·Elevation above Core Bottom	m	-1.74	8.93	5.50	5.50	21.39	7.84
·Break Simulation	-	24 Inst. Tubes	2-inch Pipe	2-inch Pipe	2-inch Pipe	1 PORV Open	3.2 U-tubes
·Break Orifice I.D.	mm	7.2	7.2	7.2	7.2	6.83	7.2
Initial Conditions							
·PR Pressure	MPa	15.4	15.4	15.5	15.5	15.7	15.4
·Total Core Power	MW	10.0	10.0	10.0	10.0	10.0*2	10.0
·Total Core Flow Rate*1	kg/s	48.6	48.8	48.8	49.5	49.5	48.8
·Primary Loop ΔT	K	35	35	35	35	35	35
·Secondary Pressure (A/B)	MPa	7.3/7.4	7.3/7.4	7.3/7.4	7.4/7.4	7.3/7.4	7.3/7.4
Failure Assumption*3		AFW,HPI	AFW,HPI	AFW,HPI	AFW,HPI	AFW,HPI	AFW,HPI
Transient & ECCS Conditions							
·Scram Trip Pressure	MPa	12.97	12.97	12.97	12.97	12.97	12.97
·Primary Pump Trip	-	Scram	Scram	Scram	Scram	Scram	Scram
·SG Isolation	-	Scram	Scram	Scram	Scram	Scram	Scram
·HPI & Charging Actuation	-	Manual	Manual	Manual	Manual	Manual	Manual
·ECC Flow Distribution (A:B)	-	1:1	3:1	3:1	3:1	1:1	3:1
·ACC, ACH & LPI Systems ·	-	Available	Available	Available	Available	Available	Available
Core Dryout Detection for HPI	-	HL Temp.	HL Temp.	Rod Temp.	Rod Temp.	Delayed	HL or Rod T.

*1 Increased to 92 kg/s after the break except for AT-SB-03. *2 Power curve differes from other 5 tests.

*3 Loss of off-site AC power is also assumed.

Table 6.2 Comparison of break line pipings for six tests

Test RUN	Break Line Piping	Total Length (m)	Free Volume (m^3)	Total Pipe Height (m)
SB-PV-01*1	Lower Plenum - Catch Tank	15.8	0.497	0.46
SB-PV-02	Upper Head - Catch Tank	29.9	0.941	11.13
SB-CL-12	Cold Leg (Middle) - Catch Tank	35.9	1.128	7.70
SB-HL-03	Hot Leg (Middle) - Catch Tank	24.0	0.758	7.70
AT-SB-03	PR Top - Catch Tank	40.3	1.268	23.59
SB-SG-01*2	SG-B Plenum - Secondary S.	15.4	0.020	-

*1 See Fig. 2.4 (a) and (b)

*2 Break line is from SG-B inlet plenum to bottom of SG-B boiler section.

Table 6.3 Chronology of major events for six break location parameter tests

	Timings of Events (s)					
	SB-PV-01	SB-OV-02	SB-CL-12	SB-HL-03	AT-SB-03	SB-SG-01
Break Initiation	0	0	0	0	0	0
Scram Trip	82	87	80	81	64	116
Primary pump Stop (PC-A)	331	336	332	340	314	365
Primary Pump Stop (PC-B)	517	336	483	340	314	365
Level Decrease in Loop-seal A	1090	1464	1000	1125	4125	-
Level Decrease in Loop-seal B	1237	1686	1240	1100	3750	-
Temporary PV Level Decrease	-	-	1526	-	-	-
Continous PV Level Decrease*1	1420	2718	1815	2057	4870	-
Core Top Dryout Initiation	1498	3552	1981	2370	5510	-
Core Bottom Dryout Initiation	1638	-	-	-	-	-
HPI & Charging Actuation	1676	3930	2254	2782	6600	-
Two-phase Discharge at Break	1700	164	507	100	250	211
PCT observed	1775*2	3974	2283	2828	6364*3	-
Steam Discharge at Break	2000	2196	1684	1650	4340	-
Loop-seal Clearing	2057	3970	1680	2825	6600	-
Final Core Cooling	2248	3982	2348	2838	6943	-

*1 Level decrease below the primary loop nozzle elevation.

*2 Due to core power trip. *3 Due to core power degradation.

Table 6.4 Discharged primary fluid mass for six break location parameter tests

Time after Break	SB-PV-01	SB-PV-02	SB-CL-12	SB-HL-03	AT-SB-03*1	SB-SG-01*2
200 s*3	677 kg	725 kg	670 kg	615 kg	0(94)	495 kg
400 s	1249	1055	1275	1110	150(277)	844
600 s	1807	1325	1830	1520	300(373)	1100
800 s	2361	1630	2375	1985	420(519)	1267
1000 s	2911	1950	2850	2460	550(665)	1397
1200 s	3470	2235	3300	2960	695(810)	1508
1400 s	4028	2550	3710	3455	845(960)	1609
1600 s	4589	2845	4115	3945	1015(1130)	1679
1800 s	5101	3160	4370	4115	1150(1265)	
2000 s	5495	3465	4460	4225	1270(1385)	
2200 s	5879	3770	4570	4310	1395(1510)	
2400 s	6192	3895	4675	4415	1540(1655)	
2600 s	6470	4010	4760	4500	1690(1805)	
2800 s	6793	4120		4615	1835(1950)	
3000 s	7101	4205		4730	1980(2095)	
3500 s		4475			2340(2455)	
4000 s		4720			2735(2850)	
4500 s		5050			3050(3165)	
5000 s					3300(3415)	
600 s					3750(3865)	

*1 Discharged steam mass was not counted in the initial 250 s due to condensation in break line pipings.

*2 Measured by Venturi flow meter, which showed correct value in the initial 200 s.

*3 Scattering error of ± 80 kg was observed among the five tests during the initial 100 s.

Table 6.5 Comparison of average break flow rates derived from ST level data for six tests

	Unit	SB-PV-01	SB-PV-02	SB-CL-12	SB-HL-03	AT-SB-03*1	SB-SG-01
Initial Water (steam) Discharge							
Time Period	s	0-100	0-100	0-100	0-100	0-250*2	0-200
Average Break Flow Rate	kg/s	3.4	4.0	3.2	3.4	0.47(0.52)	2.48
Mass Flux	kg/sm^2	$8.4x10^4$	$9.8x10^4$	$7.9x10^4$	$8.4x10^4$	$1.27x10^4$	$6.1x10^4$
Two-Phase Discharge							
Time Period (I)	s	600-1600*3	600-2000	600-1600	600-1600	1000-4000	-
Average Break Flow Rate	kg/s	2.78	1.53	2.29	2.43	0.73(0.81)	-
Mass Flux	kg/sm^2	$6.8x10^4$	$3.8x10^4$	$5.6x10^4$	$6.0x10^4$	$2.0x10^4$	-
Time Period (II)	s	1600-1800	-	-	-	-	-
Average Break Flow Rate	kg/s	2.56	-	-	-	-	-
Mass Flux	kg/sm^2	$6.3x10^4$	-	-	-	-	-
Steam or High-Quality Tow-Phase Flow Dischrage							
Time Periodd	s	-	2200-3500	1800-2200	1800-2600	4500-6000	-
Average Break Flow Rate	kg/s	-	0.54	0.50	0.48*4	0.47(0.52)	-
Mass Flux	kg/sm^2	-	$1.33x10^4$	$1.23x10^4$	$1.18x10^4$	$1.27x10^4$	-

*1 Break area is 90% of the other tests. *2 Initial steam discharge flow calculated by RELAP5 code.

*3 Almost saturated water flow. *4 Almost saturated steam flow.

Table 6.6 Estimation of two-phase break flow conditions for five tests (assuming a constant slip ratio of K=5)

		SB-PV-01	SB-PV-02	SB-CL-12	SB-HL-03	AT-SB-03
Time Period (I)	s	600-1600	600-2000	600-1600	600-1600	1000-4000
Primary Pressure Range	MPa	8.2-8.0	8.3-8.1	8.3-8.1	8.3-8.0	8.4-8.1
Break Mass Flow Rate	kg/s	2.78	1.53	2.29	2.43	0.73(0.81)*3
Mass Flux	kg/sm^2	$6.8x10^4$	$3.8x10^4$	$5.6x10^4$	$6.0x10^4$	$1.99x10^4$
Void Fraction, α*3	-	0.0*1	0.54(0.55)	0.21(0.22)	0.15(0.15)	0.86(0.87)
Steam Quality, χ*3	-	0.0*1	0.17(0.18)	0.04(0.05)	0.03(0.03)	0.51(0.55)
Time Period (II)	s	1600-1800	2200-3500	1800-2600	1800-2600	4500-6000
Primary Pressure Range	MPa	8.0-6.8	8.2-8.0	8.1	8.1-8.0	8.2-8.1
Break Mass Flow Rate	kg/s	2.56	0.54	0.50	0.48	0.47(0.52)*4
Mass Flux	kg/sm^2	$6.3x10^4$	$1.33x10^4$	$1.23x10^4$	$1.23x10^4$	$1.28x10^4$
Void Fraction, α*3	-	0.10(0.10)	0.97(0.99)	0.99(1.00)	1.00*2(1.00)	0.98(1.00)
Steam Quality, χ*3	-	0.02(0.02)	0.87(0.94)	0.95(1.00)	1.00*2(1.00)	0.91(0.98)

*1 Upstream condition was almost saturated water (W_{fc})

*2 Upsteam condition was almost saturated steam (W_{gc})

*3 Void fraction was calculated as $\alpha = (W_{fc}-W)/(W_{fc}-W_{gc})$ and steam quality was calculated as $\chi = \alpha W_{gc}/W$, where W_{fc} = 2.78 kg/s, W_{gc} = 0.48 kg/s (0.51 kg/s for the bracketed data).

*4 Equivallent flow rate with the same break area as the others.

Table 6.7 Remaining primary fluid mass in five break location parameter tests

Time after Break (s)	SB-PV-01		SB-PV-02		SB-CL-12		SB-HL-03		AT-SB-03	
	M (kg)	M/Mo	M (kg)	M/Mo	M (kg)	M/Mo	M (kg)	M/Mo	M (kg)	M/Mo
200	5083	0.882	5035	0.874	5090	0.884	5145	0.893	5666	0.984
400	4511	0.783	4705	0.817	4485	0.779	4650	0.807	5533	0.961
600	3953	0.686	4435	0.770	3930	0.682	4240	0.736	5387	0.935
800	3399	0.590	4130	0.717	3385	0.588	3775	0.655	5241	0.910
1000	2849	0.495	3810	0.661	2910	0.505	3300	0.573	5095	0.885
1200	2290	0.398	3525	0.612	2460	0.427	2800	0.486	4950	0.859
1400	1732	0.301	3210	0.557	2050	0.356	2305	0.400	4800	0.833
1600	1171	0.203	2915	0.506	1645	0.286	1815	0.315	4630	0.804
1800	836	0.145	2600	0.451	1390	0.241	1645	0.286	4495	0.780
2000	785	0.136	2295	0.398	1300	0.226	1535	0.266	4375	0.760
2200	914	0.159	1990	0.345	1190	0.207	1450	0.252	4250	0.738
2400	1996	0.345	1865	0.324	1297	0.225	1345	0.234	4105	0.713
2600	2123	0.369	1750	0.304	1502	0.261	1260	0.219	3955	0.687
2800	2216	0.385	1640	0.285			1170	0.203	3810	0.661
3000	2323	0.403	1555	0.270			1341	0.233	3665	0.636
3500			1285	0.223					3305	0.574
4000			1133	0.197					2910	0.505
4500									2595	0.451
5000			1578	0.274					2345	0.407
6000									1895	0.329

* Remaining mass (M) was calculated by using the discharged mass (M_D), injected ECC mass (M_E) and the initial mas of M_o, as $M = M_o - M_D + M_E$.

Table 6.8 Primary mass inventory ratio for key events in five tests

Key Events	Transient Mass Ratio to Initial Mass (M/M_o, %)				
	SB-PV-01	SB-CL-12	SB-HL-03	SB-PV-C2	AT-SB-03
Initiation of two-phase discharge	15	73	94	90	98
Initiation of Loop-seal Level Decrease	38-45	43-50	52-53	49-55	49-54
Loop-seal Clearing*1	14	26	20	19	28
Steam Discharge at Break (Break Uncovery)	14	25	30	35	46
Initiation of Core Dryout	25	23	24	22	37
Whole Core Dryout	18	-	-	-	-
HPI Systems Actuation	16	21	20	19	28
Accumulators Actuation	14	-	-	-	-

*1 Loop-seal clearing occurred immediately after the HPI actuation in SB-HL-03, SB-PV-02 and AT-SB-03 tests and immediately after the accumulator actuation in SB-PV-01 test.

Table 6.9 Efficiency of ECC water accumulation in primary system

Items	Unit	SB-PV-01	SB-PV-02	SB-C1-12	SB-HL-03	AT-SB-03
Phase I (HPI Systems)						
Time Period	s	1700-2000	4000-4500	2300-2600	2800-3000	6600-7000
Primary Pressure Range	MPa	7.8-5.0	7.8-5.6	8.1-6.7	8.1-7.1	7.0-5.9
Injected ECC Water, M_E	kg	486	775	435	286	290
Discharged Fluid Mass, M_D	kg	650	330	138	115	63
Accumulation Efficiency*, E_a	-	-0.34	0.57	0.68	0.60	0.67
Phase II (HPI & Accumulators)						
Time Period	s	2000-2400				
Primary Pressure Range	MPa	5.1-1.8				
Injected ECC Water, M_E	kg	1910				
Discharged Fluid Mass, M_D	kg	697				
Acccumulation Efficiency*. E_a	-	0.64				
Phase III (HPI Systems)						
Time Period	s	2400-3000				
Primary Pressure Range	MPa	2.0-2.1				
Injected ECC Water, M_E	kg	1238				
Discharged Fluid Mass, M_D	kg	909				
Acumulation Efficiency*, E_a	-	0.27				
Total Efficiency (Phase I-III)	-	0.38				

* Efficiency is defined as a ratio of remained mass devided by injected mass as $E_a = (M_E - M_D)/M_E$.

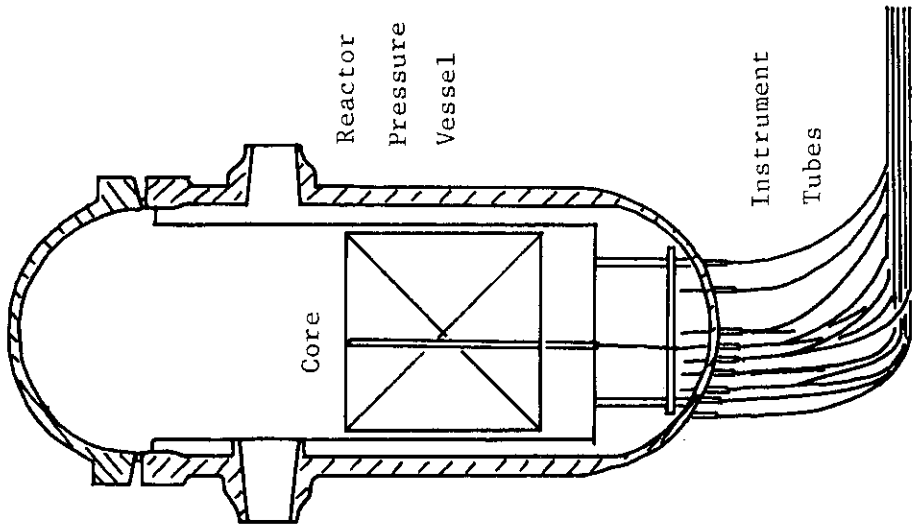

Fig. 1.2 Instrument tubes at the bottom of pressure vessel

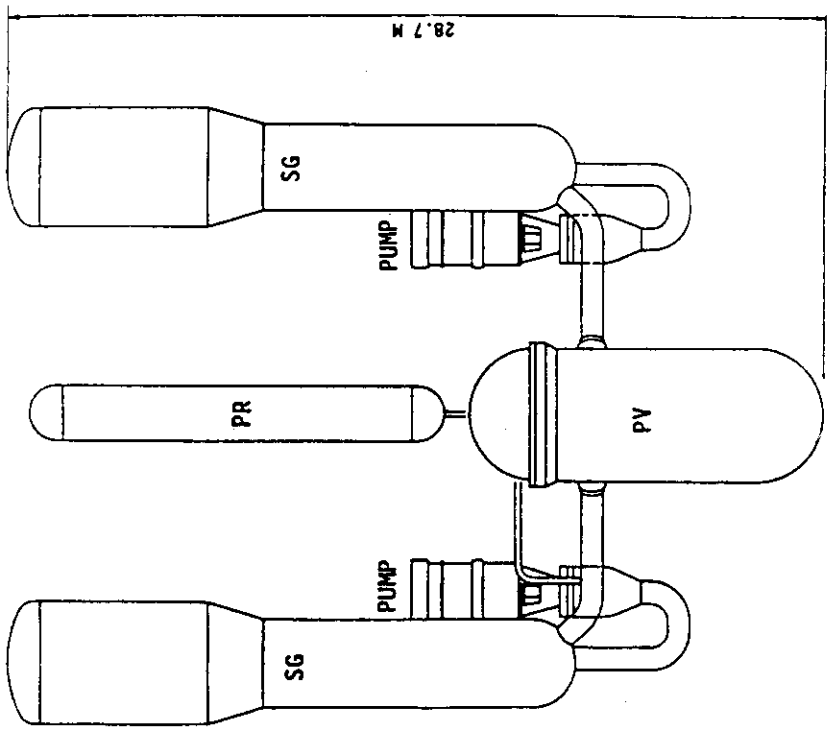

Fig. 1.1 Outline of 4-loop PWR

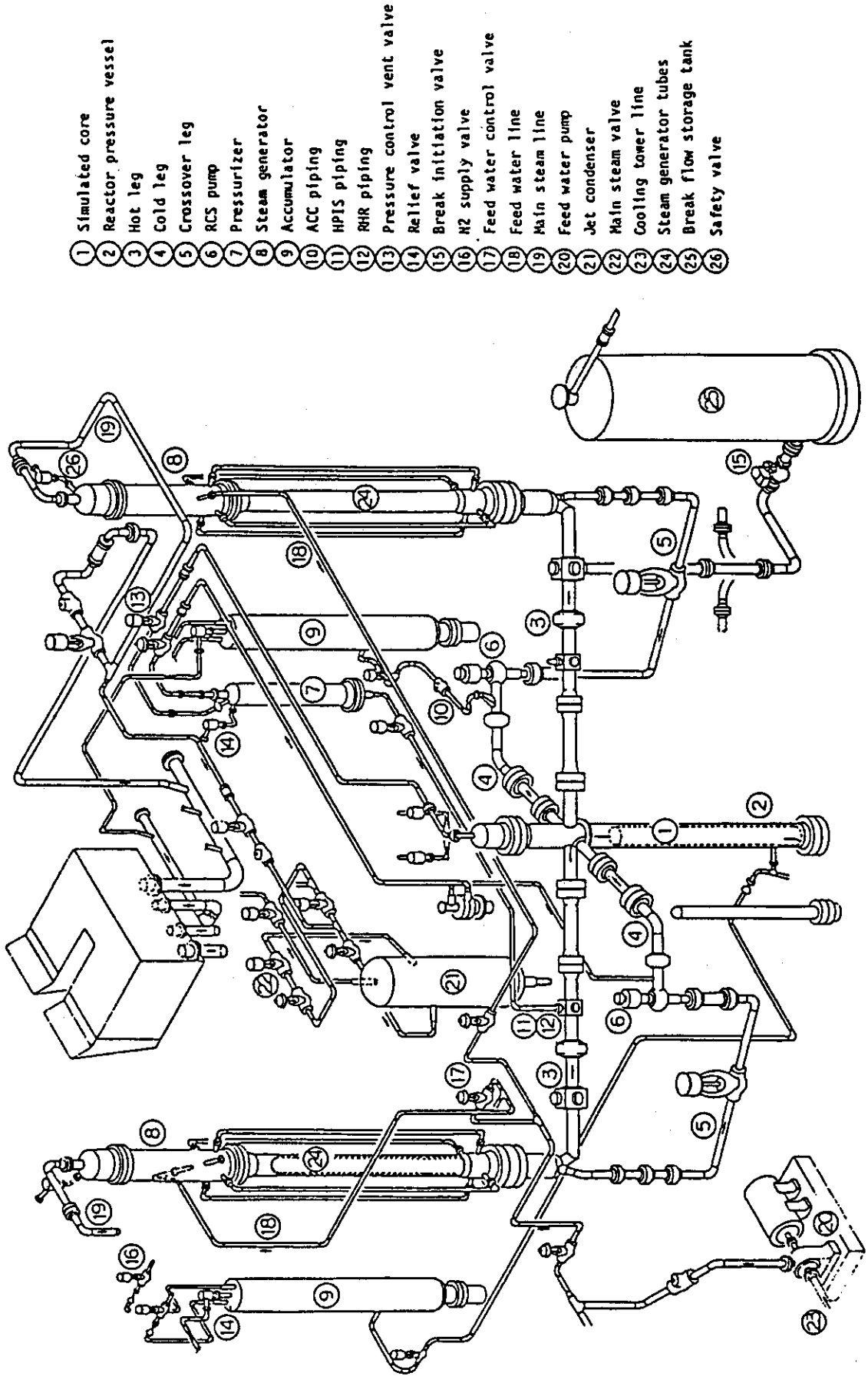

Fig. 2.1 General structure of Large Scale Test Facility (LSTF)

Location	Description	Material
1	Venturi Flow Meter	SUSF316L
2	Spool Piece	SUS316L
3	R.O. Piece 1/2	SUS316L
4	R.O. Piece 1/2	SUS316L
5	Break Valve	SCS13

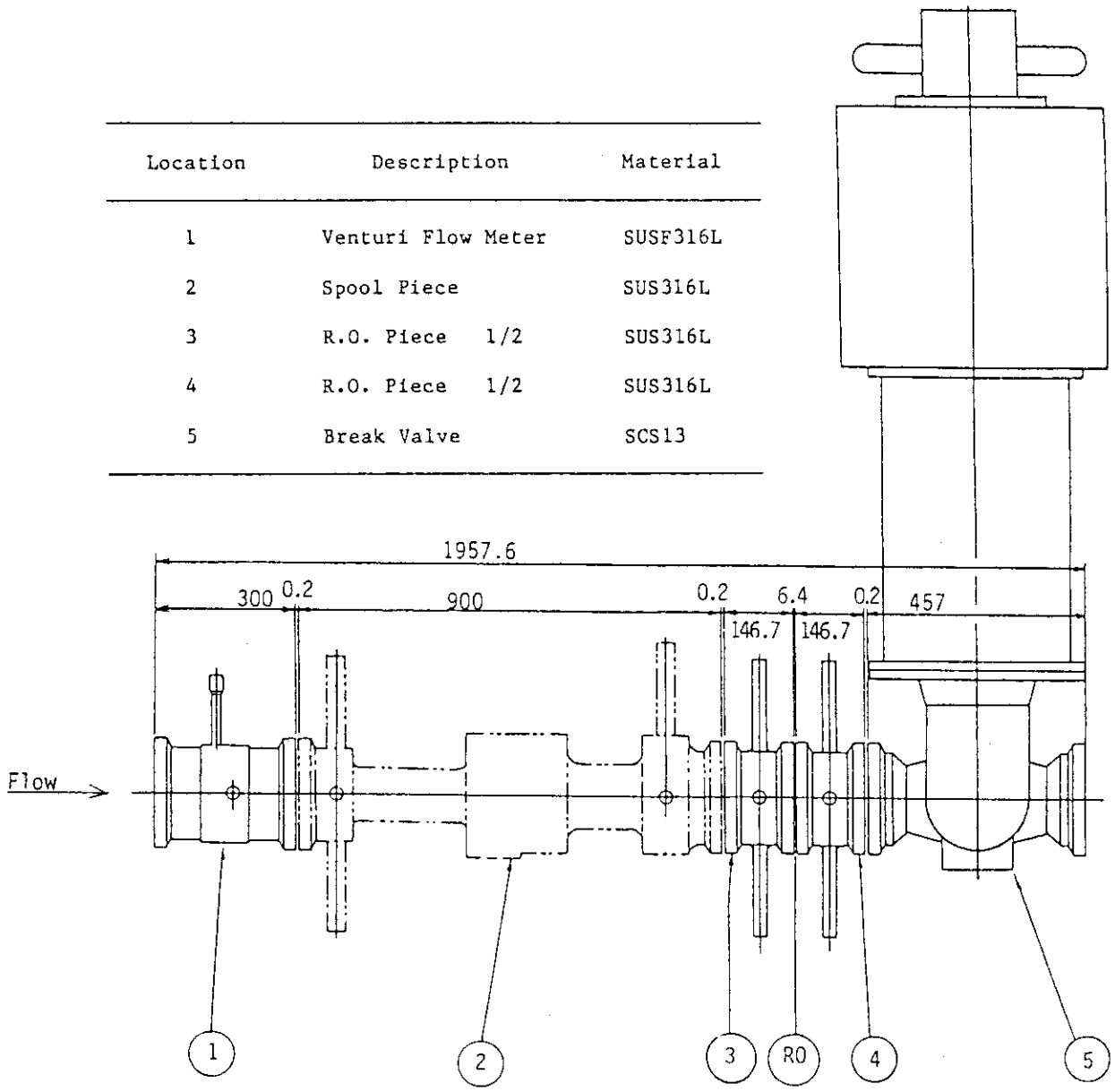

Fig. 2.2 Break unit

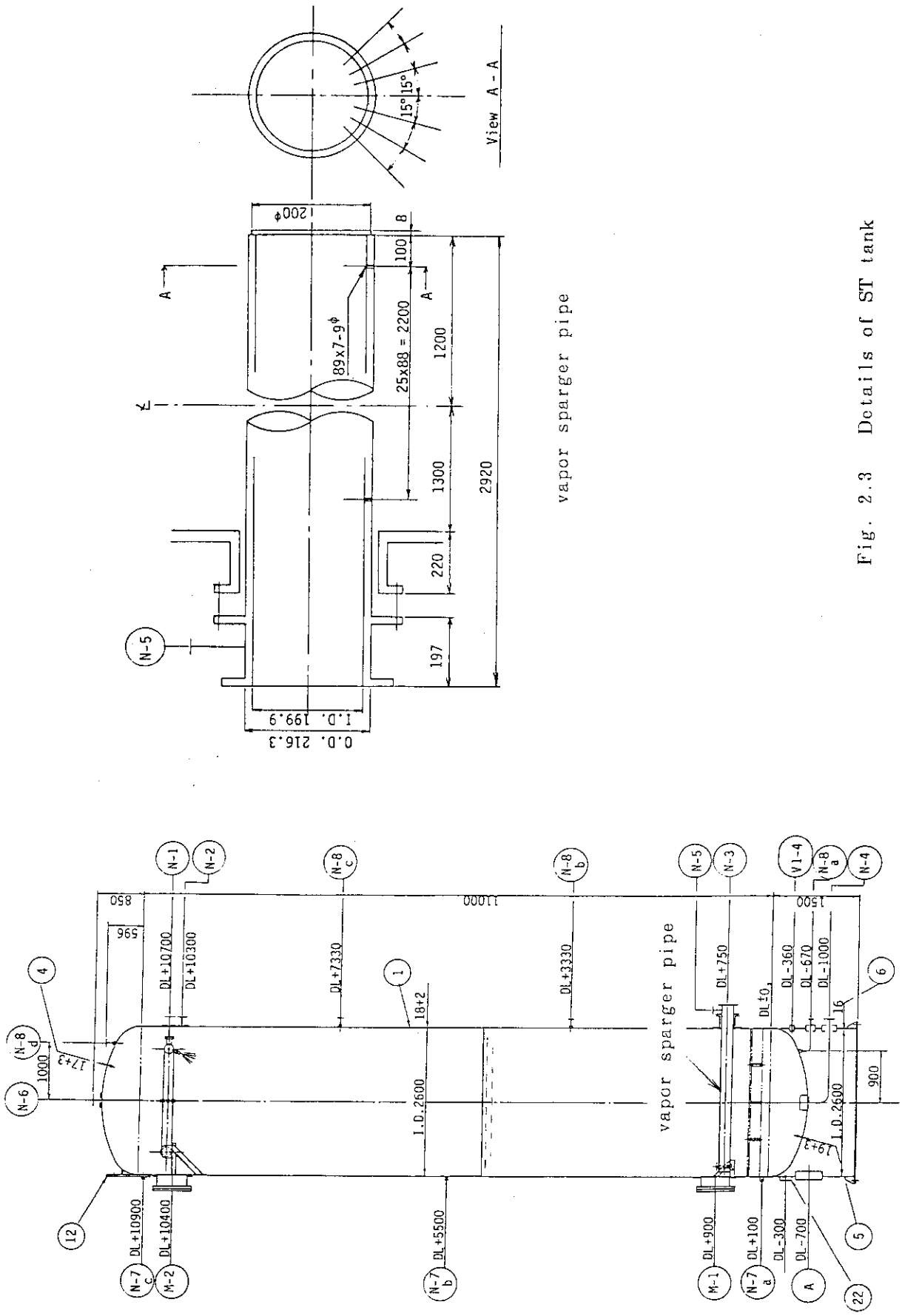

Fig. 2.3 Details of ST tank

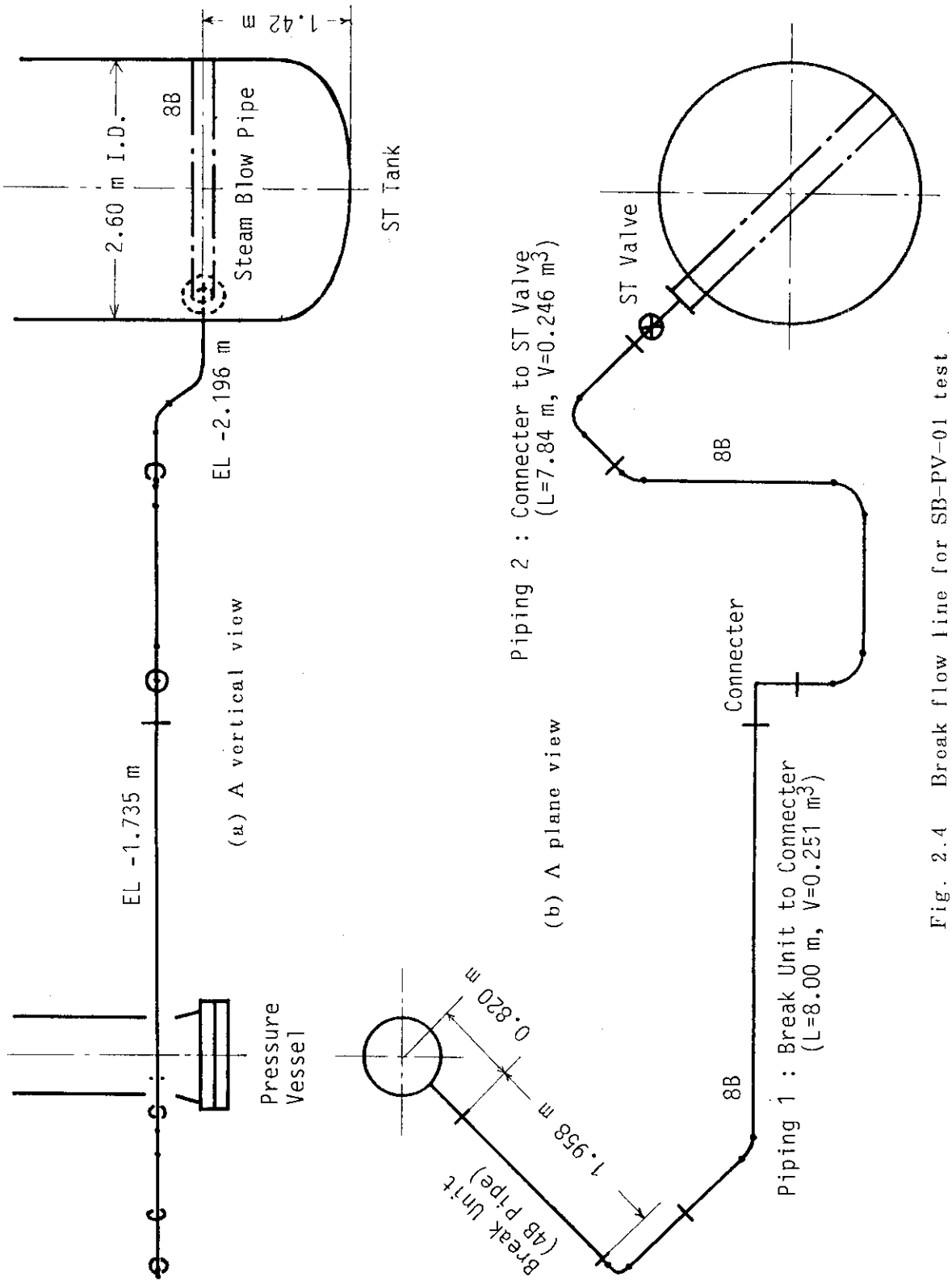

Fig. 2.4 Break flow line for SB-PV-01 test

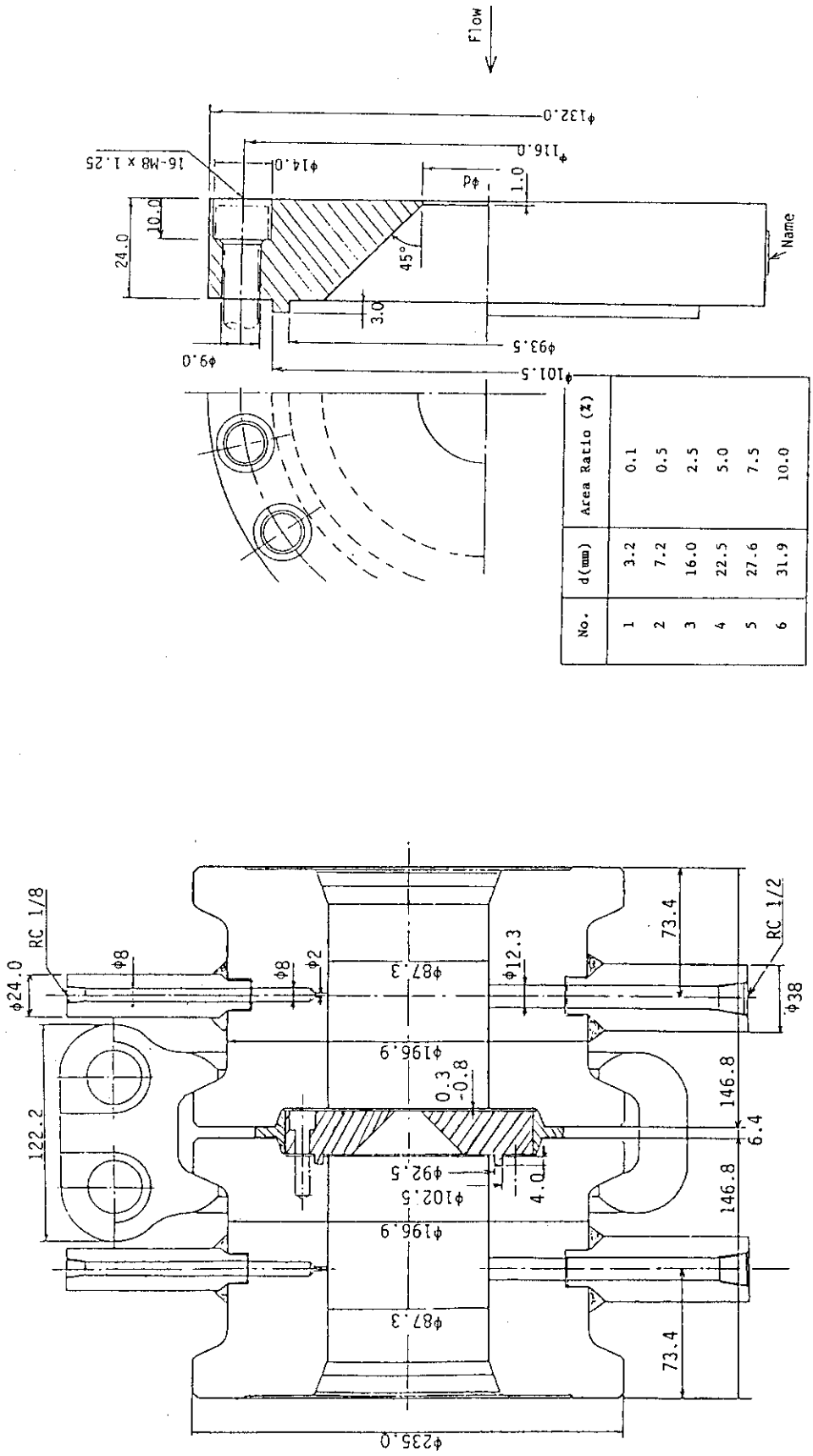

No.	d(mm)	Area Ratio (%)
1	3.2	0.1
2	7.2	0.5
3	16.0	2.5
4	22.5	5.0
5	27.6	7.5
6	31.9	10.0

Fig. 2.5 Construction and configuration of break orifice

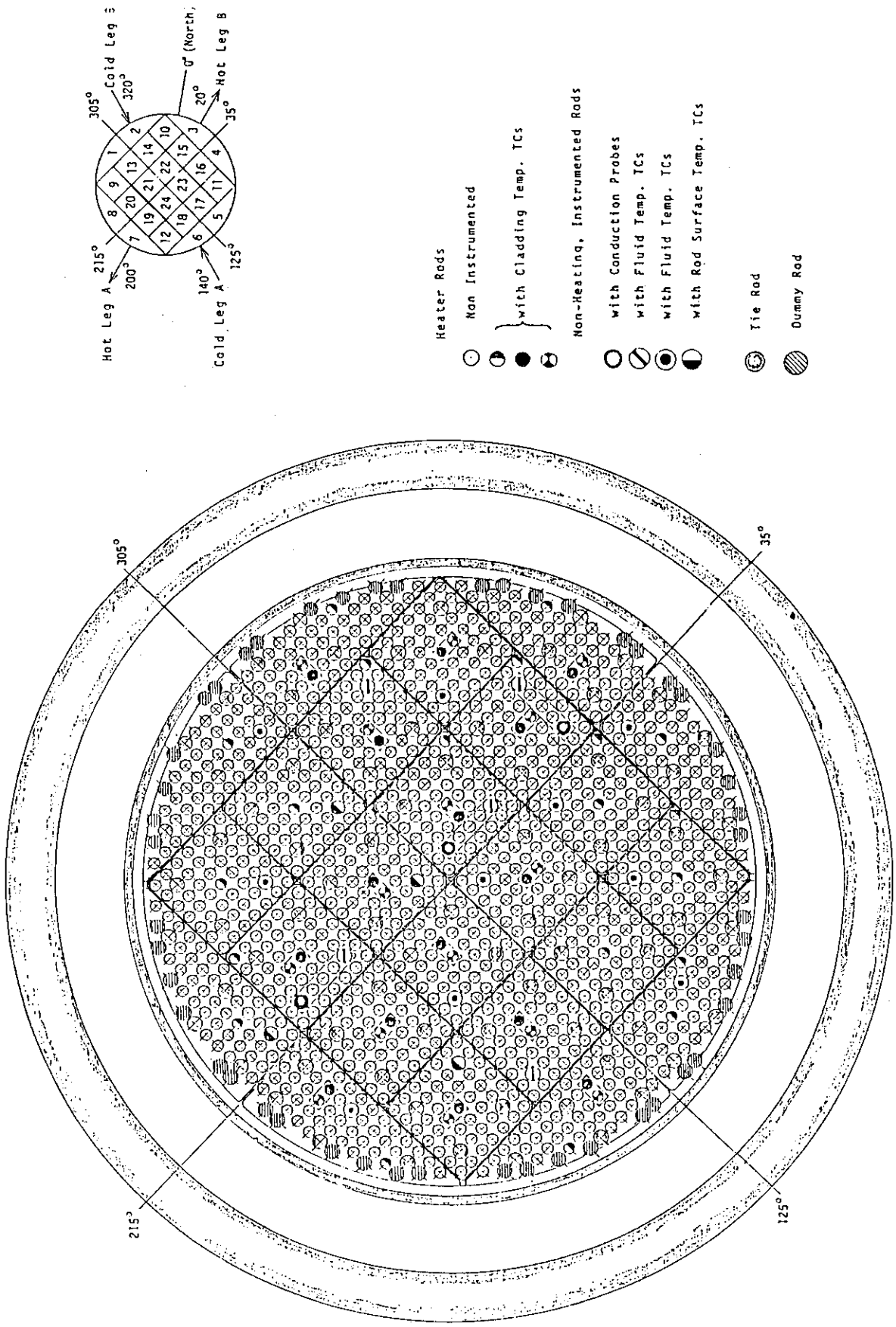

Fig. 2.6 Core cross section and heater rod arrangement

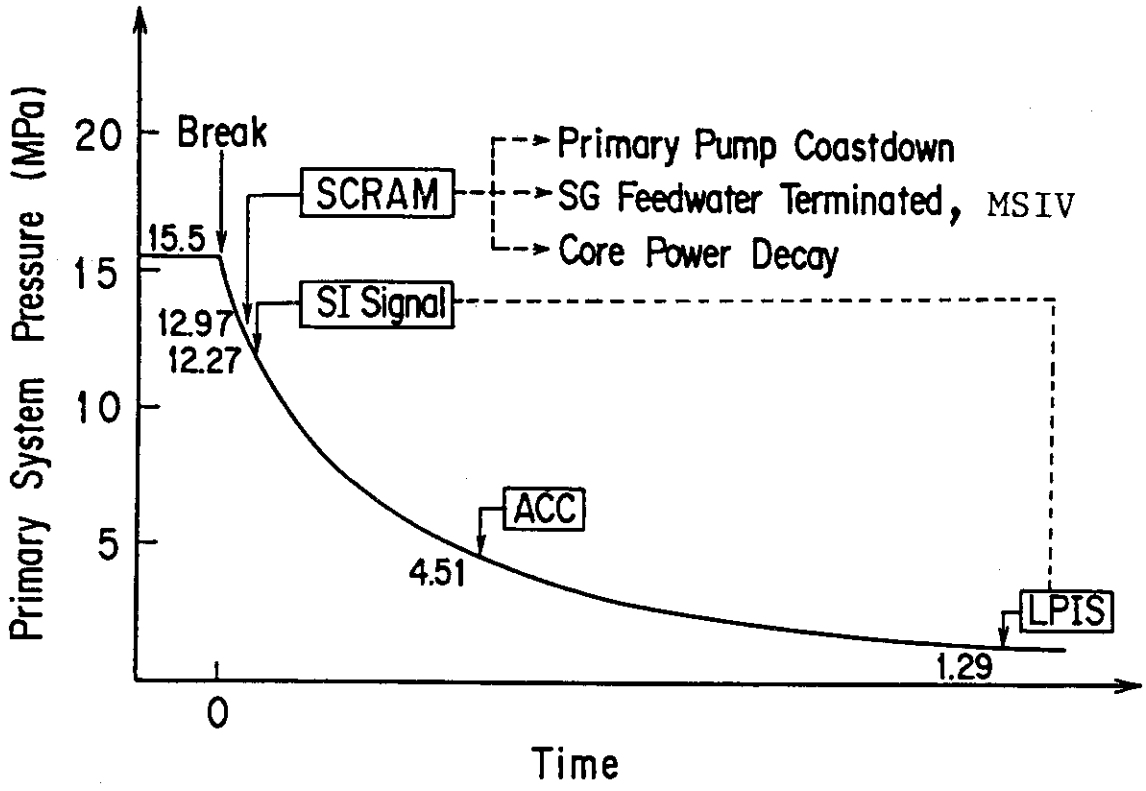

Fig. 3.1 ECCS actuation logic

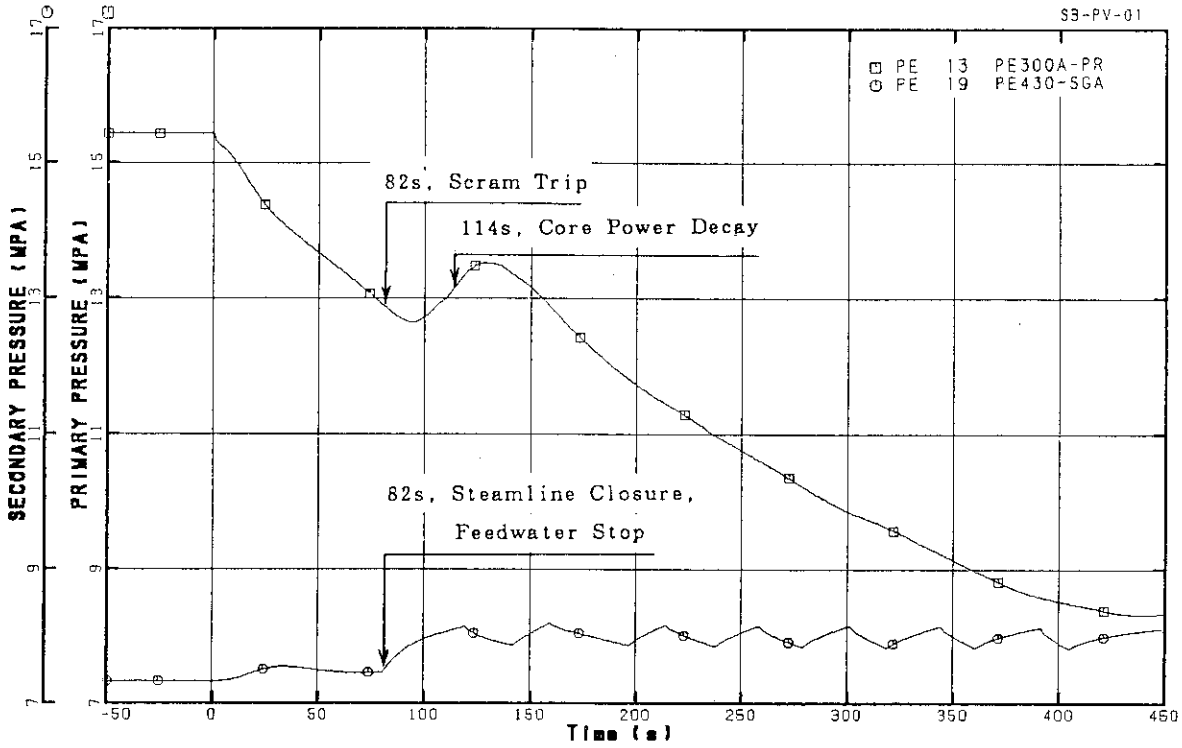

(a) Initial blowdown phase (until 450 s)

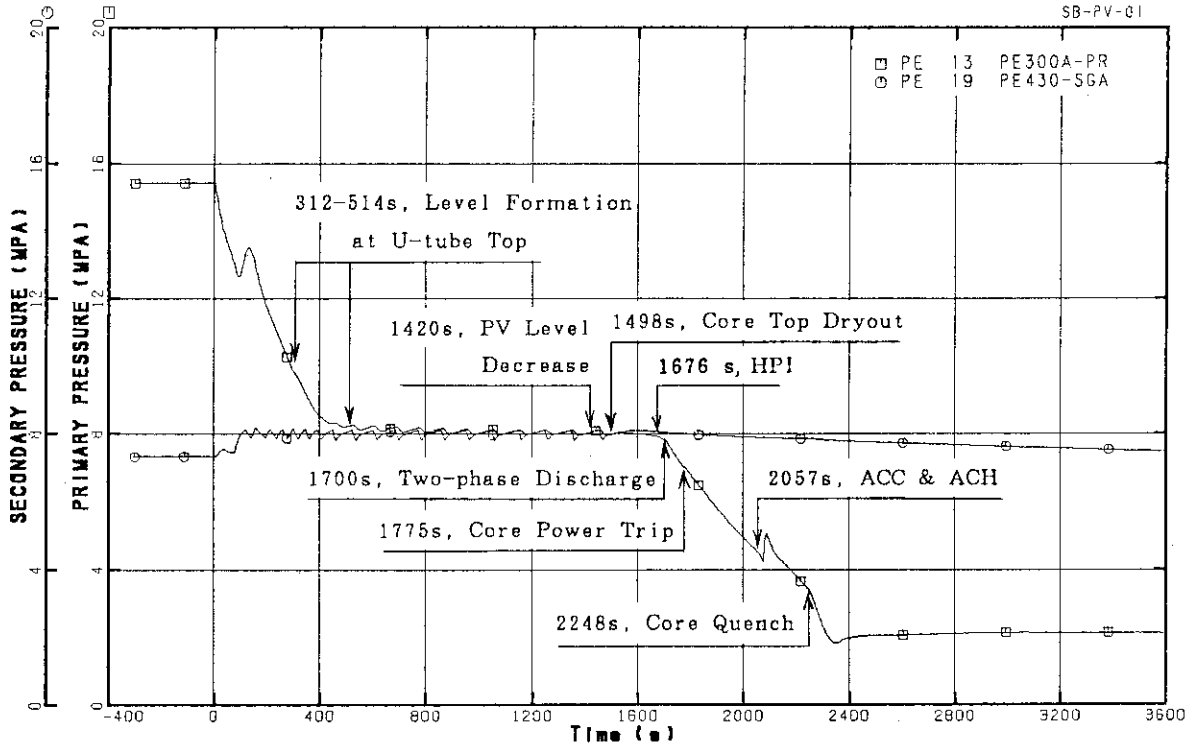

(a) Whole test period (until 3600 s)

Fig. 5.1 Representative pressures in primary and secondary systems related with major events

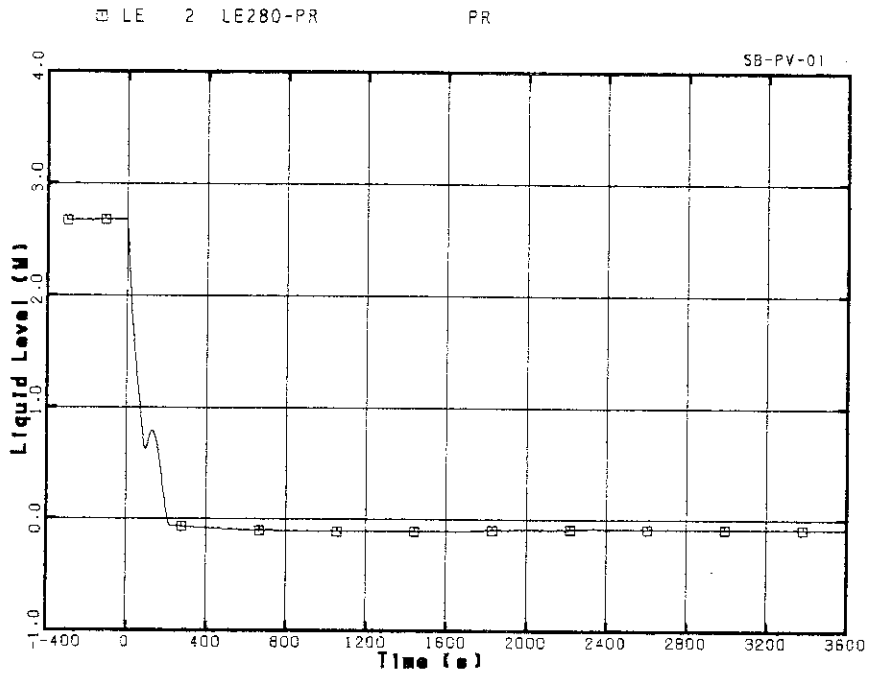

Fig. 5.2 Water level in pressurizer

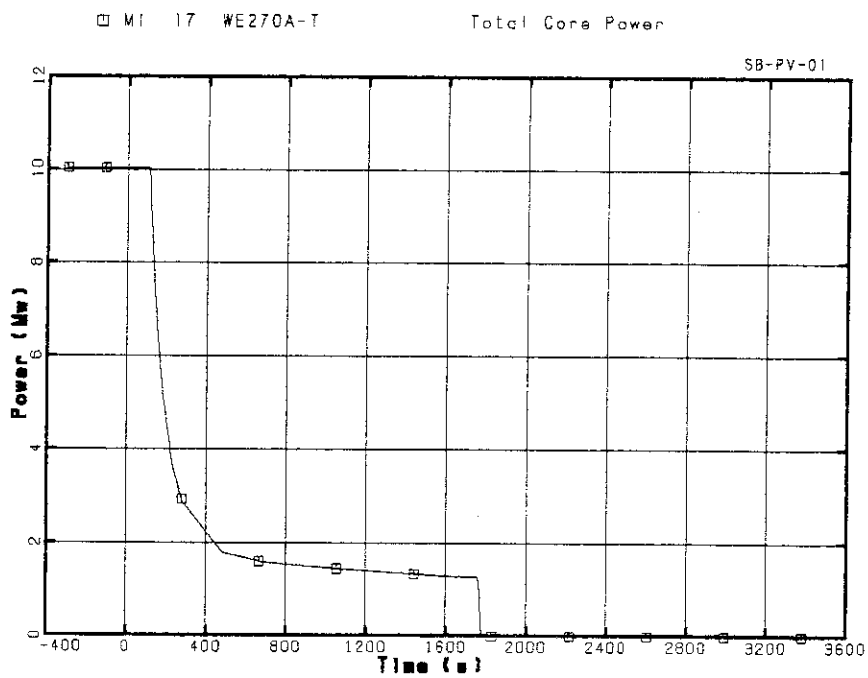

Fig. 5.3 Total core power

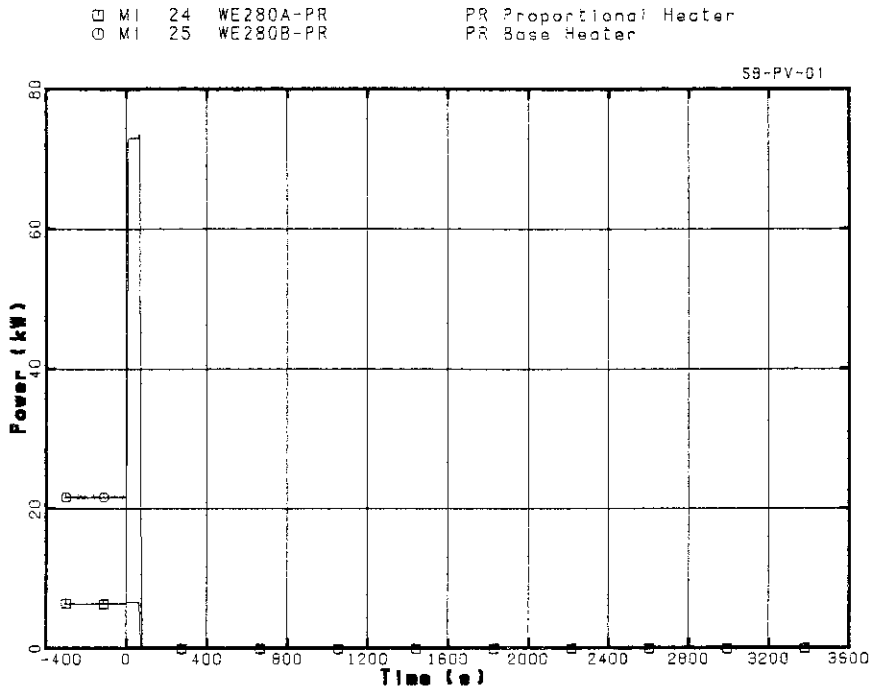

Fig. 5.4 Pressurizer heater power

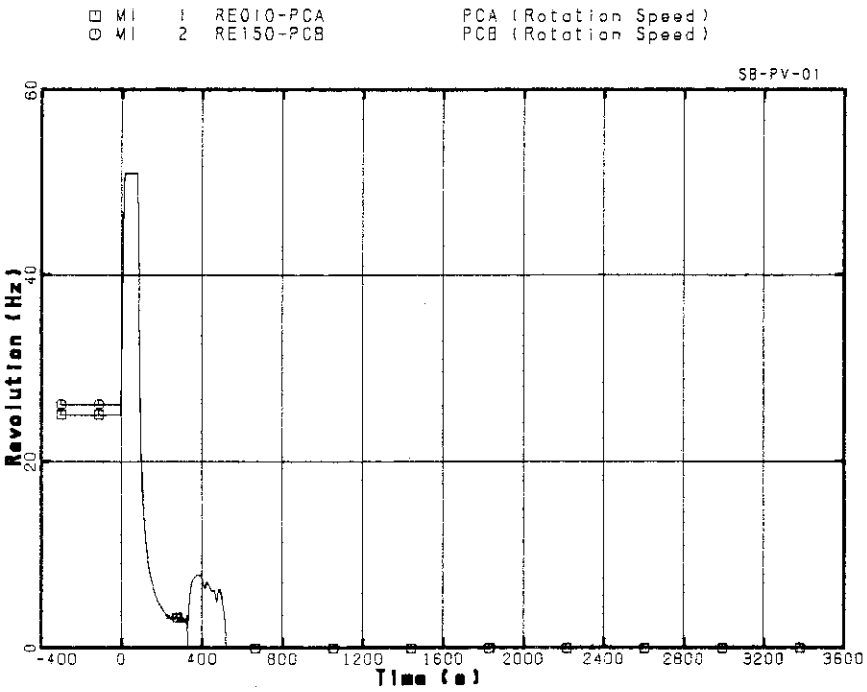

Fig. 5.5 PC-A,B pump speeds

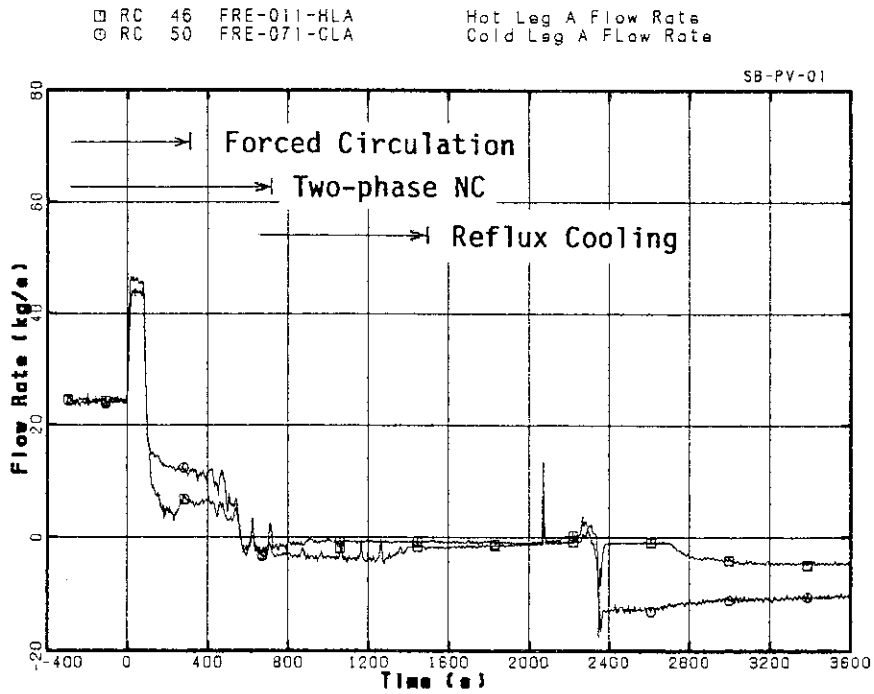

(a) Loop-A

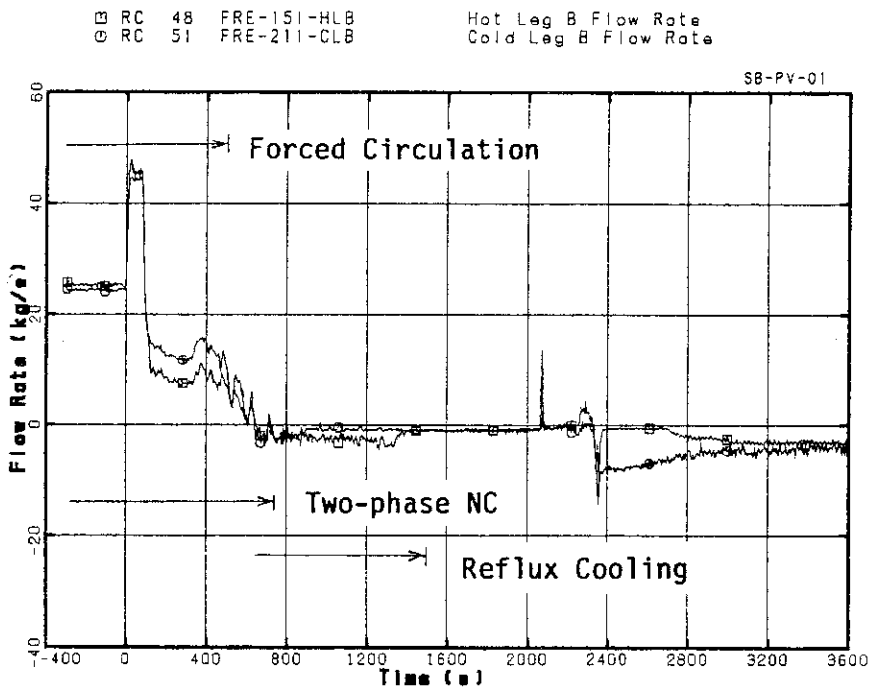

(b) Loop-B

Fig. 5.6 Primary loop flow rates (high range)

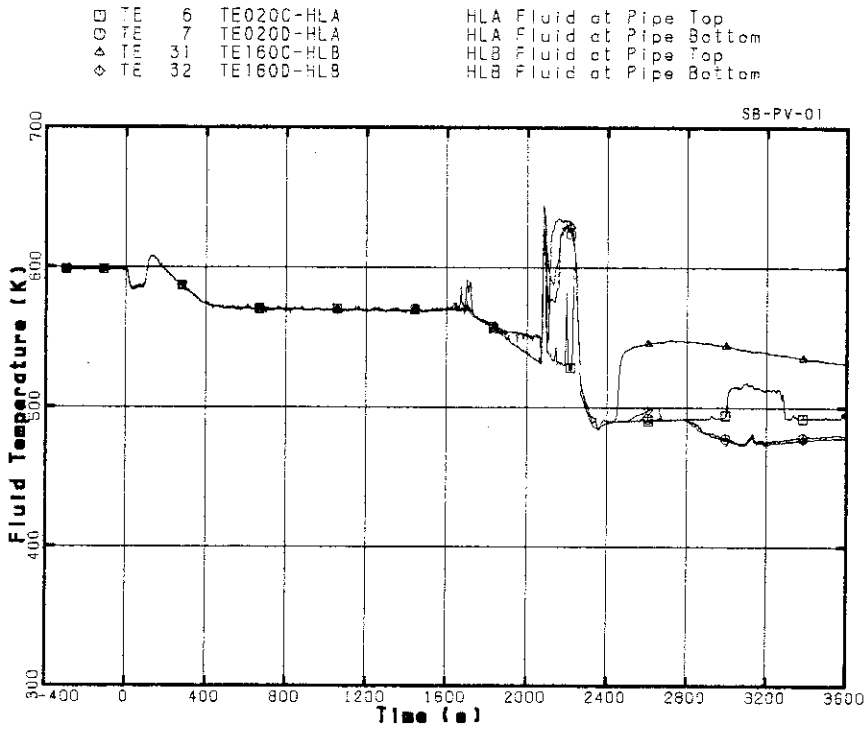

(a) Hot leg temperatures for operator detection

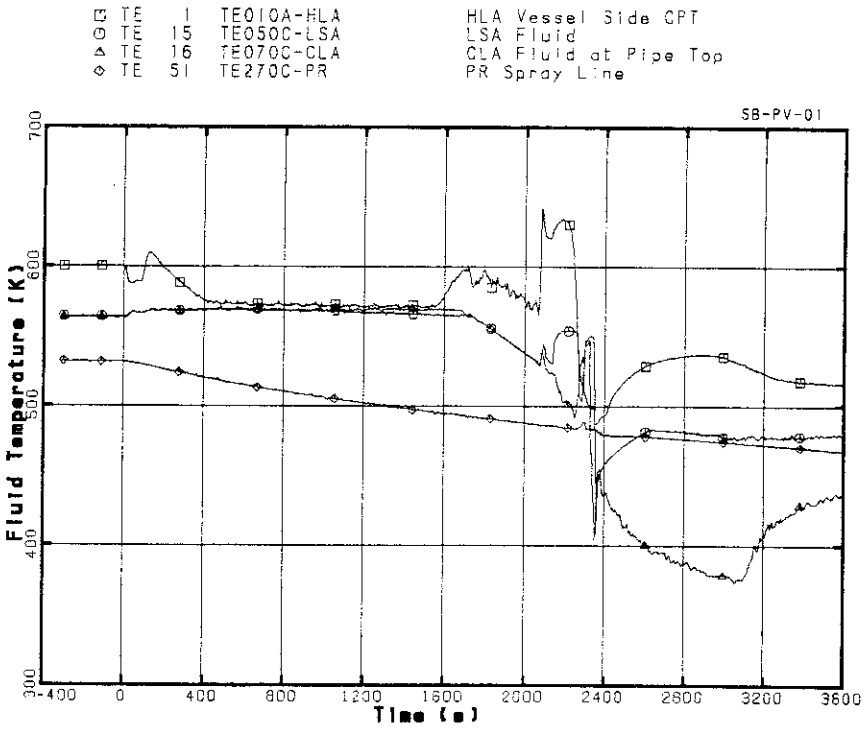

(b) Pressurizer and Loop-A

Fig. 5.7 Fluid temperatures in pressurizer and loop-A and B

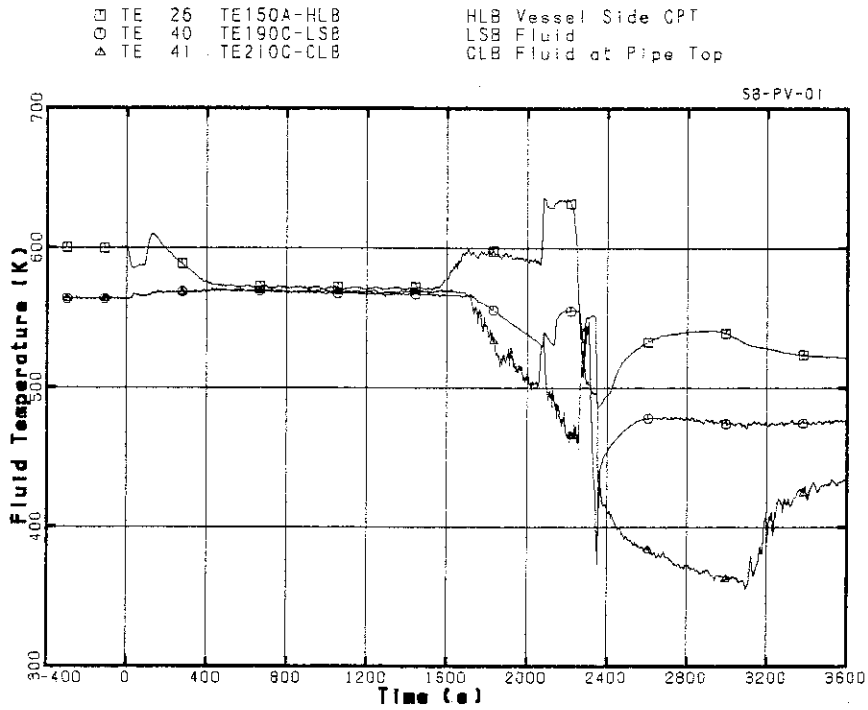

(c) Loop-B

Fig. 5.7 Fluid temperatures in pressurizer and loop-A and B (Cont'd)

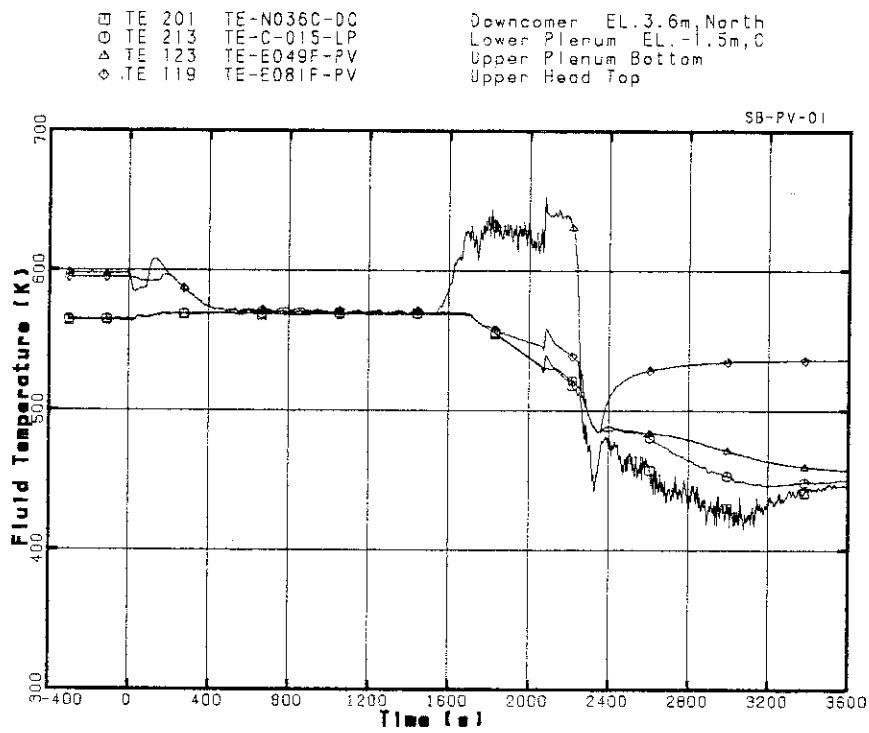

Fig. 5.8 Fluid temperatures in downcomer, lower plenum, upper plenum and upper head

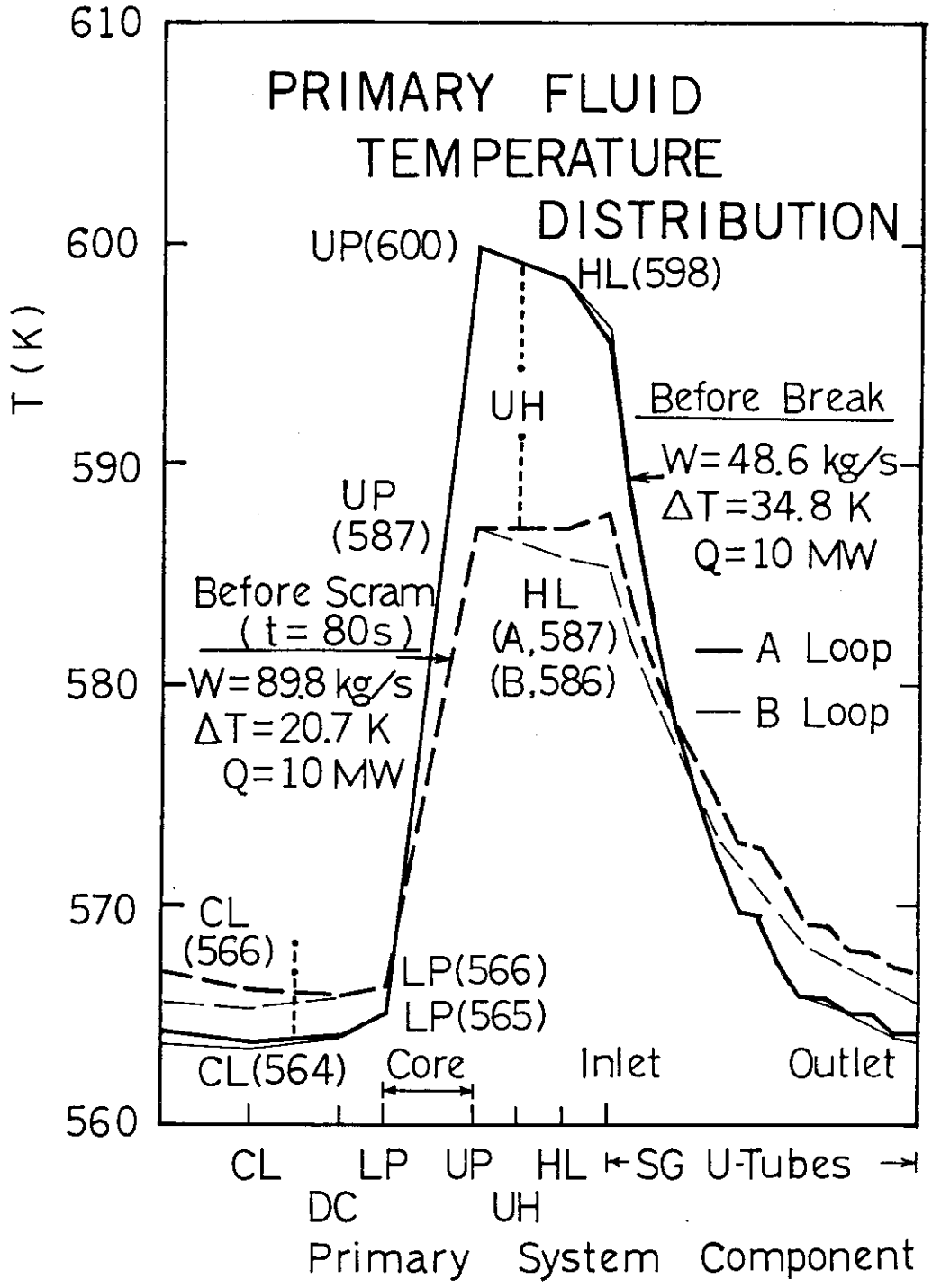

Fig. 5.9 Temperature distributions in primary system before break and before scram trip

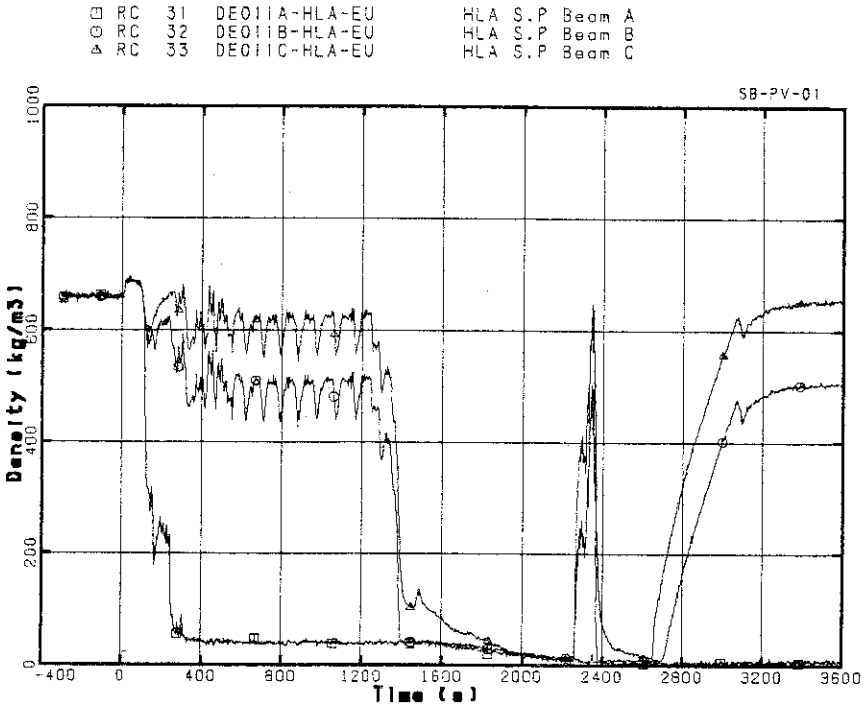

Fig. 5.10 Fluid densities at loop-A hot leg

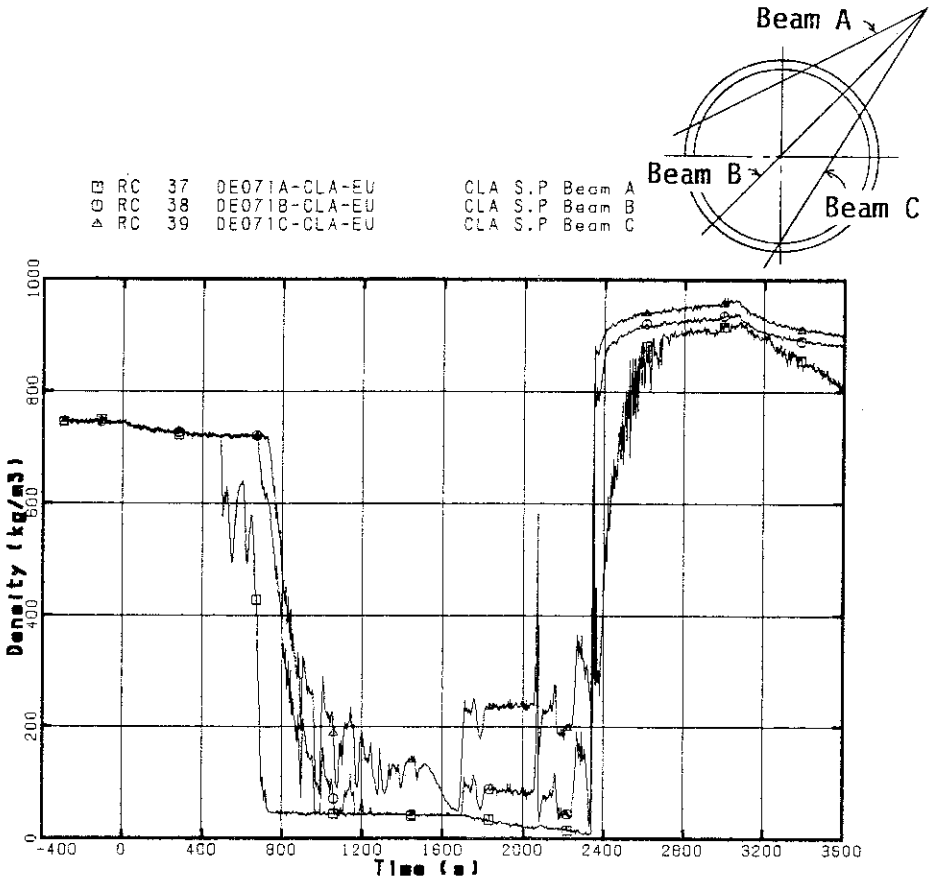

Fig. 5.11 Fluid densities at loop-A cold leg

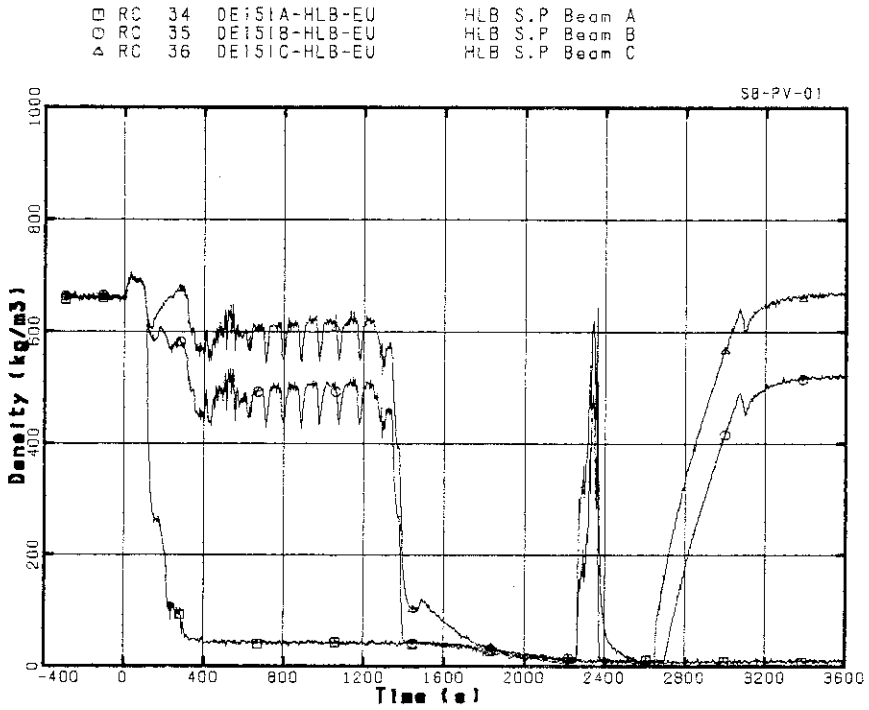

Fig. 5.12 Fluid densities at loop-B hot leg

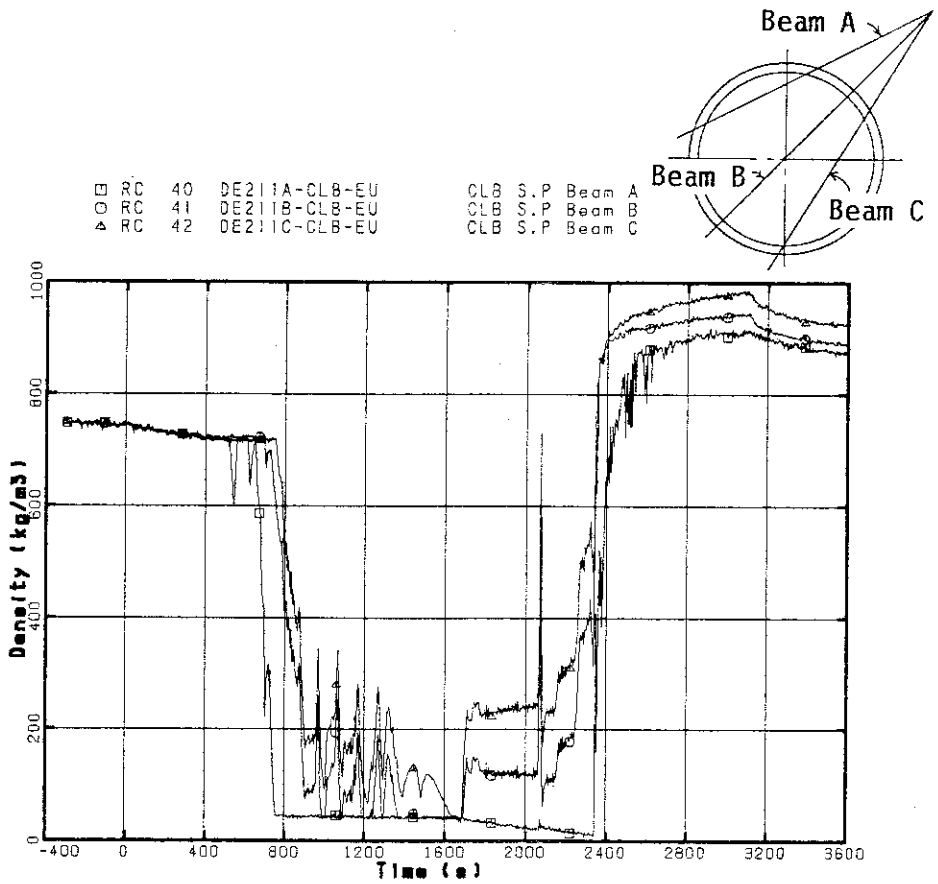

Fig. 5.13 Fluid densities at loop-B cold leg

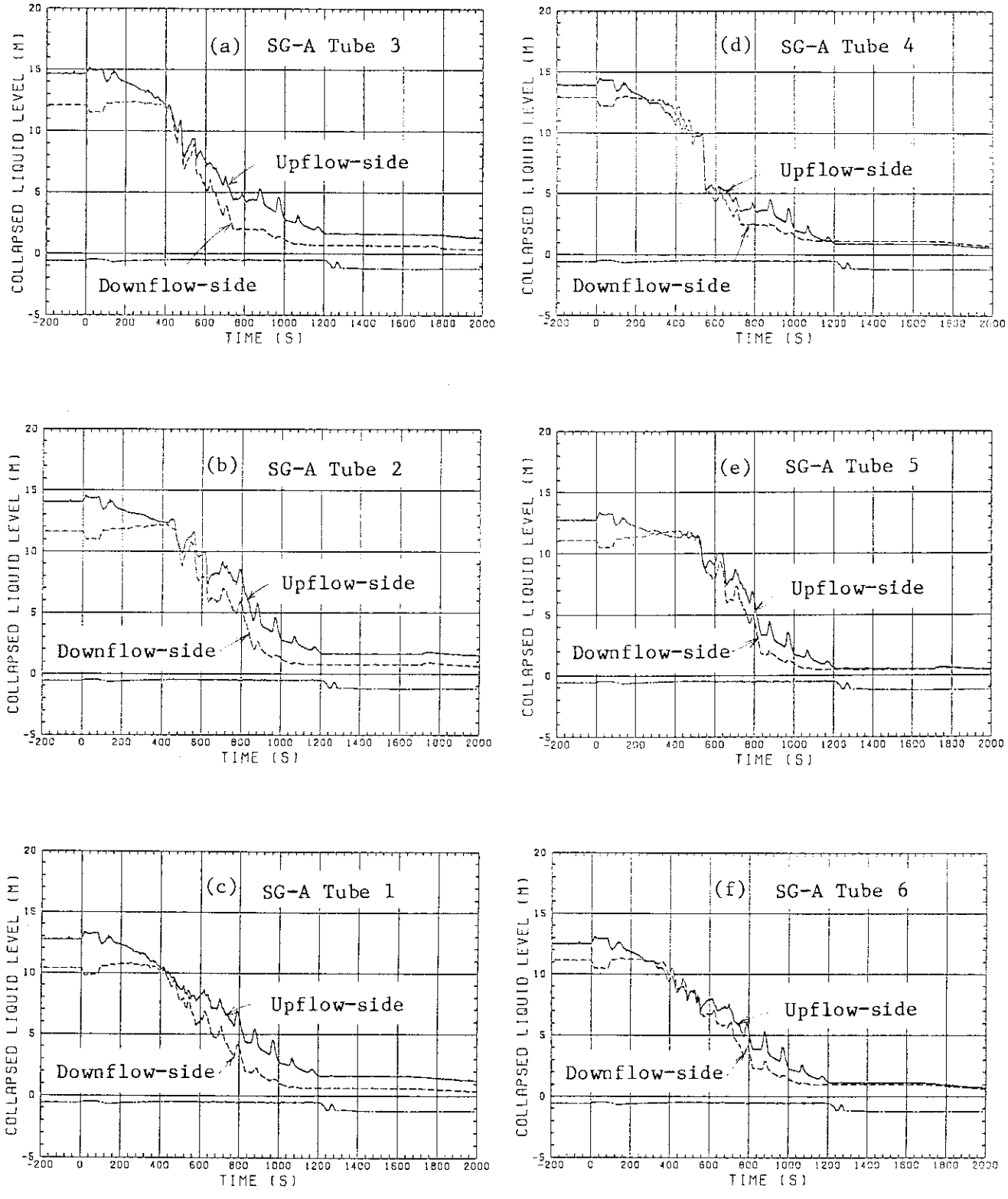

Fig. 5.14 Collapsed water levels in up- and down-flow sides of six instrumented U-tubes in SG-A (a through f)

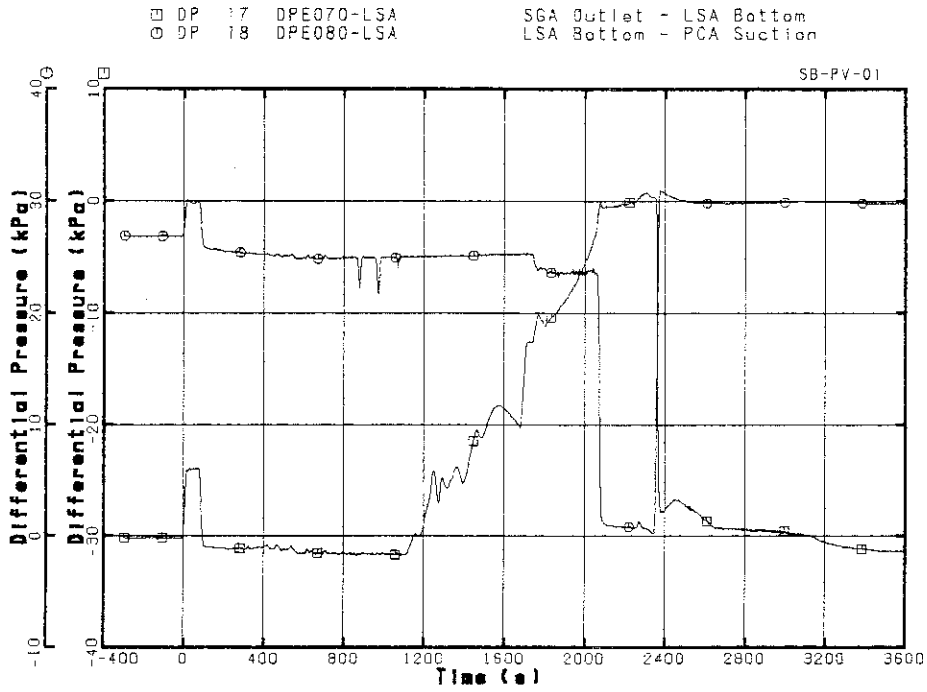

(a) Loop-seal A

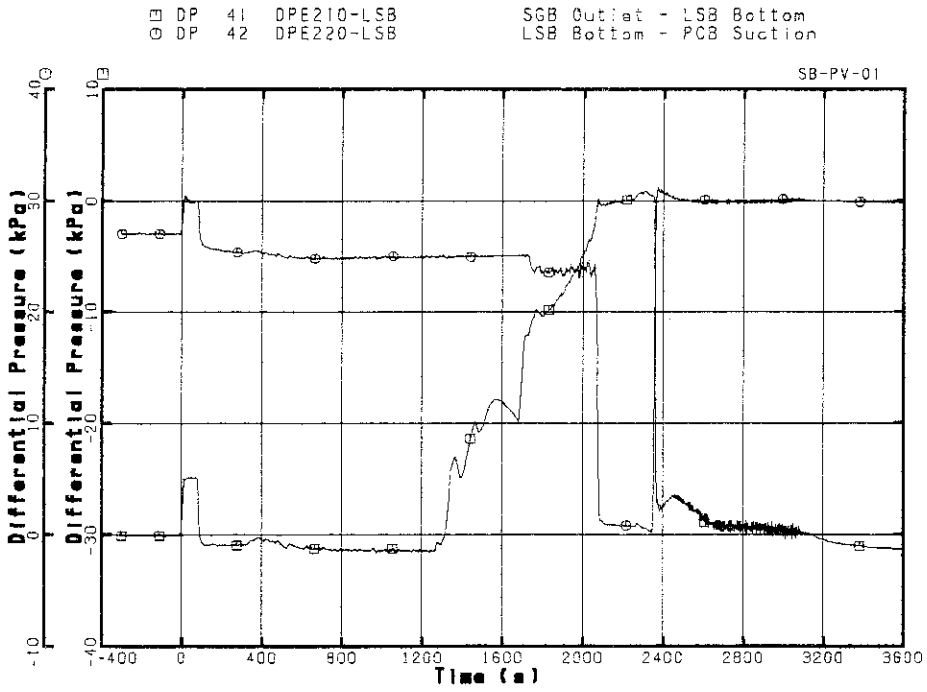

(b) Loop-seal B

Fig. 5.15 Differential pressures in loop-seal regions

Timing of Mass Distribution at Each Typical Phase

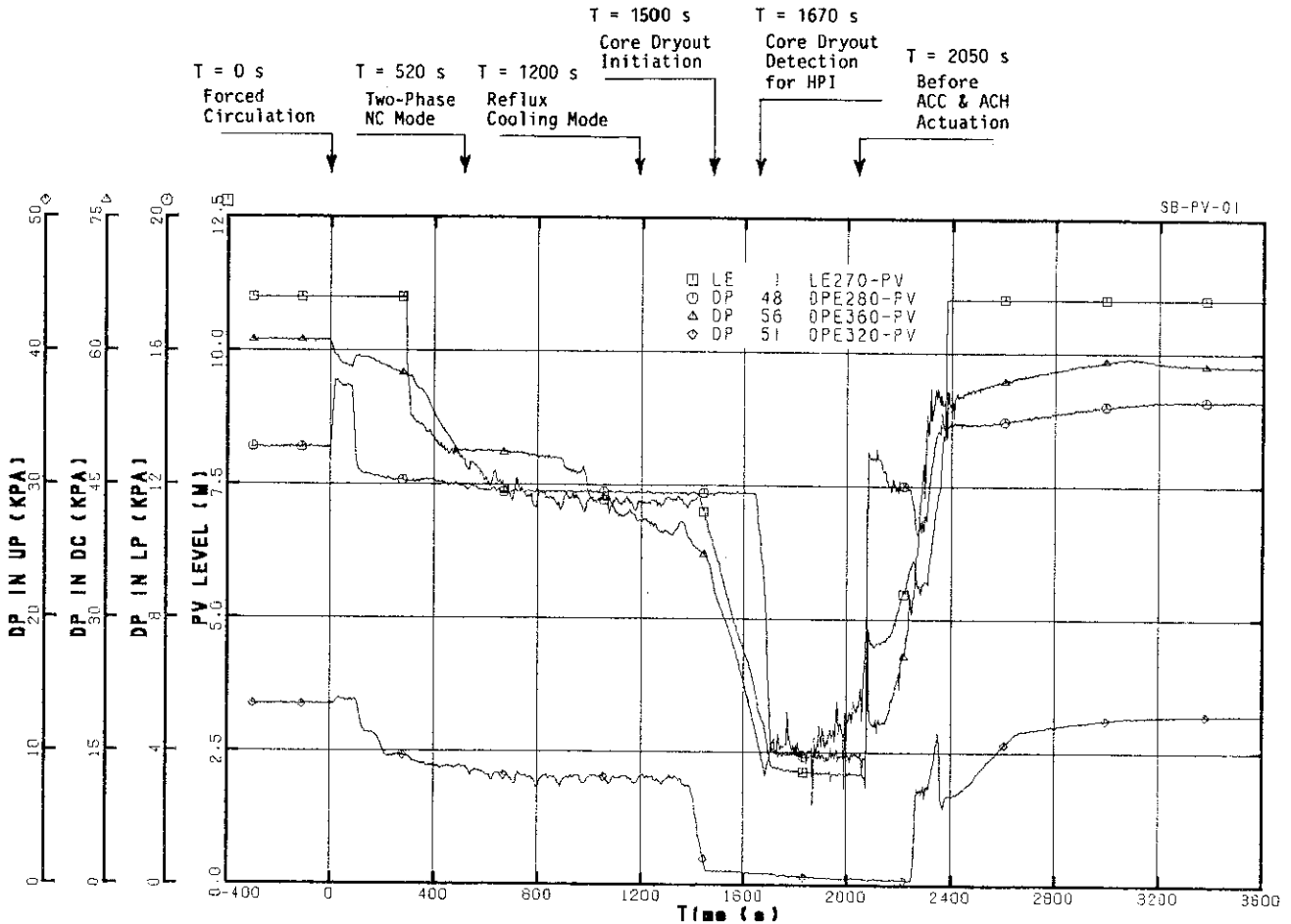

(a) Water level and differential pressures in PV with timings of transient primary mass distribution

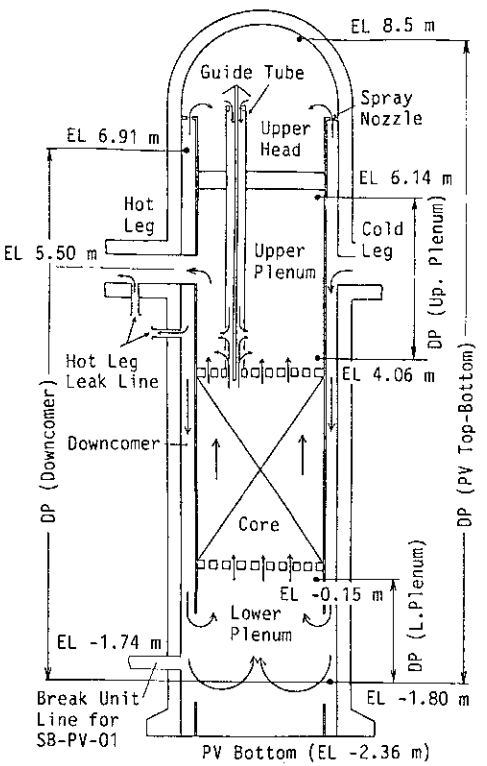

LSTF Pressure Vessel

(b) Measuring spans for PV differential pressures

Fig. 5.16 Responses of PV mass inventory in SB-PV-01 test

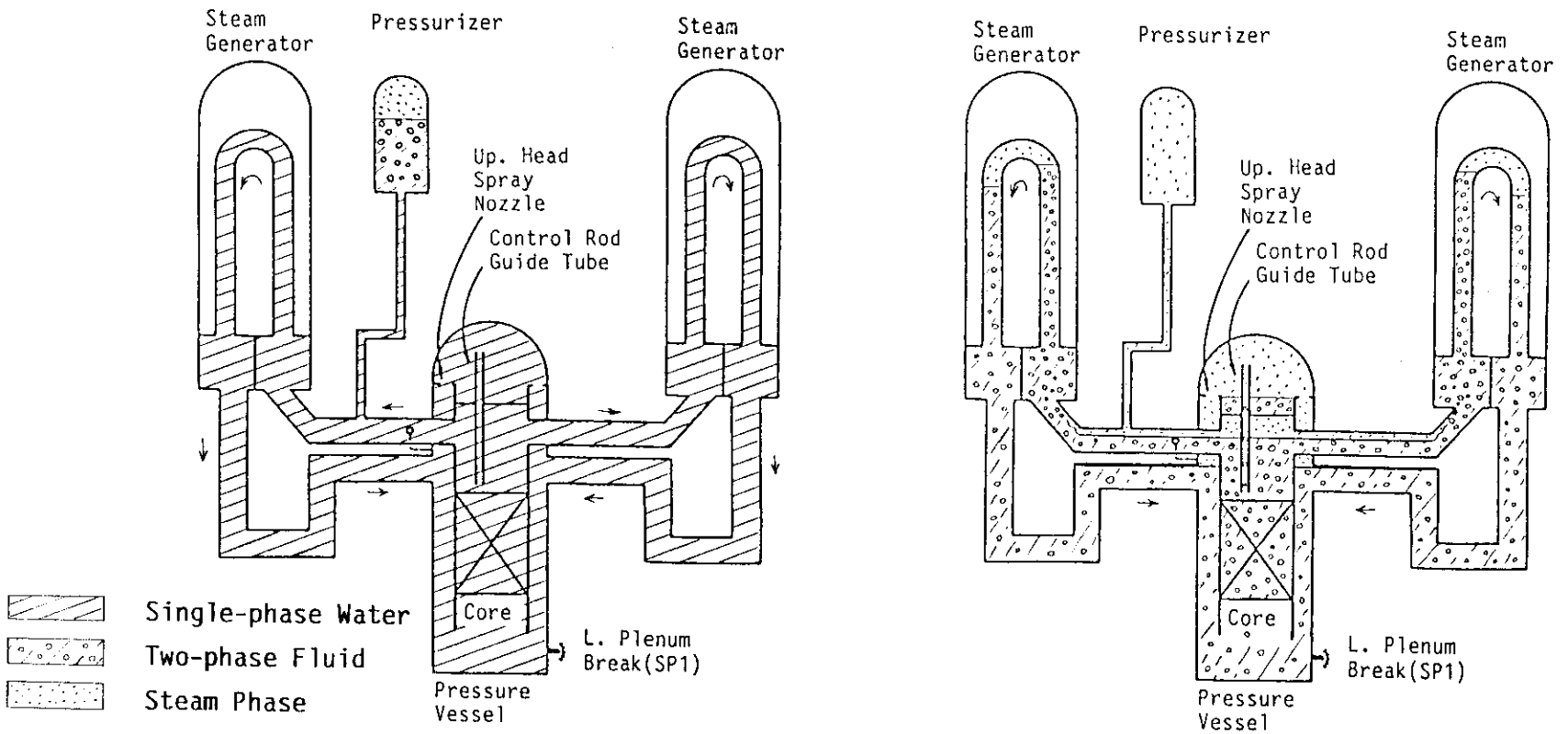

(a) Initiation of break (t = 0 s) ;
Forced circulation in subcooled primary system except for saturated pressurizer at 15.5 MPa

(b) Two-phase natural circulation (t = 520 s) ;
Phase separation at top of hot and cold legs at 8.2 MPa

Fig. 5.17 Transient primary mass distribution for SB-PV-01 test

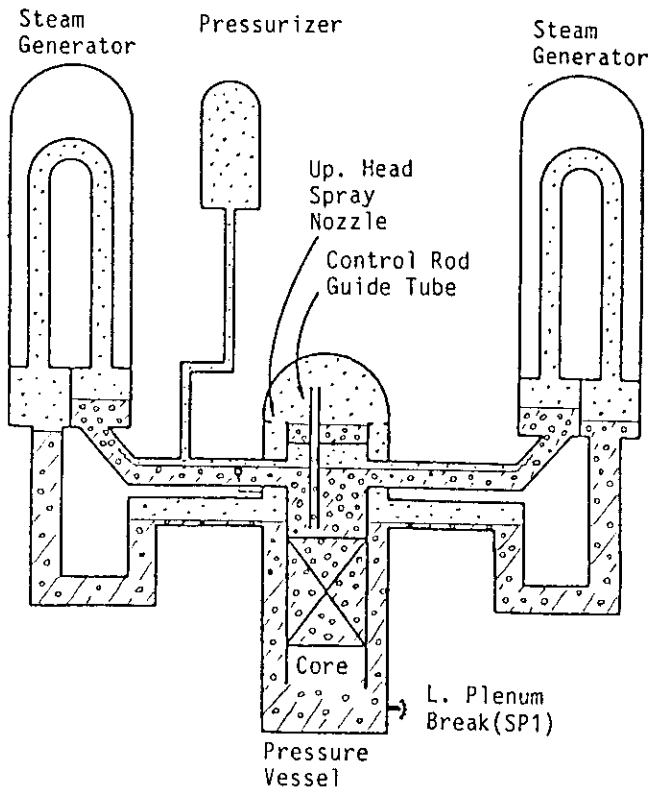

(c) Reflux cooling mode at SGs (t = 1200 s) ;
Almost emptied U-tubes and cold legs at 8.1 MPa

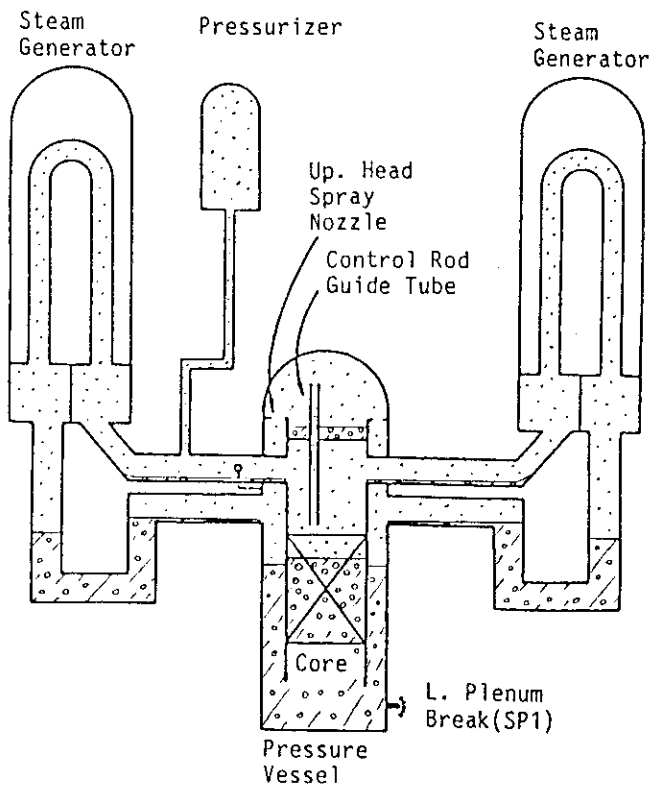

(d) Initiation of core dryout (t = 1500 s) ;
Core mixture level decrease and small amount of remaining water in hot and cold legs at 8.0 MPs

Fig. 5.17 Transient primary mass distribution for SB-PV-01 test (Cont'd)

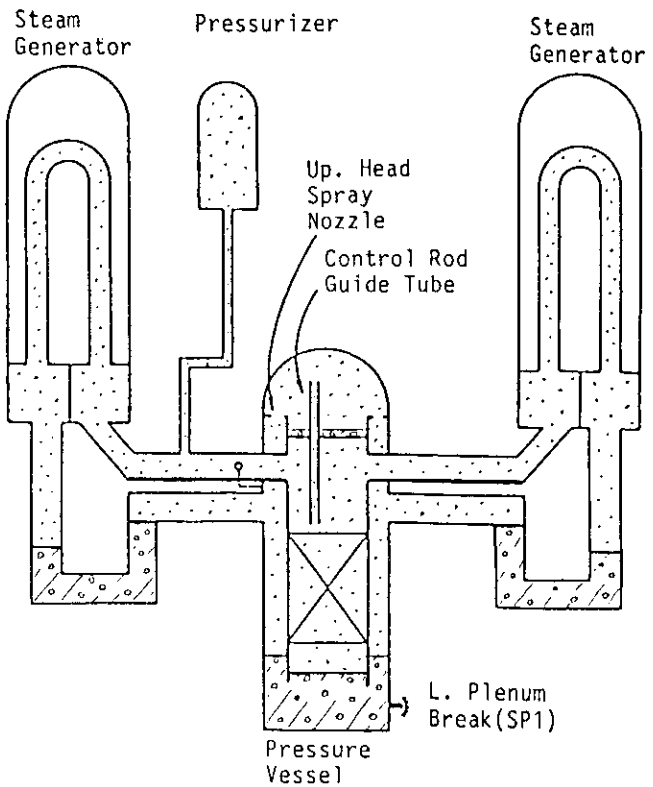

(e) Detection of core dryout (t = 1670 s) ;
Superheated steam at hot legs, whole core dryout and no heat exchange at SGs at 7.9 MPa

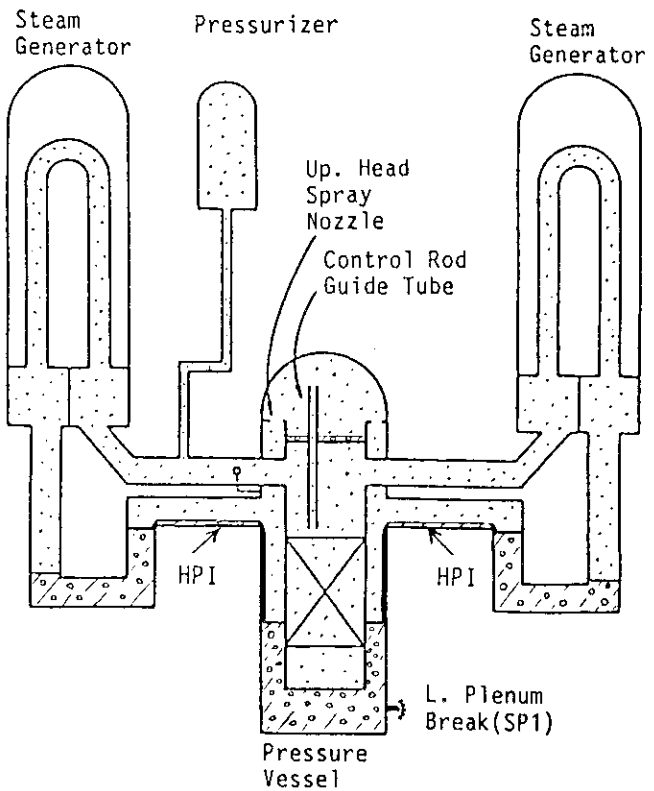

(f) Before ACC and ACH actuation (t = 2050 s) ;
Lowest primary mass and downcomer mass recovery under HPI injection into cold legs at 4.6 MPa

Fig. 5.17 Transient primary mass distribution for SB-PV-01 test (Cont'd)

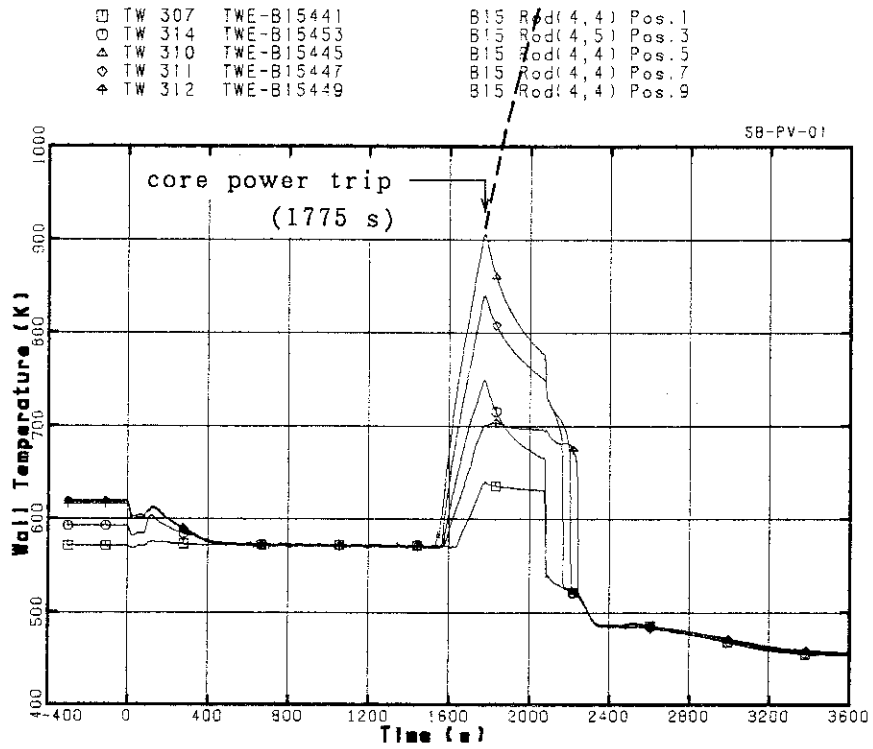

Fig. 5.18 Representative heater rod surface temperatures in high-power bundle (B-15)

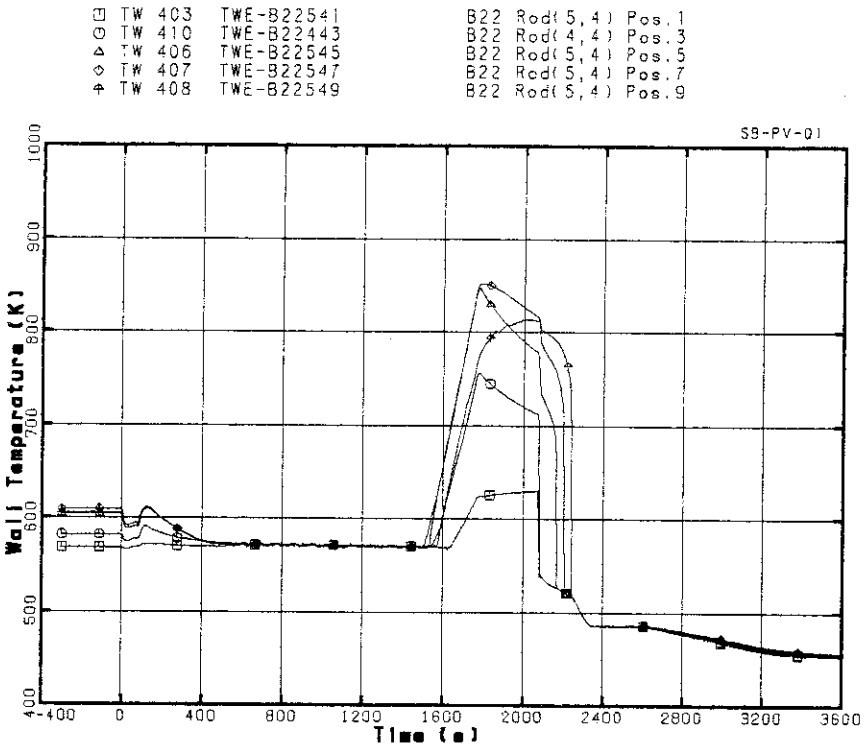

Fig. 5.19 Representative heater rod surface temperatures in middle-power bundle (B-22)

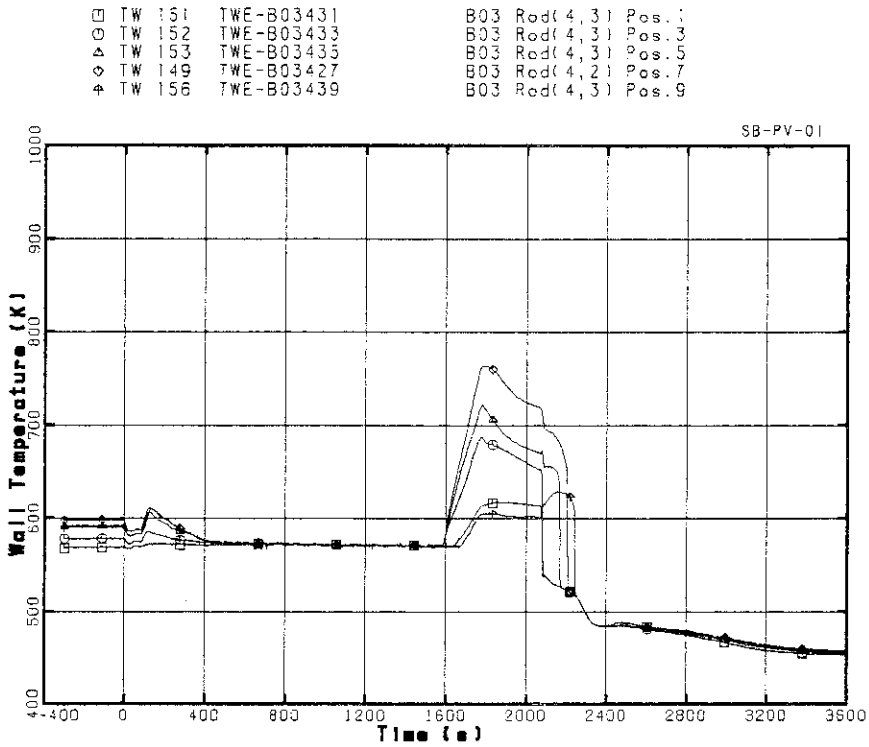

Fig. 5.20 Representative heater rod surface temperatures in low-power bundle (B-03)

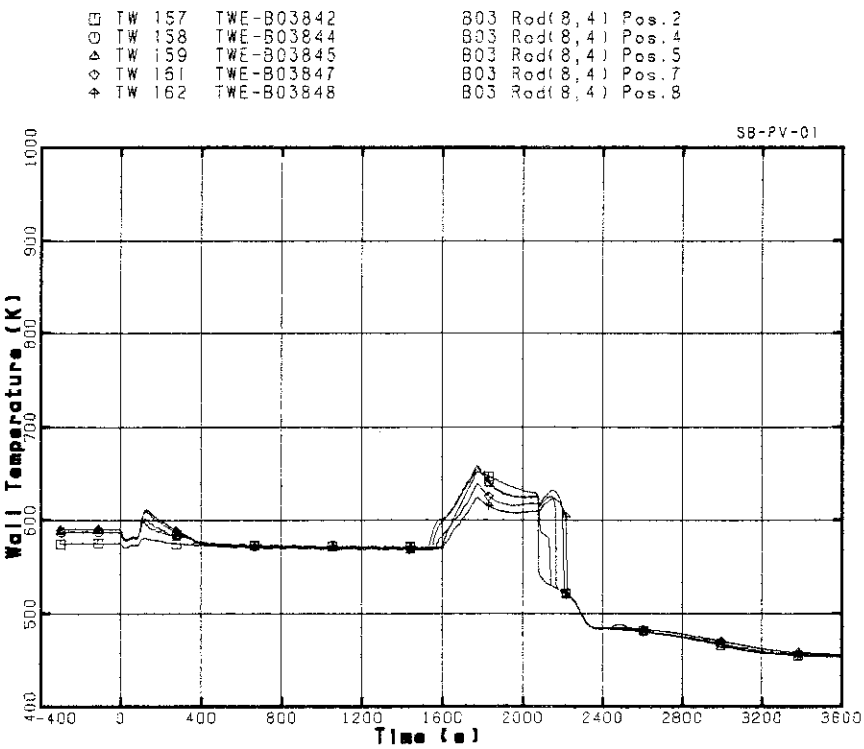

Fig. 5.21 Representative heater rod surface temperatures at outer region of B-03 bundle

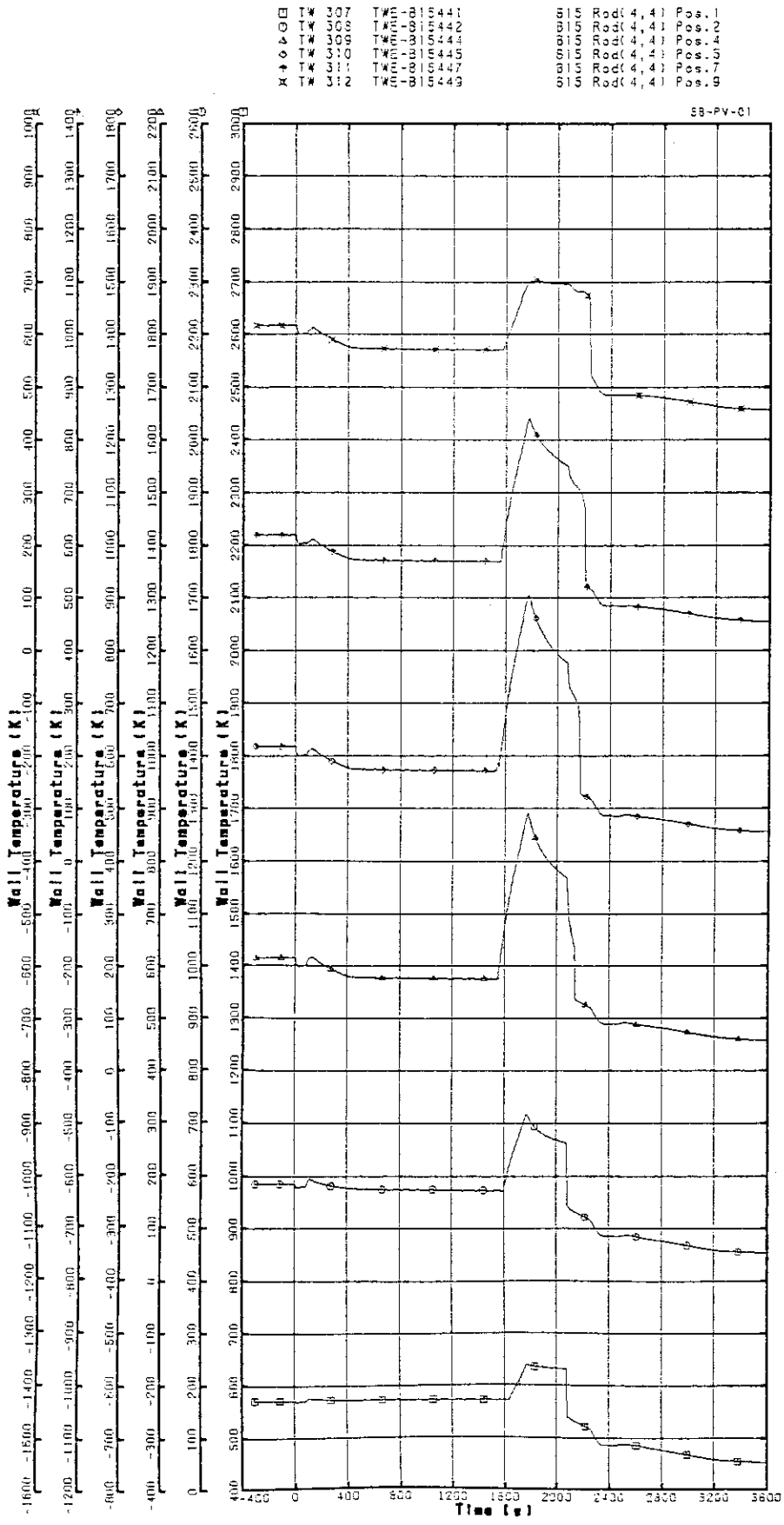

Fig. 5.22 Heater rod surface temperatures at nine axial elevetions

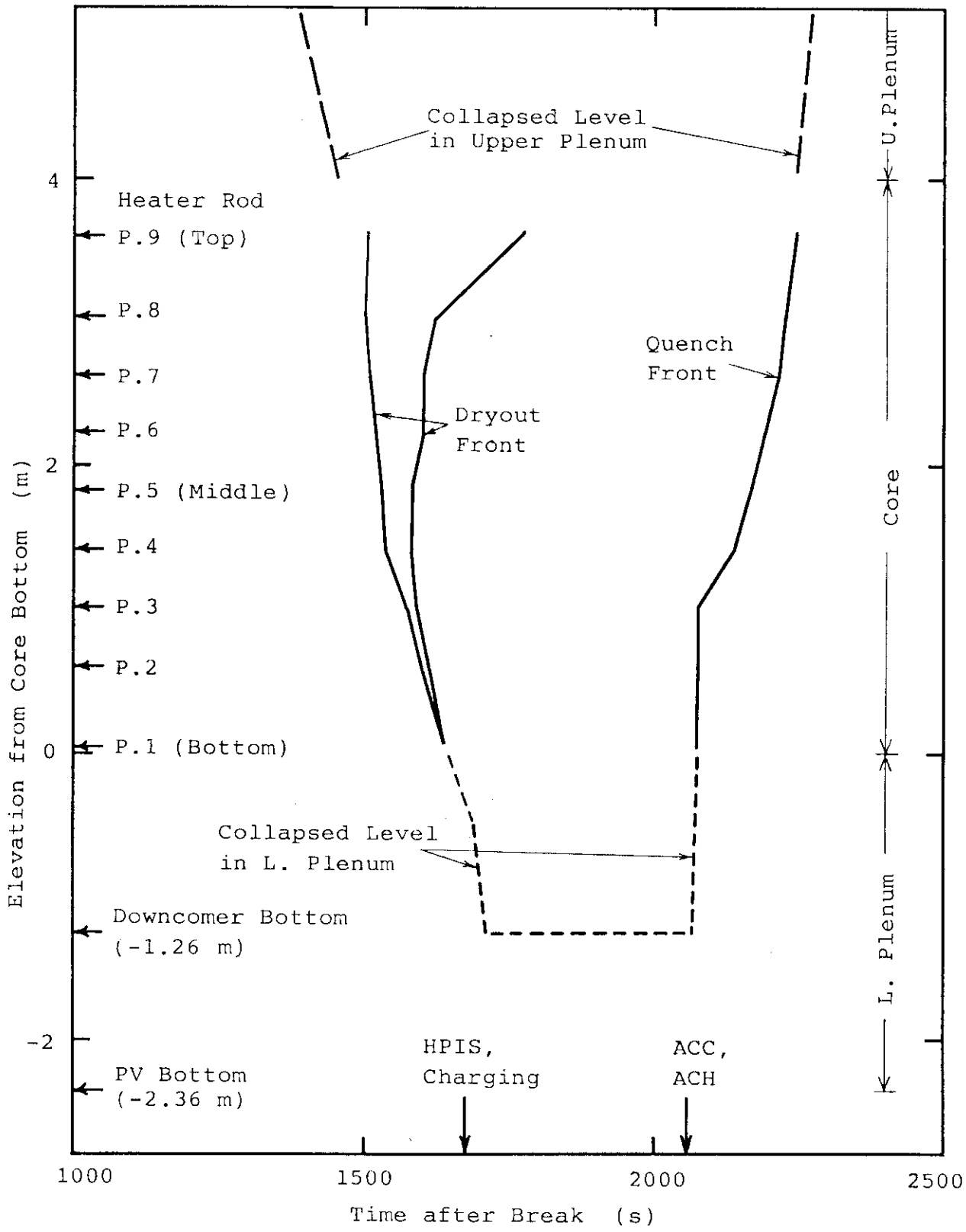

Fig. 5.23 Dryout and quench timings of heater rods and collapsed levels in upper and lower plena

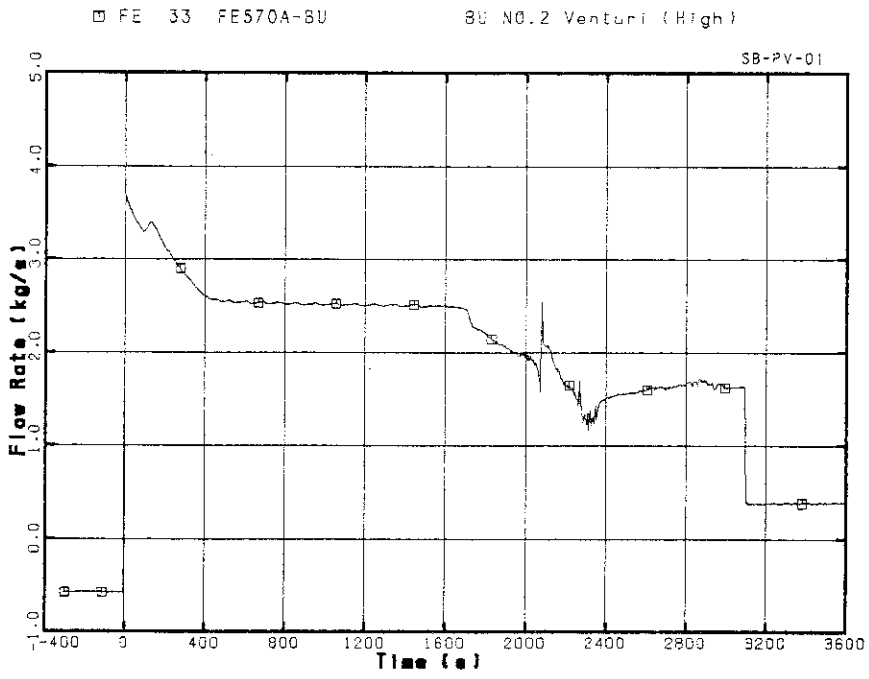

Fig. 5.24 Break flow rate at No.2 Venturi-meter

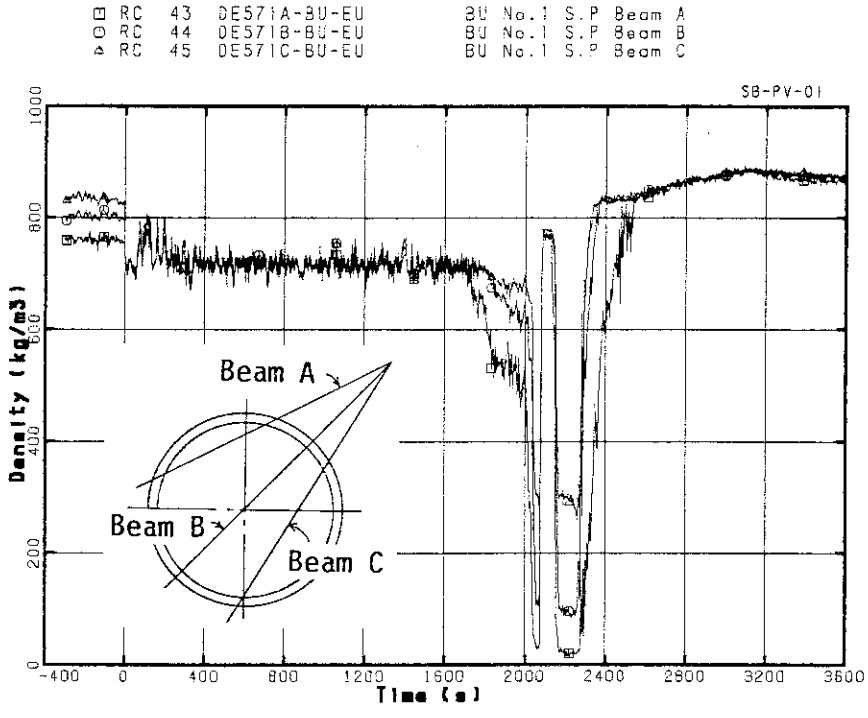

Fig. 5.25 Fluid densities at break unit

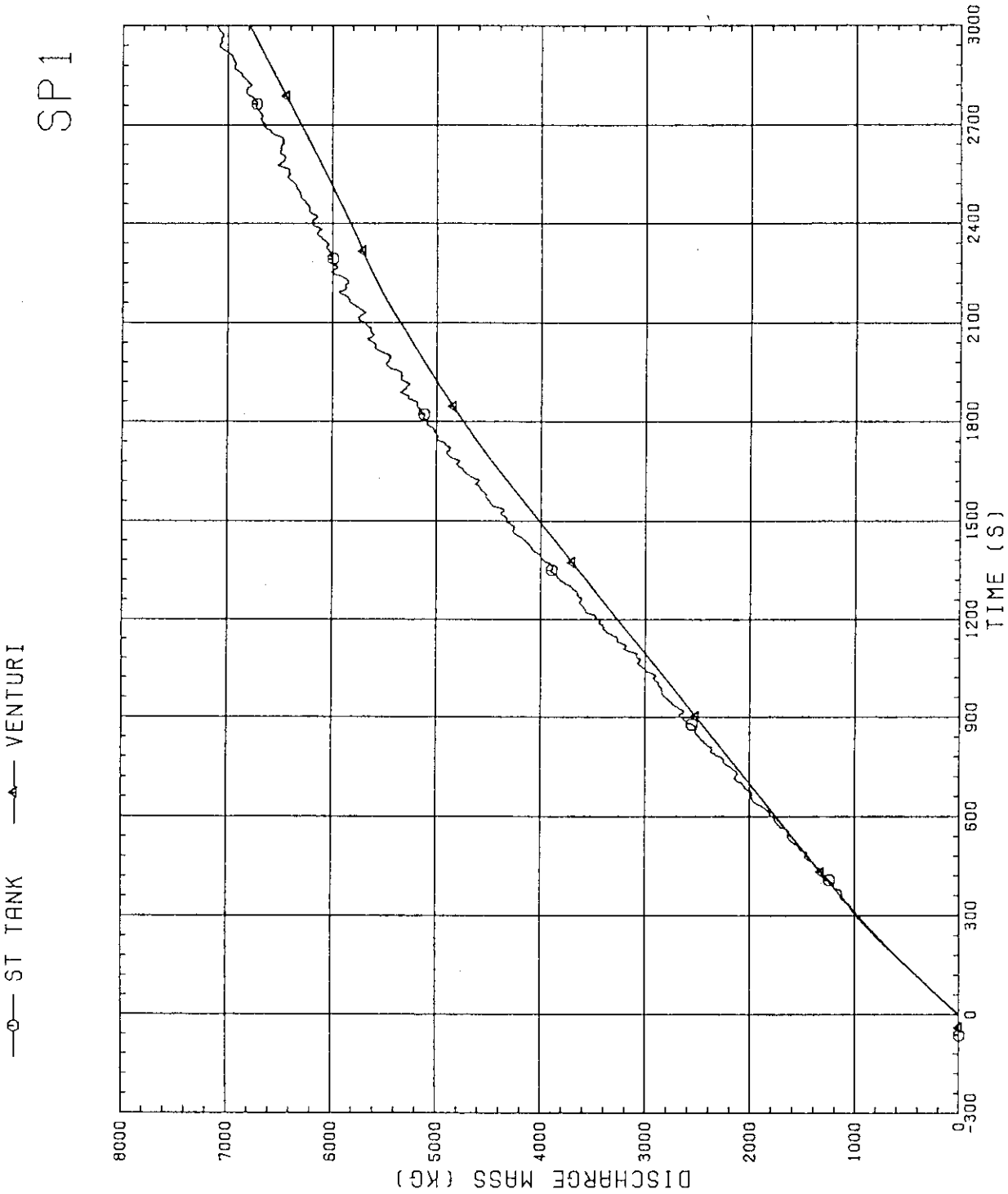

Fig. 5.26 Integrated discharged water mass at catch tank

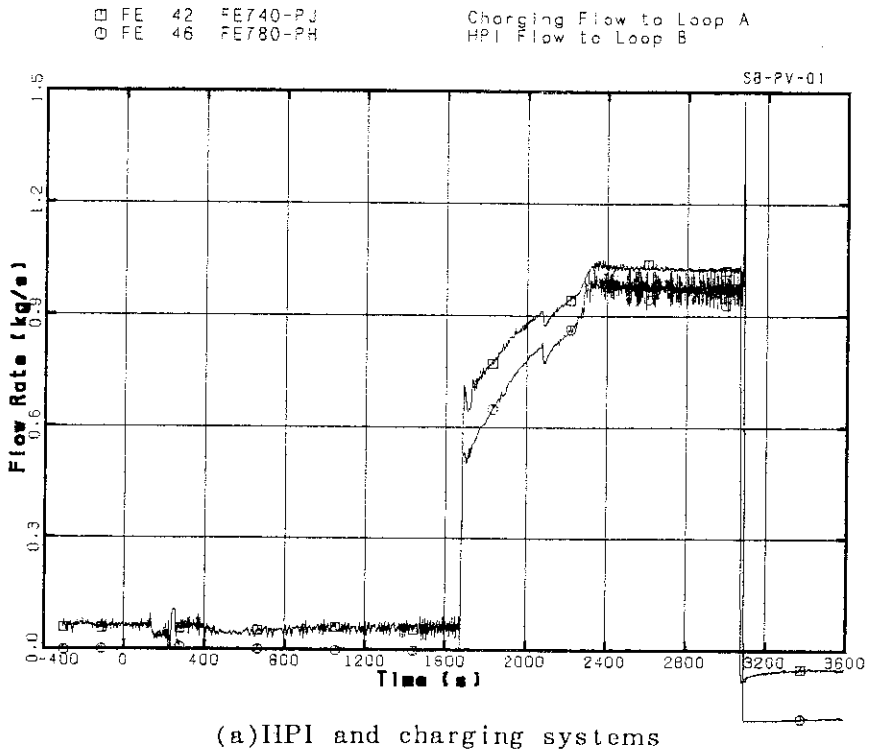

(a)HPI and charging systems

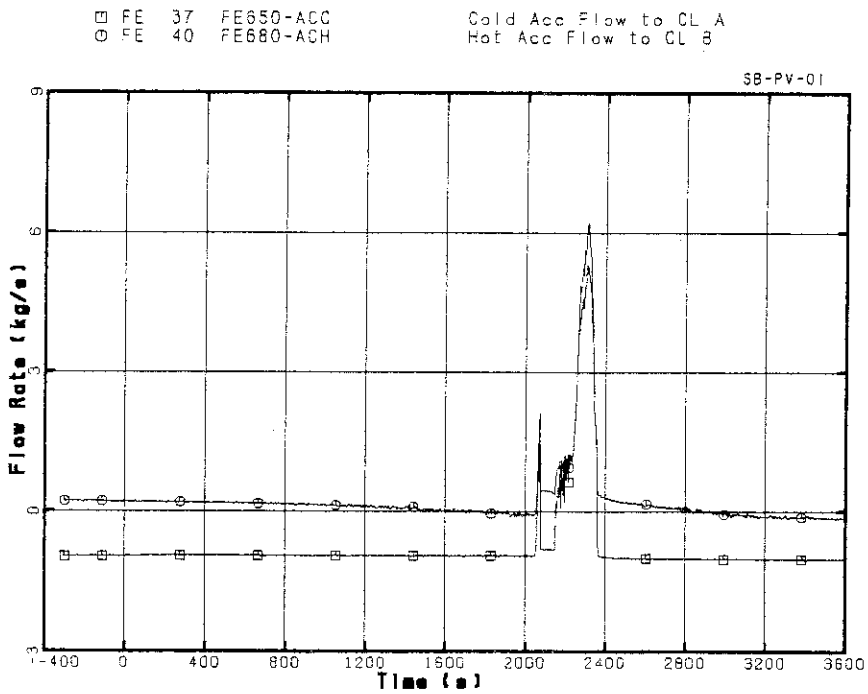

(b)Accumulators of ACC and ACH

Fig. 5.27 ECC water injection flow rates

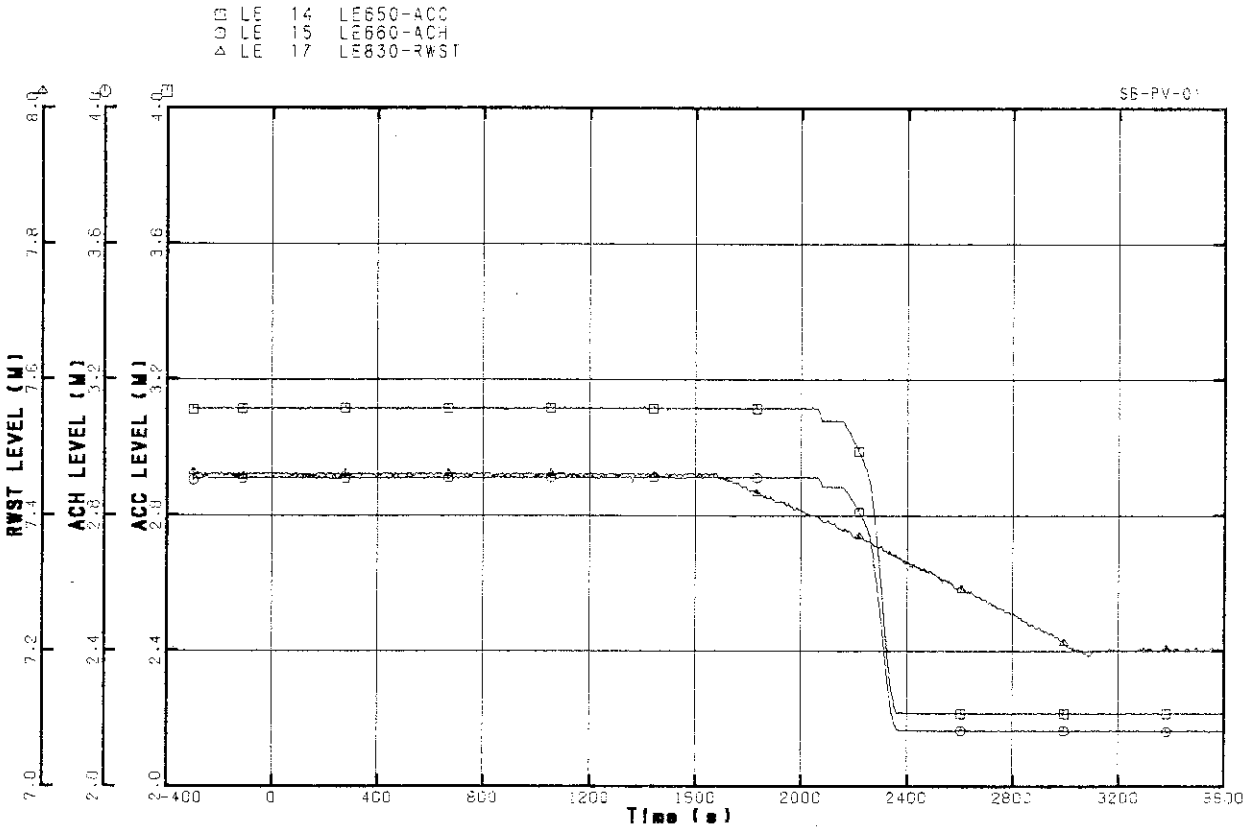

Fig. 5.28 Water levels for ACC, ACH and RWST tanks

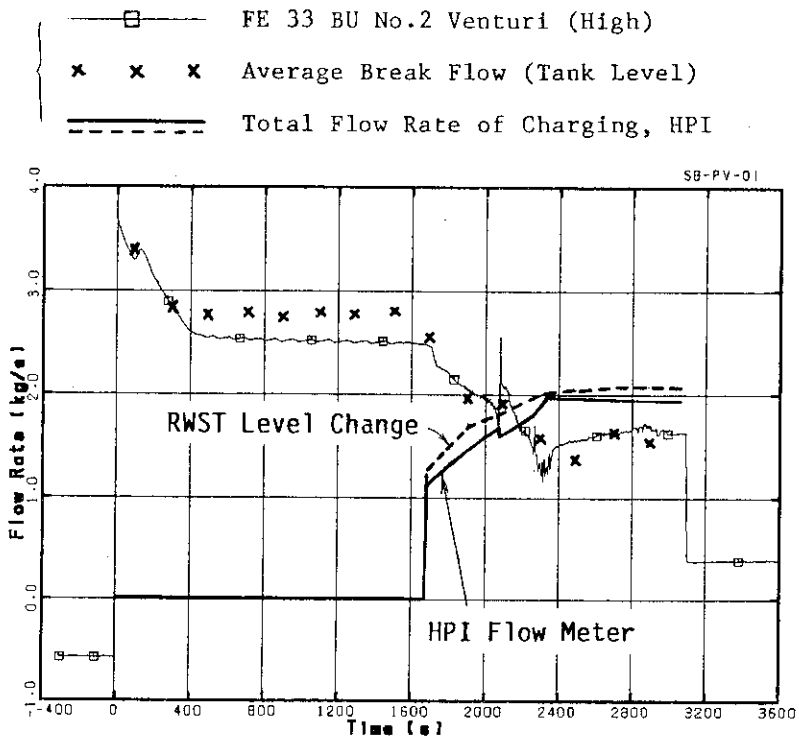

(a) Time responses of flow rates

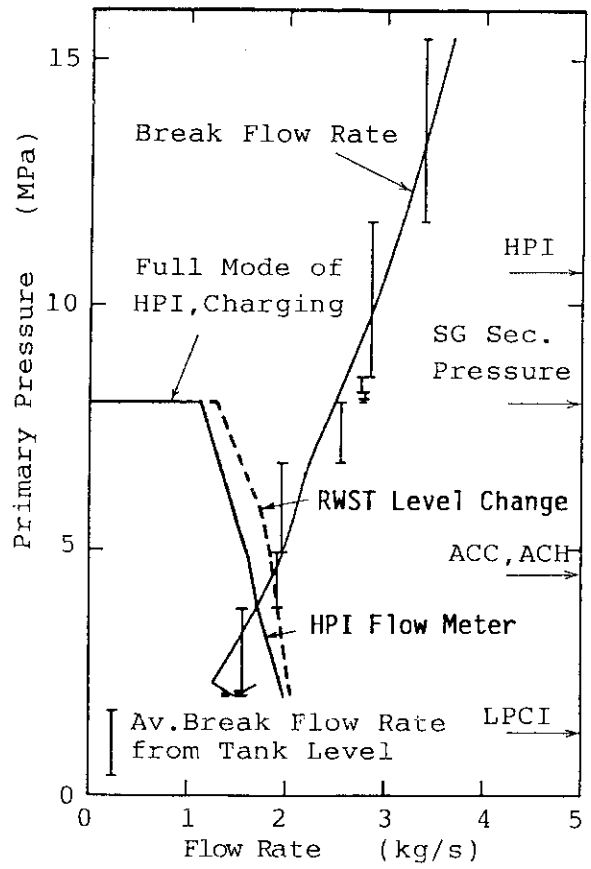

(b) Flow rates related to primary pressure

Fig. 5.29 Total injection flow rate compared with break flow rate

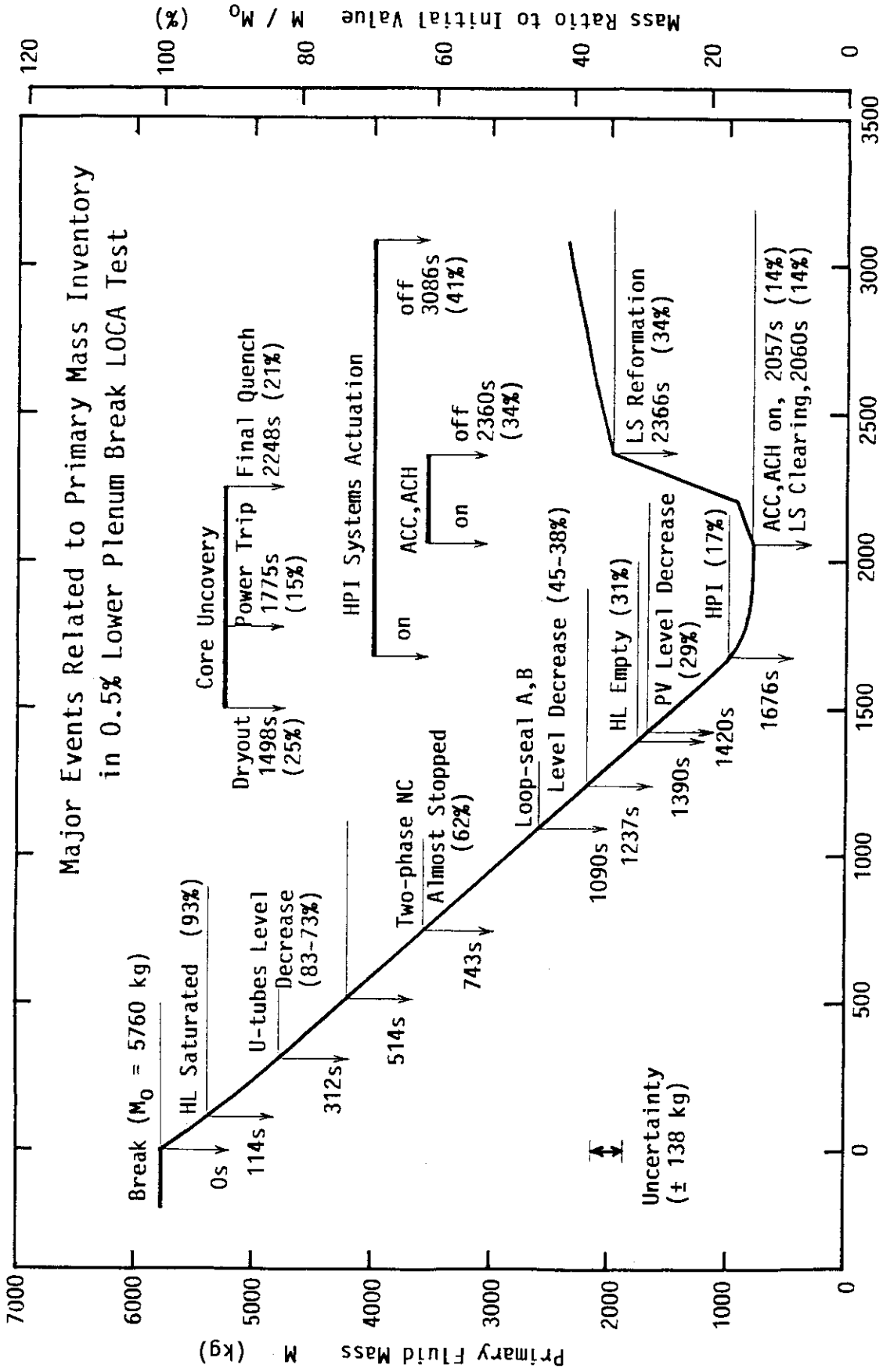

Fig. 5.30 Major events related to primary mass inventory in SB-PV-01 test

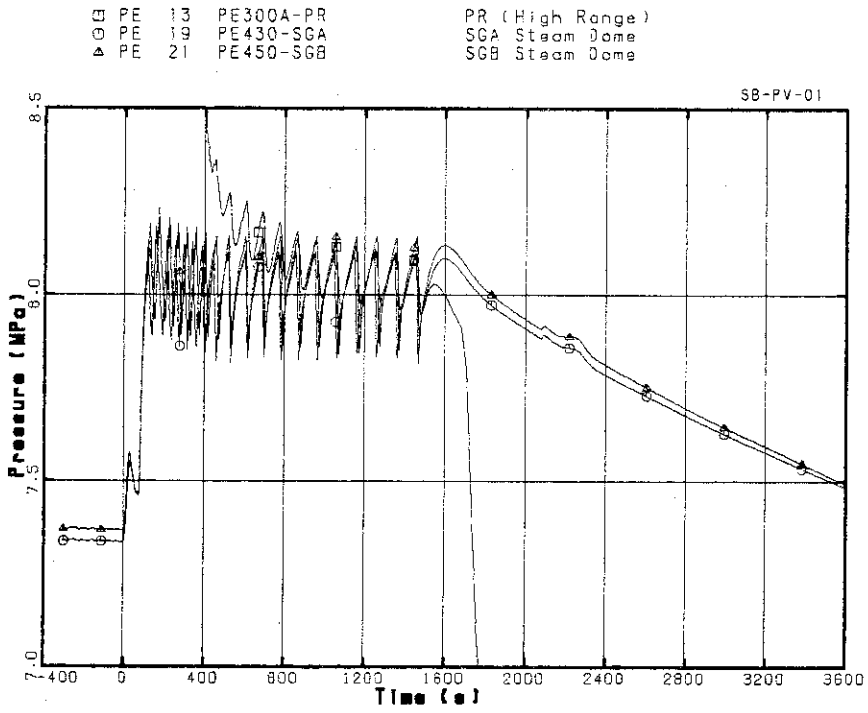

Fig. 5.31 Representative pressure at steam dome in SG-A and SG-B

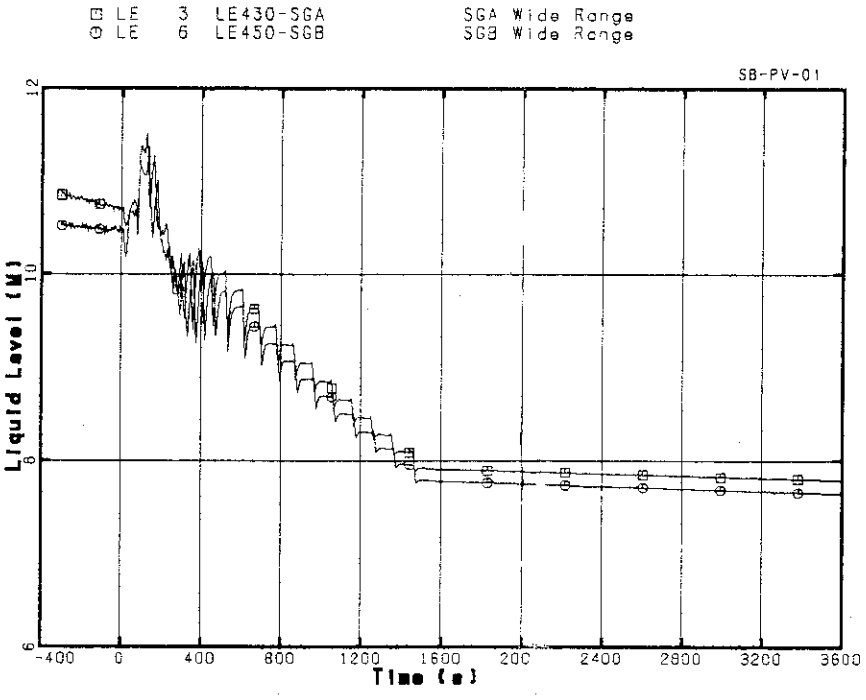

Fig. 5.32 Wide range water levels in SG-A and SG-B

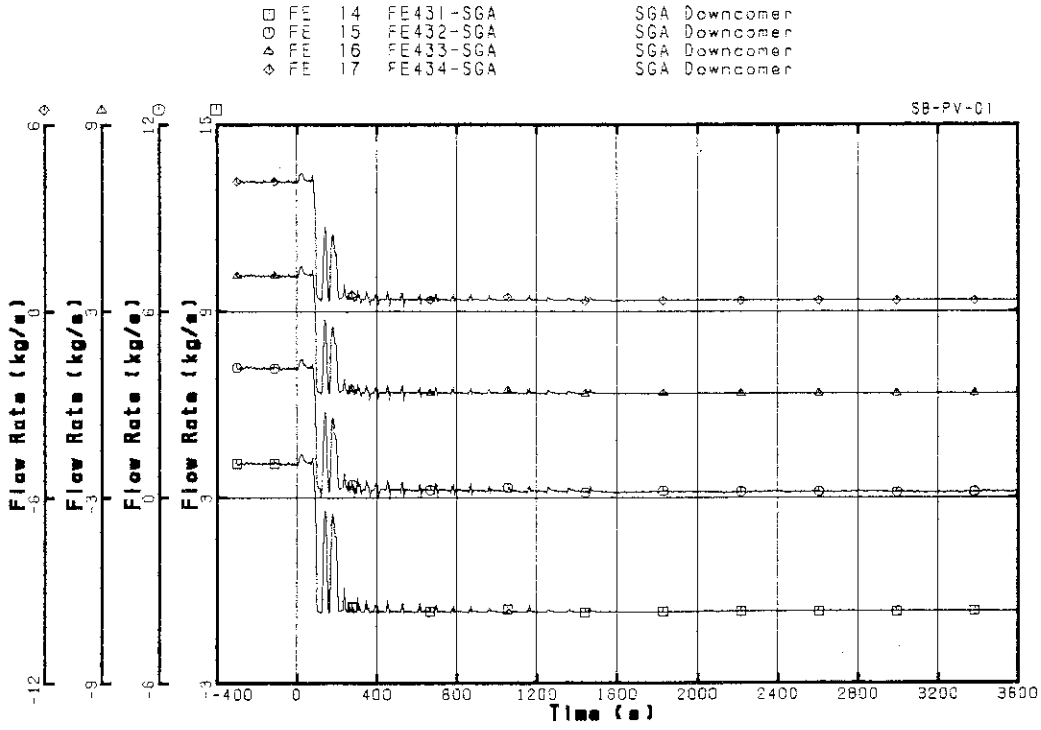

(a) SG-A

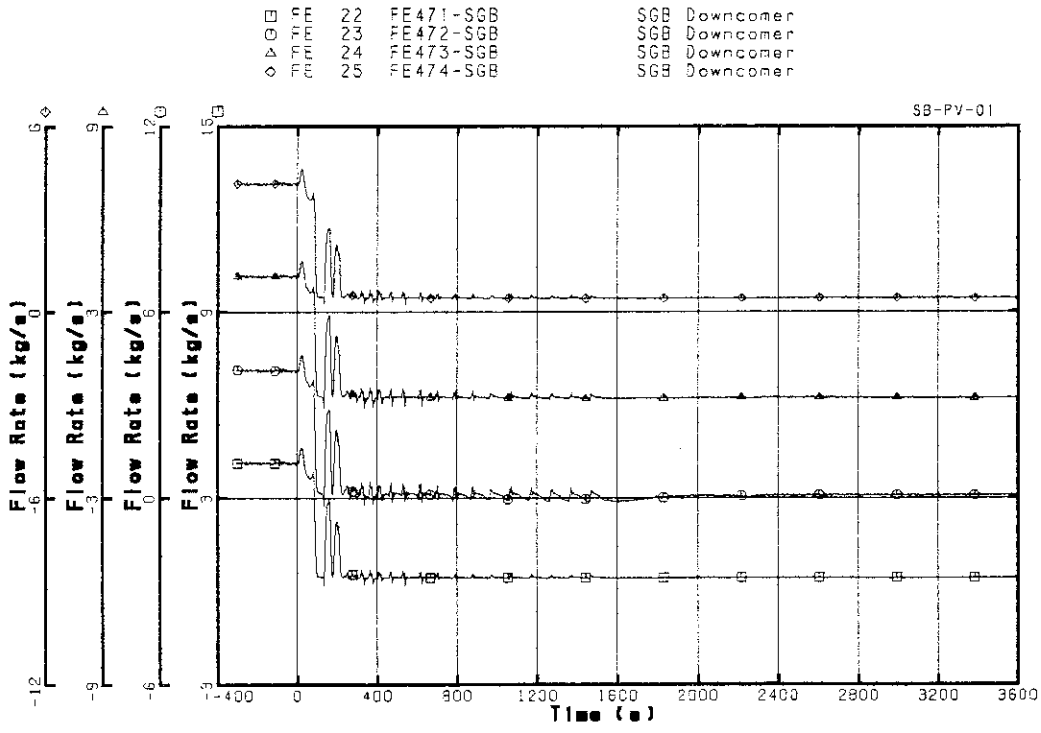

(b) SG-B

Fig. 5.33 Water flow rates in four SG downcomer pipngs

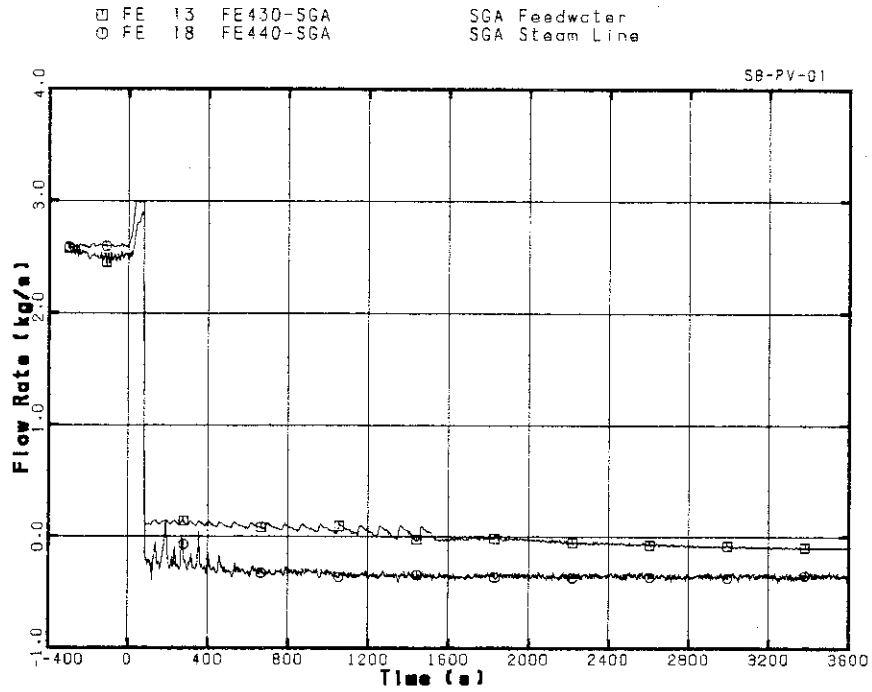

(a) SG-A

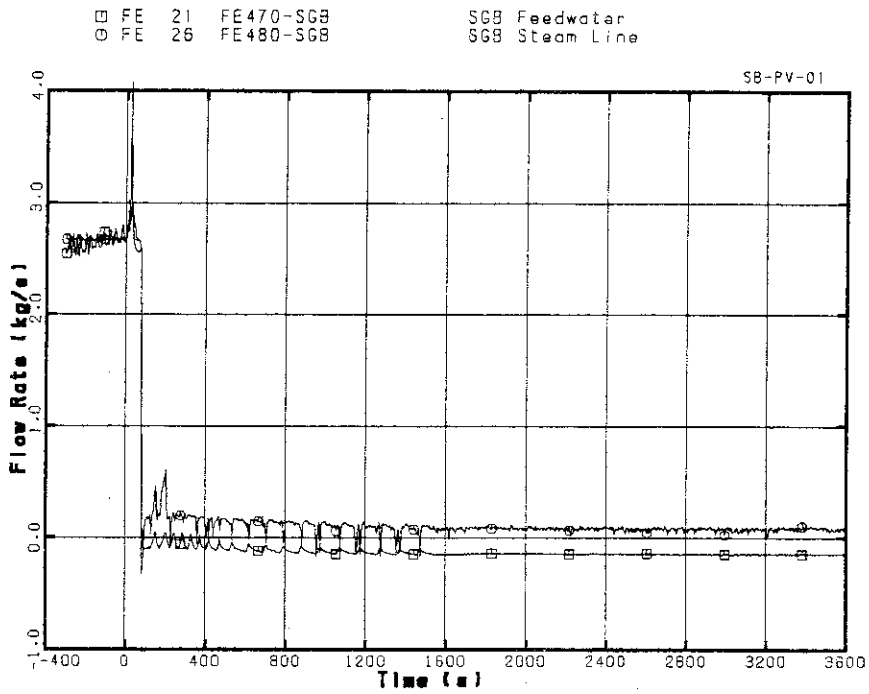

(b) SG-B

Fig. 5.34 Steam and feedwater flow rates

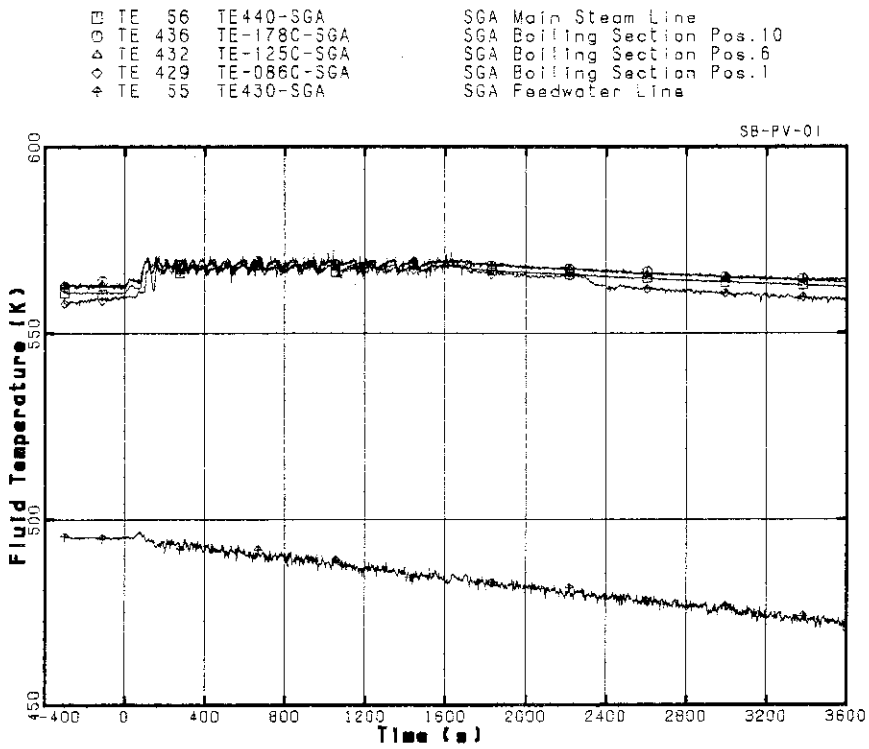

Fig. 5.35 Fluid temperatures in steam dome, feedwater and boiler section of SG-A

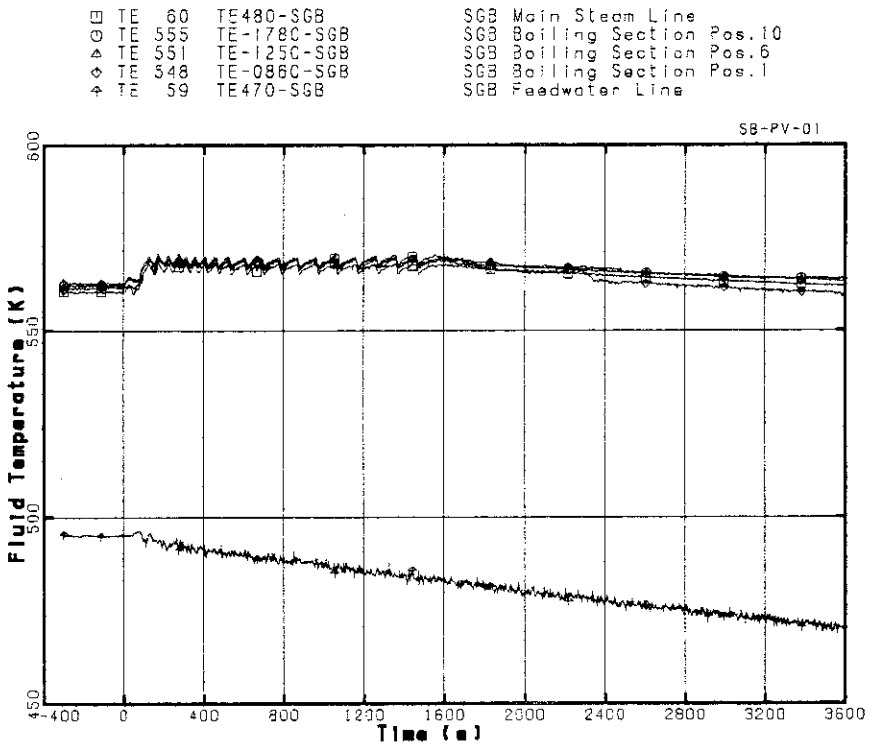

Fig. 5.36 Fluid temperatures in steam dome, feedwater and boiler section of SG-B

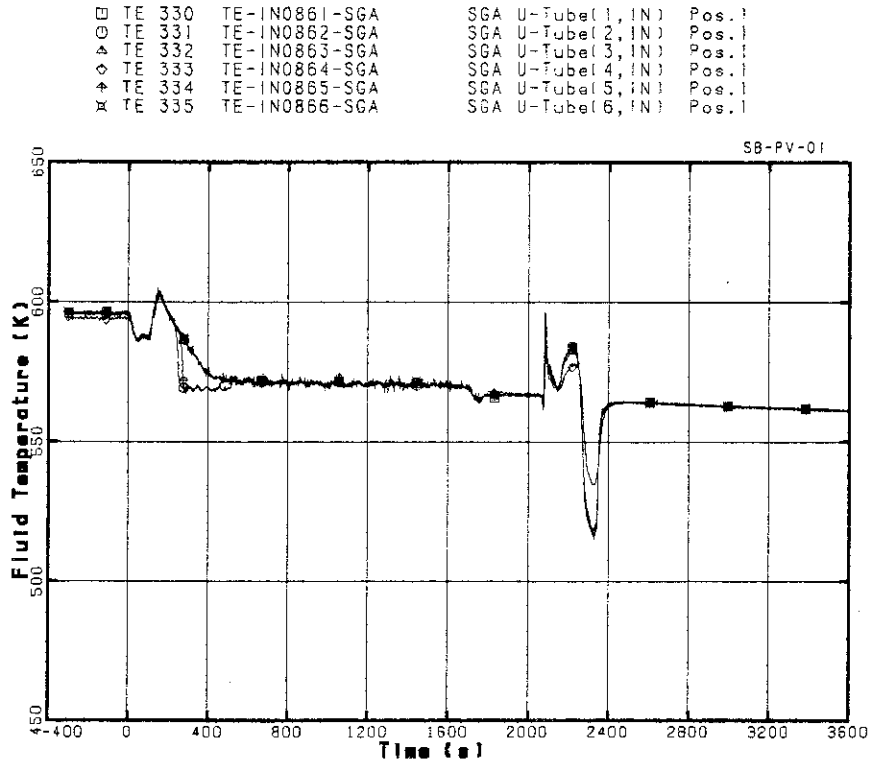

(a) Up-flow side

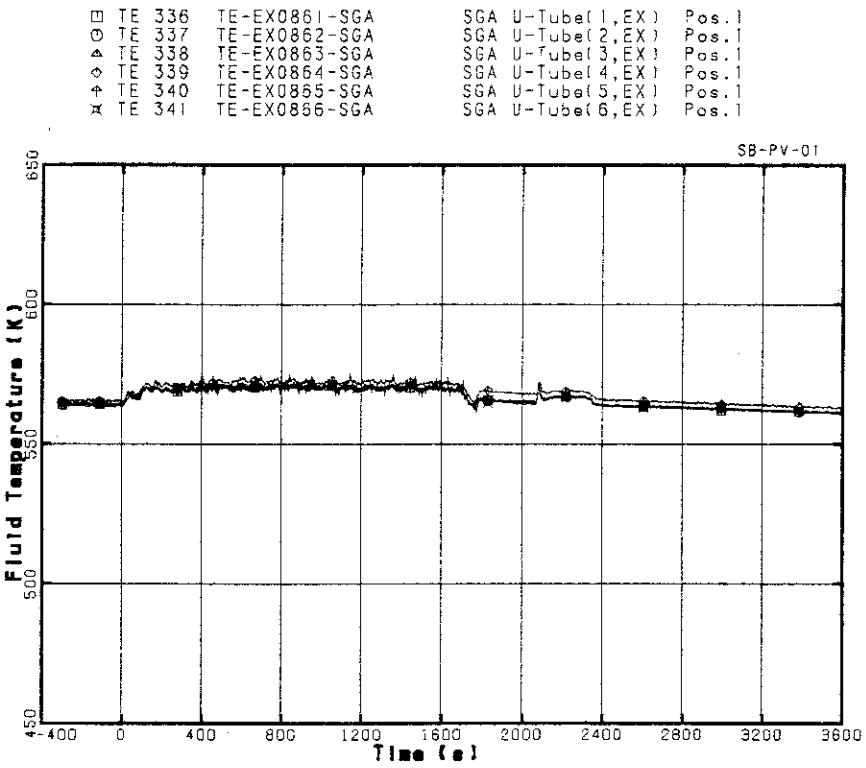

(b) Down-flow side

Fig. 5.37 Distribution of primary fluid temperatures at lowest level of six SG-A U-tubes (Position 1)

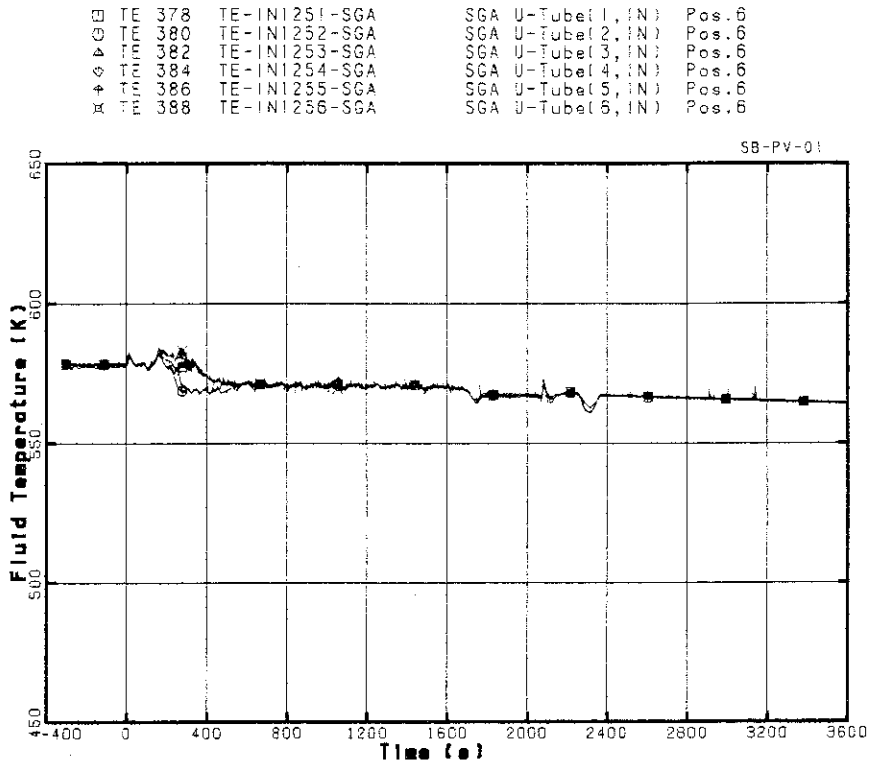

(a) Up-flow side

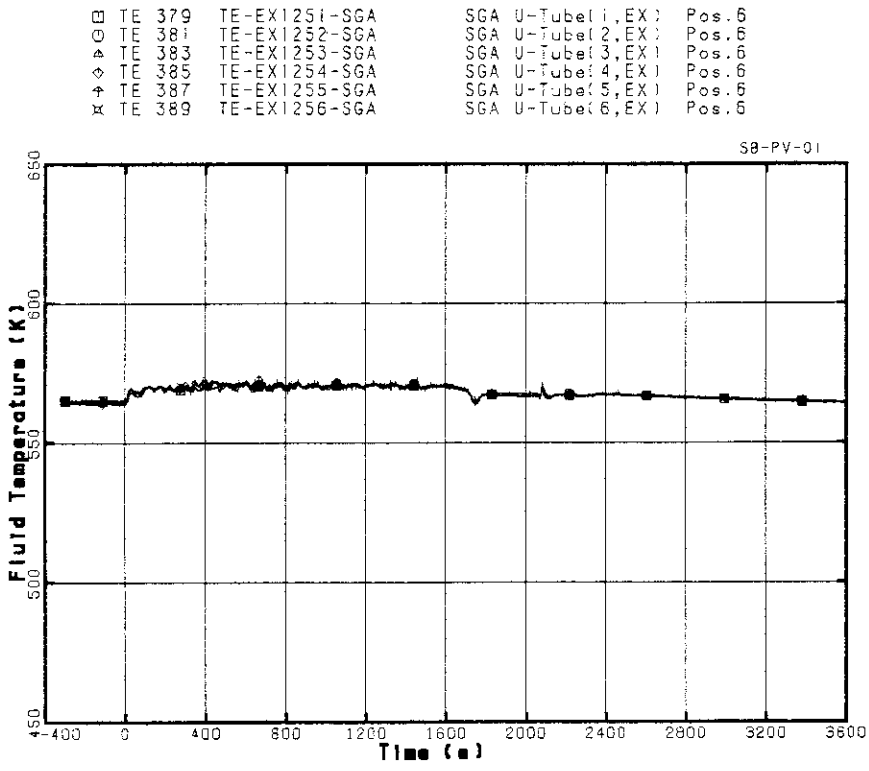

(b) Down-flow side

Fig. 5.38 Distribution of primary fluid temperatures at middle level of six SG-A U-tubes (Position 6)

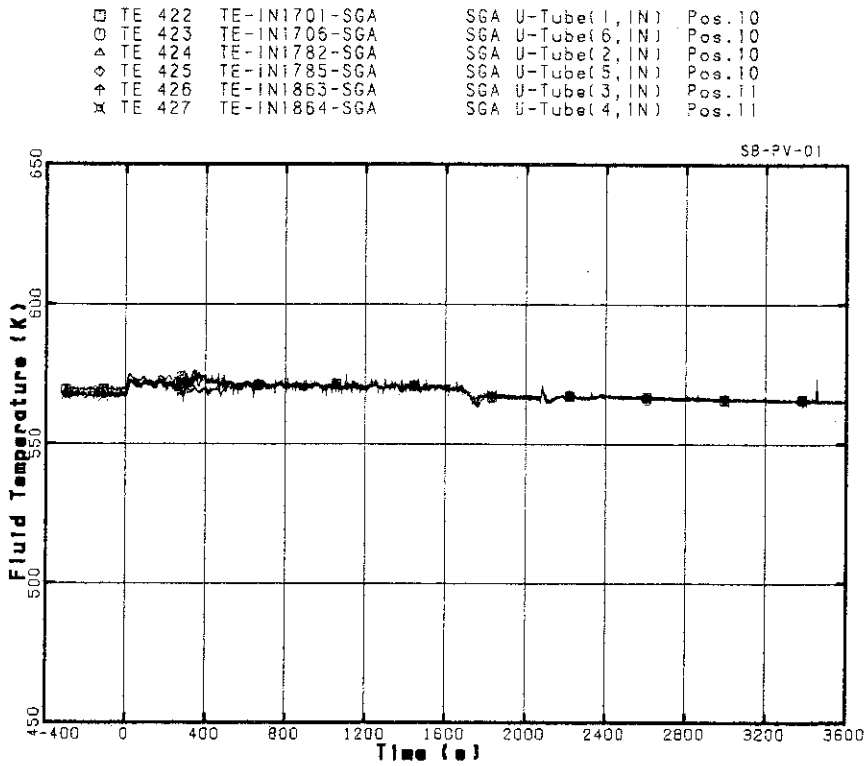

Fig. 5.39 Distribution of primary fluid temperatures at highest level of six SG-A U-tubes (Positions 10-11)

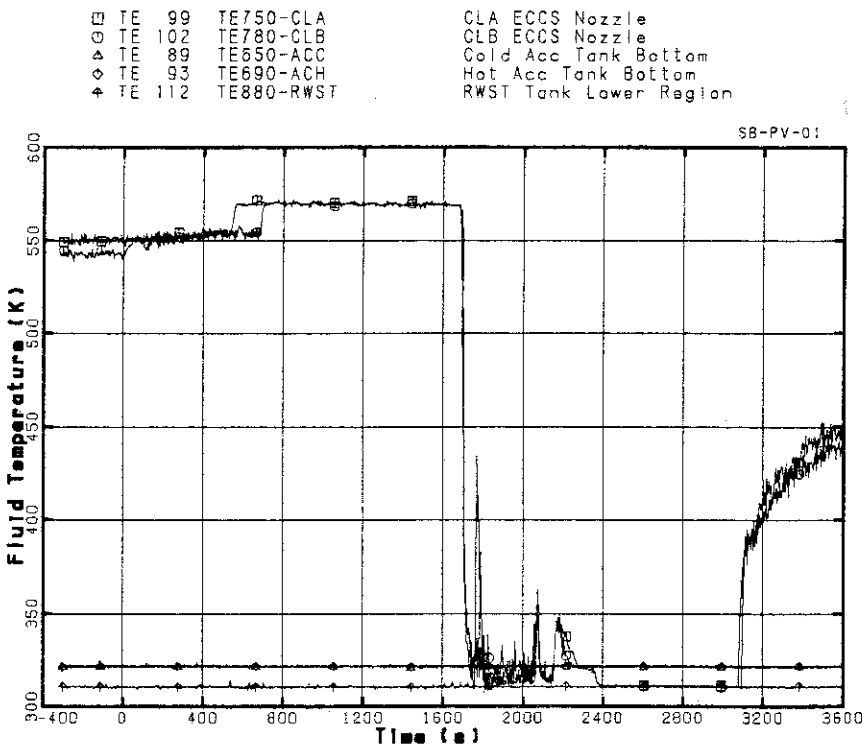

Fig. 5.40 Fluid temperatures of injection water for HPI, charging system, ACC, ACH and in RWST

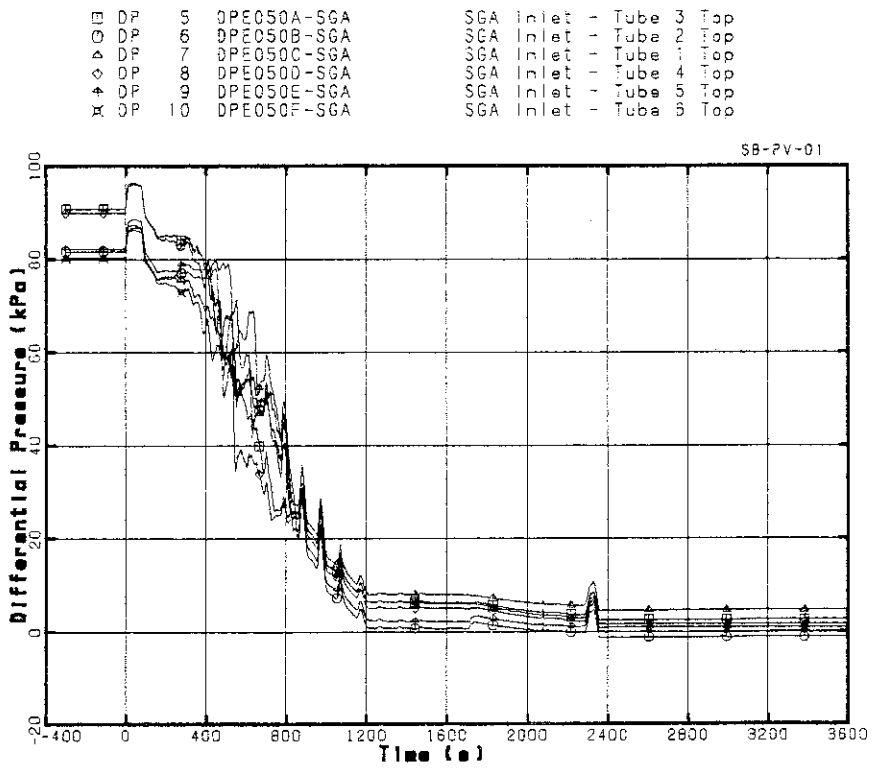

(a) Up-flow side

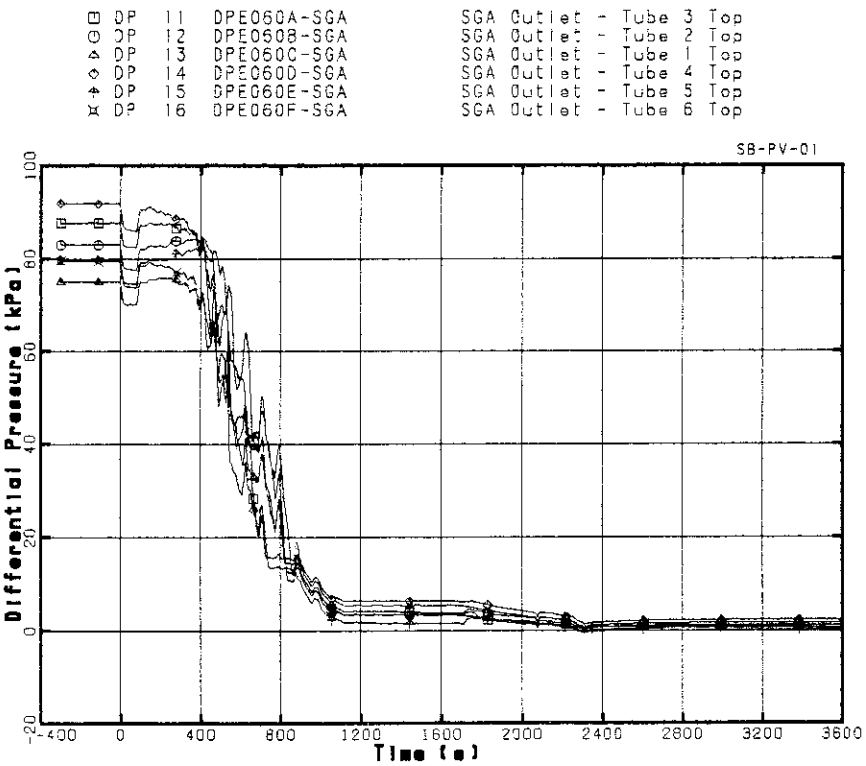

(b) Down-flow side

Fig. 5.41 Differential pressures in SG-A U-tubes

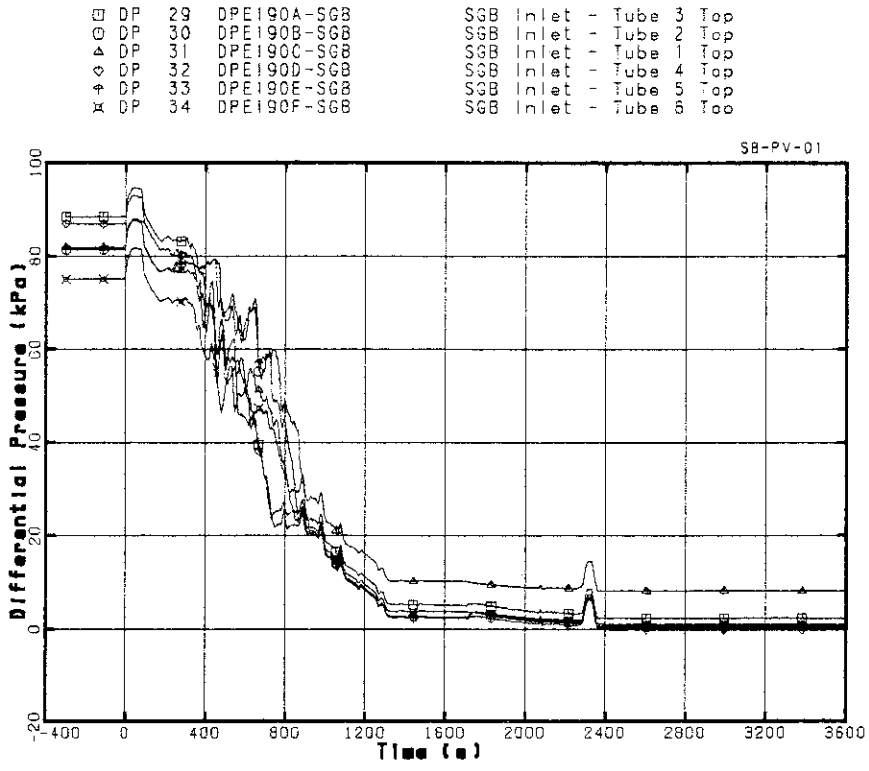

(a) Up-flow side

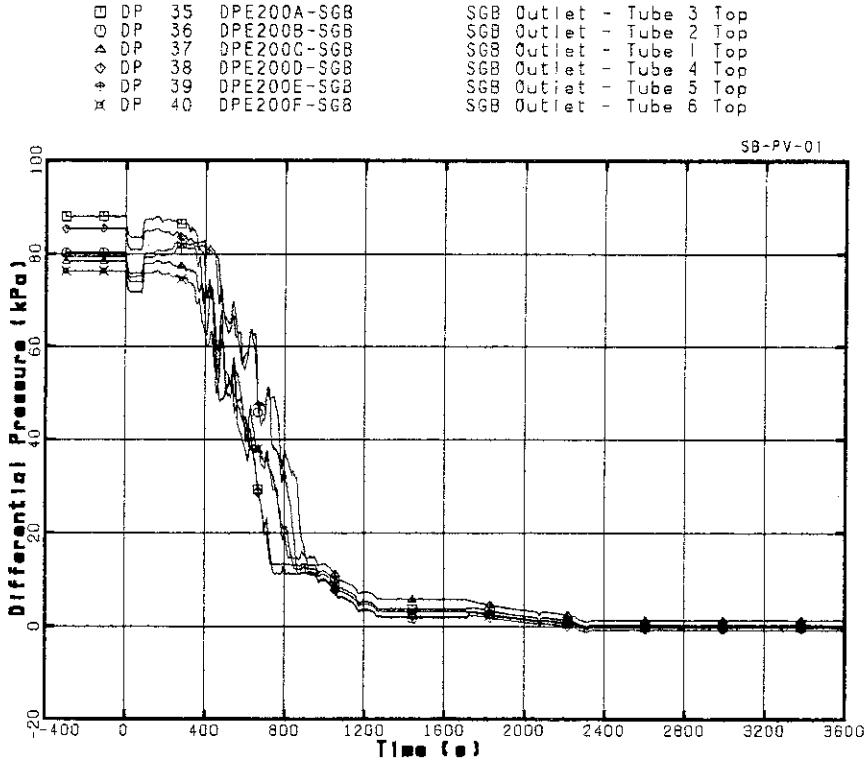

(b) Down-flow side

Fig. 5.42 Differential pressures in SG-B U-tubes

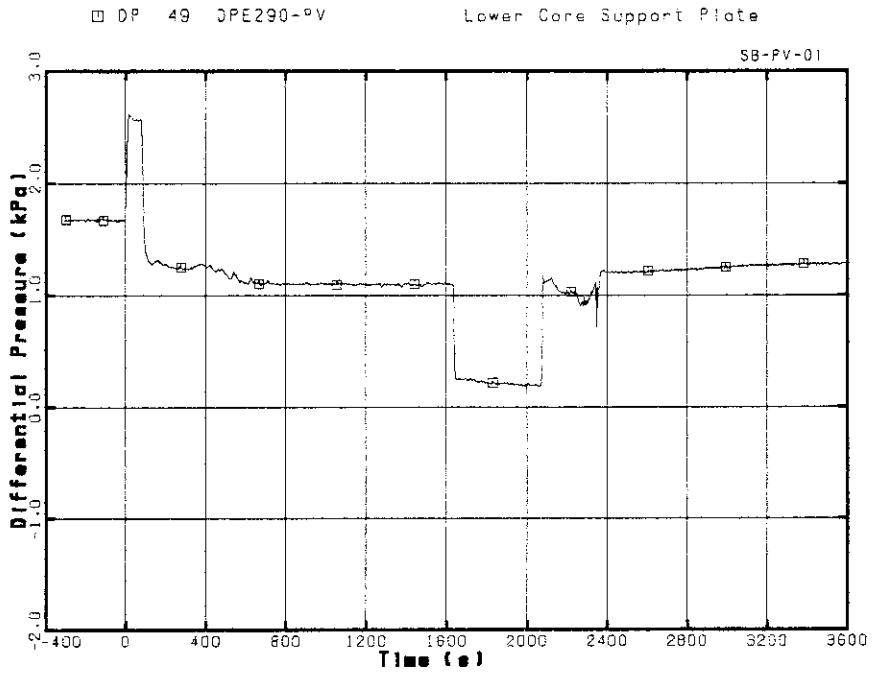

Fig. 5.43 Differential pressure across lower core support plate

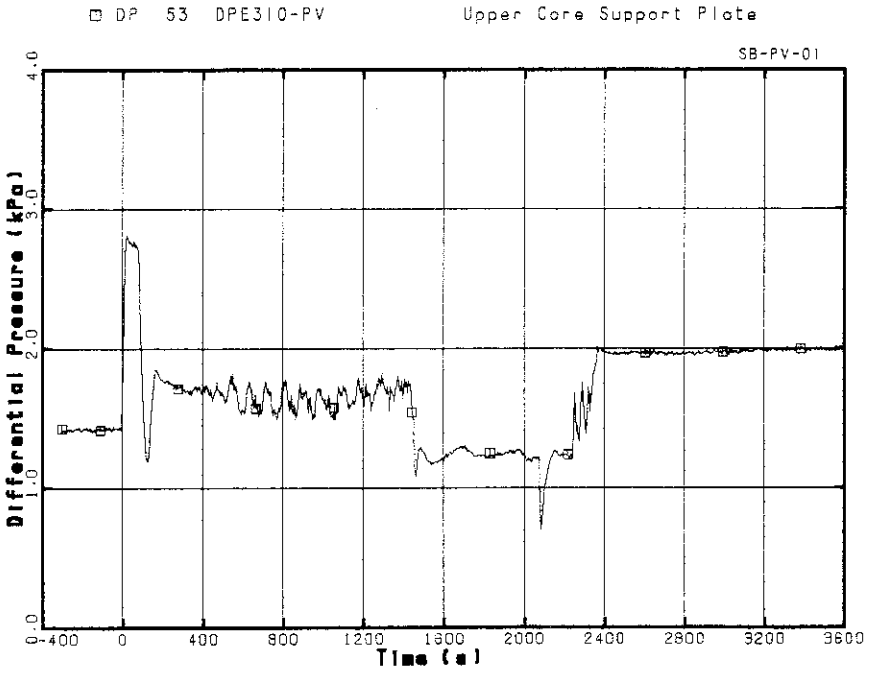

Fig. 5.44 Differential pressure across upper core plate

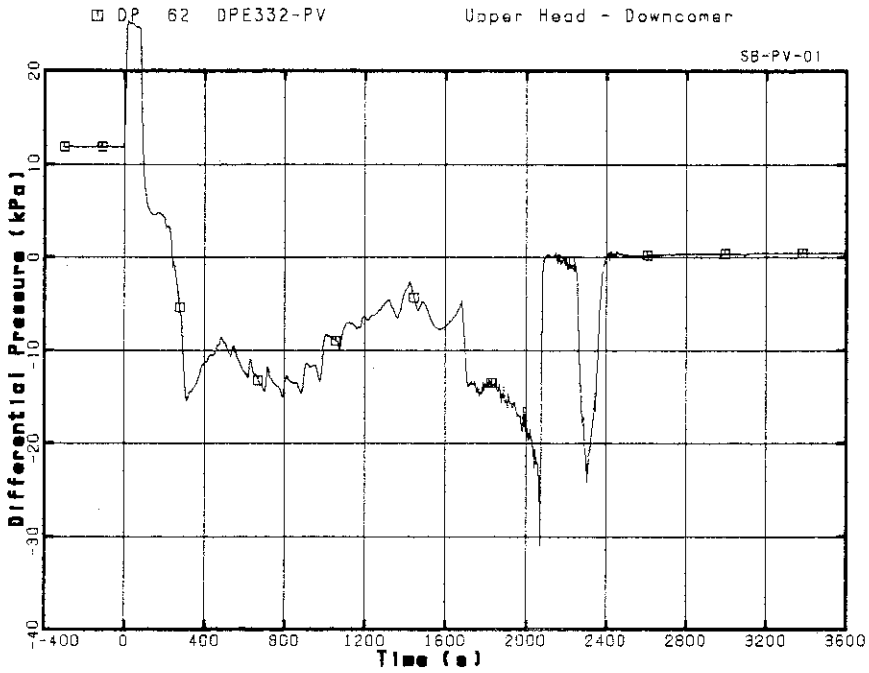

Fig. 5.45 Differential pressure between upper head and downcomer top

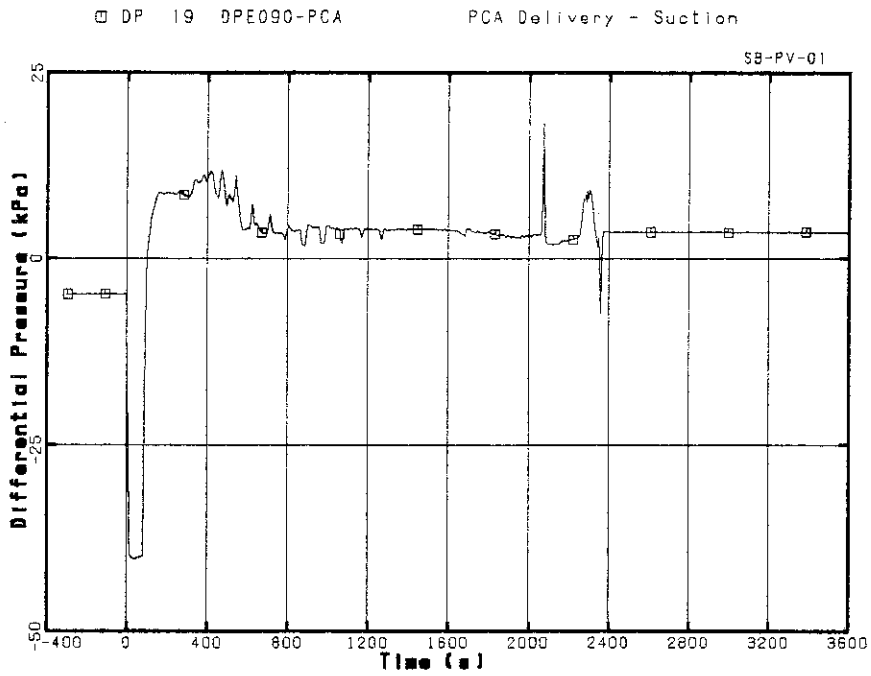

Fig. 5.46 Differential pressure across PC-A pump

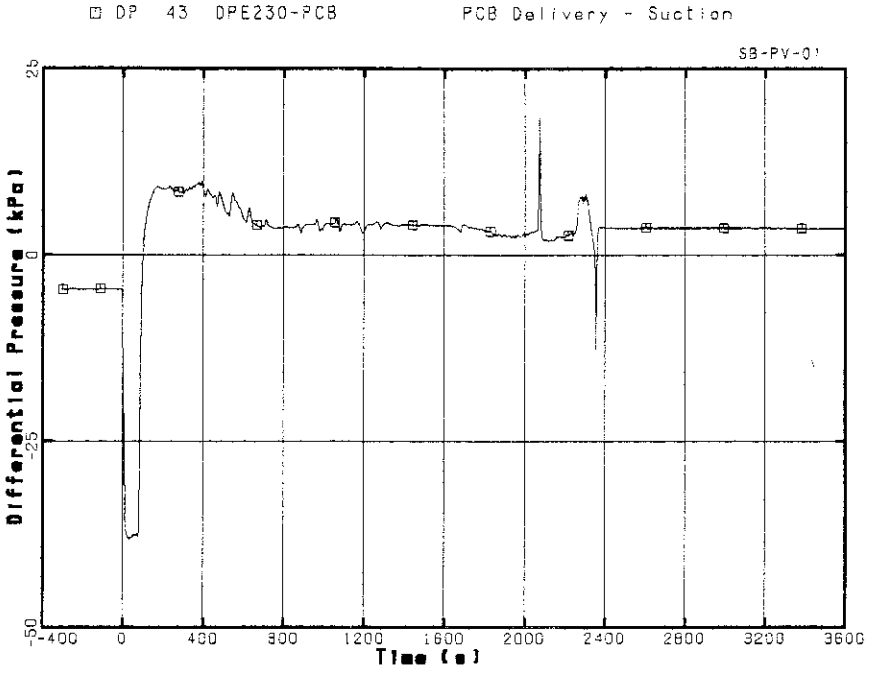

Fig. 5.47 Differential pressure across PC-B pump

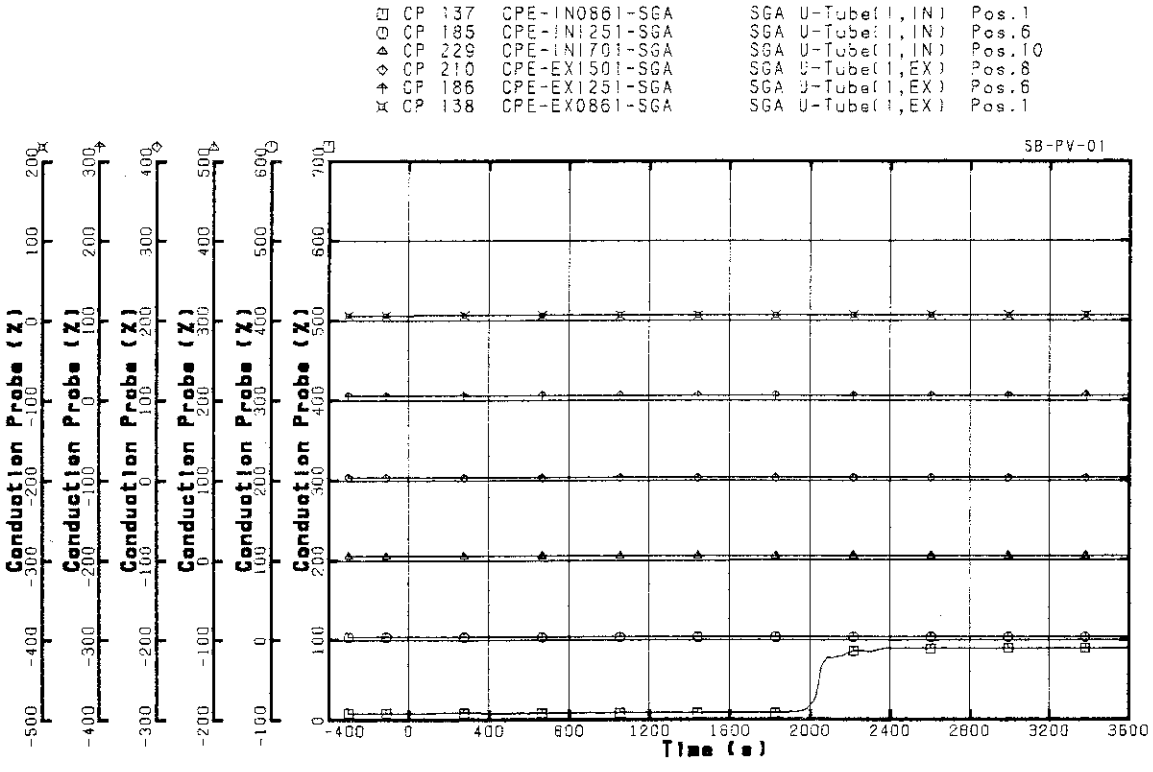

Fig. 5.48 Conduction probe signals in SG-A U-tube 1 (Short tube)

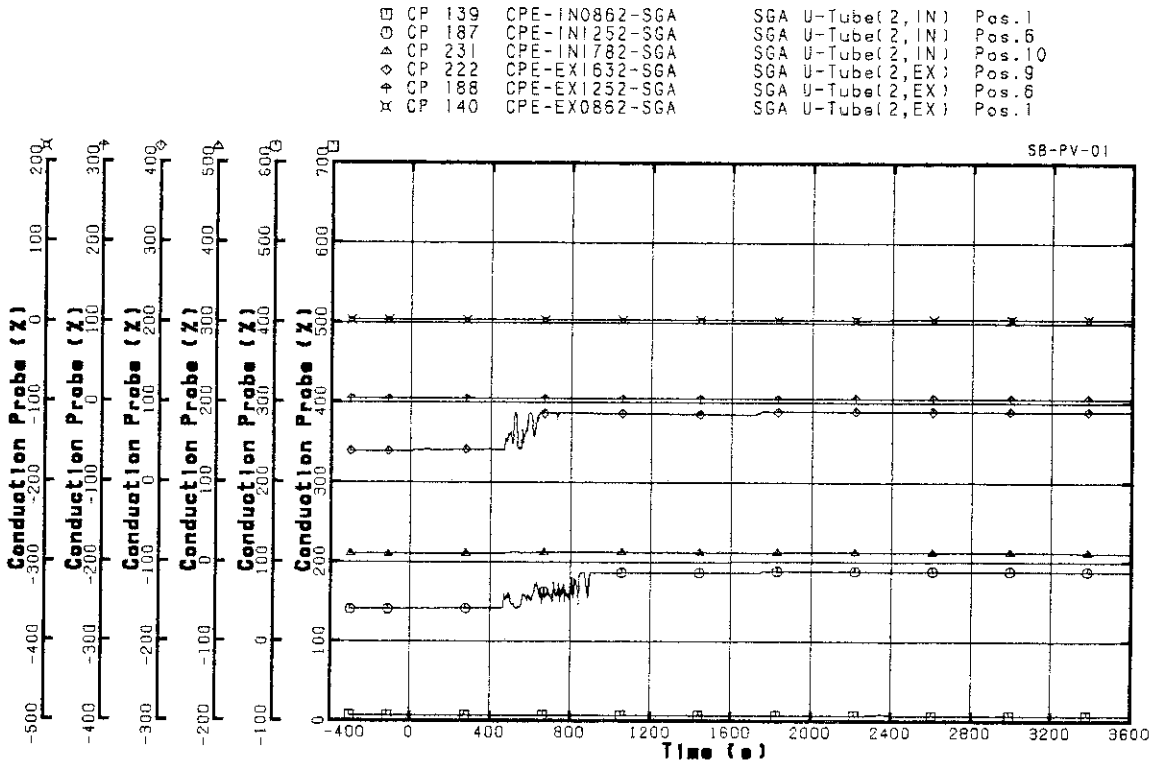

Fig. 5.49 Conduction probe signals in SG-A U-tube 2 (Middle)

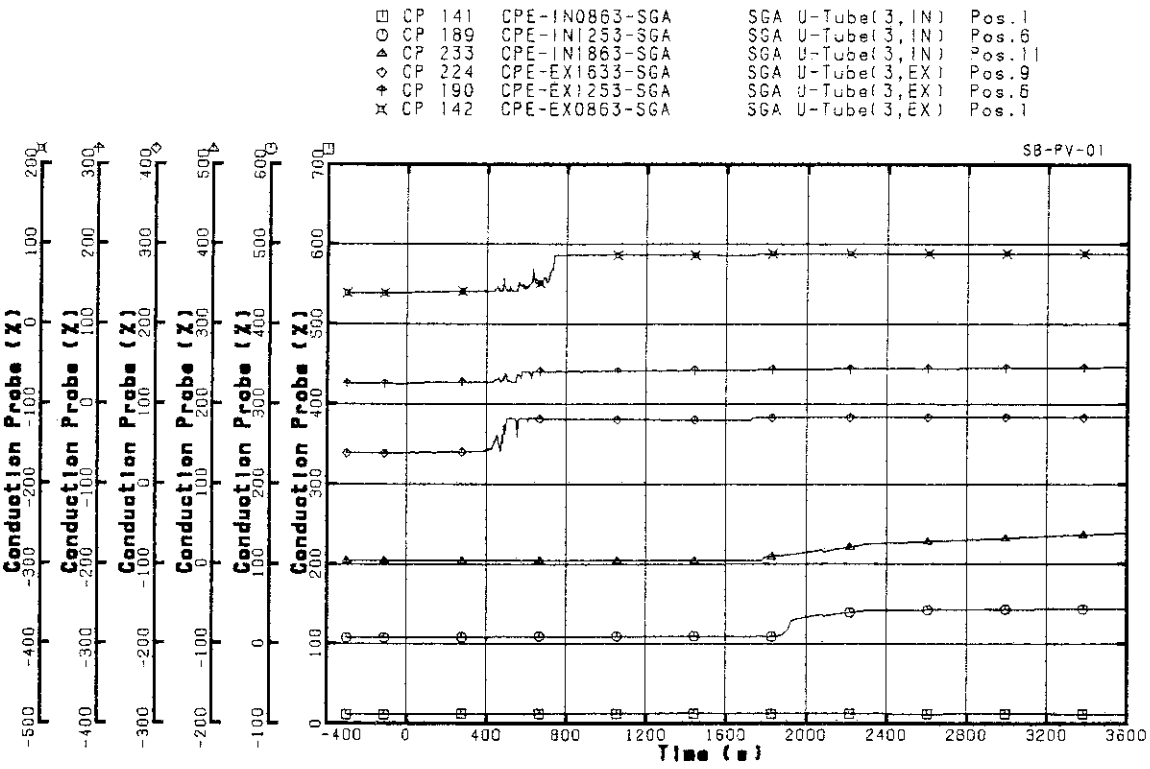

Fig. 5.50 Conduction probe signals in SG-A U-tube 3 (Long tube)

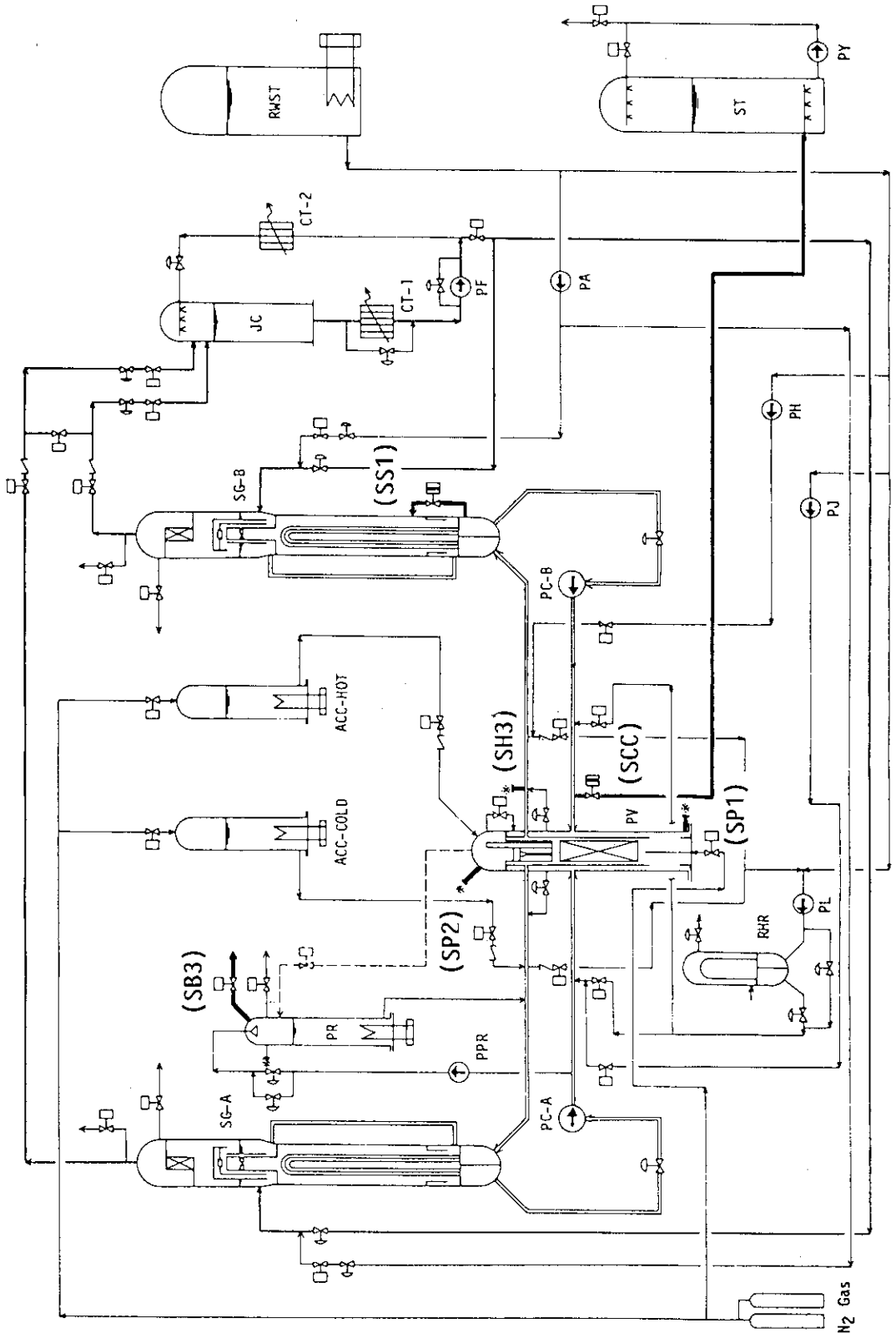

(a) Total system flow diagram

Fig. 6.1 Six break locations in the LSTF primary system

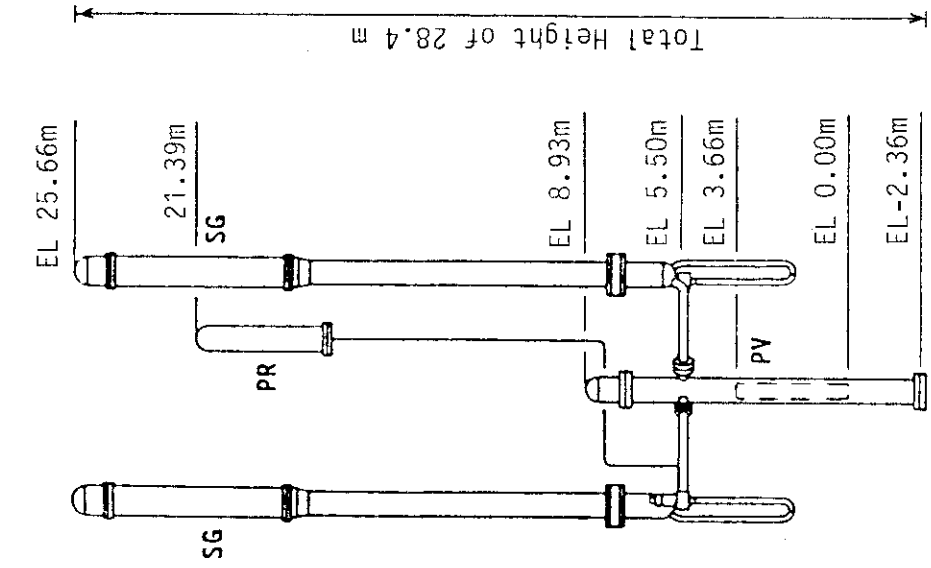

(c) Height and elevation of the LSTF system

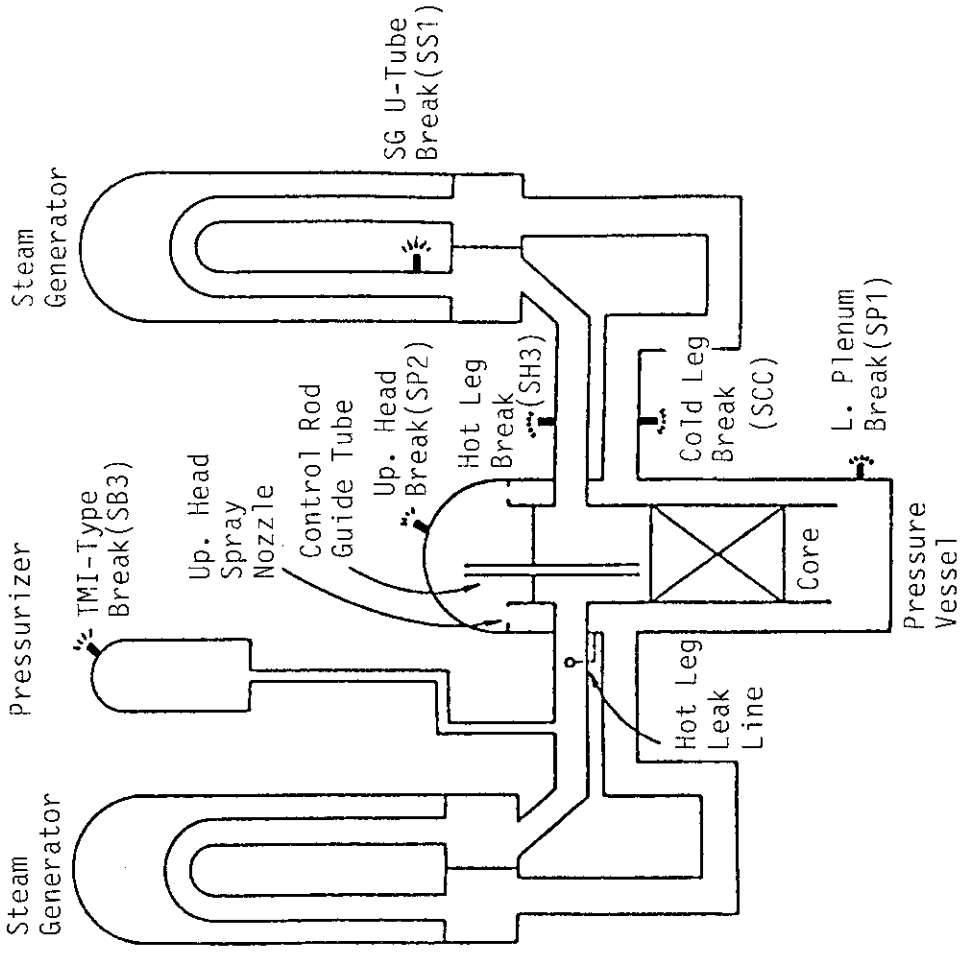

(b) Break locations in primary system

Fig. 6.1 Six break locations in the LSTF primary system (Cont'd)

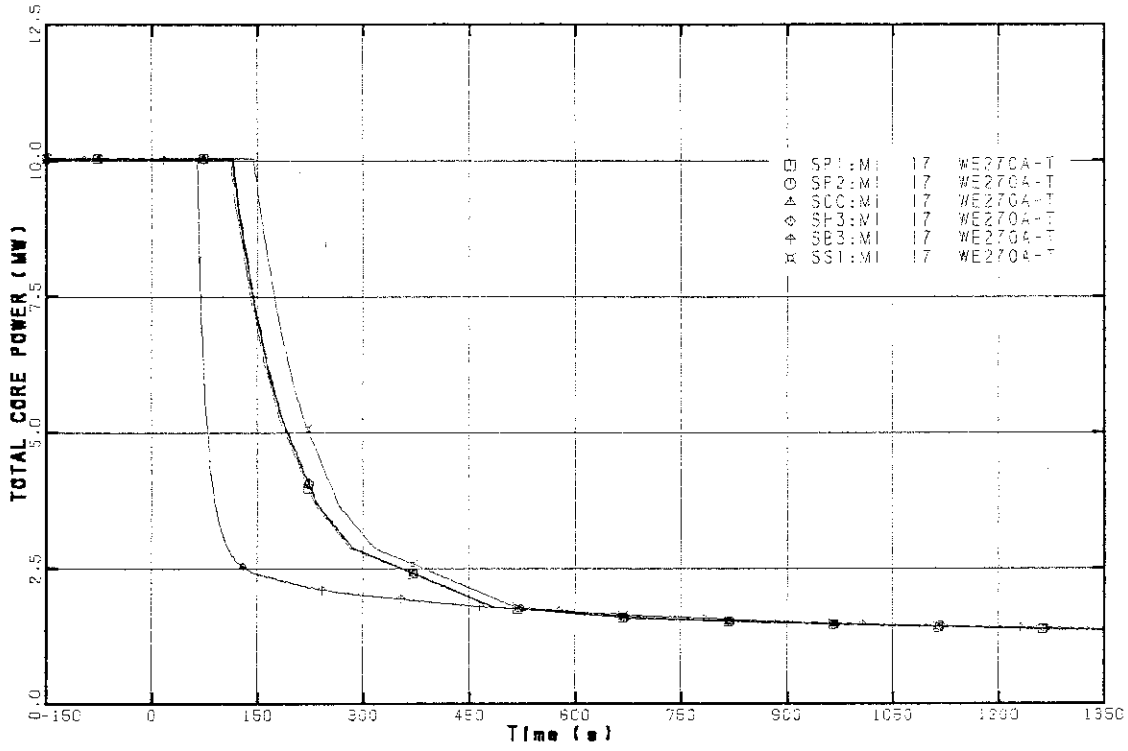

(a) Power curve in a short range (until 1350 s)

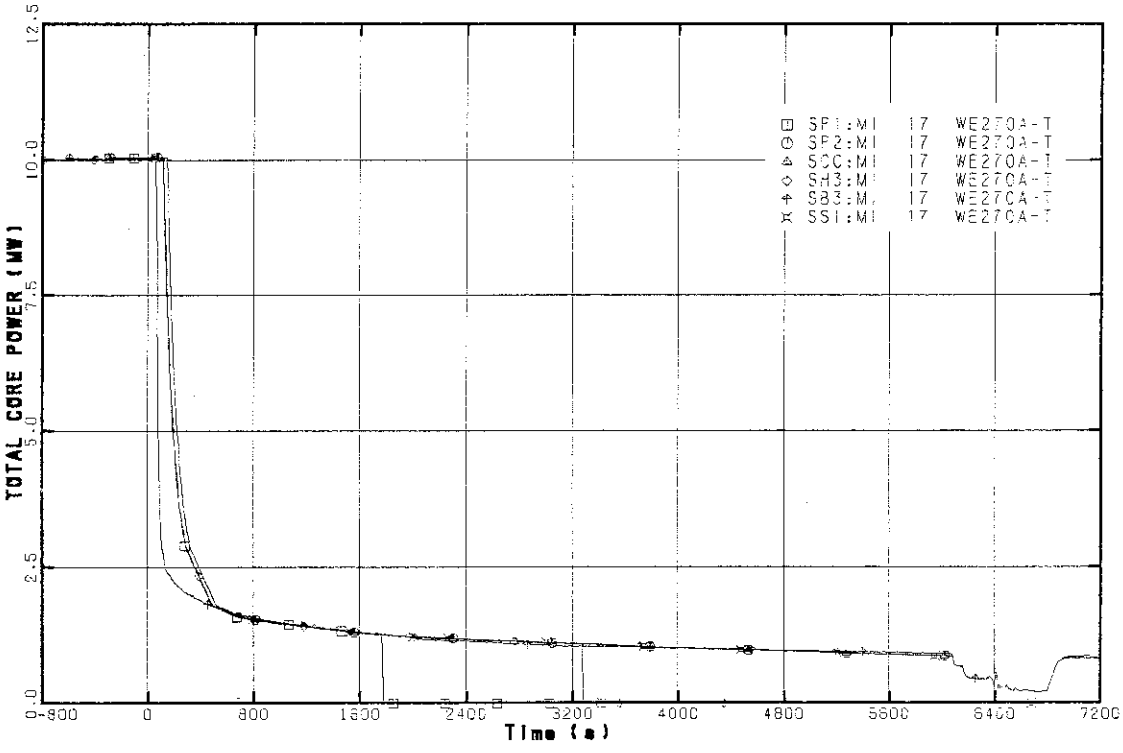

(b) Power curve in a long range (until 7200 s)

Fig. 6.2 Total core power in six tests

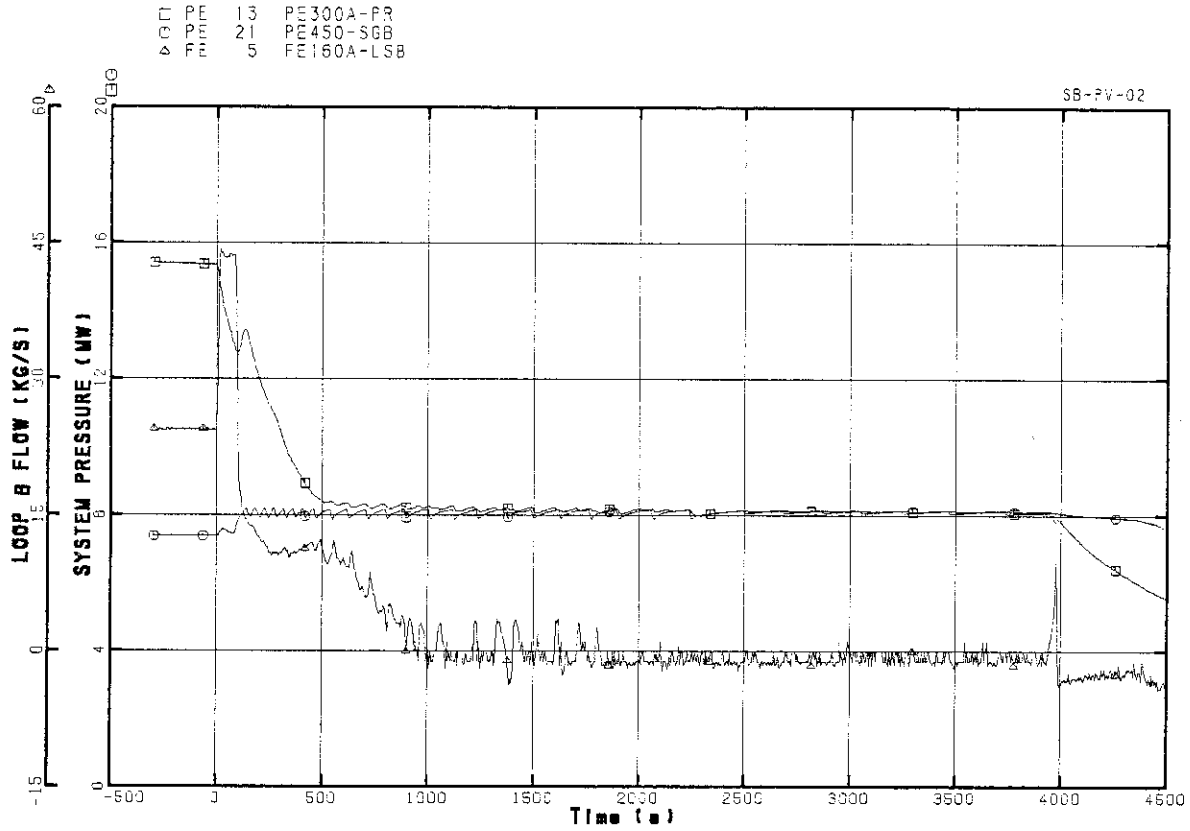

(a) Primary and secondary pressures and primary flow rate

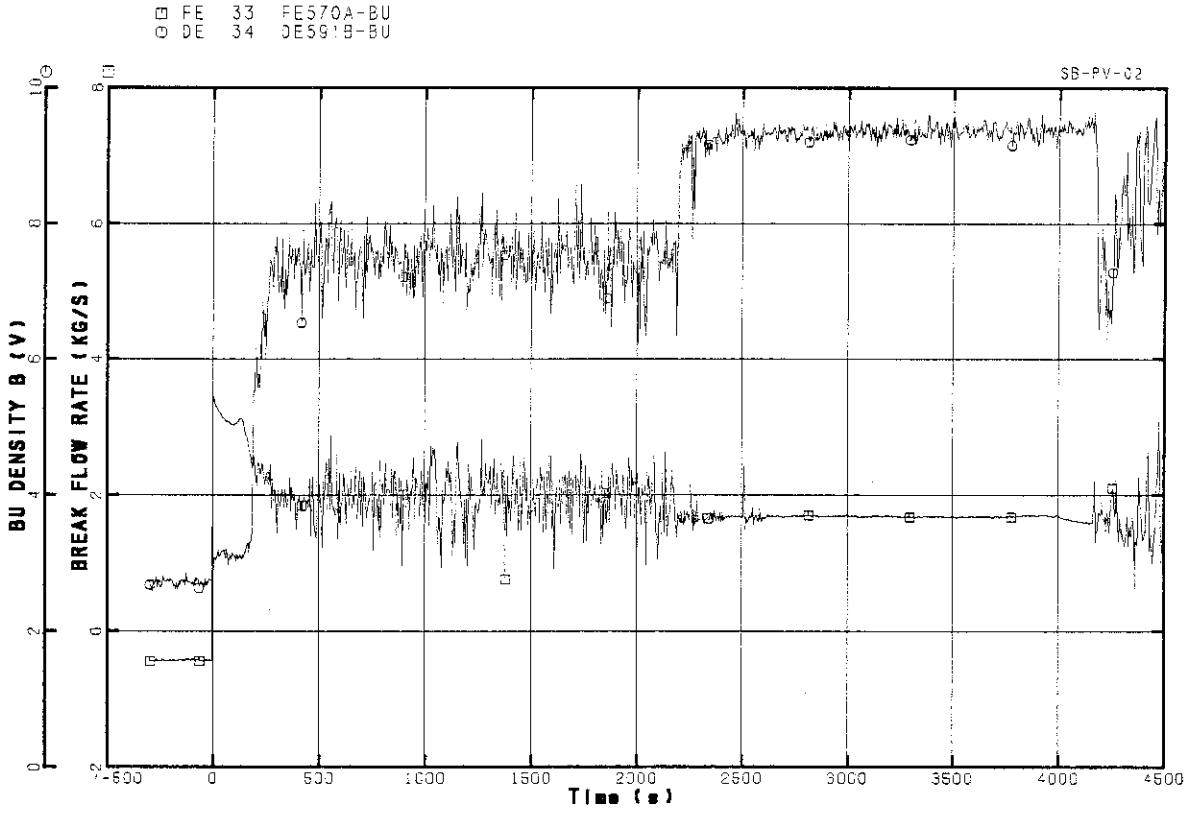

(b) Break flow rate and break density (Beam B)

Fig. 6.3 Major results for upper head break LOCA test (SP2)

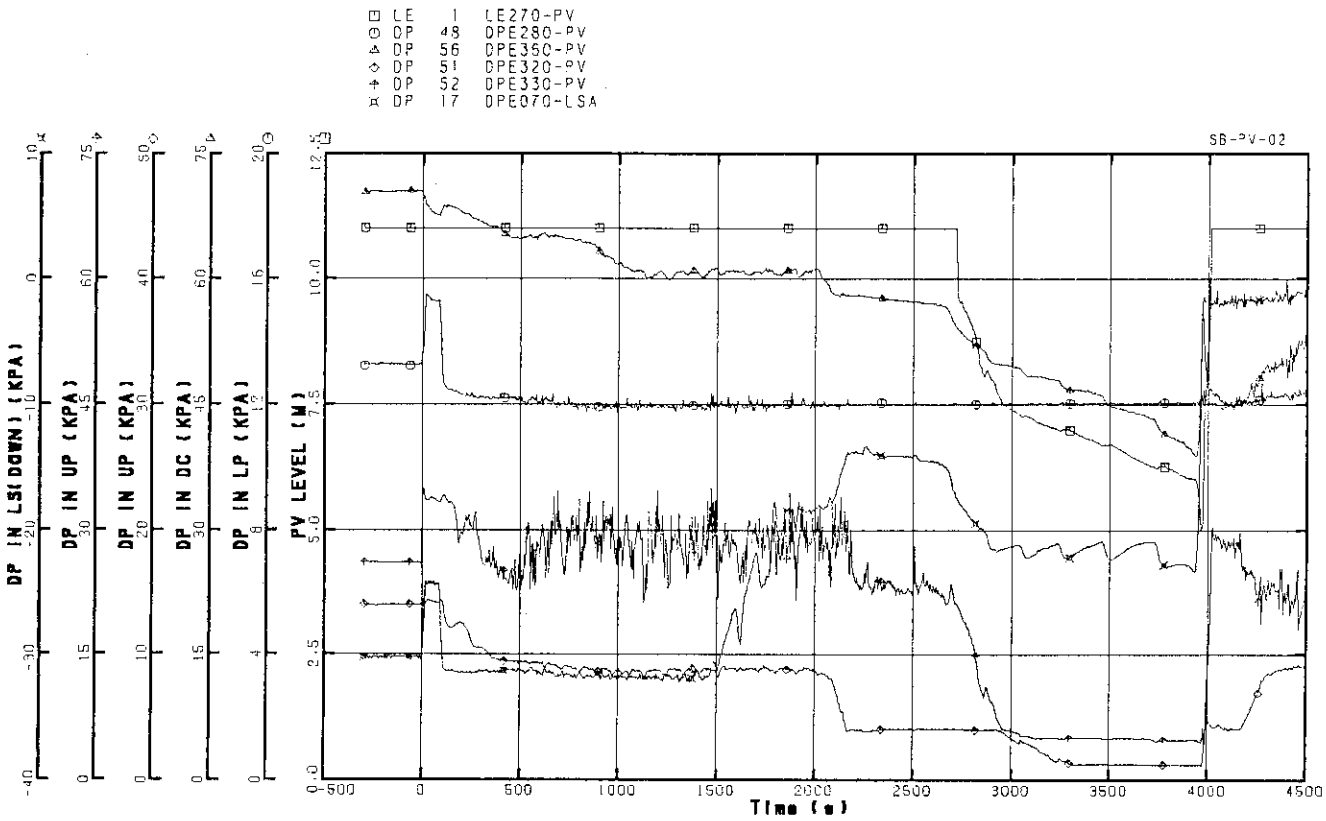

(c) Water level and differential pressures

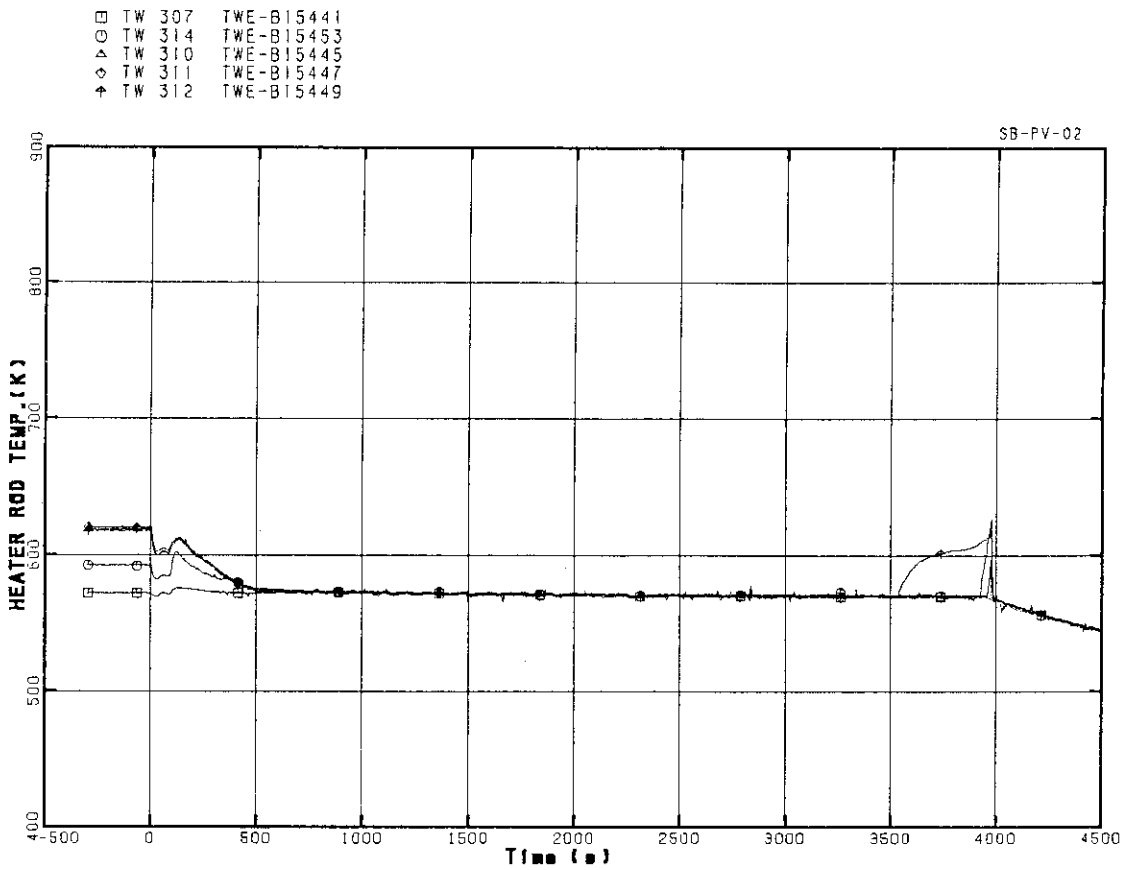

(d) Heater rod surface temperatures (high-power bundle)

Fig. 6.3 Major results for upper head break LOCA test (SP2) (Cont'd)

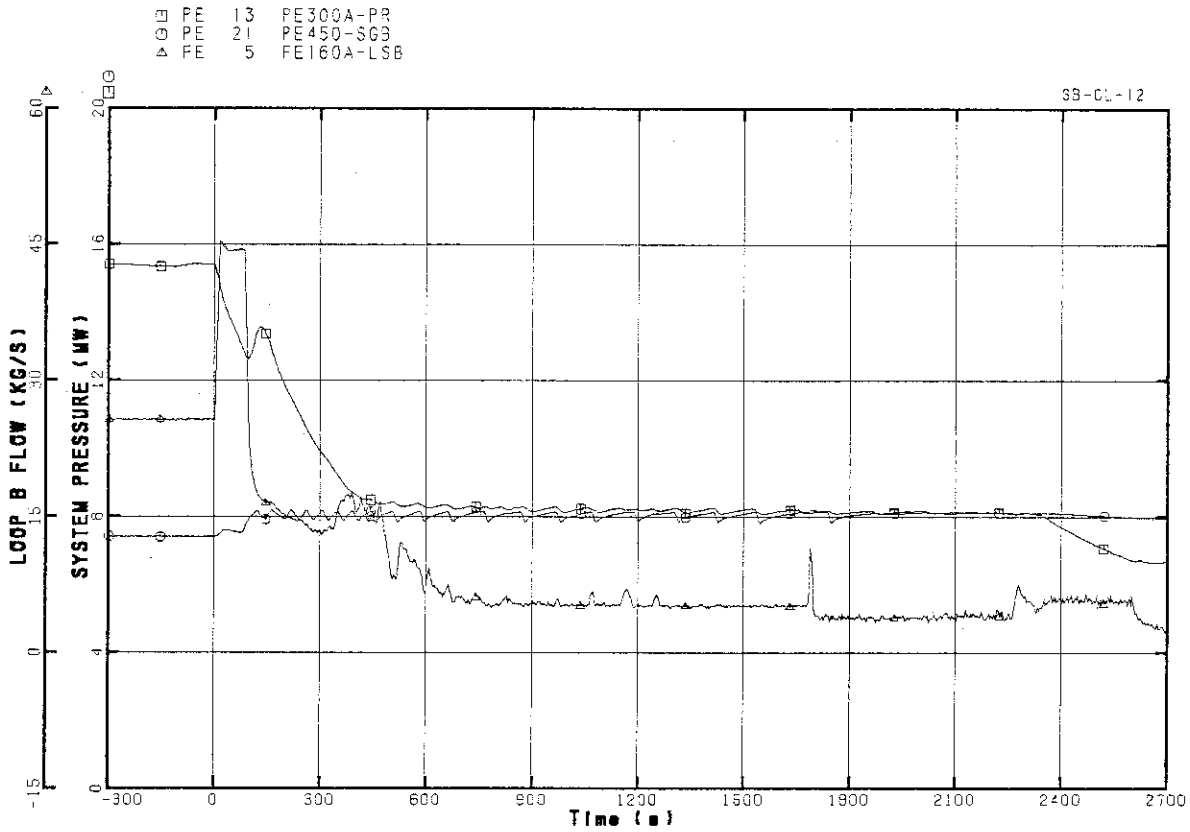

(a) Primary and secondary pressures and primary flow rate

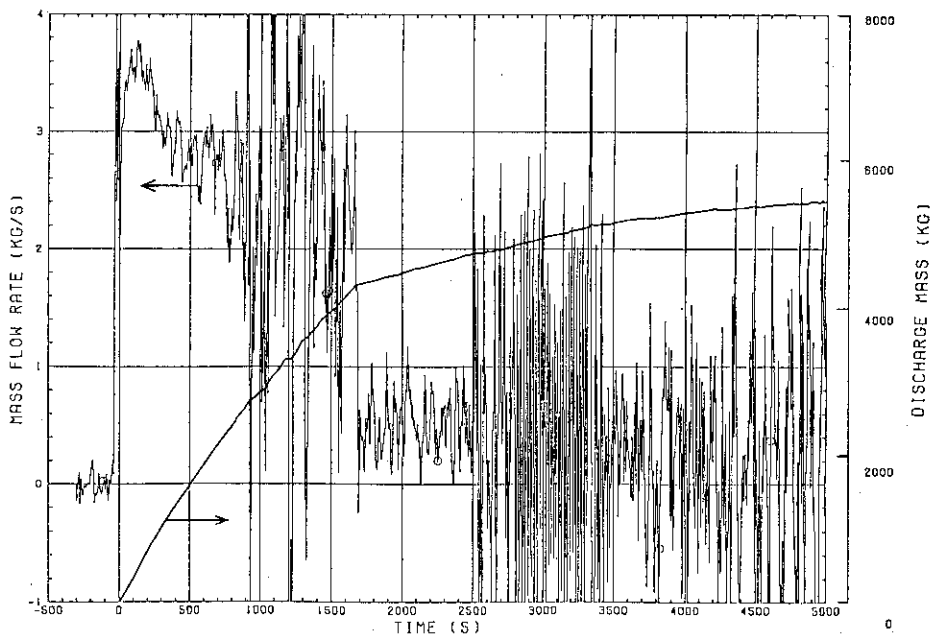

(b) Discharged mass and reduced break flow

Fig. 6.4 Major results for cold leg break LOCA test (SCC)

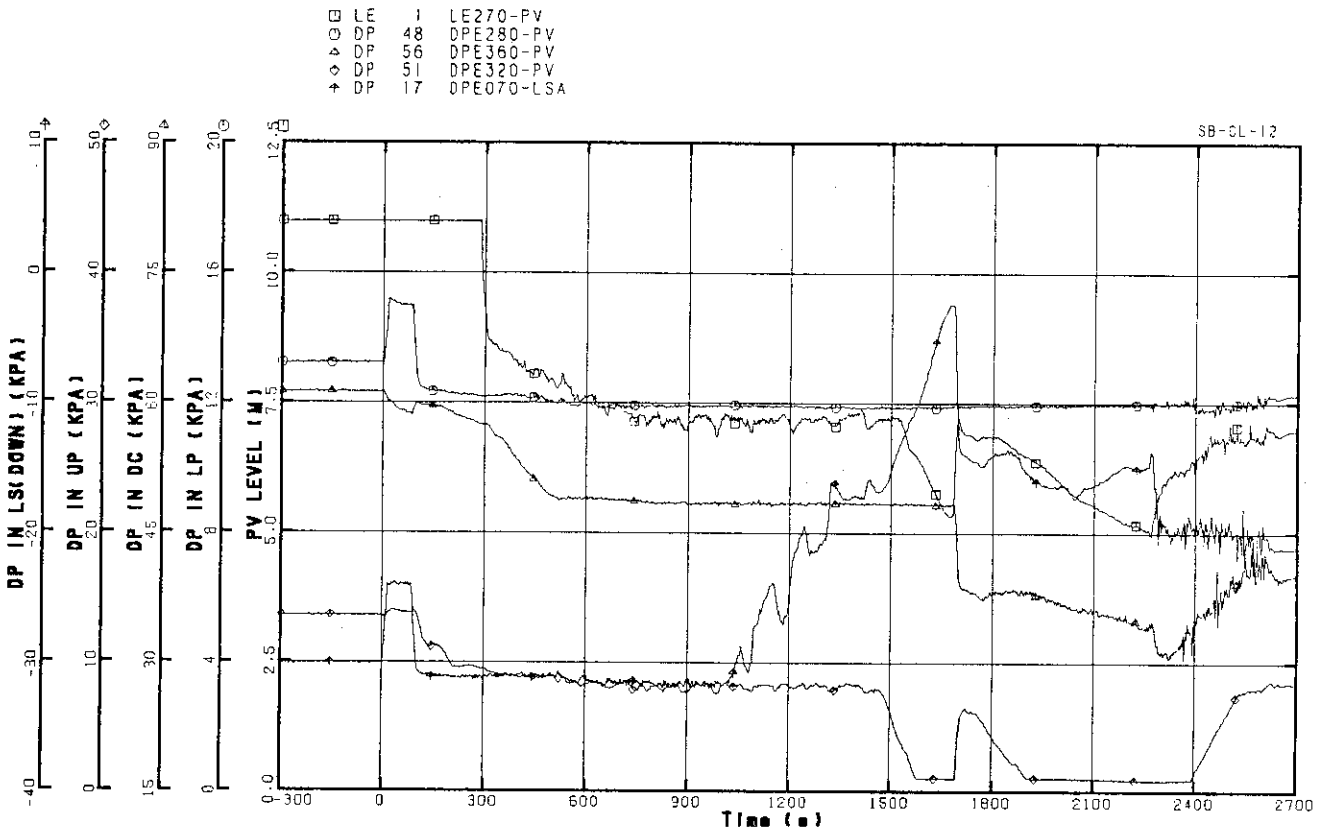

(c) Water level and differential pressures

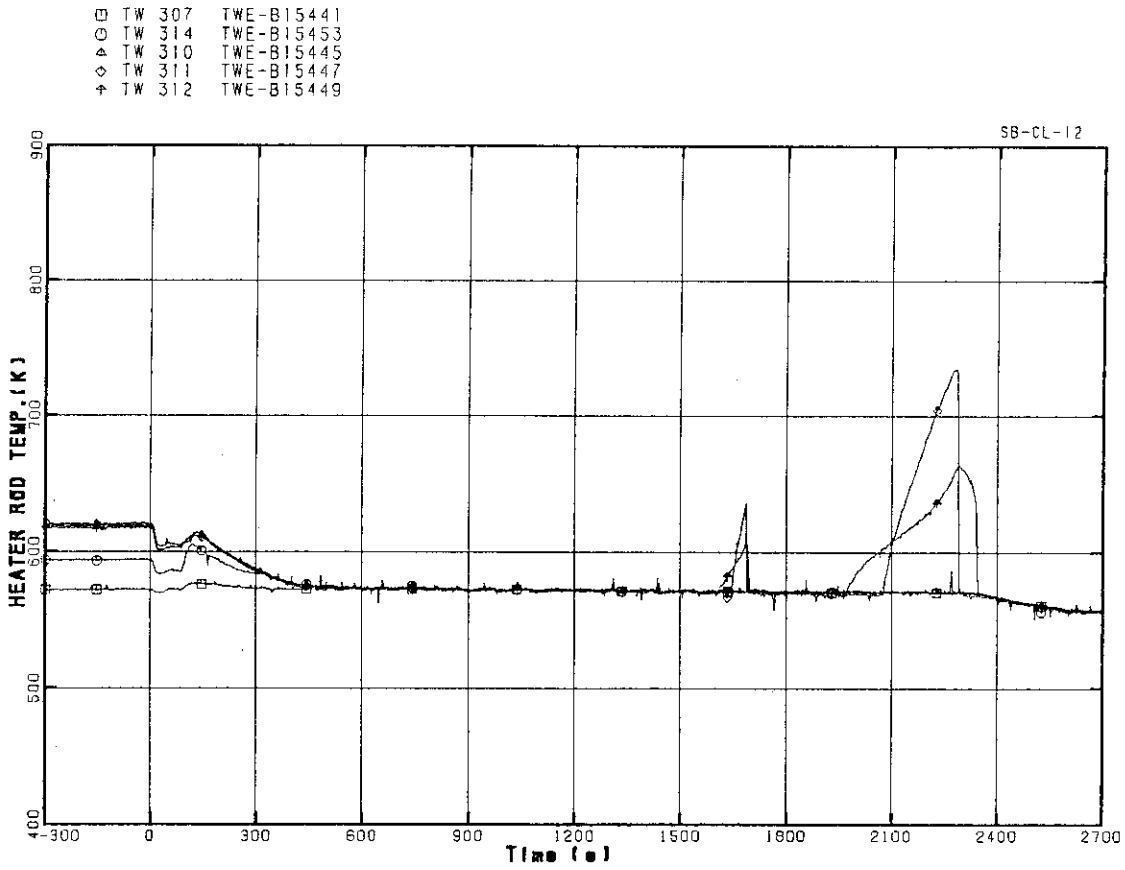

(d) Heater rod surface temperatures (high-power bundle)

Fig. 6.4 Major results for cold leg break LOCA test (SCC) (Cont'd)

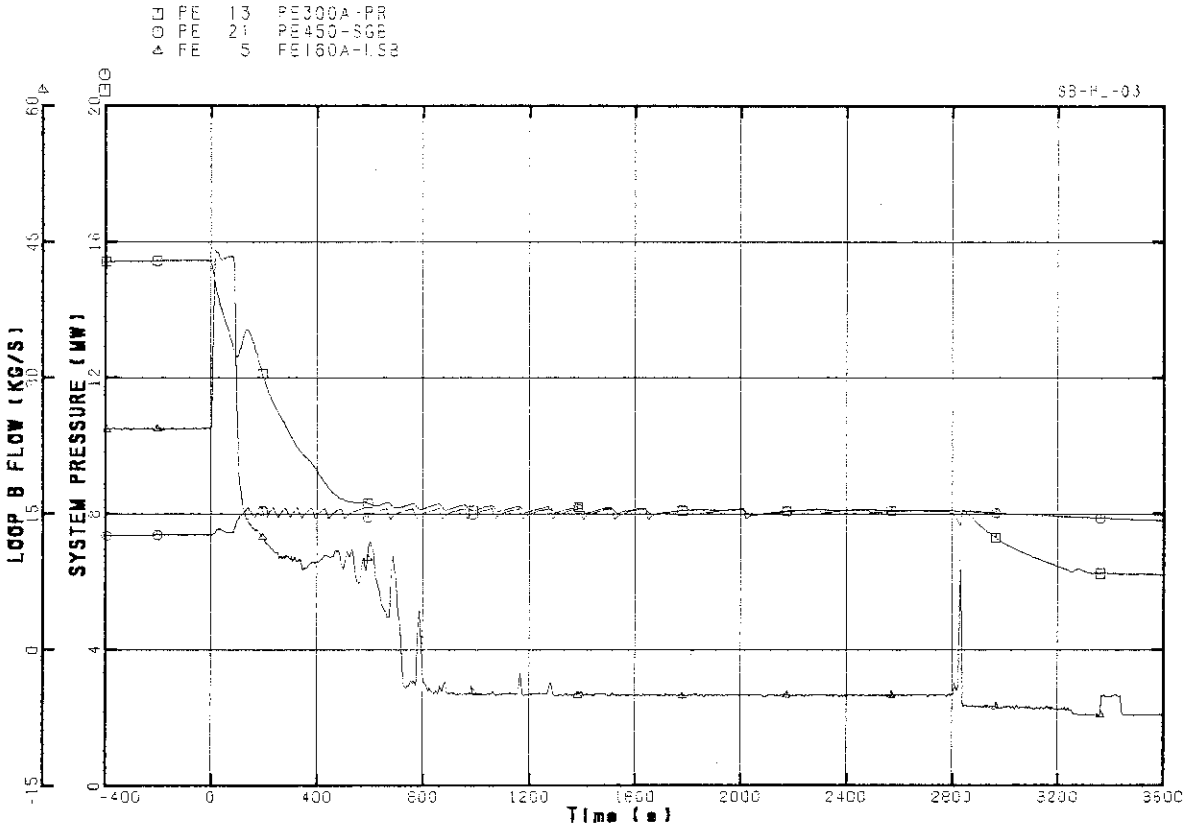

(a) Primary and secondary pressures and primary flow rate

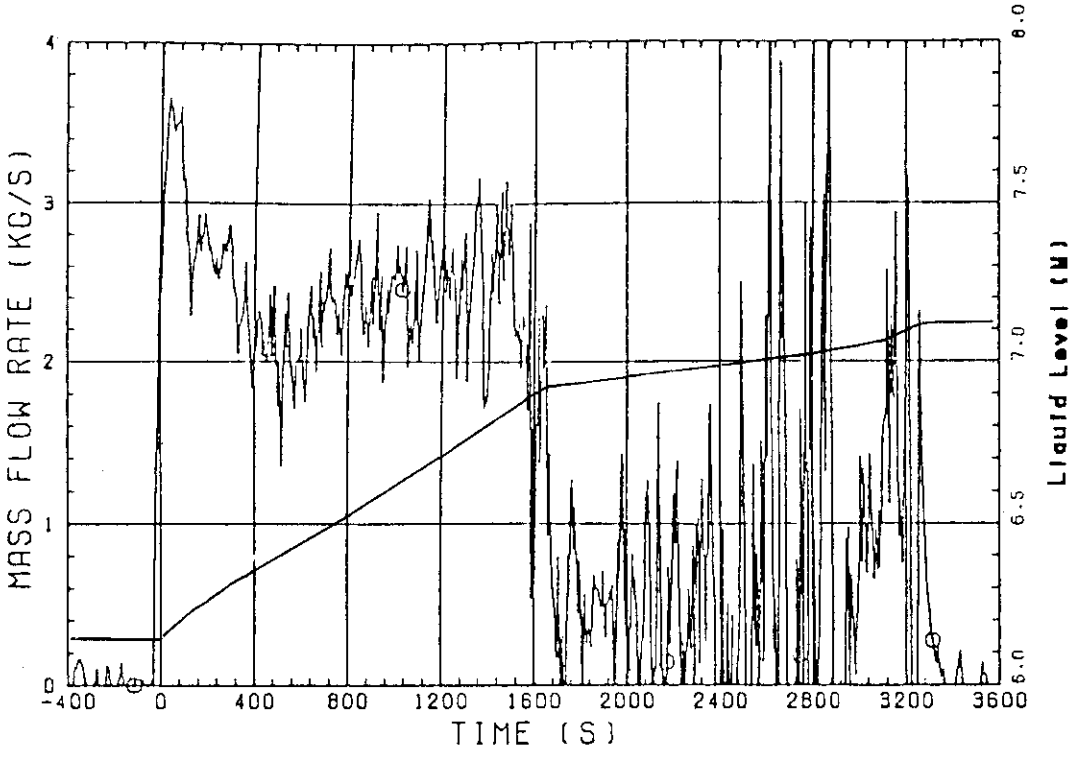

(b) ST level and reduced break flow

Fig. 6.5 Major results for hot leg break LOCA test (SH3)

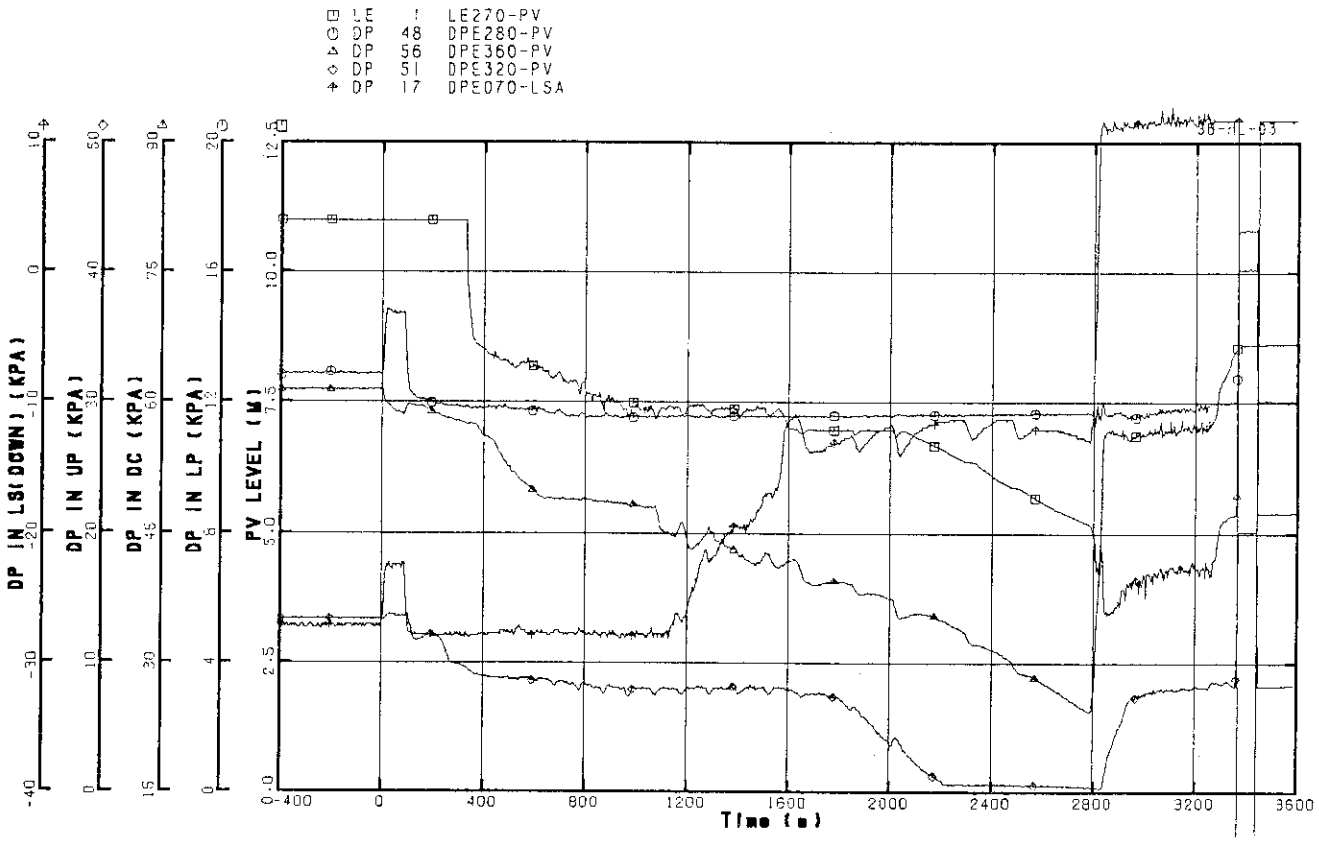

(c) Water level and differential pressures

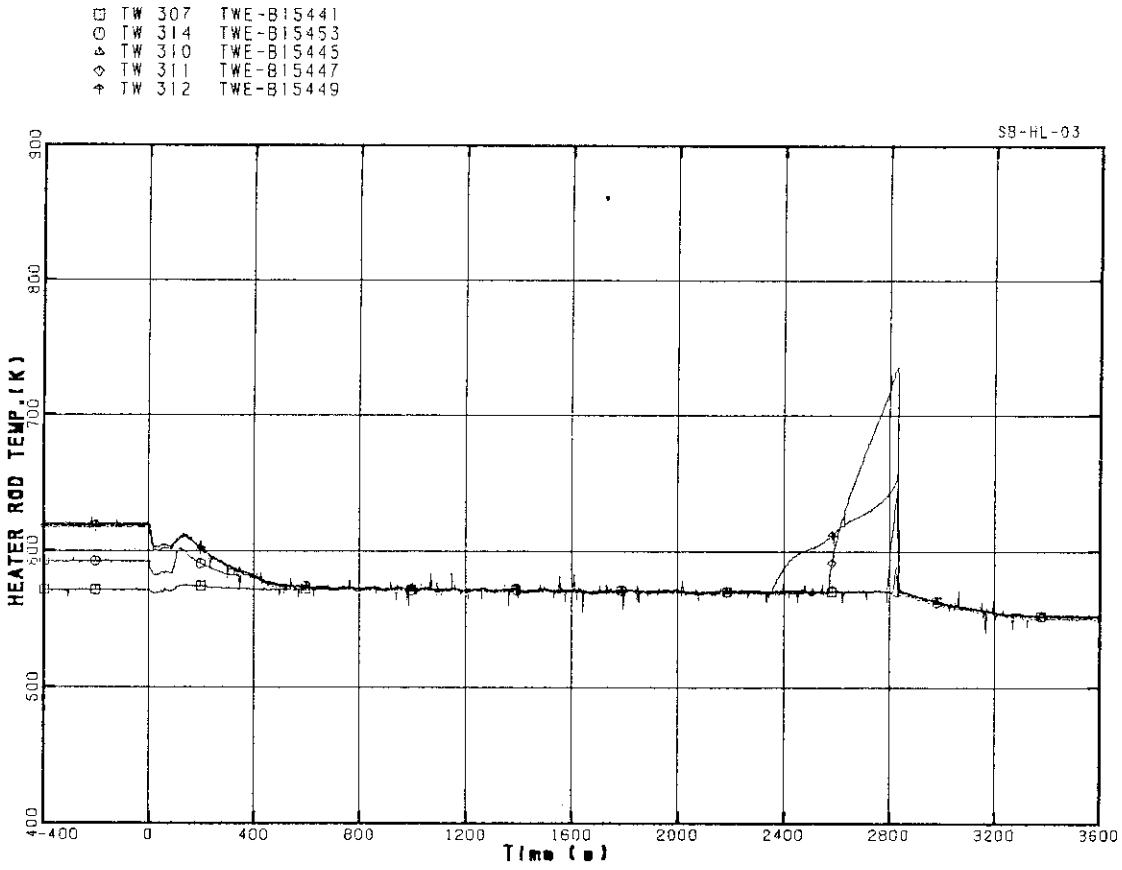

(d) Heater rod surface temperatures (high-power bundle)

Fig. 6.5 Major results for hot leg break LOCA test (SH3) (Cont'd)

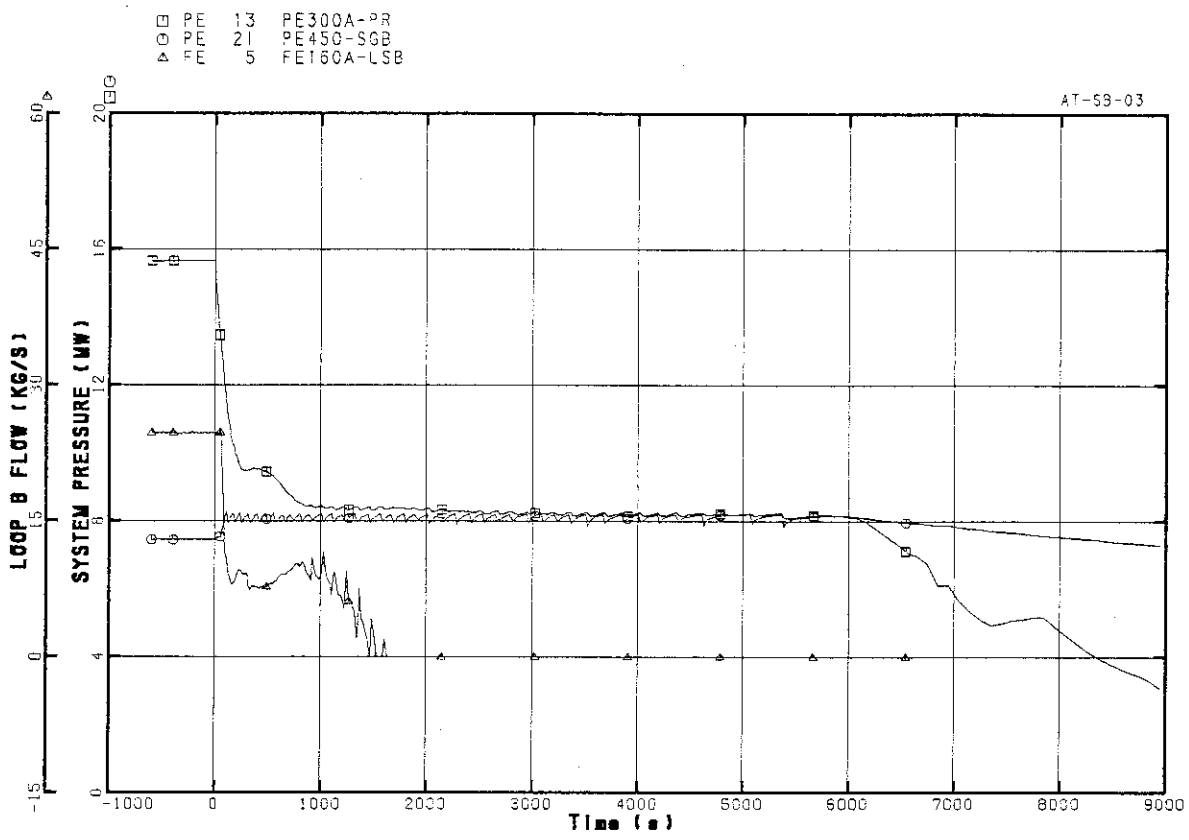

(a) Primary and secondary pressures and primary flow rate

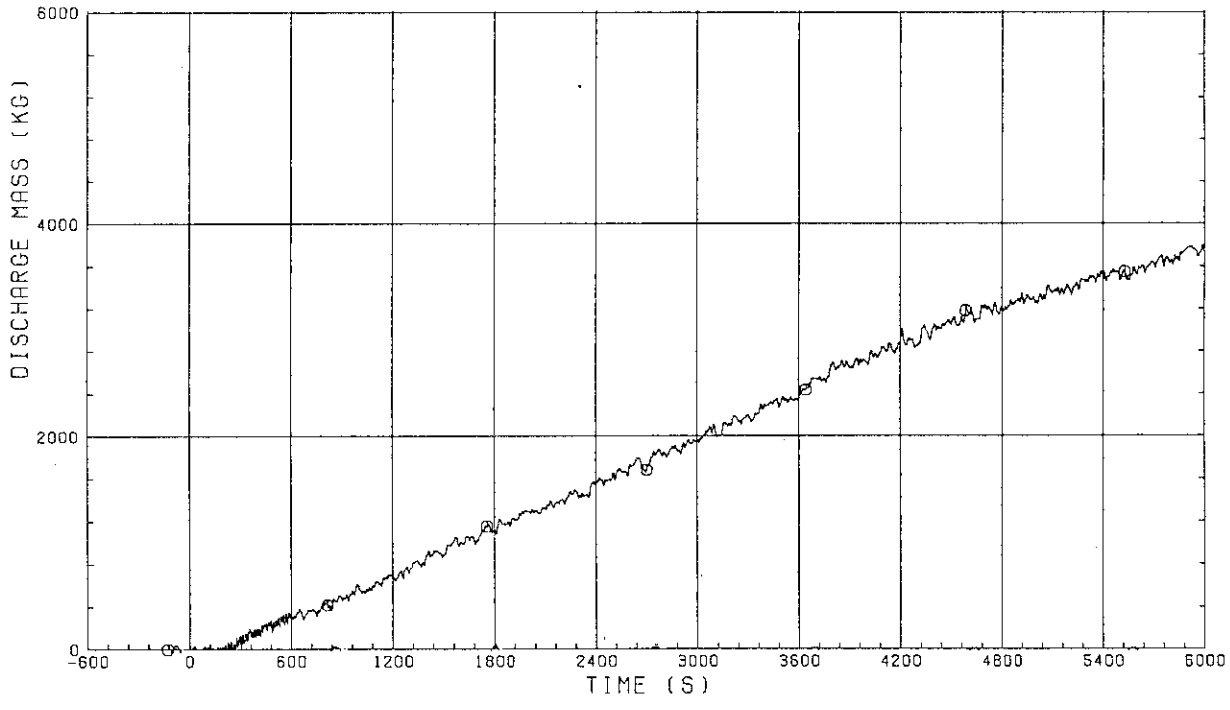

(b) Discharged primary mass in ST tank

Fig. 6.6 Major results for pressurizer top break LOCA test (SB3)

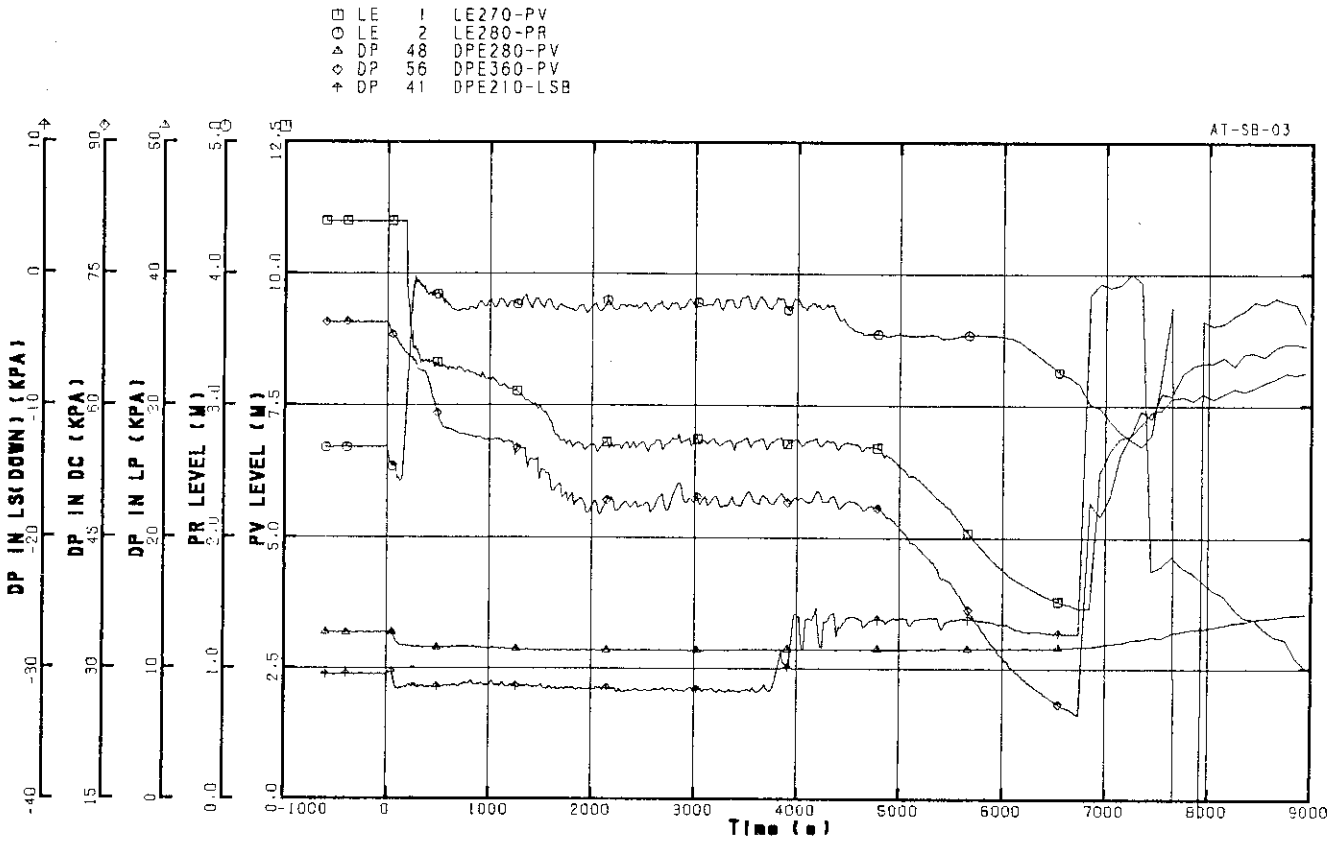

(c) Water level and differential pressures

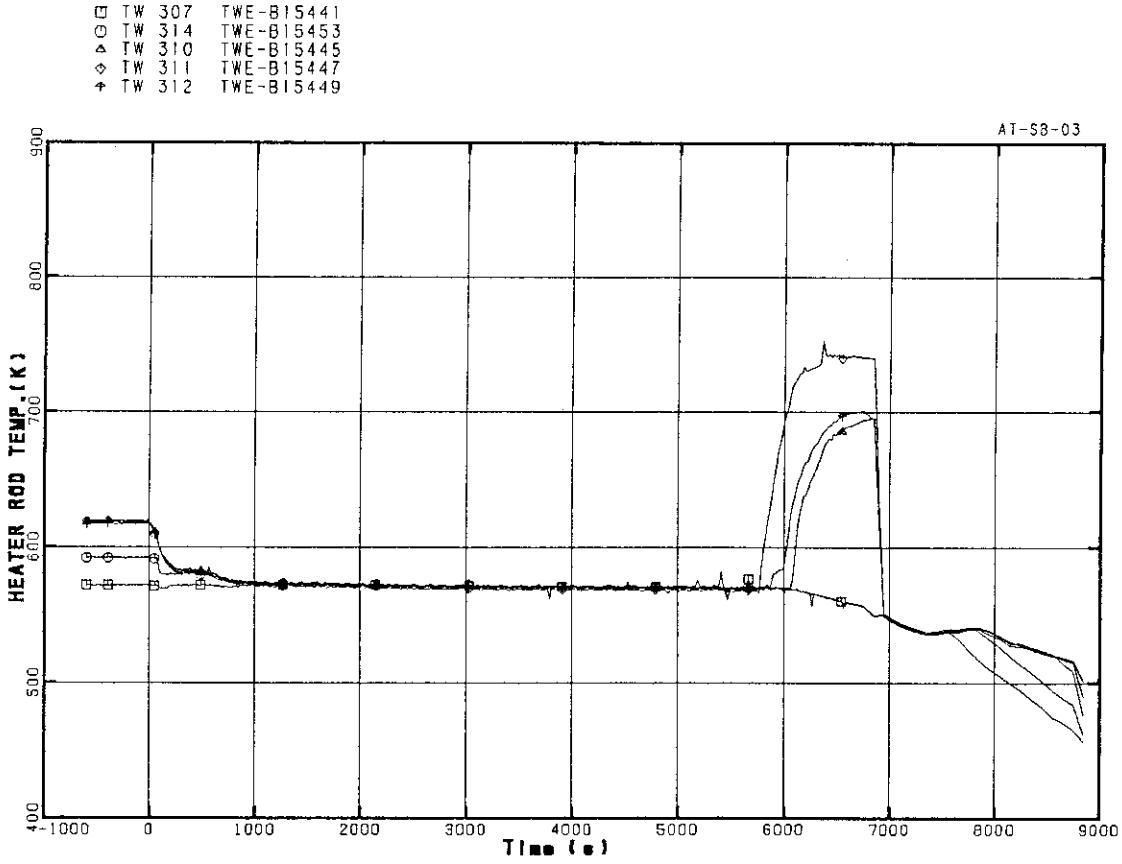

(d) Heater rod surface temperatures (high-power bundle)

Fig. 6.6 Major results for pressurizer top break LOCA test (SB3) (Cont'd)

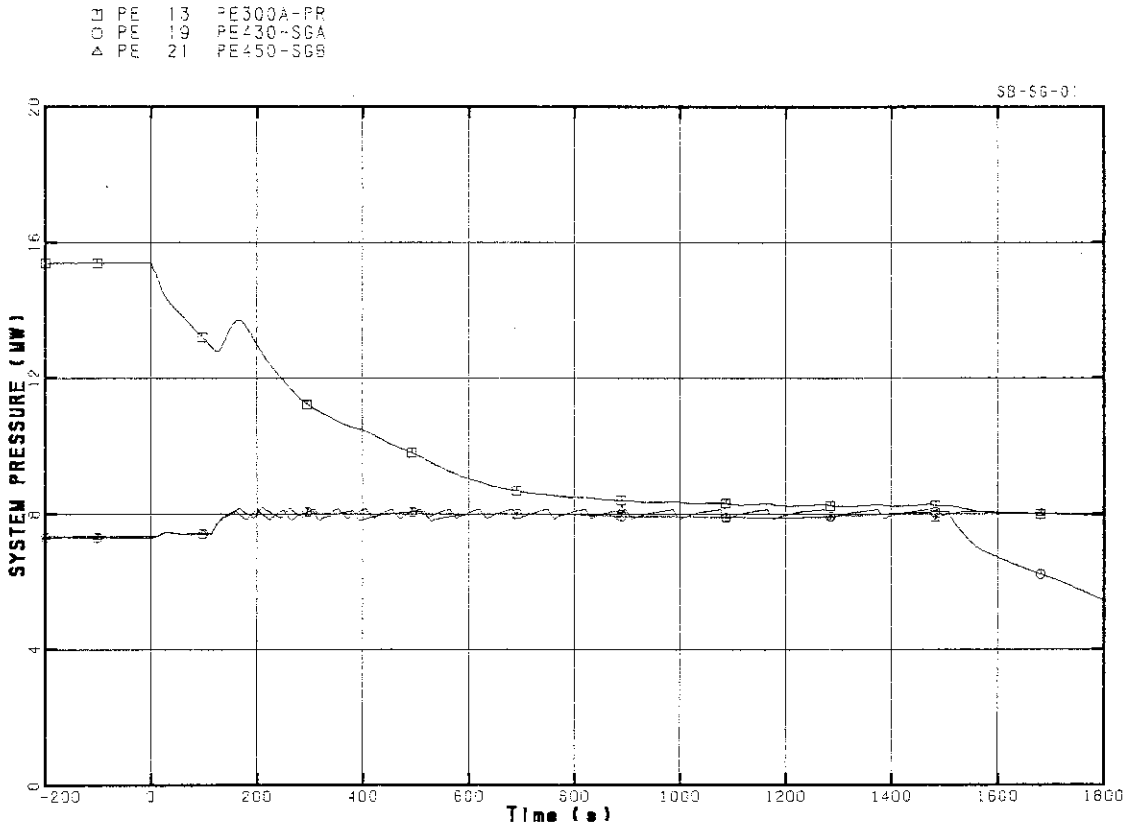

(a) Primary and secondary pressures

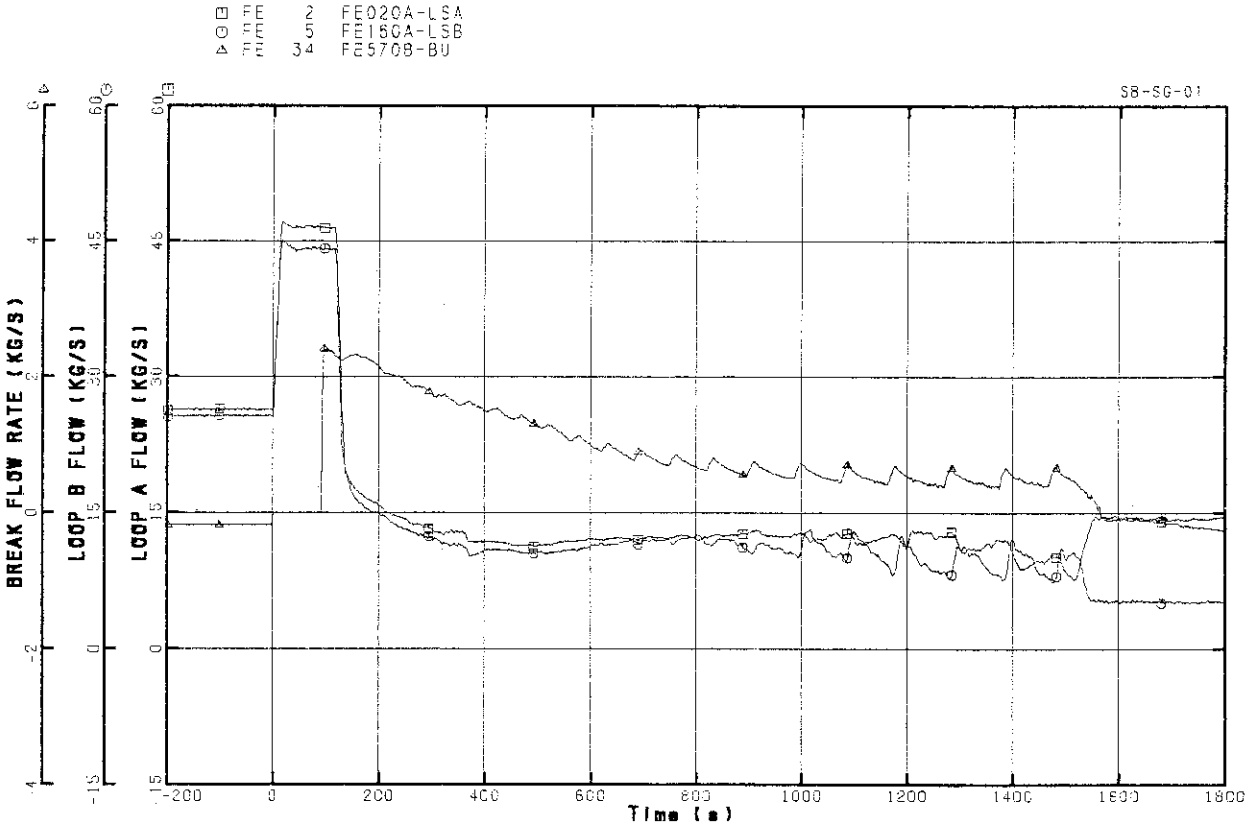

(b) Primary and break flow rates

Fig. 6.7 Major results for SG U-tube break LOCA test (SS1)

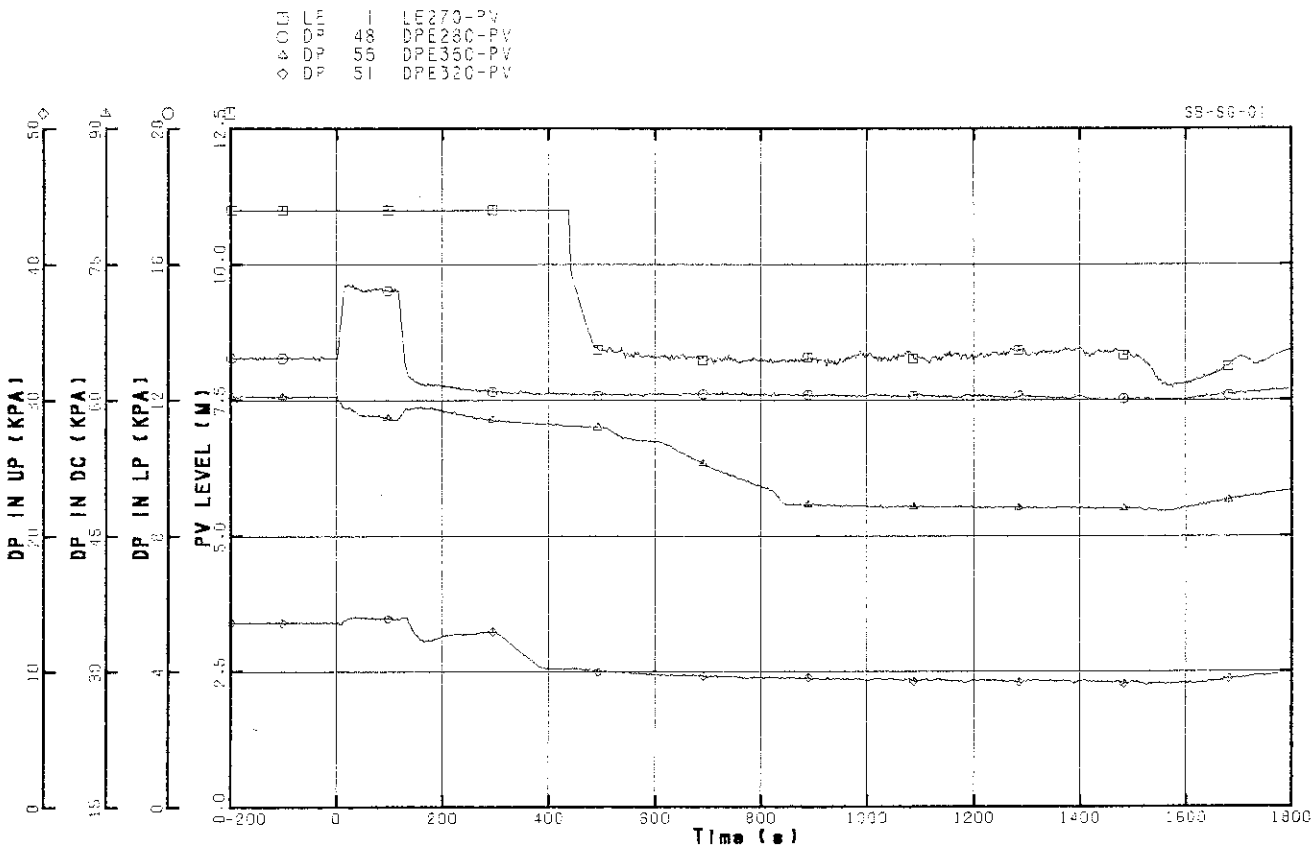

(c) Water level and differential pressures

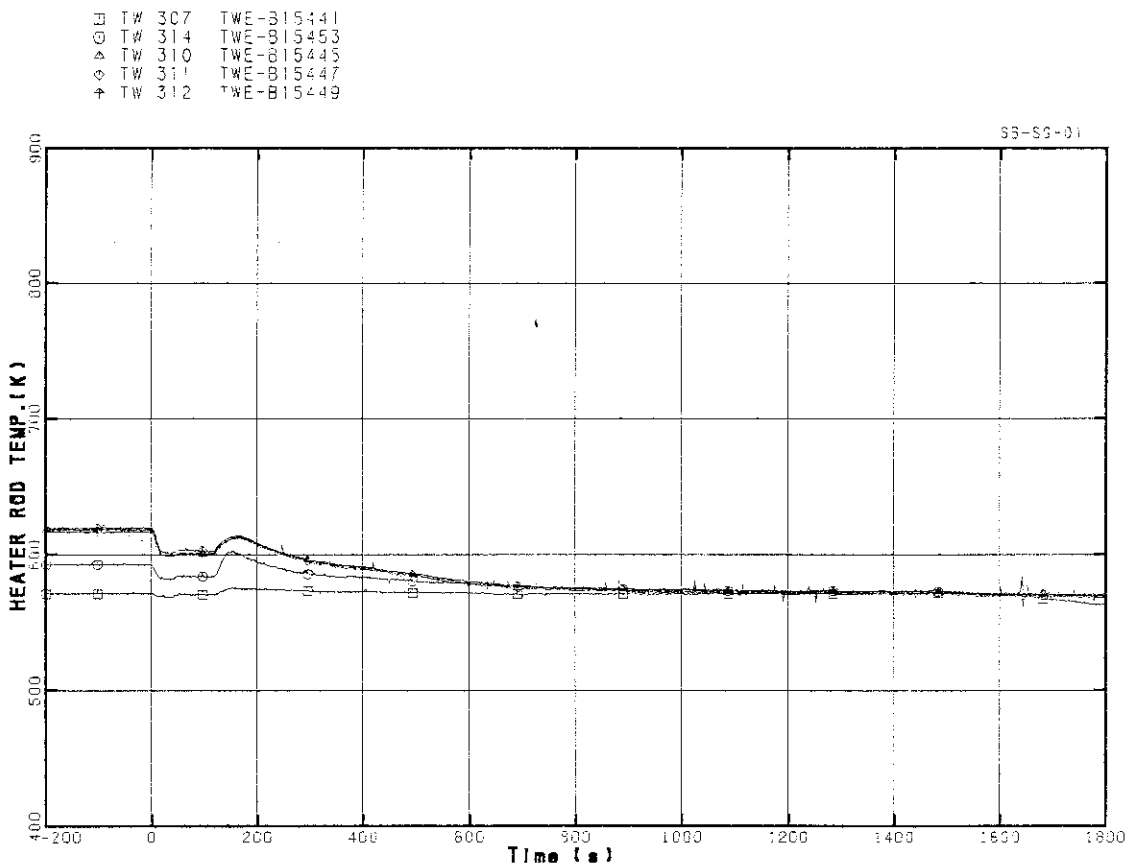

(d) Heater rod surface temperatures (high-power bundle)

Fig. 6.7 Major results for SG U-tube break LOCA test (SS1) (Cont'd)

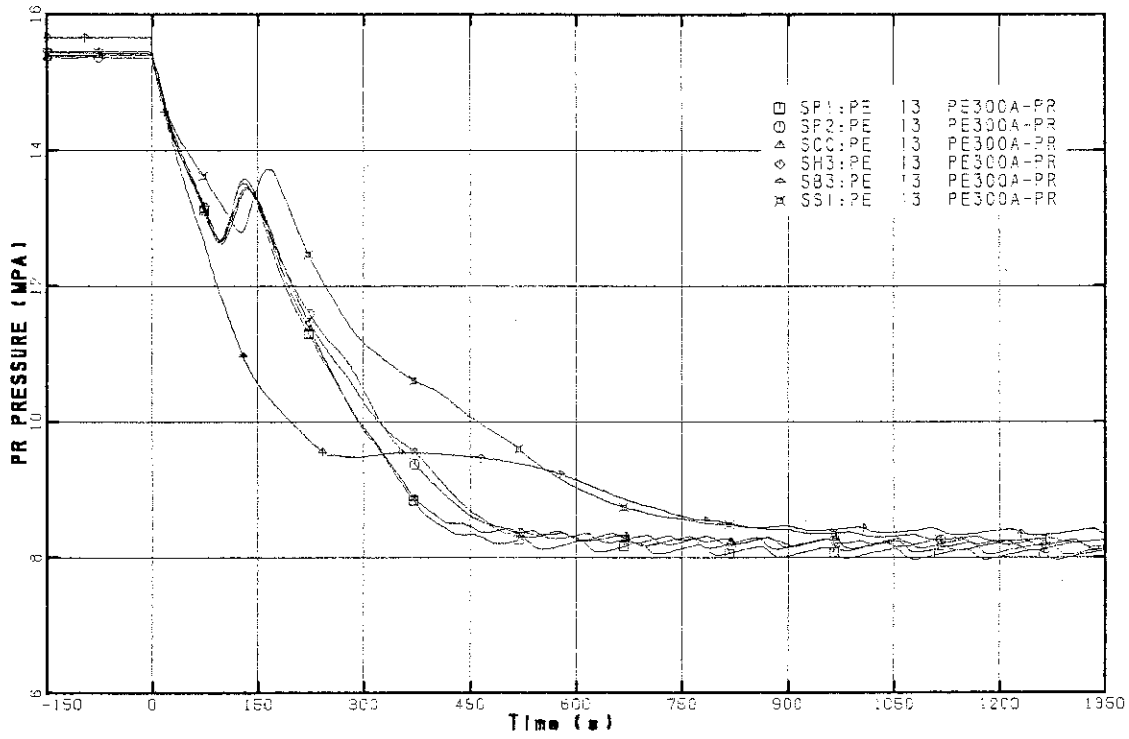

(a) Early pressure transient (until 1350 s)

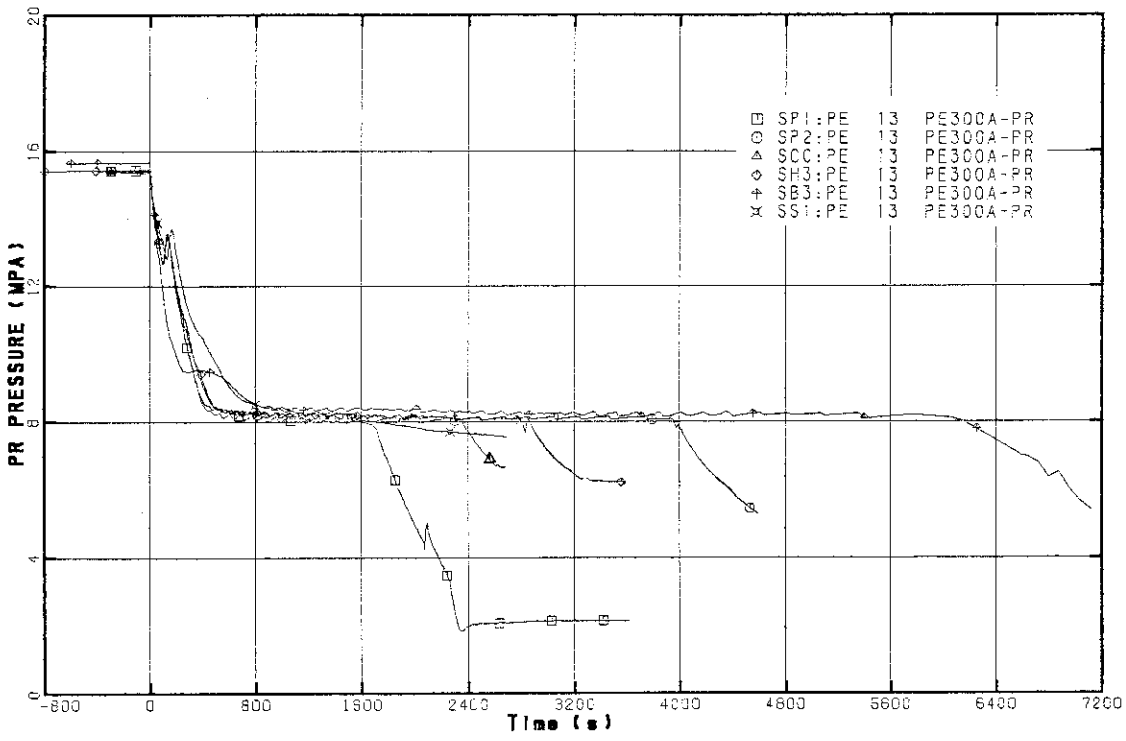

(b) Long pressure transient (until 7200 s)

Fig. 6.8 Comparison of primary pressure responses for six tests

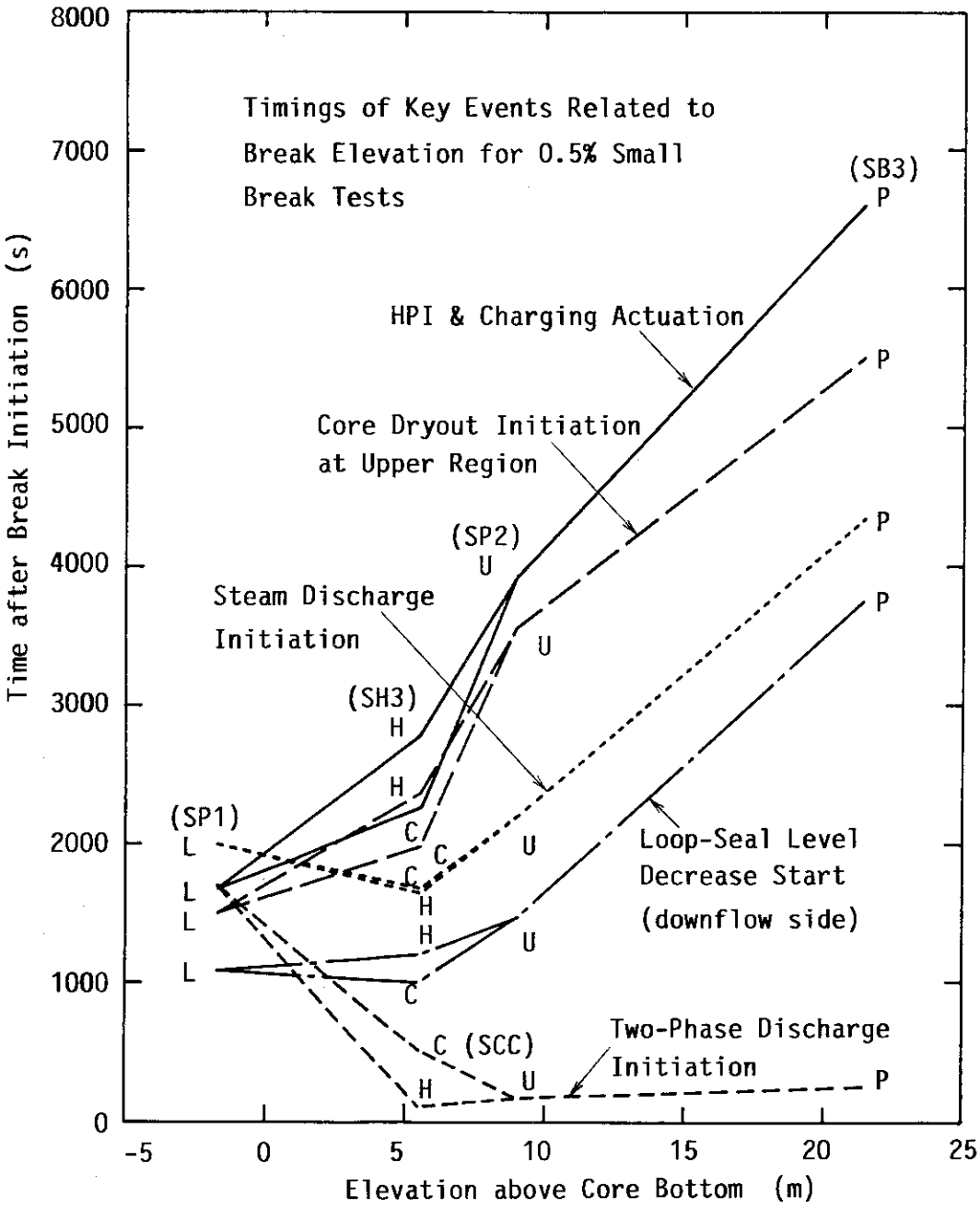

Fig. 6.9 Effect of break elevations on key event timings (SB3 test with 0.45% break area)

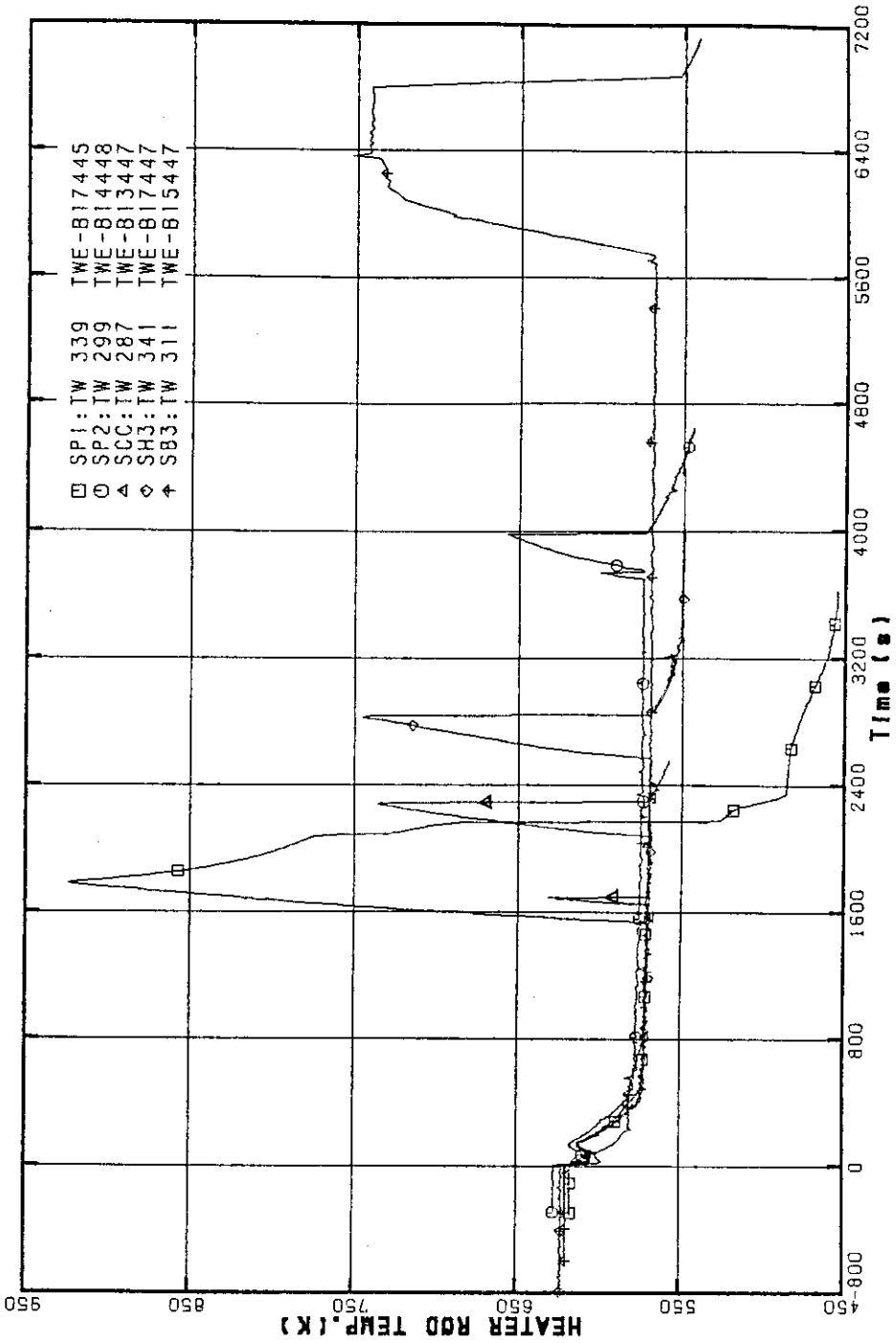

Fig. 6.10 Comparison of PCT for five tests

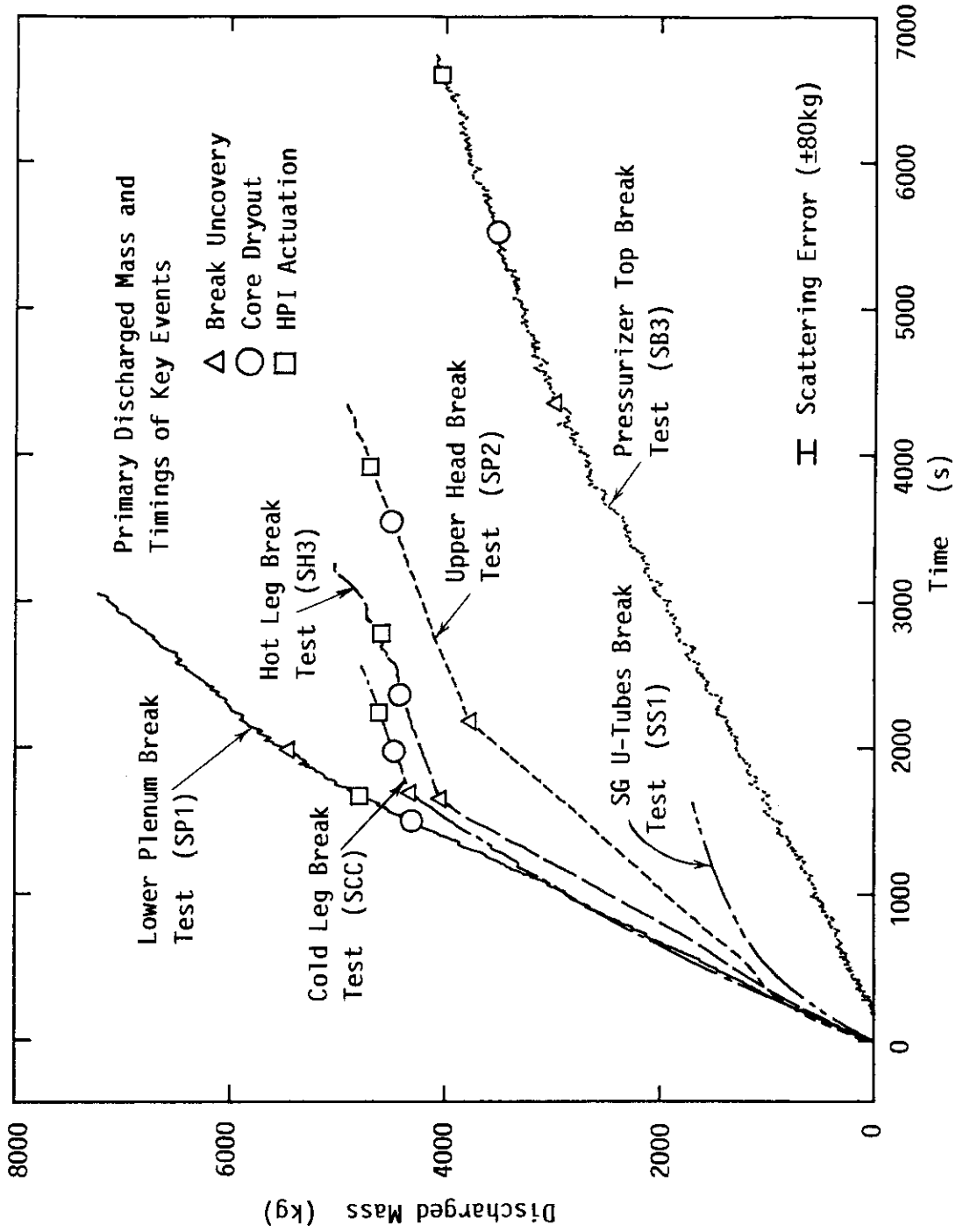

Fig. 6.11 Comparison of discharged primary mass for six tests

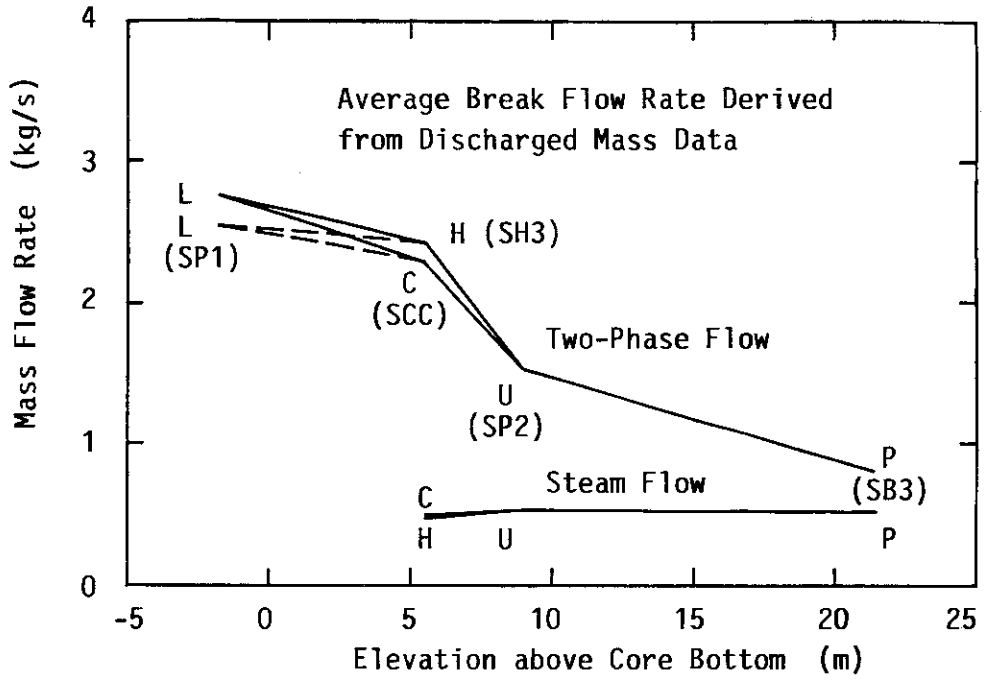

(a) Average break flow rates for two-phase and steam flows in five tests

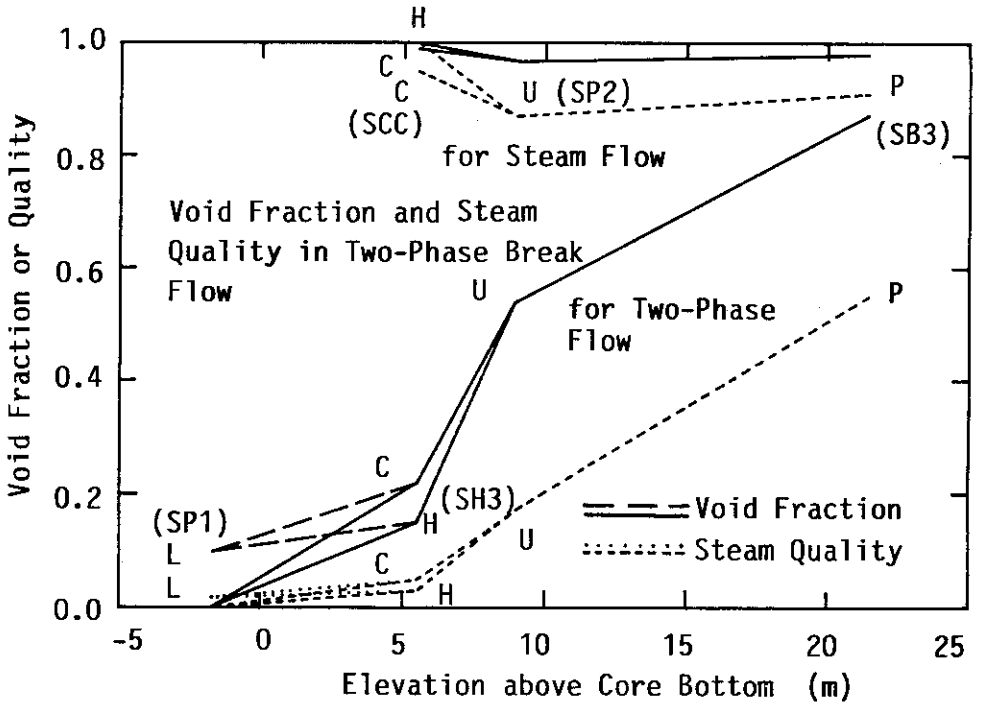

(b) Average void fraction and steam quality in two-phase flow for five tests (assuming a constant slip ratio of K=5)

Fig. 6.12 Effect of break elevations on average break flow rates and two-phase flow conditions for equivalent 0.5% break area

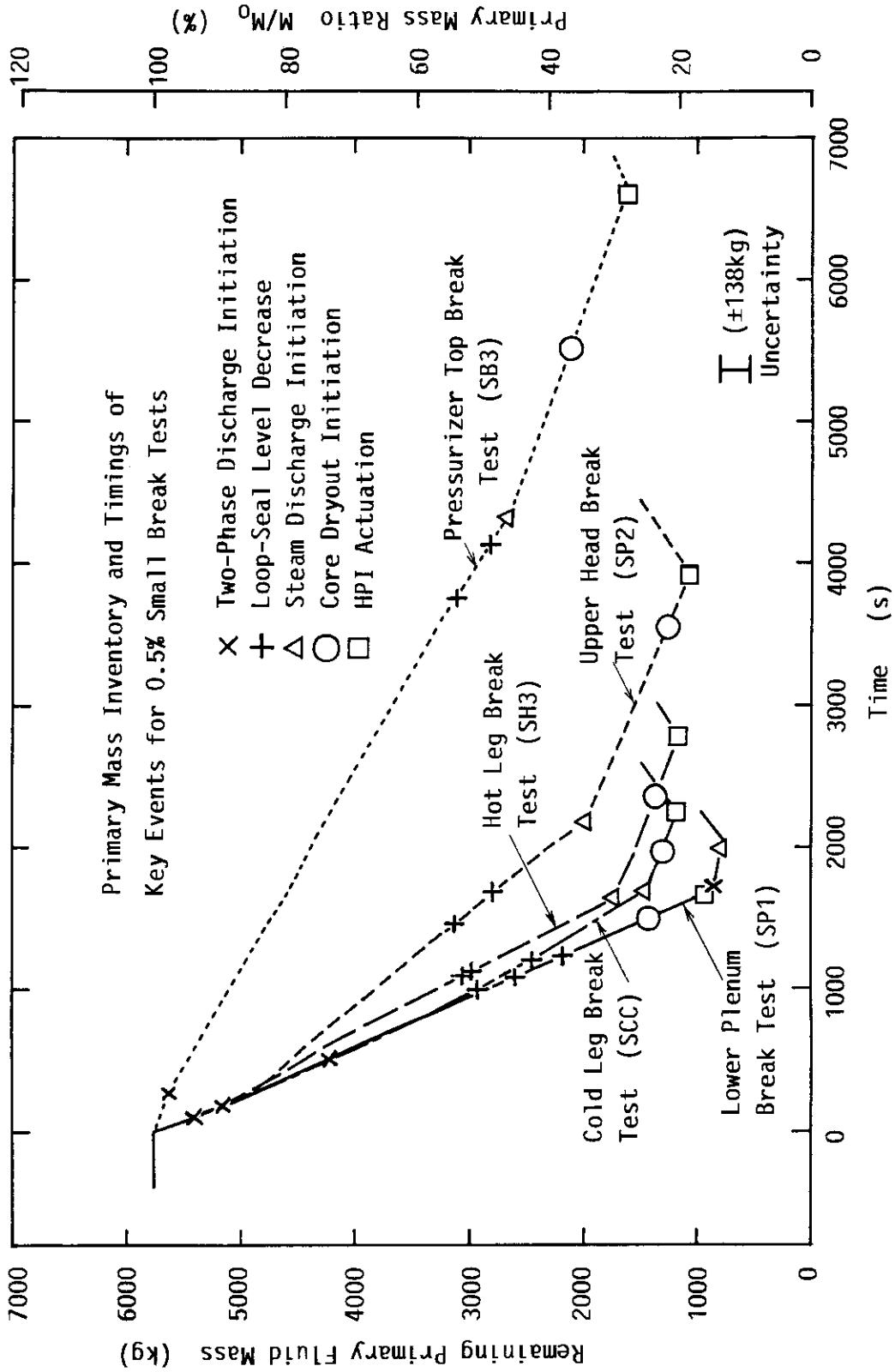

Fig. 6.13 Primary remaining fluid mass and key events in five tests (SB3 test with 0.45% break area)

Appendix A Instrument Location

Instrument locations for the primary and secondary systems of the LSTF are shown in Figs.A.1 through A.27.

List of Figures

Fig.A.1 Primary loop A instruments (I)
Fig.A.2 Primary loop A instruments (II)
Fig.A.3 Primary loop B instruments (I)
Fig.A.4 Primary loop B instruments (II)
Fig.A.5 Instruments of pressurizer and associated lines
Fig.A.6 Suppression tank and break unit type I instruments
Fig.A.7 Break unit type II instruments
Fig.A.8 Main feedwater line, aux. feedwater line and jet condenser instruments
Fig.A.9 Main steam line, relief valve line and safety valve line instruments
Fig.A.10 Vertical locations of pressure vessel instruments (Except simulated core) (I)
Fig.A.11 Vertical locations of pressure vessel instruments (Except simulated core) (II)
Fig.A.12 Vertical locations of pressure vessel instruments (Except simulated core) (III)
Fig.A.13 Horizontal locations of pressure vessel instruments (Except simulated core) (I)
Fig.A.14 Horizontal locations of pressure vessel instruments (Except simulated core) (II)
Fig.A.15 Horizontal locations of pressure vessel instruments (Except simulated core) (III)
Fig.A.16 Horizontal locations of pressure vessel instruments (Except simulated core) (IV)
Fig.A.17 Horizontal locations of pressure vessel instruments (Except simulated core) (V)

Fig.A.18 Locations of pressure vessel simulated core instruments
Fig.A.19 Locations of selected primary loop A and B instruments
Fig.A.20 Instruments locations on inlet pipe of steam generator B
Fig.A.21 Locations of selected primary loop A and B instruments
Fig.A.22 Locations of temperature measurements for steam generators A and B (I)
Fig.A.23 Locations of temperature measurements for steam generators A and B (II)
Fig.A.24 Locations of pressure and differential pressure measurements for steam generators A and B
Fig.A.25 Locations of steam generatorss A and B secondary liquid level and downcomer flow measurement
Fig.A.26 Locations of steam generators A and B conduction probe measurements
Fig.A.27 Locations of pressurizer measurements

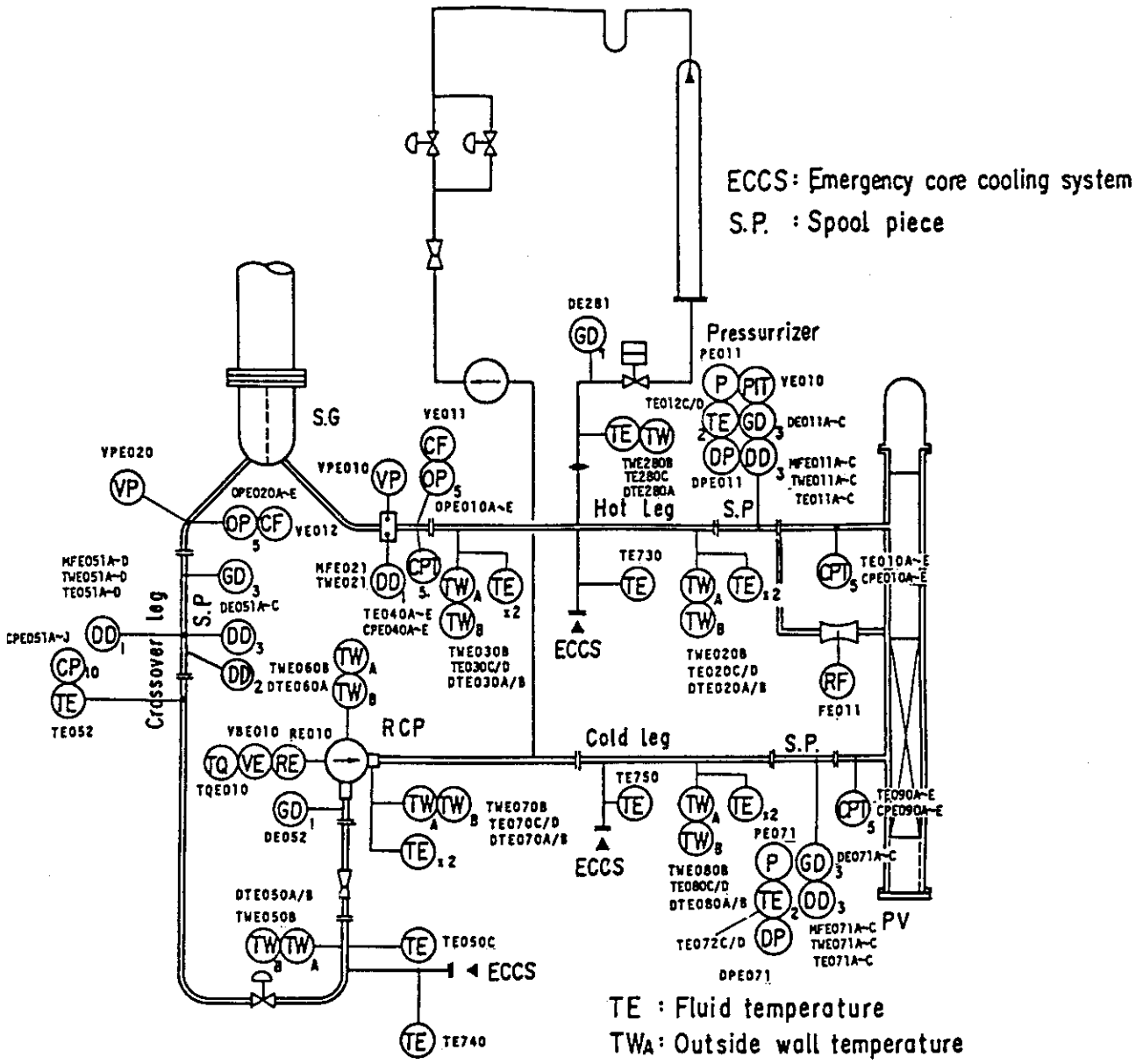

Fig.A.1 Primary loop A instruments (I)

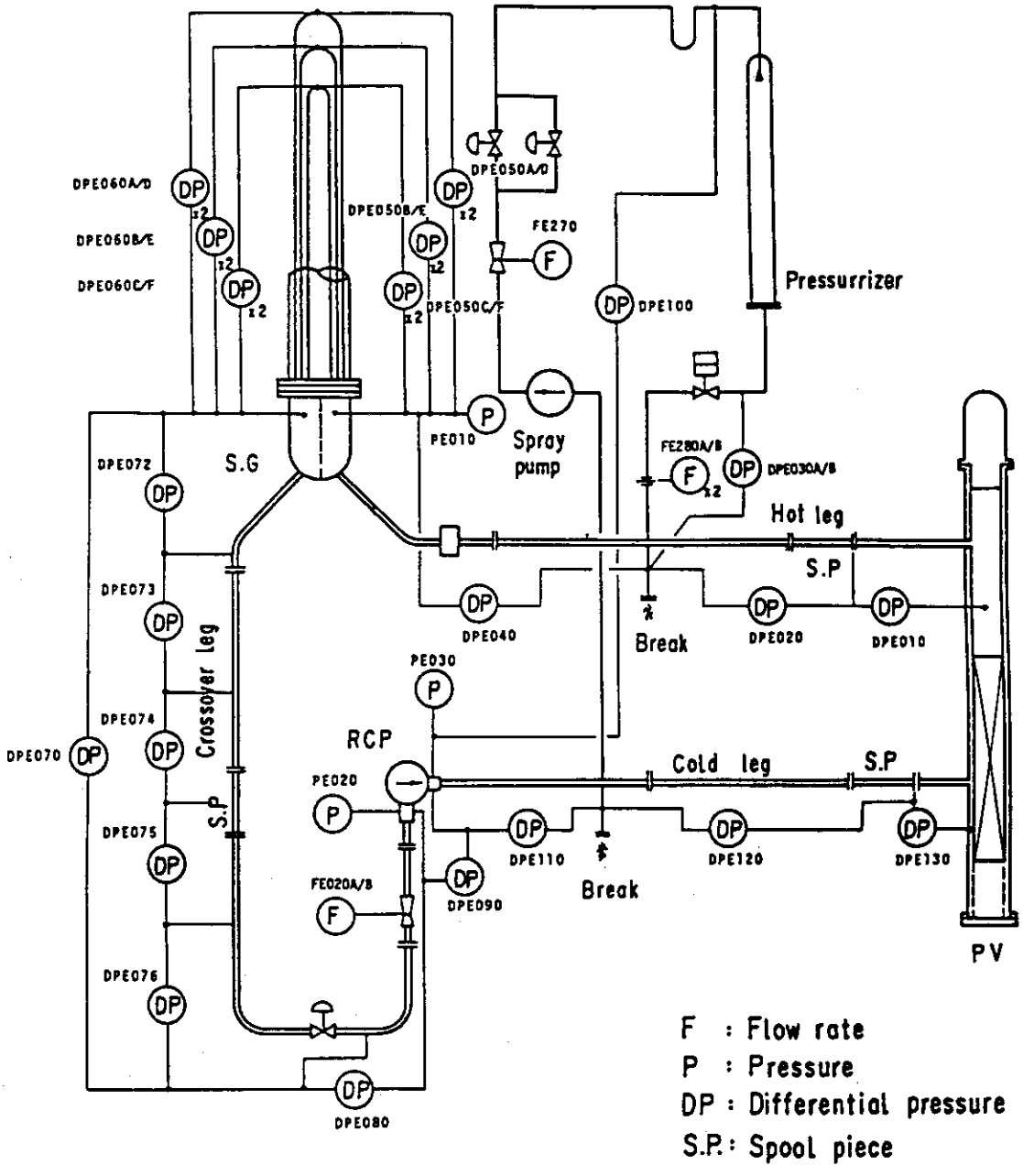

Fig.A.2 Primary loop A instruments (II)

VP : Video probe
GD_3 : 3 beams γ－densitometer
DD : Drag disk flow meter
PIT : Pitot－tube velocimeter
OP_5 : Optical liquid level detector
CP_{10} : Conductance probe
RF : Reflux flow meter
DP : Differential pressure
P : Pressure
CPT_5 : Conductance probe with TC
TE : Fluid temperature
TW : Outside wall temperature
TW : Inside wall temperature
RE : Rotation speed
VE : Pump oscillation
TQ : Pump torque

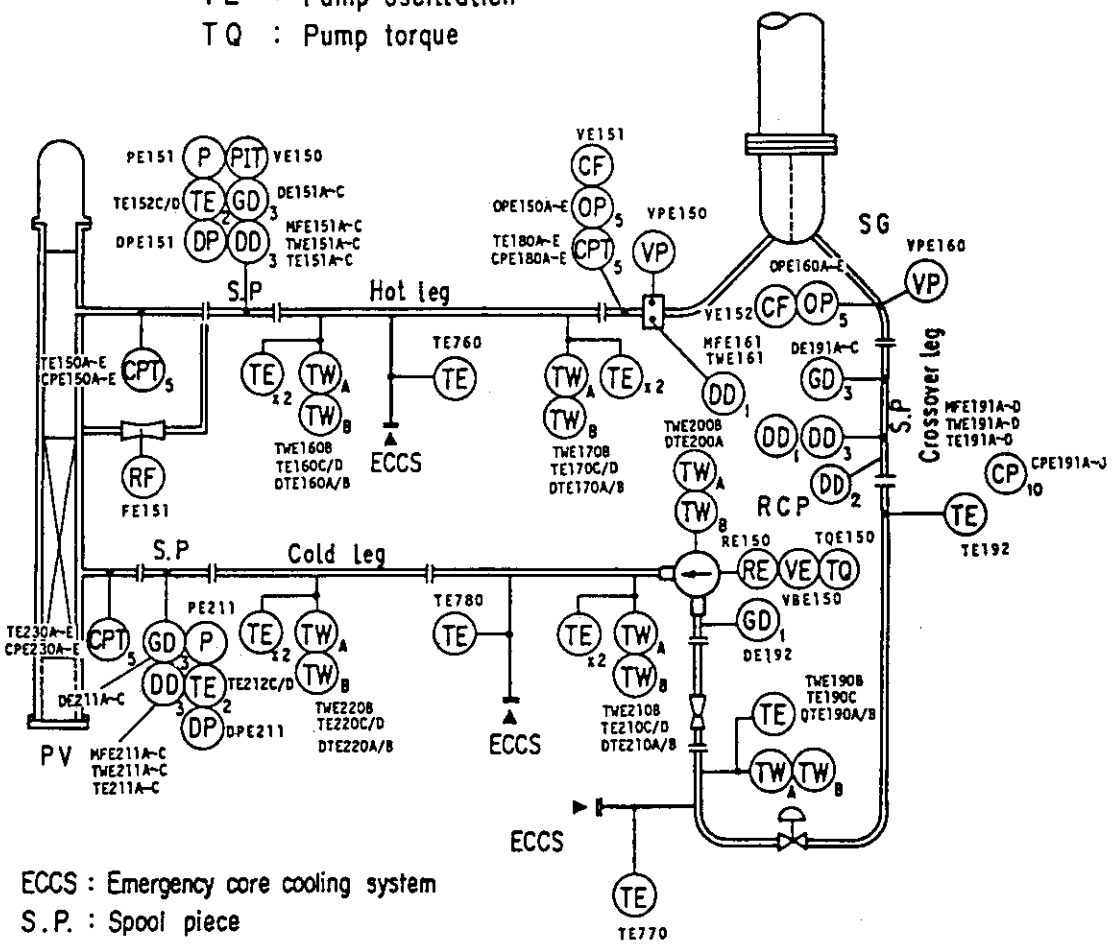

ECCS : Emergency core cooling system
S.P. : Spool piece

Fig.A.3 Primary loop B instruments (I)

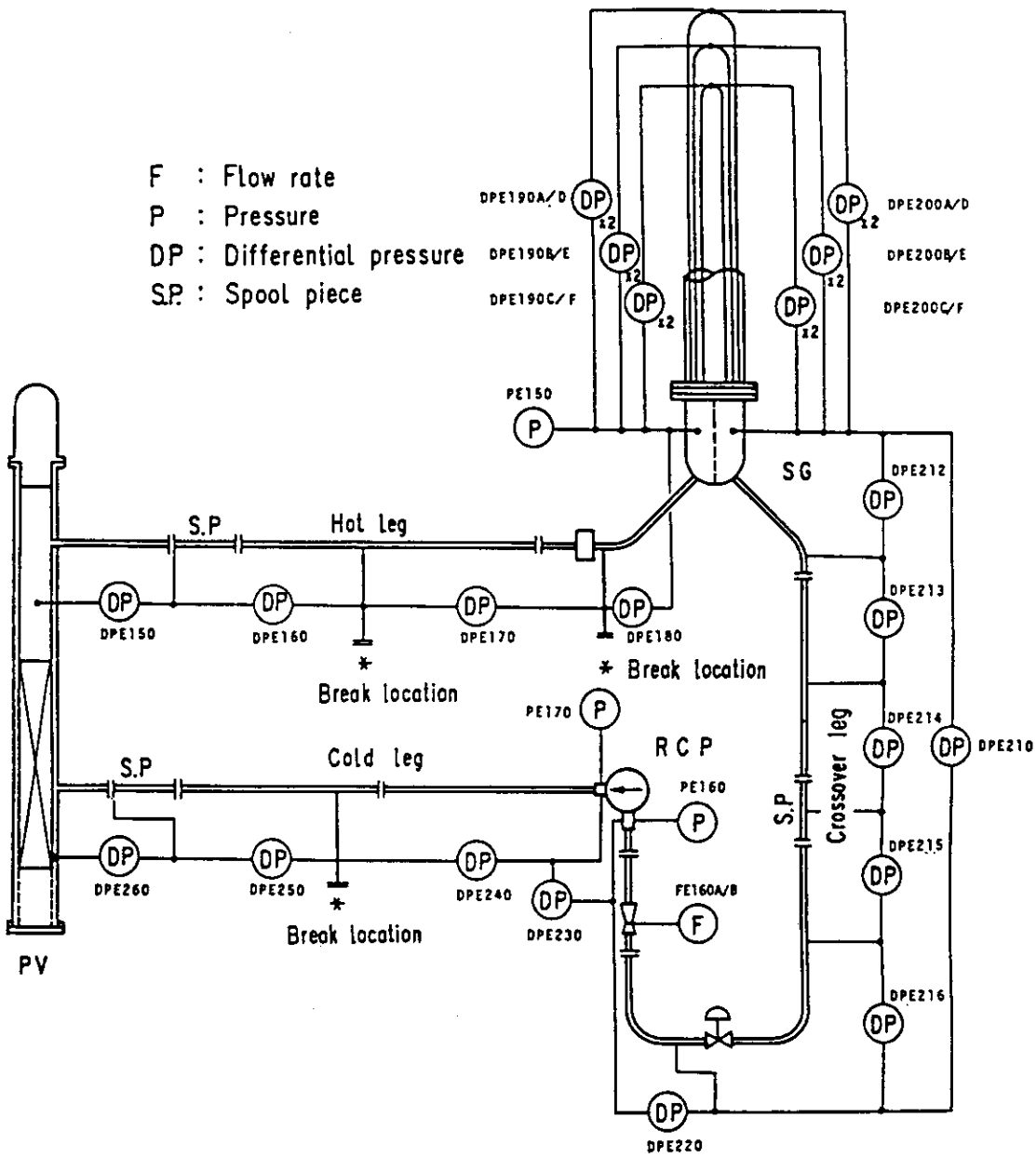

Fig.A.4 Primary loop B instruments (II)

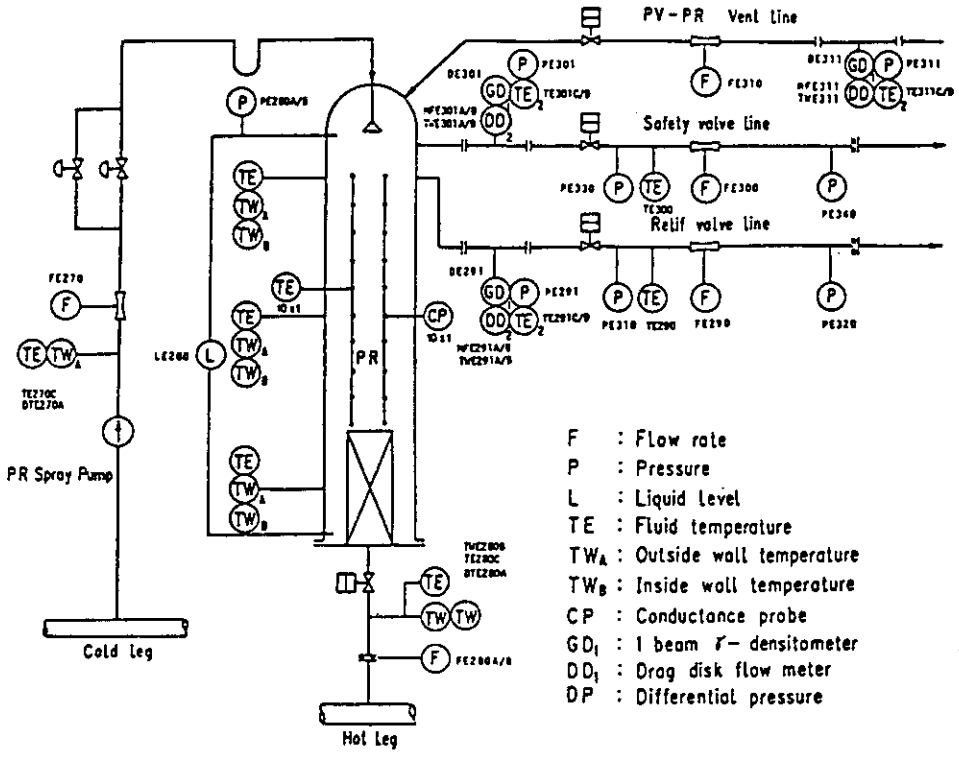

Fig.A.5 Instruments of pressurizer and associated lines

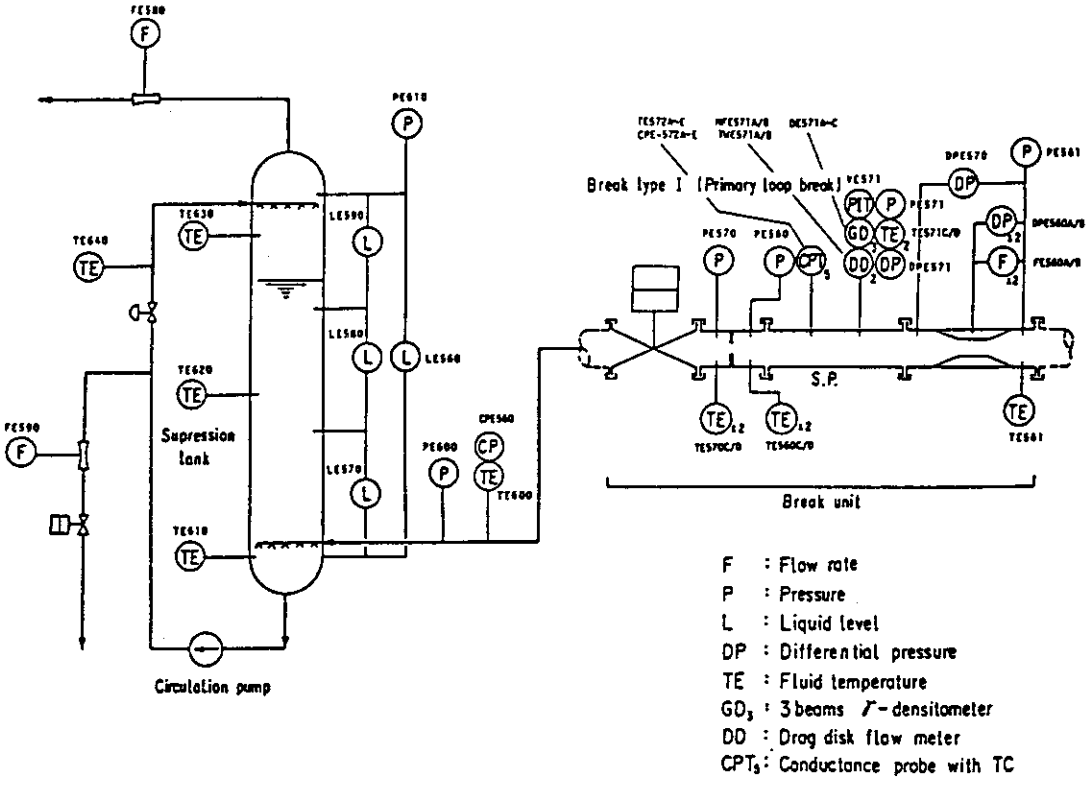

Fig.A.6 Suppression tank and break unit type I instruments

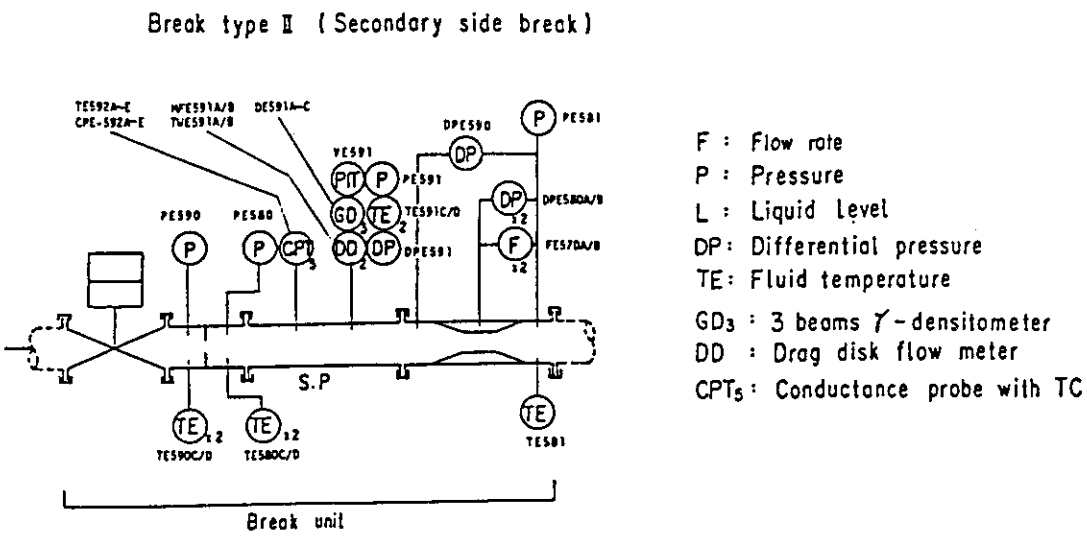

Fig.A.7 Break unit type II instruments

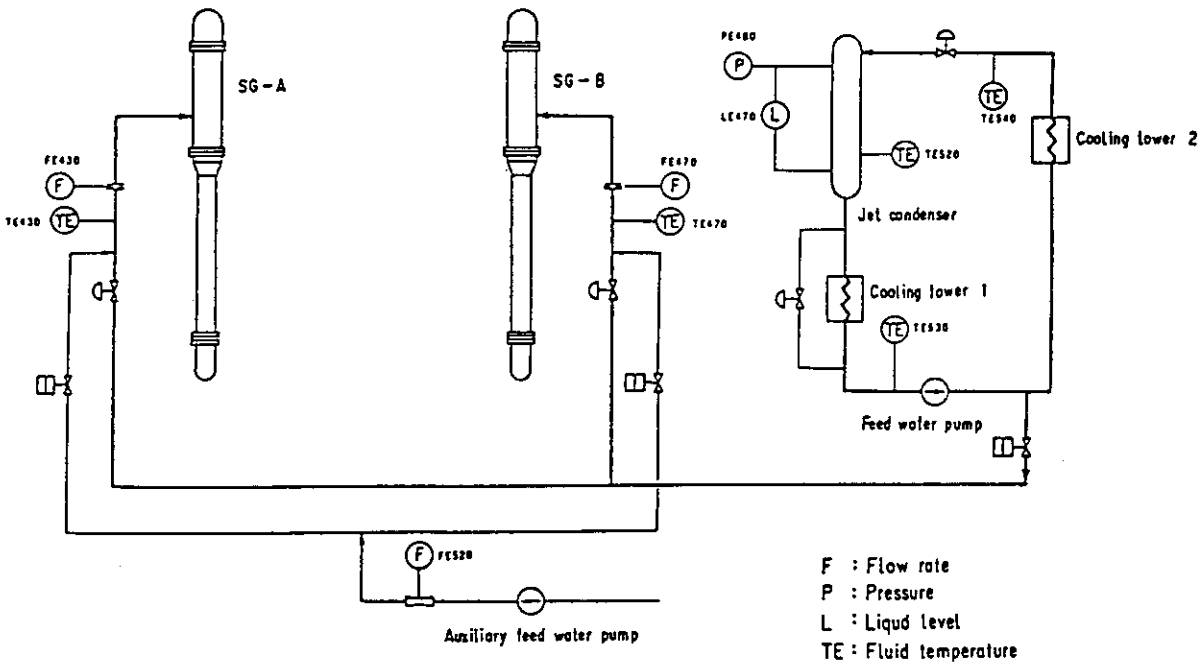

Fig.A.8 Main feedwater line, aux. feedwater line and jet condenser instruments

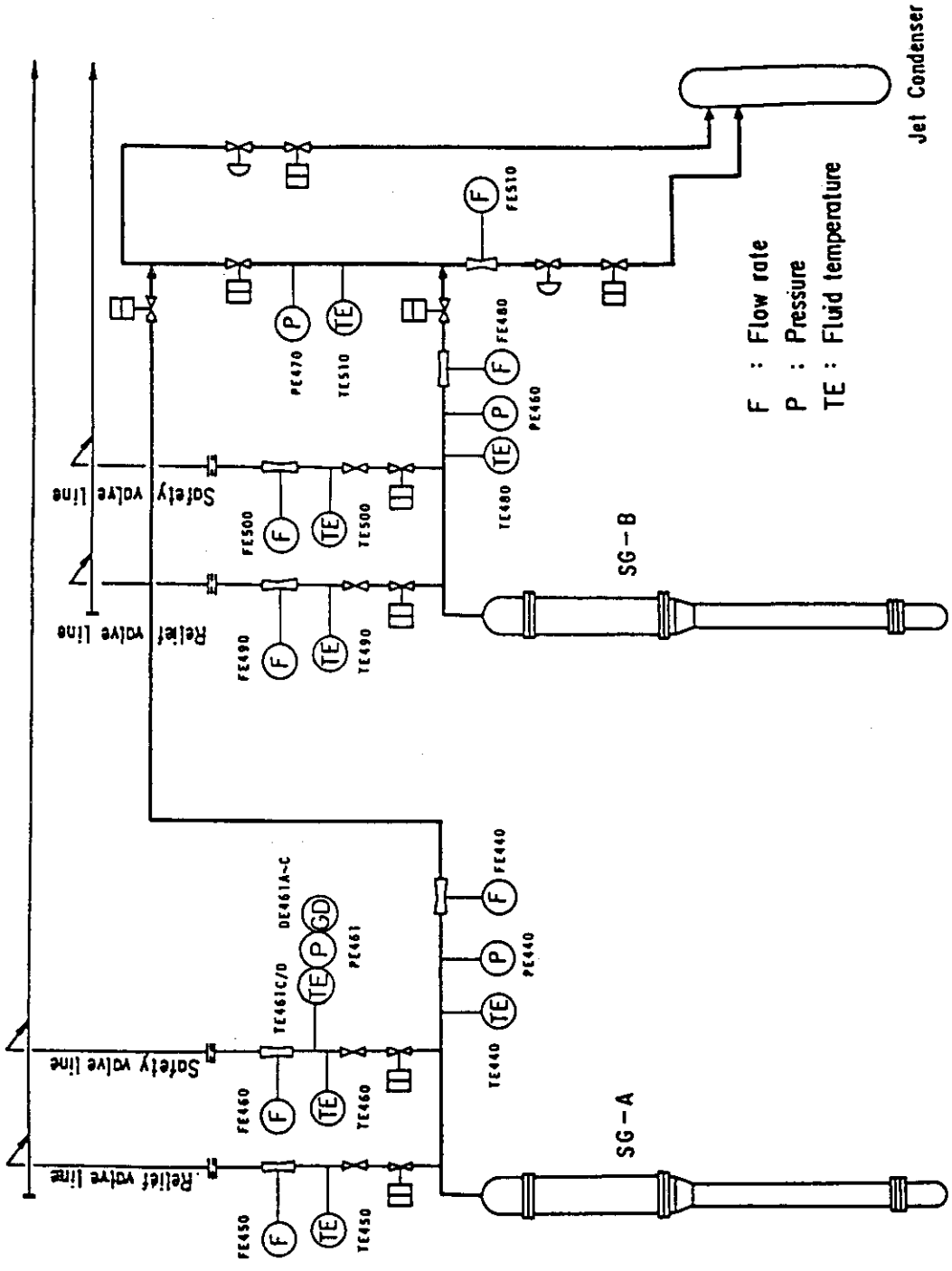

Fig.A.9 Main steam line, relief valve line and safety valve line instruments

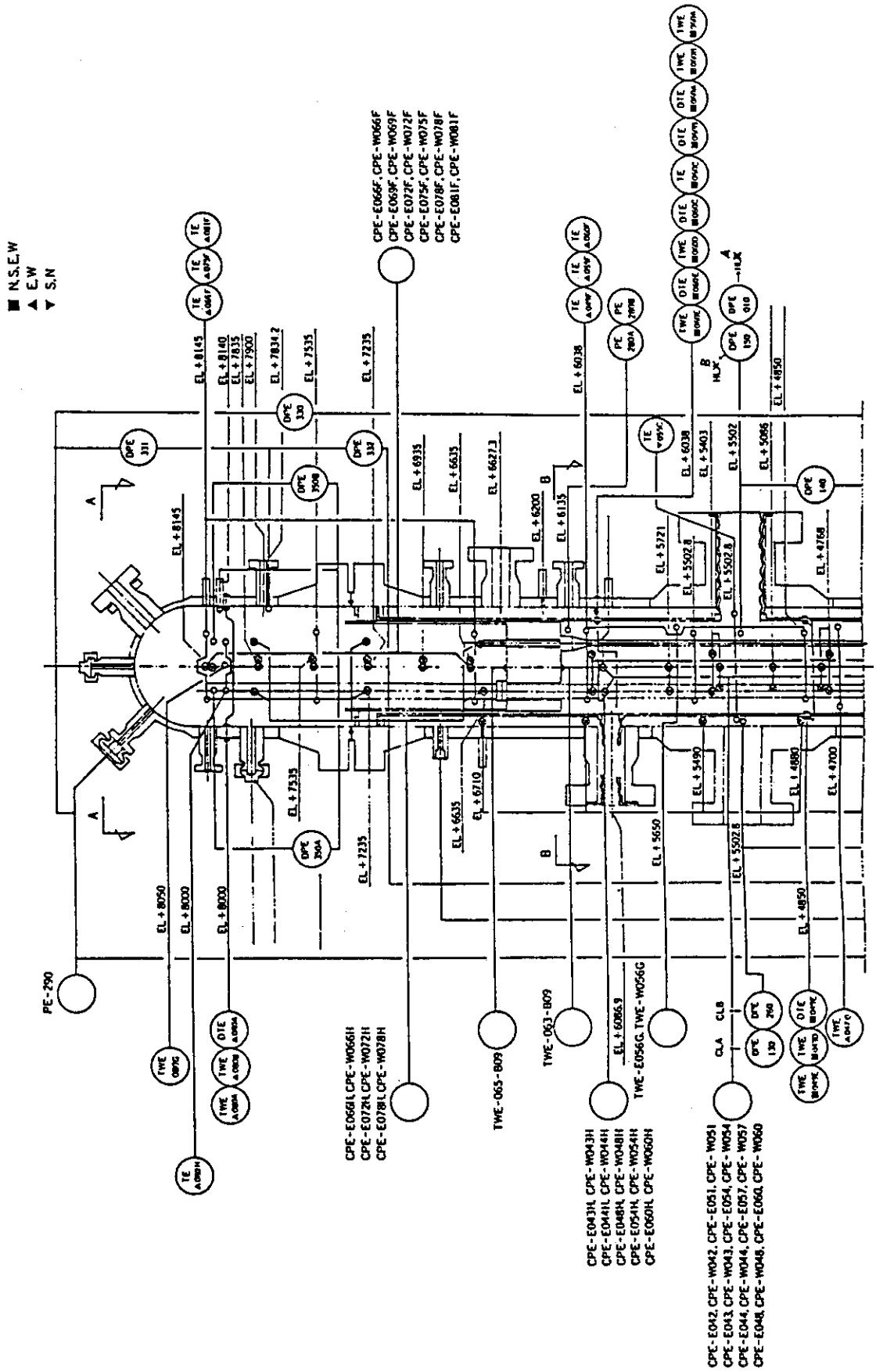

Fig.A.10 Vertical locations of pressure vessel instruments (Except simulated core) (I)

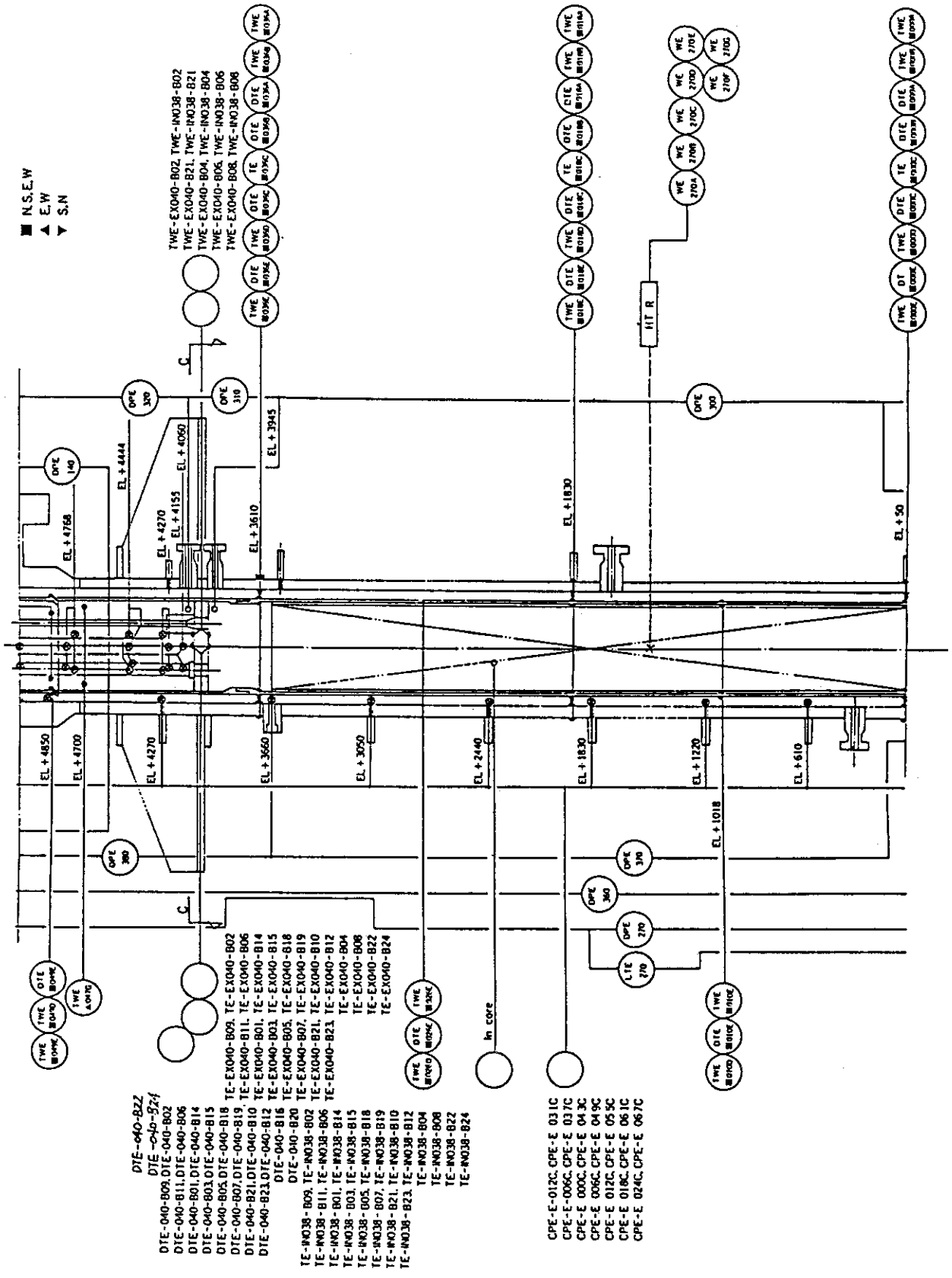

Fig.A.11 Vertical locations of pressure vessel instruments (Except simulated core) (II)

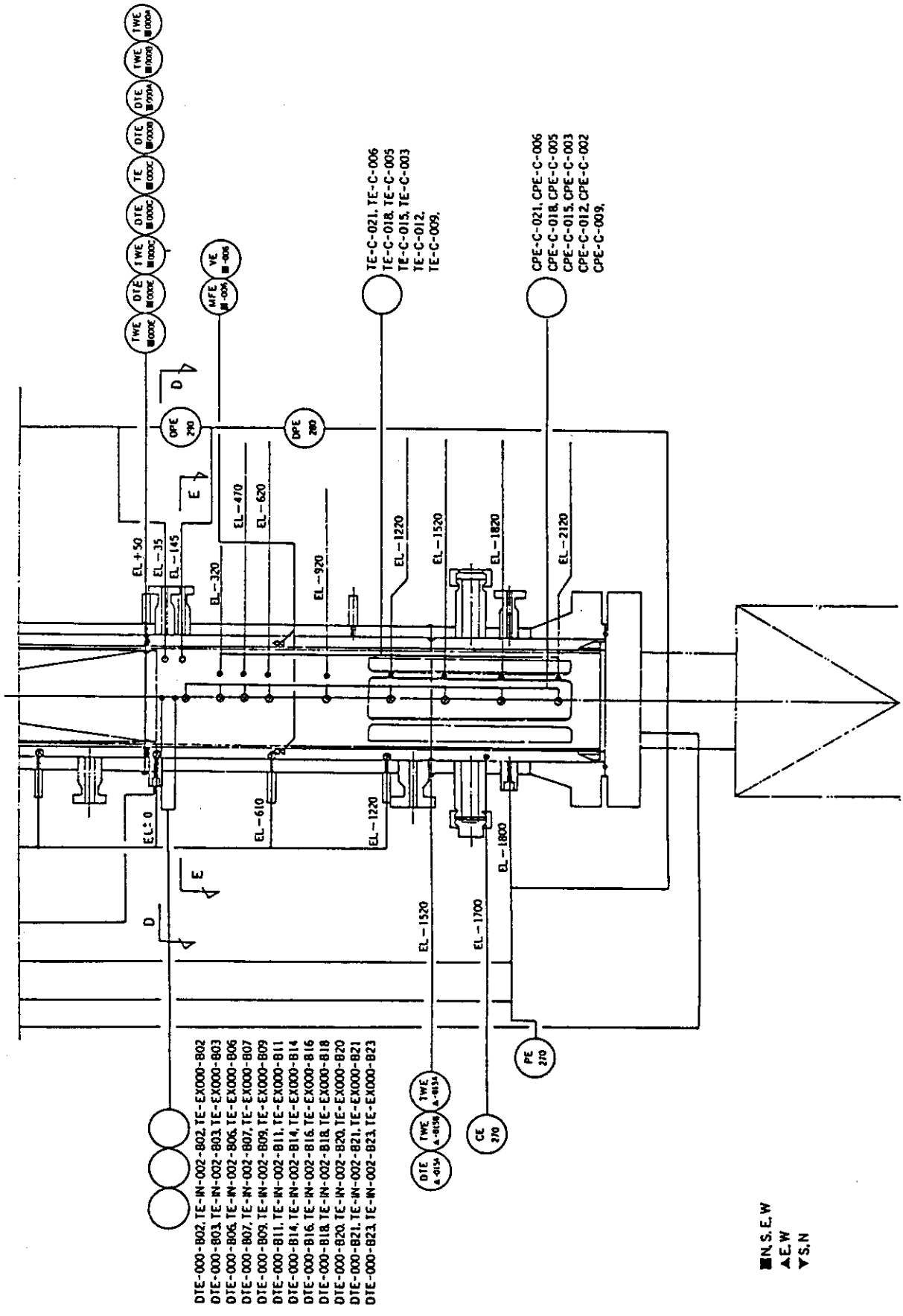

Fig.A.12 Vertical locations of pressure vessel instruments (Except simulated core) (III)

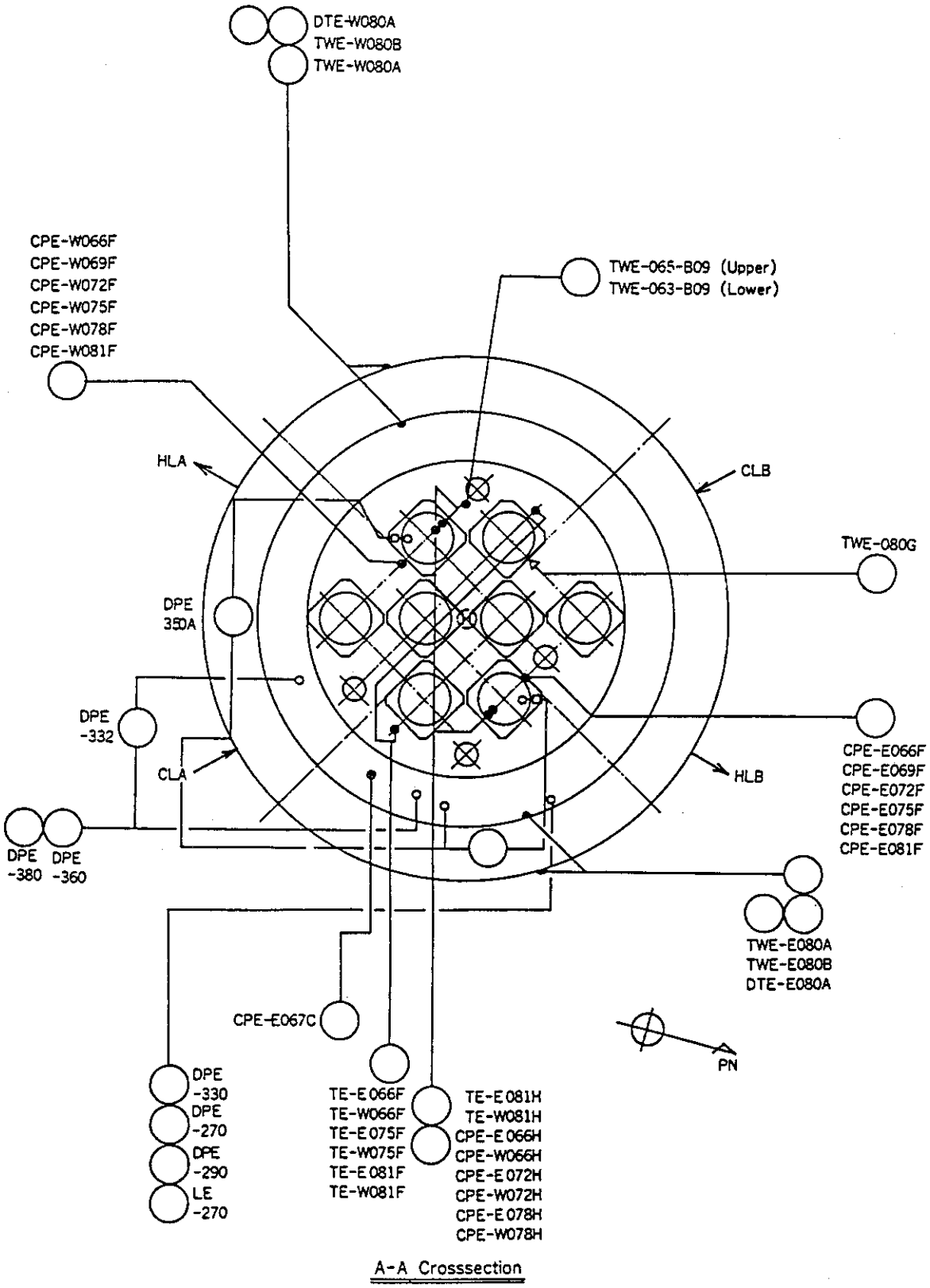

Fig.A.13 Horizontal locations of pressure vessel instruments (Except simulated core) (I)

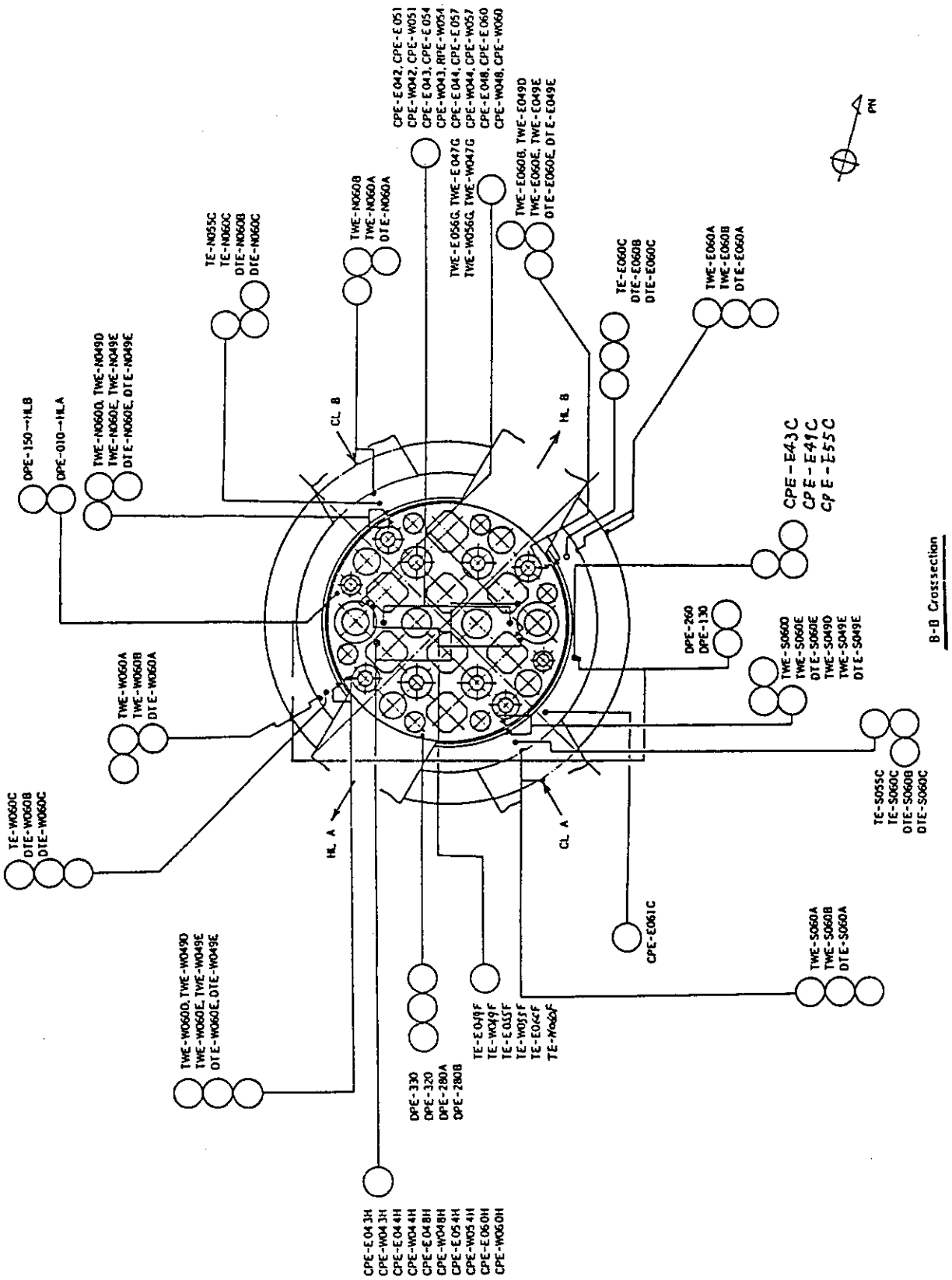

Fig.A.14 Horizontal locations of pressure vessel instruments (Except simulated core) (II)

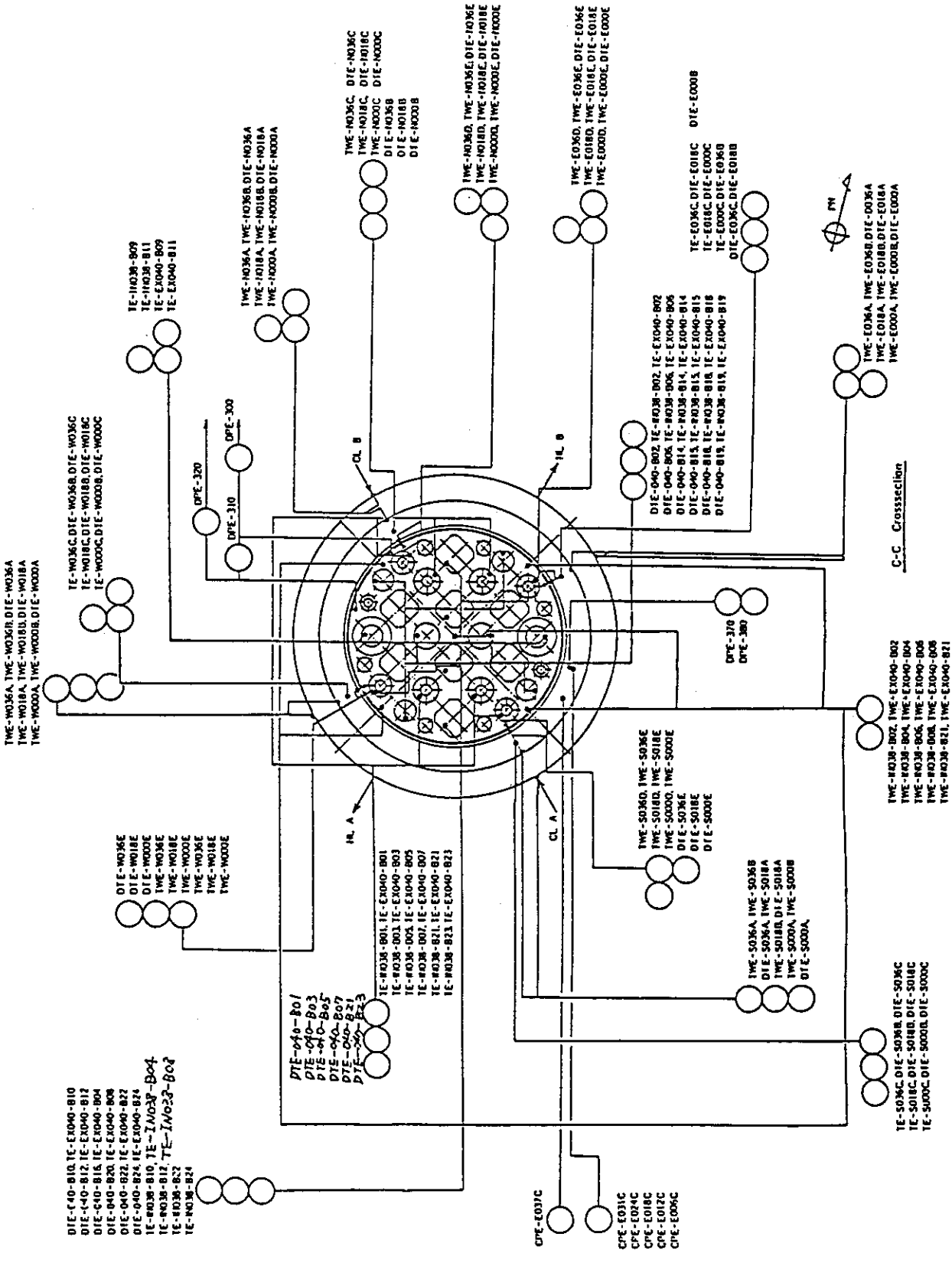

Fig.A.15 Horizontal locations of pressure vessel instruments (Except simulated core) (III)

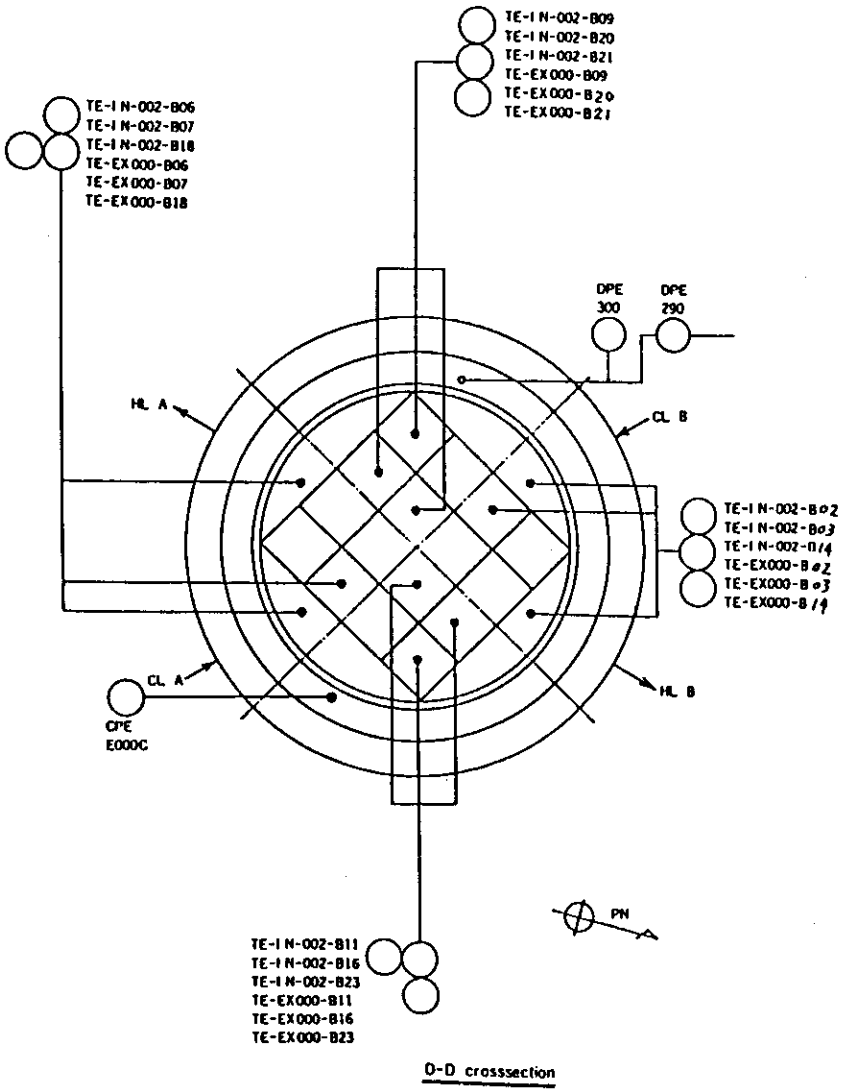

Fig.A.16 Horizontal locations of pressure vessel instruments (Except simulated core) (IV)

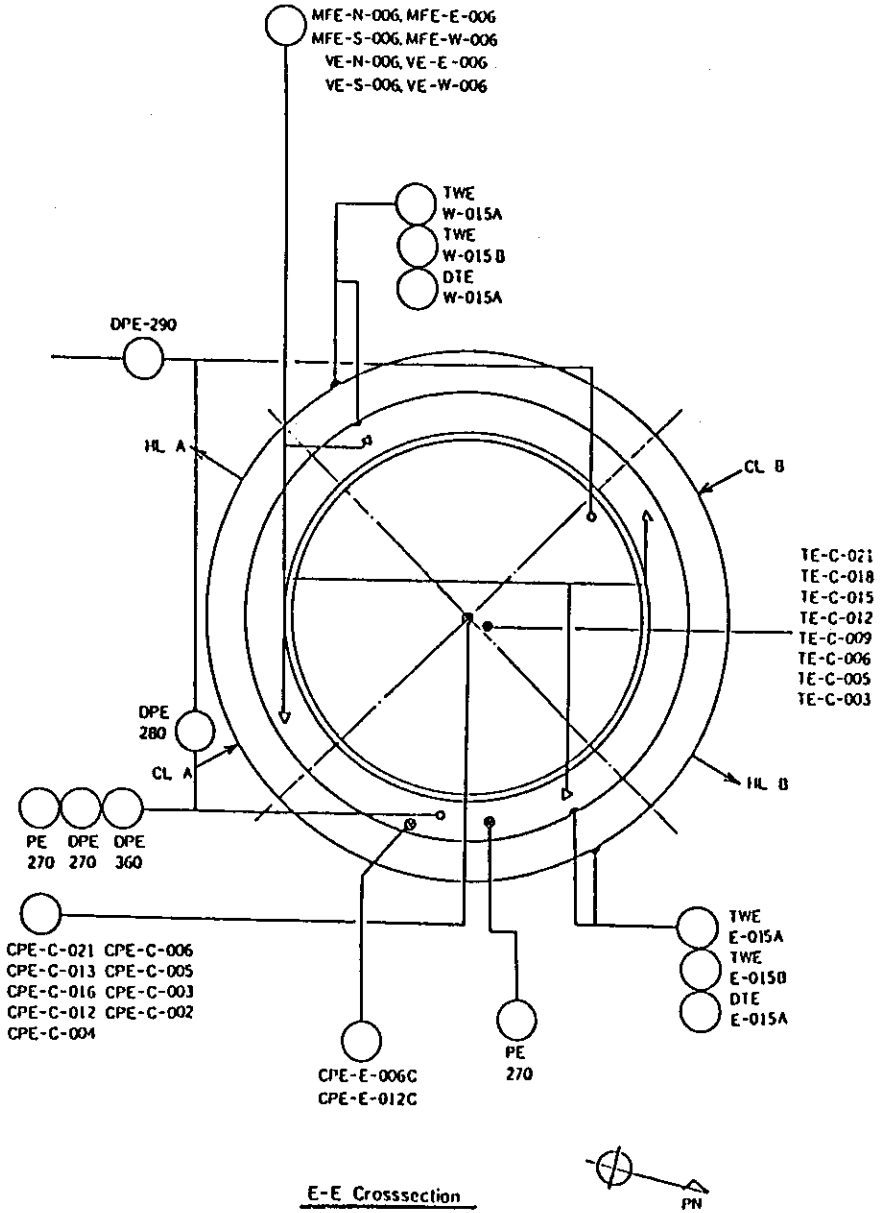

Fig.A.17 Horizontal locations of pressure vessel instruments (Except simulated core) (V)

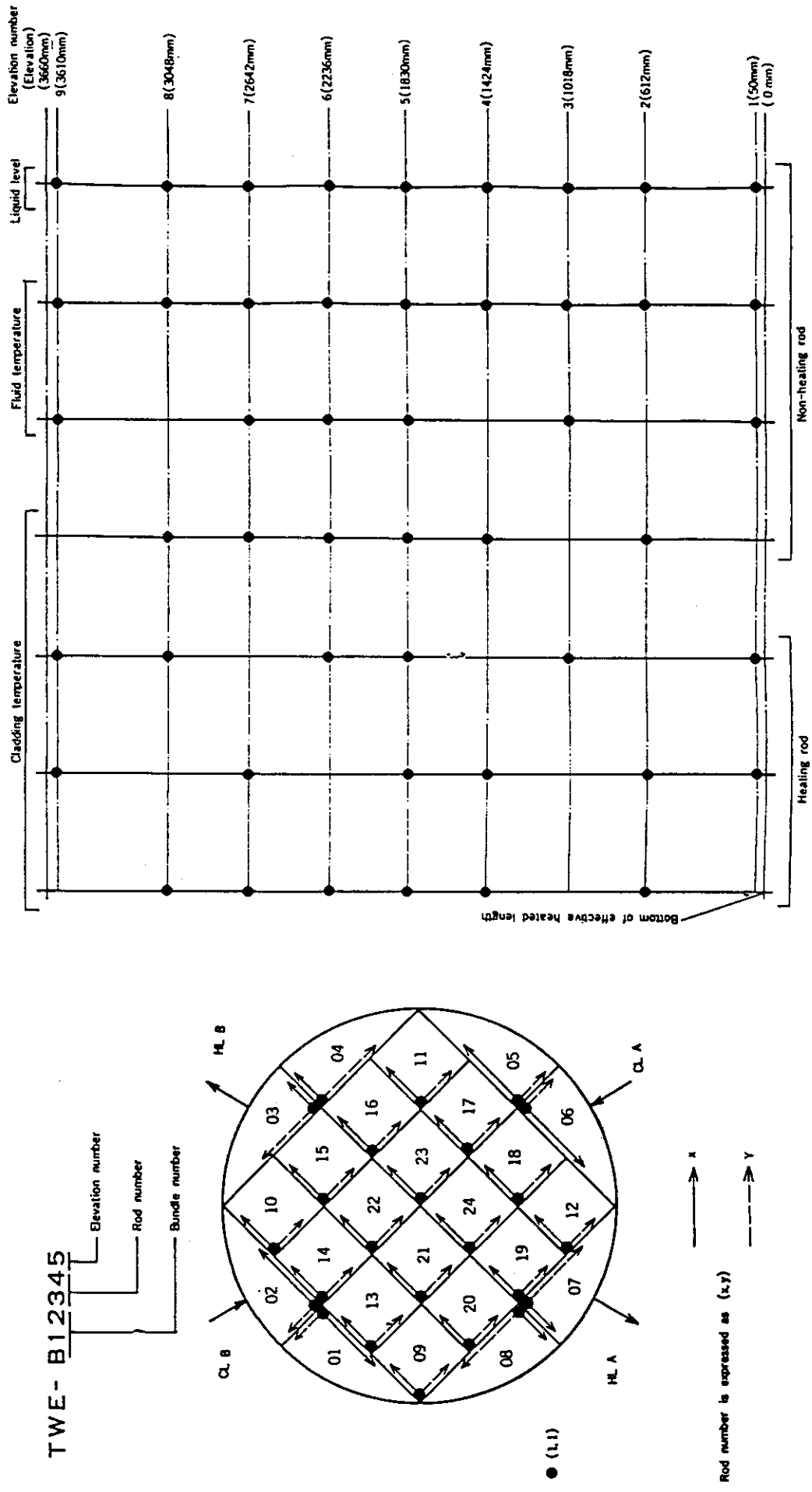

Fig.A.18 Locations of pressure vessel simulated core instruments

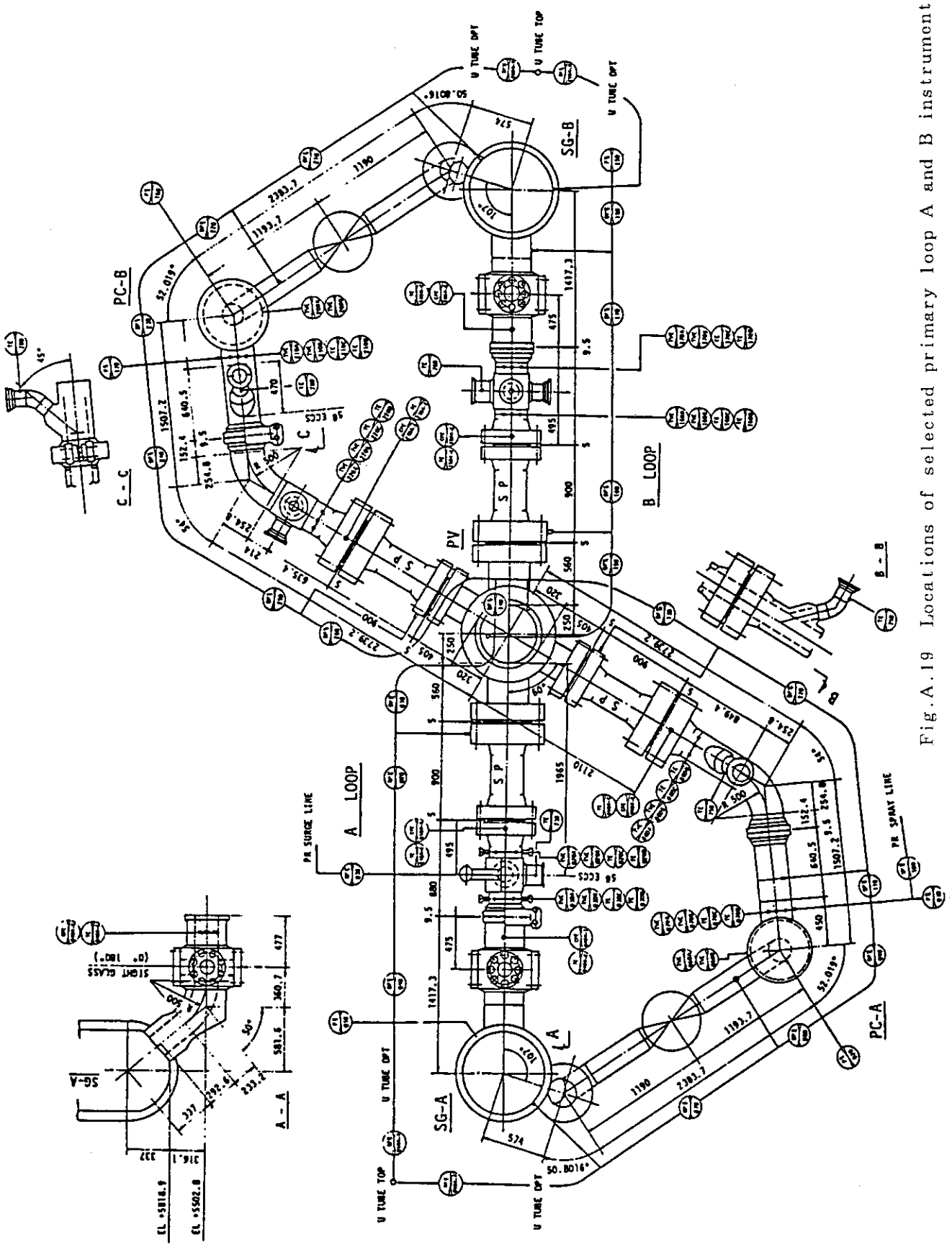

Fig.A.19 Locations of selected primary loop A and B instruments

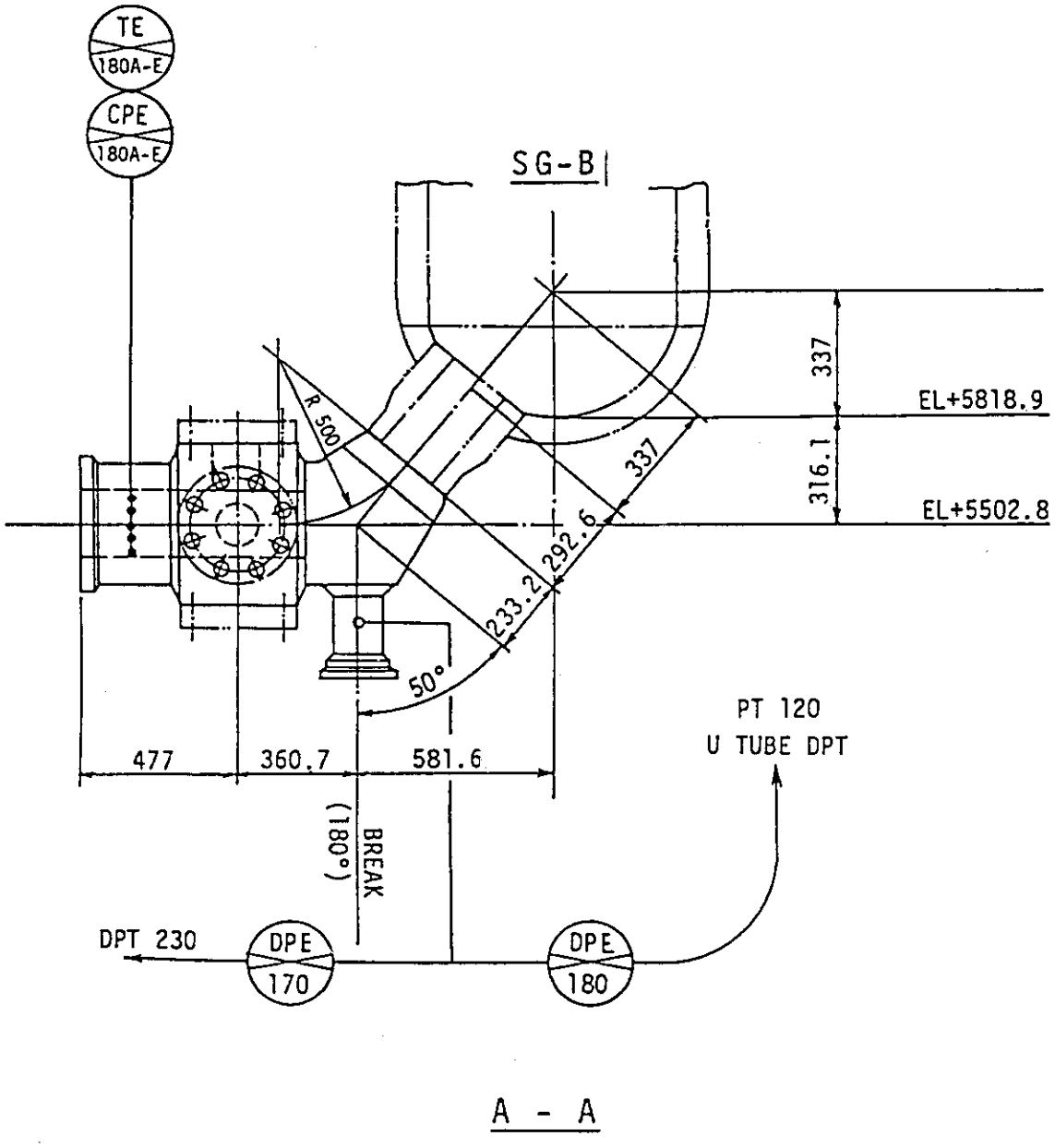

Fig.A.20 Instruments locations on inlet pipe of steam generator B

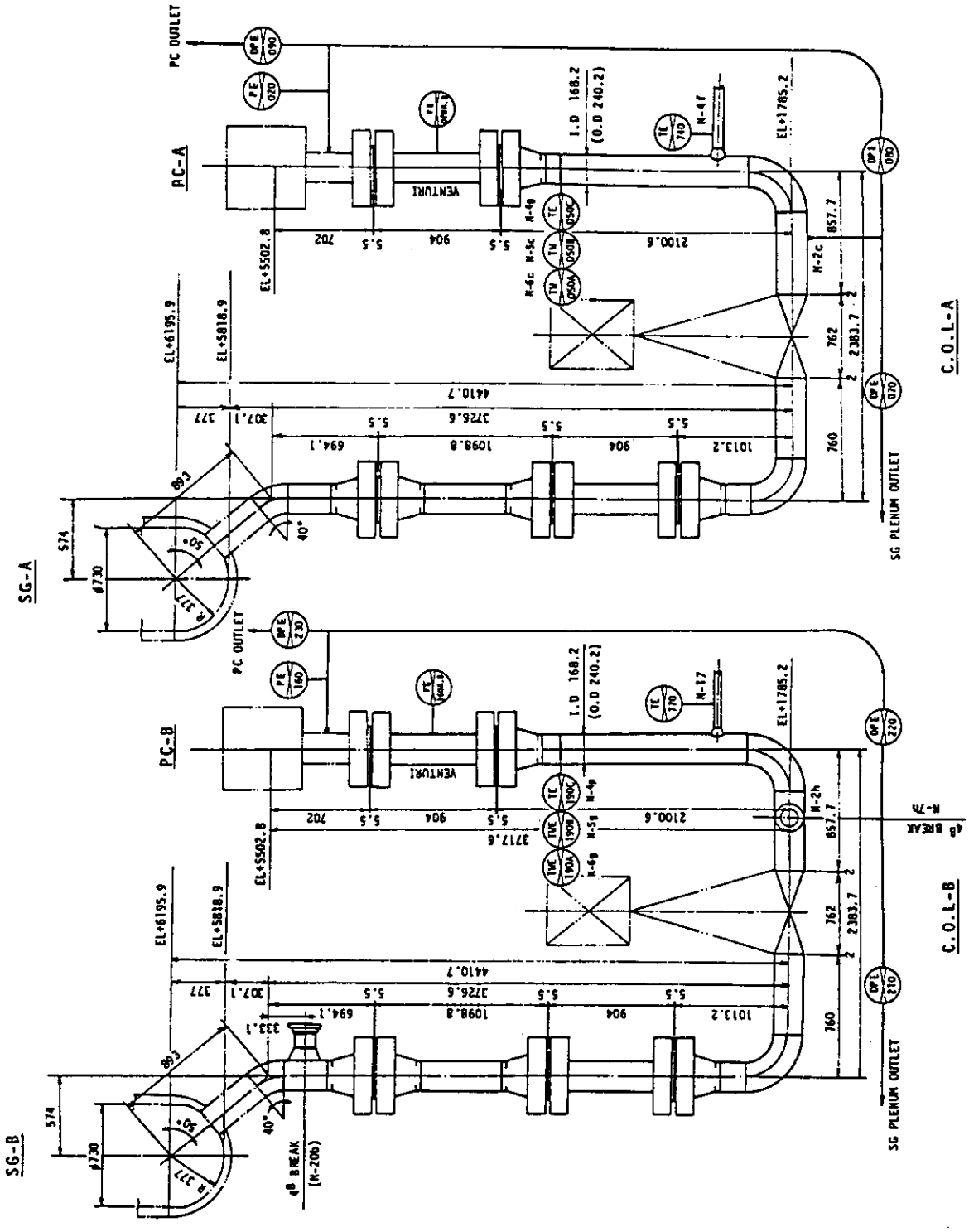

Fig.A.21 Locations of selected primary loop A and B instruments

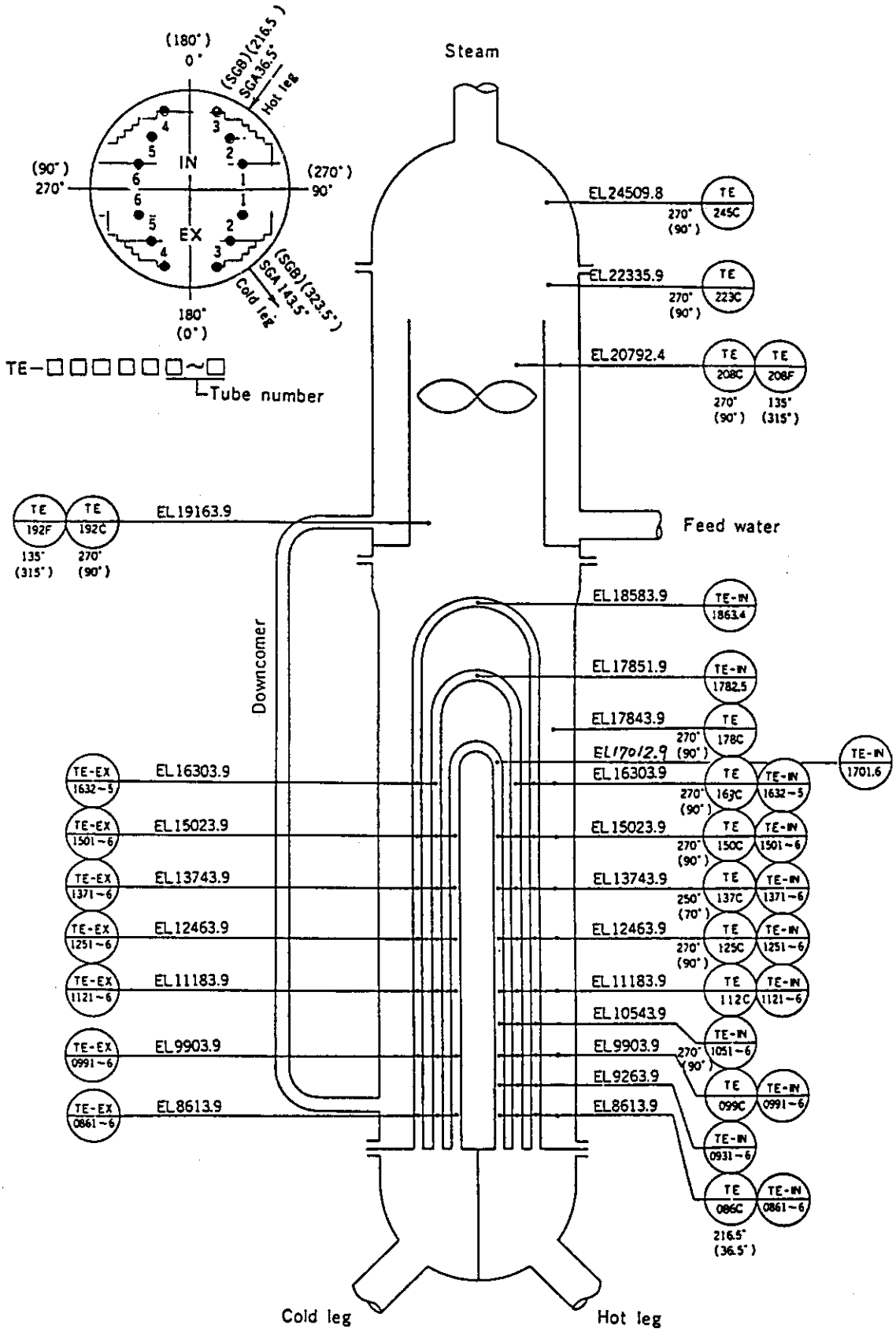

Fig.A.22 Locations of temperature measurements for steam generators A and B (I)

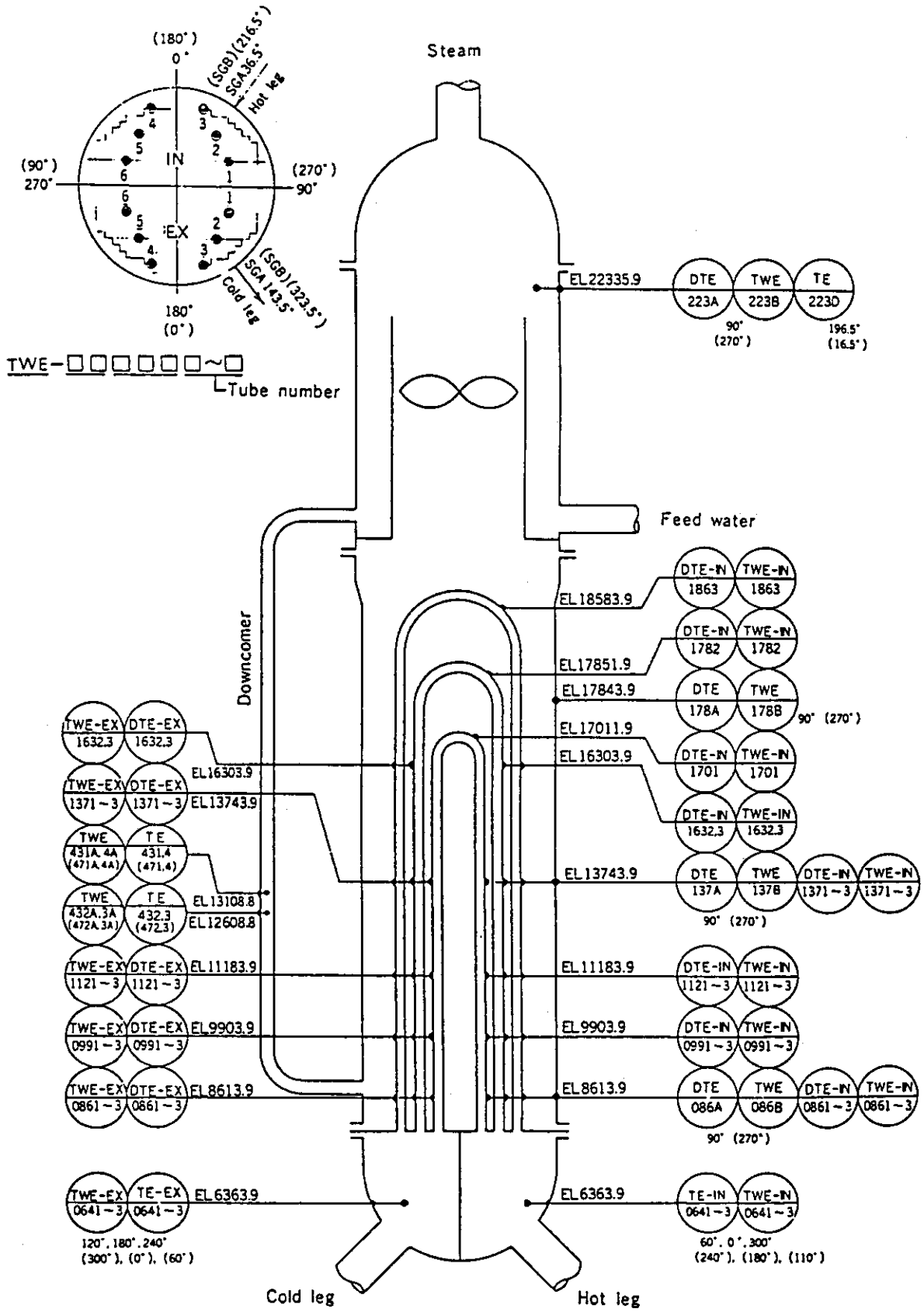

Fig.A.23 Locations of temperature measurements for steam generators A and B (II)

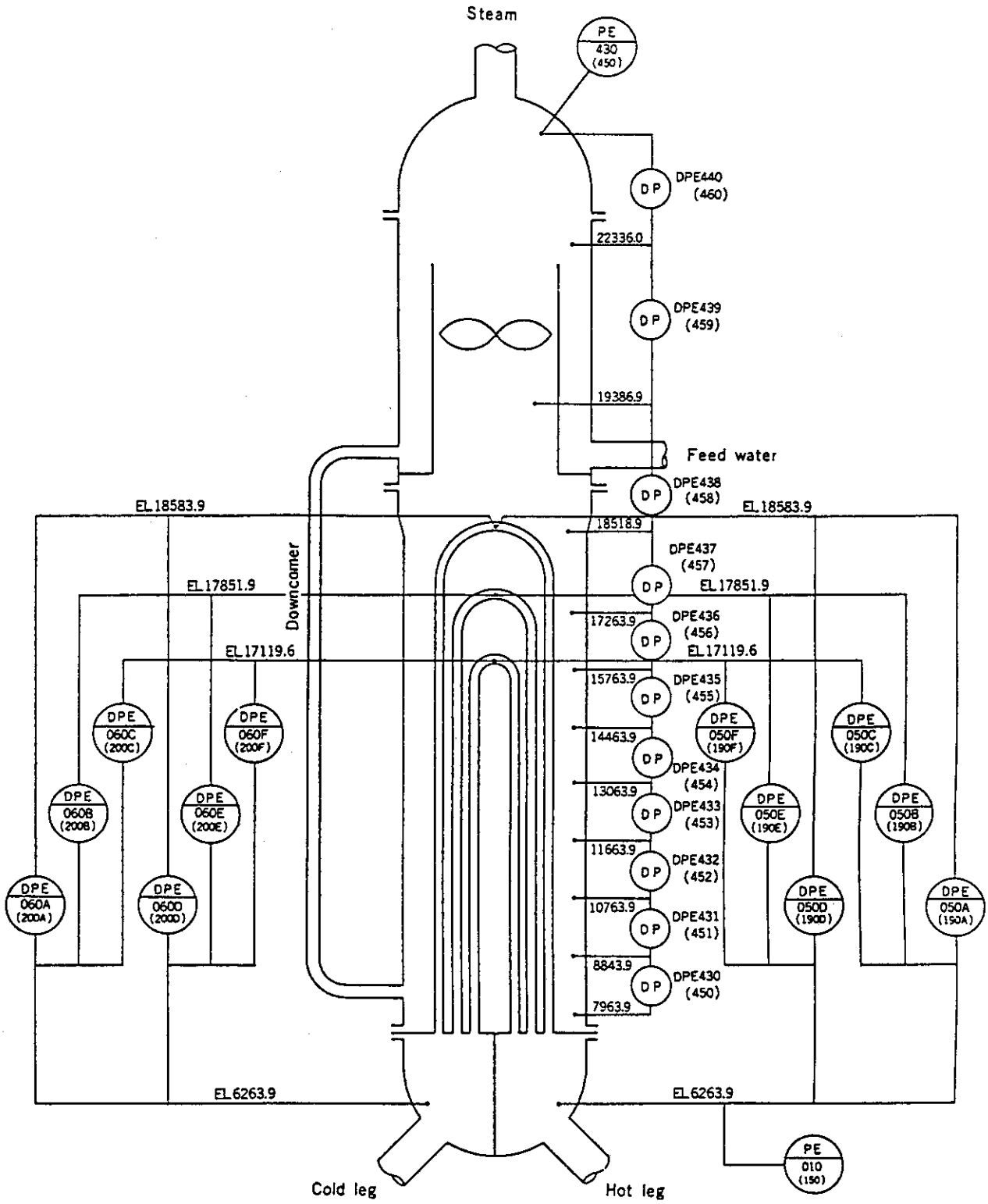

Fig.A.24 Locations of pressure and differential pressure measurements for steam generators A and B

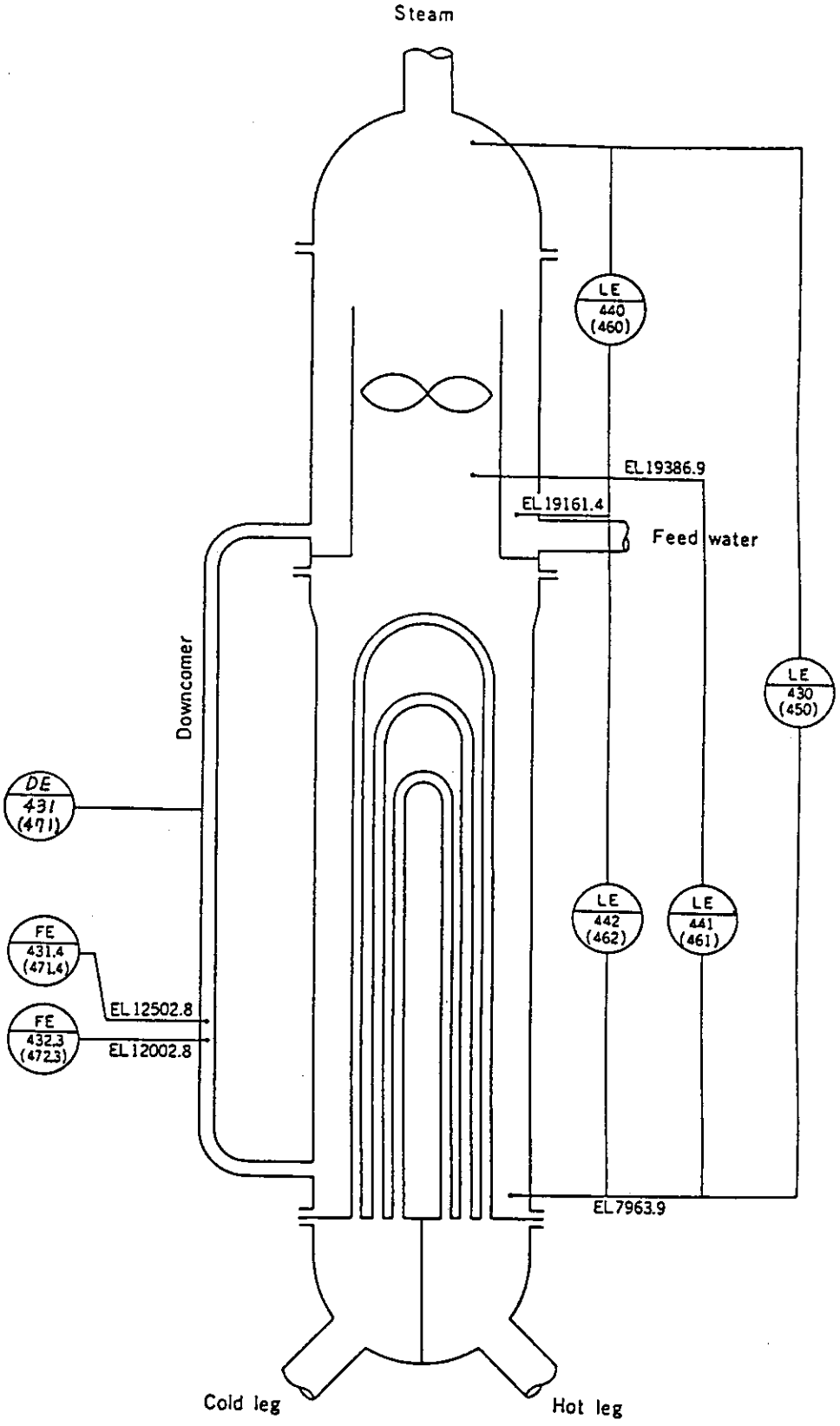

Fig.A.25 Locations of steam generatorss A and B secondary liquid level and downcomer flow measurement

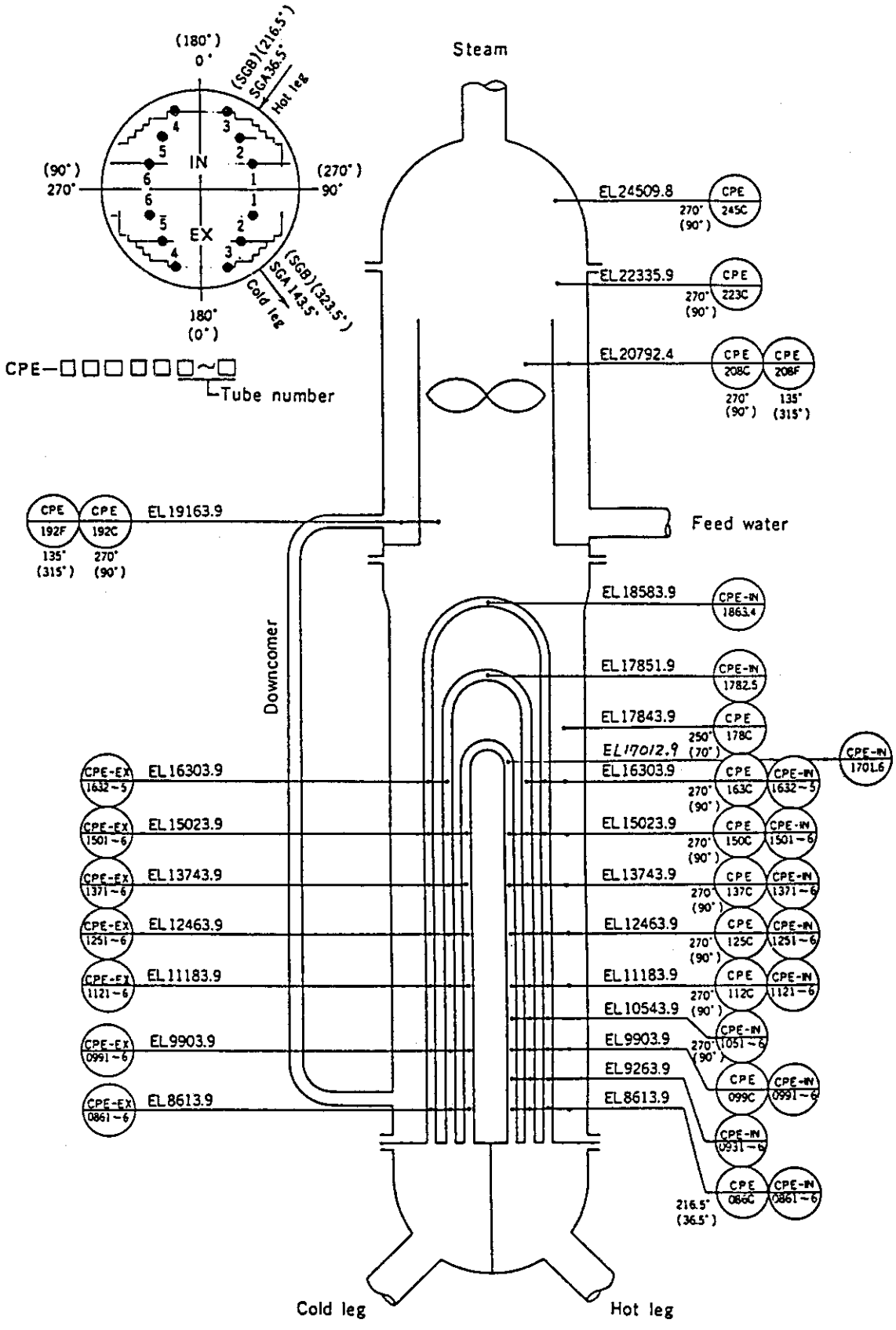

Fig.A.26 Locations of steam generators A and B conduction probe measurements

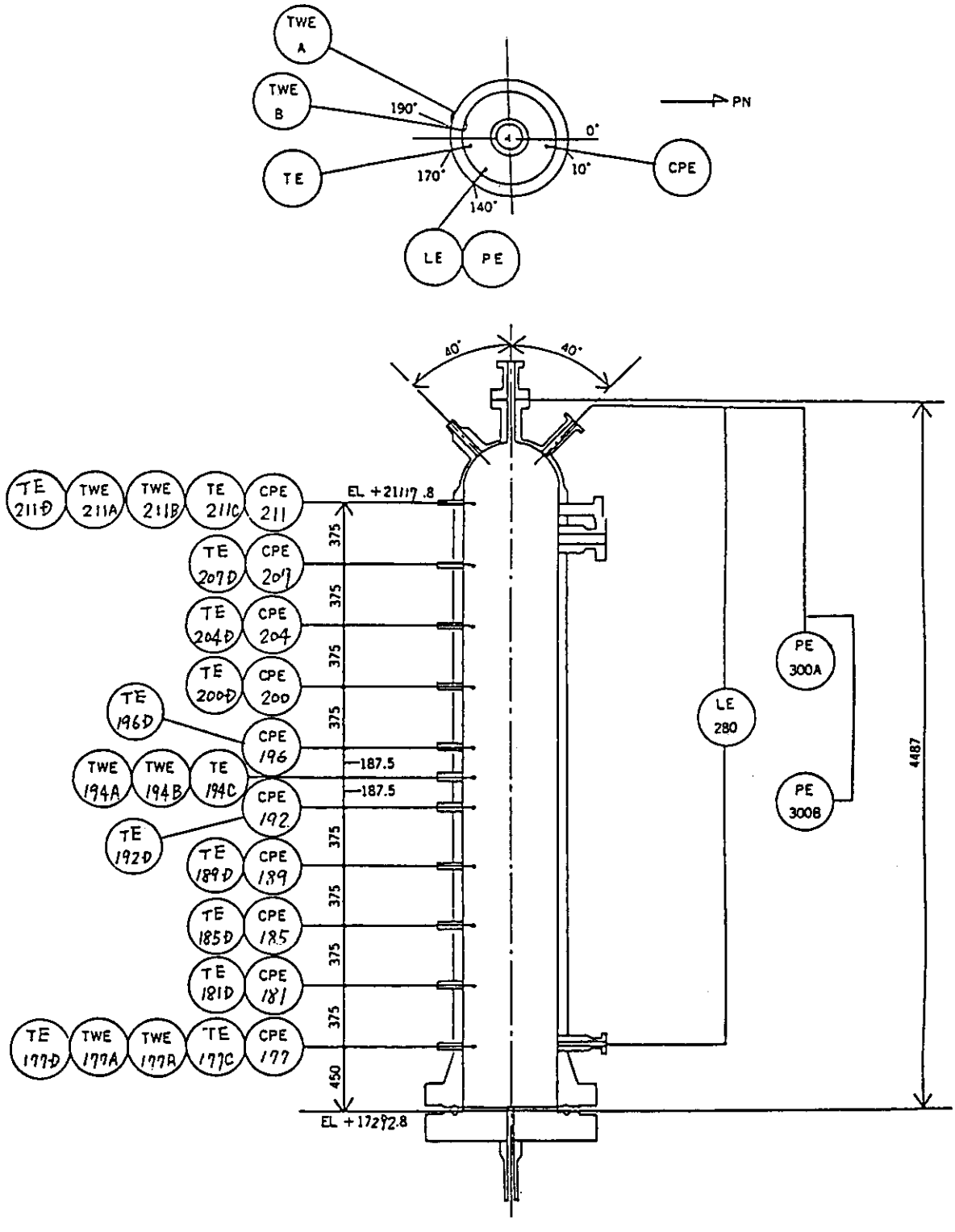

Fig.A.27 Locations of pressurizer measurements

Appendix B Experiment Description Summary for SB-PV-01

Experiment descriprion summary, blow down system flow diagram and ECCS injection schematics are shown below in Table B.1, Figs.B.1 and B.2, respectively.

List of Table and Figures

Table B.1 Experiment description summary for SB-PV-01
Fig.B.1 Blow down system flow diagram
Fig.B.2 ECCS injection schematics

Table B.1 Experiment description summary for SB-PV-01

I. Test Number: SB-PV-01

II. Test objectives:
To investigate characteristic features of pressure vessel bottom small break LOCA with break area of 0.5%.

III. Test type:
(A.) Break
1. Primary or secondary? : Primary
2. Size(s) (% and diameter in mm.) : 0.5% (7.2 mm ID)
3. Location(s) (see Figure 1) : PV Bottom
B. Operational transient
1. Type, e.g. loss of feedwater etc.
C. Other, e.g. natural circulation experiment, etc.
1. Type:

IV. Assumed plant equipment failure (summarize failed components including time of failure)
A. Valve failure
(B.) Auxiliary feedwater system
C. Control system failure
D. Pump failure
E. Emergency AC power
(F.) Other : HPI and charging systems are actuated by operator action after core dryout.

V. Initial and boundary conditions
A. Initial conditions
1. Primary system
a. Core Power
(1) Steady-state power level (MW) : 10.0
(2) Radial distribution (Case 1, 2 or 3) : 3
(Reference LSTF System Description, page 171)
b. Pressurizer pressure (MPa) : 15.43
c. Pressurizer water level (m) : 2.68
d. Downcomer to upper head leakage (kg/s) : 0.19
e. Loop characteristics

	Loop A	Loop B
(1) Flow rate (kg/s)	24.3	24.3
(2) Hot leg fluid temperature (K) :	598.5	598.7
(3) Cold leg fluid temperature (K) :	563.6	563.6
(4) Pump speed (Hz) :	25.05	26.12
(5) Flow control valve (% open) :	Full	Full
(6) Downcomer/hot leg leak (kg/s) :	0.053	0.045

2. Secondary system loop characteristics

a. Steam generator (SG) pressure (MPa) :	7.34	7.37
b. SG water level (m) :	10.7	10.5
c. Feedwater flow rate (kg/s) :	2.50	2.66
d. Steam flow rate (kg/s) :	2.59	2.68

Table B.1 Experiment description summary for SB-PV-01 (Cont'd)

e. Feedwater temperature (K) : 495.1 495.1

B. Trip setpoins

1. Reactor trip : (PR Pressure) 12.97 MPa
2. SI signals : (PR Pressure) 12.27 MPa
   a. HPIS : Operator Action (*)
   b. LPIS : SI + 17 s (1.29 MPa)
   c. Accumulators, initial & final level (m): 6.09/4.51
3. Secondary relief valves : 8.03 MPa/7.82MPa
4. Pressurizer power operated relief valve : ---
5. Pressurizer safety valve : 17.26 MPa/17.06 MPa
6. Main steam line isolation valves : Scram
7. Main feedwater termination : Scram
8. Auxiliary feedwater actuation : no
9. Pressurizer heaters off : break
10. Turbine bypass actuation : no
11. External heating of the pipes : break
12. Others.

C. Boundary conditions

1. Power decay curve : JAERI Curve
2. ECCS available - see Fig. 2

Type	Setpoints	Injection location & %	Time inj. began (s)
a. HPIS	Manual(*)	CLB	1676
b. LPIS	1.29 MPa	CLA/B(1:1)	-----
c. Accumulator	4.51 MPa	CLA	2057
d. Accumulator	4.51 MPa	CLB	2057
e. PJ	Manual(*)	CLA	1676

3. Pump coastdown : 83 s
4. ECCS temperature : 320 (ACC, ACH), 310 (PJ, HPIS, LPIS)
5. Steam generator relief valve orifice diameter : 19.4 mm
6. Steam generator discharge valve orifice diameter : 26.6 mm
7. Pressurizer relief valve orifice diameter : 6.83 mm
8. Pressurizer discharge valve orifice diameter : 14.5 mm

VI. Test and recovery procedure - attach if available

VII. Preliminary test chronology

A. List primary-events, e.g. time of break, assumed equipment failure, valve closures, pump startups, core heatup, core quench, etc.

B. Length of test

(*) Operator action for HPI and charging system actuations by detecting "high" hot leg fluid temperature than saturated temperature.

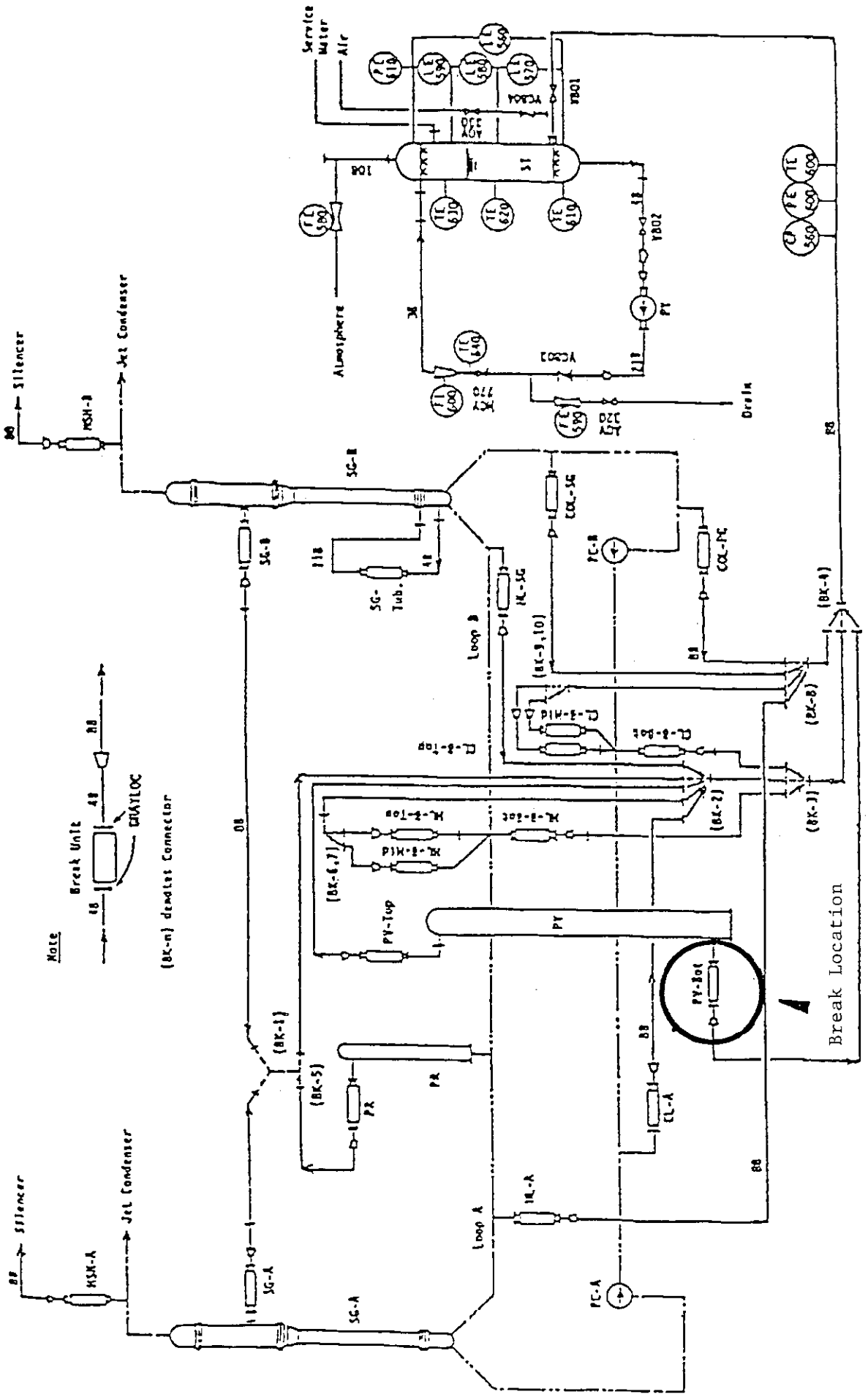

Fig.B.1 Blow down system flow diagram

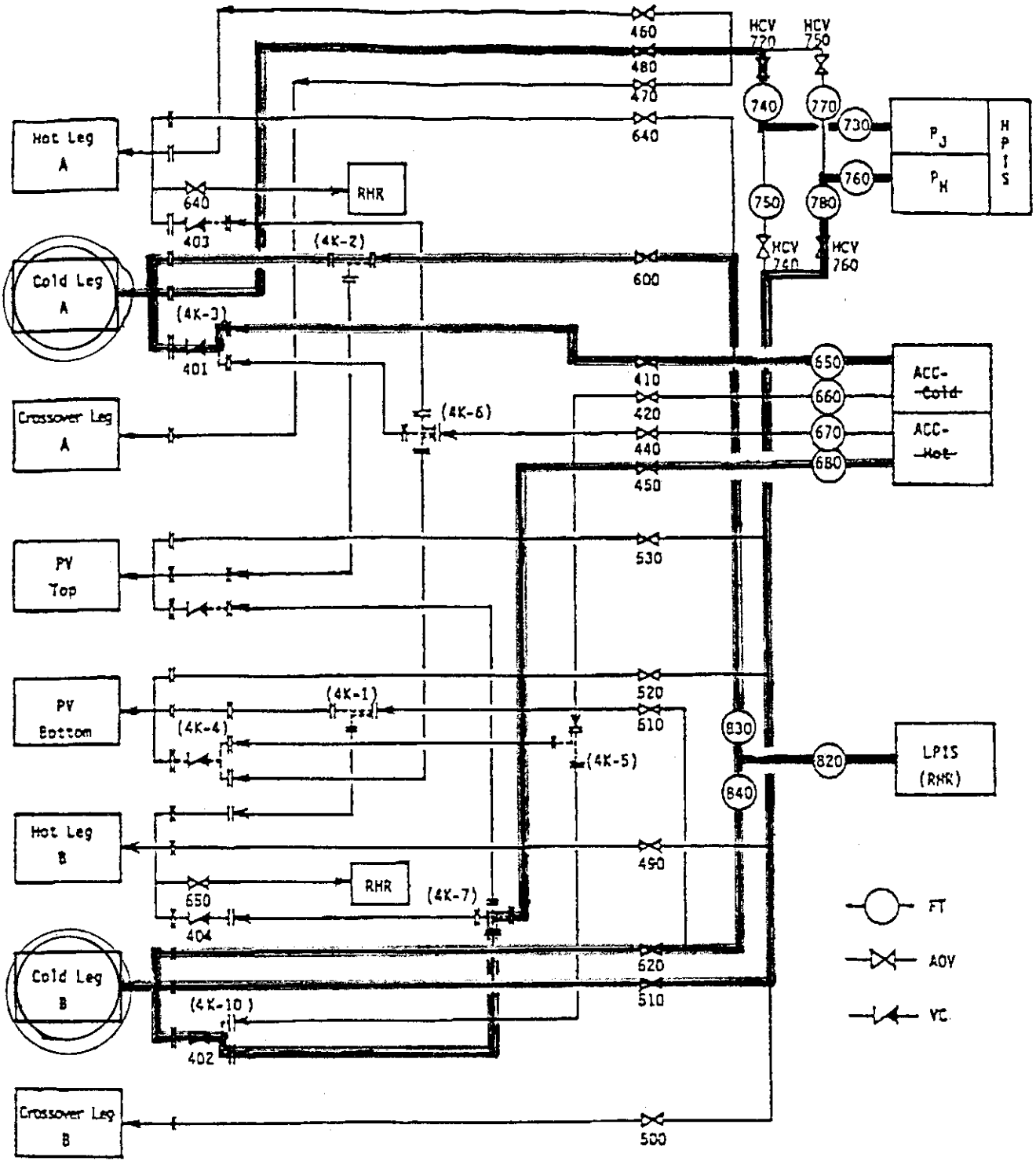

Fig.B.2 ECCS injection schematics

Appendix C Measurement List and All Experiment Data (Microfiches) for SB-PV-01

All of the experiment data measured in SB-PV-01 test are listed in Table C.1 and are shown in figures (both on microfiches). Included in the table are the Function ID, Tag Name, Measuring Span, Units, Uncertainty and Data Qualifications. The Function ID is explained in the section 2.2. Qualified data are classified into five parts in Table C.1, i.e., GOOD, BAD, QUESTIONABLE, UNQUALIFIED and UNUSED.

Appendix D Estimation of Remaining Primary Mass in SB-PV-01 Test before HPI Actuation (t = 1670 s)

The remaining primary fluid mass was directly estimated at the time of core dryout detection (1670 s) by using the experiment results. The steam phase in the upper components was in a saturated or super-heated condition. The water was in the saturated condition at 7.93 MPa. As shown in the lower plenum differential pressure data (see Fig.5.16), void fraction in the lower plenum was negligiblly small due to the almost stable thermal condition and no heat release into the fluid from the surrounding metal structures. This can be applied to water phase in the other regions. The fluid densities for the water and steam are as follows,

$\rho' = 723.5$ kg/m^3 ; for saturated water,

$\rho'' = 42.1$ kg/m^3 ; for saturated steam,

$\rho = 38.5$ kg/m^3 ; for steam at T = 590 K,

$\rho = 36.8$ kg/m^3 ; for steam at T = 600 K.

The water level in the hot leg region was derived from the fluid density data and the collapsed water level (L) for the other regions was calculated from the corresponding differential pressure (DP) data by using the following relation, as

$$DP = \rho' gL + \rho'' g(H - L),$$

where g is the gravitational constant and H is the DP measuring height for each region (m in unit).

As shown in section 5.4, the primary water remained mainly in the cross-over legs, downcomer and lower plenum (see Table 5.2).

The hot leg water level was derived from the cord density data (see Figs.5.10 and 5.12) of the Beam C. The cord density of the beam A or B showed a lower value than that of the saturated steam and the beam C density was 60 kg/m^3 in both loops, which corresponded to water level of 0.0125 m in height. This level was applied to all horizontal regions of the hot legs and the remaining water was obtained as 0.005 m^3.

The water levels in cross-over legs were calculated from the DP data shown in Figs.5.15(a) and (b). The down-flow side levels were 2.72 m for the loop-A and 2.59 m for the loop-B above the bottom of EL 1.79 m. The up-flow sides of both loops were filled completely by the water. As the

remaining water volume in two loops was 0.121 m^3 in the down-flow sides, 0.106 m^3 in the horizontal regions and 0.165 m^3 in up-flow sides, the total remaining water in the cross-over legs was 0.392 m^3. An uncertain value for the down-flow side volume was derived from the DP uncertainty as ± 0.002 m^3 in total.

In the SG plenum regions some amount of water could remain at the spheric bottom and it was 0.002 m^3 for two SGs.

The lower plenum water level was 1.37 m above the EL -1.80 m and it corresponded to 0.43 m below the core bottom. On the other hand, the downcomer water level was 1.59 m above the same level. Therefore, the lower plenum level was 0.22 m lower than the downcomer level at this time. By using the PV free volume data, which had been related to the PV height above the bottom (EL -2.36 m), the PV water volume between the bottom and the lower plenum level was obtained as 0.494 m^3. The downcomer water volume above the lower plenum level (EL -0.43 m) was 0.022 m^3. And the total remaining water volume in the lower plenum and downcomer was 0.516 m^3. As the nominal accuracies for the lower plenum and downcomer DPs were ± 0.07 m and ± 0.192 m, respectively, the PV volume uncertainty was ± 0.017 m^3 and that of the downcomer was ± 0.019 m^3. Thus the total uncertainty for these regions was ± 0.036 m^3.

The upper head water level at this time was assumed at the middle height of the lower well (EL 6.47 - 7.37 m). As the lower well free volume was obtained as 0.125 m^3, the remaining water volume and its uncertainty were derived as 0.063 m^3 and ± 0.062 m^3, respectively. This uncertainty was the largest among those of the primary components as shown in Table 5.7.

Thus the total primary water volume and its weight were,

$$V = 0.978 \pm 0.100\ m^3,$$

$$M = 708 \pm 72\ kg.$$

The steam mass in each primary component was estimated as shown in Table 5.7. The total steam mass was 292 kg. As the uncertainty for the steam volume was ∓ 0.100 m^3, the steam mass uncertainty was ∓ 4 kg. Therefore the total primary fluid mass (M_r) at 1670 s was obtained as,

$$M_r = 1000 \pm 68\ kg.$$